UNIVERSITAT DE BARCELONA

Invariant manifolds and transport in a Sun-perturbed Earth-Moon system

Begoña Nicolás Ávila

UNIVERSITAT DE BARCELONA

Invariant manifolds and transport in a Sun-perturbed Earth-Moon system

by

Begoña Nicolás Ávila

A thesis submitted
for the PhD Program in Mathematics and Computer Science

Advisor: **Àngel Jorba i Monte**

Department of Mathematics and Computer Science,
University of Barcelona,

January, 2022

Tesi presentada per na **Begoña Nicolás Ávila** per optar al grau de

Doctora en Matemàtiques i Informàtica

per la

Universitat de Barcelona

Certifico que la següent tesi
ha estat realitzada per en
Begoña Nicolás Ávila
sota la meva direcció.

Barcelona, gener de 2022.

Àngel Jorba i Monte

"Chaos is found in greatest abundance wherever order is being sought. It always defeats order, because it is better organised."

Terry Pratchett, Interesting times

Contents

Agradecimientos

Quisiera empezar agradeciendo a Àngel el haberme dado la oportunidad de hacer el doctorado con él aún sin conocernos y sin tan siquiera saber lo que era un objeto invariante. Gracias por tu confianza, siempre me has apoyado, motivado, y has tenido mucha paciencia con todas mis dudas, muchísimas gracias.

También quiero agradecer a mi familia, porque me han dado todo lo que he necesitado y mucho más. A mi padre, de quien he aprendido a ser tranquila y saber que por malo que sea el día siempre *debo recordar que habrá días como éste*. A mi madre, quien además de llevar adelante su clínica, tanto sabe de cocina, bricolaje, electricidad, costura,... por ti nunca he sentido que había ahí fuera algo que no era para mí. A mi hermano, por compartir a nuestros padres y todos esos momentos surrealistas y miradas cómplices que acaban en carcajadas, a veces con un velo de vergüenza.

Ahora me gustaría agradecer a muchas personas que me han acompañado a lo largo de la tesis y del camino que me ha llevado a ella, tanto académicamente como desde el ámbito más personal. Seguro que me quedan muchos nombres en el tintero, me disculpo de antemano.

A mis amigas de Carballo, por nuestras infinitas charlas, por todos los recuerdos de tantos años e historias imposibles, y porque aunque estemos dispersas por el mundo, siempre encontramos una buena excusa para volver, organizar una cena y ponernos al día como se merece.

A mis amigos de Santiago de Compostela, compañeros de la carrera y del máster, fue una de las mejores épocas y jamás lo olvidaré. Y aunque suene extraño, a Santiago en sí misma, a donde siempre me hace ilusión volver.

A mi familia de Barcelona. A Cati, la Quina, Blanca y los niños, por hacerme sentir en casa aún estando lejos.

A los profesores, compañeros y amigos de Barcelona. A Jaume por ser el salvador de numerosos problemas informáticos y todas las charlas de despacho sobre como funciona la UB, el mundo o los ordenadores. A Miquel, Joan Carles y Susana, por las clases y los momentos que hemos compartido. A Carles y Gerard, por sus trabajos, por sus preguntas y por sus respuestas, siempre con mucha amabilidad e interés. A Arturo, por todos los cafés acompañados de tertulias matemáticas de las que no entendía la mitad. Lo digo con cariño, pero ambos sabemos que es verdad. A Gladston por complementar mi personalidad y horarios, quiero creer que nos hemos afectado positivamente el uno al otro. A Marco, por formar parte de los *sistemas birrámicos* y por su sentido del humor. También agradecer en especial a Óscar, por lo que hemos compartido estos años.

A los compañeros de las comidas de los viernes, a Alex, Eloi, Ernest, Marc, Narcís, Dani, Giulia,... habéis ampliado considerablemente mi abanico culinario, sobretodo en lo que a comida asiática se refiere. Muchas gracias por las conversaciones, risas y consejos que acompañaban estas comidas. Y gracias de nuevo a Alex por ayudarme con todas las dudas burocráticas del doctorado y la defensa.

A los habituales del Seminario de Sistemas Dinámicos UB-UPC. A los compañeros del Chaotic Seminar, a Mar, Clara, Salvador, Iván, Ainoa... Y gracias a Joan, porque me encantaría tener tu capacidad organizativa, gracias por tu amistad y por las vivencias en Atlanta, parafraseándote "gracias a aquellos que me han conocido hasta ahora".

Also, I want to thank those who I met in Atlanta and that made nice my stays there; Simon, Jonathan, Cristel, Rafa,... and Wenwen, the best host I could have had.

Finalmente, agradecer al órgano burocrático que ha hecho esta experiencia posible. Esta tesis ha sido financiada por el Ministerio de Economía, Industria y Competitividad de España a través del Plan Nacional I+D+i (MTM2015-67724-R) y a través del contrato predoctoral para la formación de personal investigador BES-2016-078722.

Carballo, 7 de enero de 2022
Begoña Nicolás Ávila

Introduction

The study of the possible motions in an astrophysical system has always attracted lots of attention from the point of view of different branches of science. In particular, this dissertation is devoted to the analysis of the motion of small bodies, like asteroids, in the neighbourhood of the Earth-Moon system from a celestial mechanics approach. This analysis will give an insight of some transport phenomena that takes place in the system in a natural way and that can be also profitable for designing space missions, looking for reducing costs and increasing the efficiency on the manoeuvres.

The motion of a small particle of negligible mass subjected to the gravitational fields created by massive bodies is an extensive area of research. Many simplified mathematical models have been proposed and employed over the years, each of them focusing on different features of the real systems they attempt to describe. Simplified models allow us to describe the dynamics in the system of interest through the analysis of the invariant objects present on them, that are known to organise the dynamics of the system and hence, they provide meaning to the phenomena appearing on it.

Most widely studied dynamical systems are usually autonomous systems, since their independence on time makes them convenient for their analysis. However, considering any system as independent on time is generically a simplification, that eventually is tried to be addressed. The simplest way to introduce the time dependence in an autonomous system is through a time-periodic forcing. In this way, time can be regarded as an angular variable, $\theta \in \mathbb{T}$, and the perturbed system acquires one basic frequency. As consequence, the dimension of the dynamical system as well as the dimension of the invariant objects on it, increases by one, in such a way that the system under a time-periodic perturbation and its phase space inherits the main structures of the unperturbed system from which it comes.

The main objective of this dissertation is to study the dynamical transport in the Earth-Moon system and to develop tools that allow to understand it. Probably, the most extended simplified mathematical model employed in the analysis of these kind of systems is the well-known Restricted Three-Body Problem (RTBP), an autonomous model that describes the motion of an infinitesimal particle subjected to the gravitational fields of two punctual massive bodies, called the primaries, that are assumed to revolve in circular motion, see [Sze67].

Several modifications of this simplified model have been proposed, like introducing the eccentricity of the primaries, the accurate modelisation of the potential force in the vicinity of the massive bodies or adding other massive bodies that interact between them and affect the motion of the infinitesimal particle to create a restricted $(\mathcal{N}+1)$-body problem,... among these modifications the Bicircular Problem (BCP) is found, [Hua60, CRR64]. In this model a third punctual massive body is considered to revolve in circular motion around the original set up of the RTBP. Hence, the BCP can be understood as a RTBP plus a time-periodic forcing that affects the motion of the particle but not that of the primaries.

Since in the vicinity of the Earth-Moon system the gravitational effect of the Sun is too important to be negligible, we want to take it into account in our analysis and one of the simplest ways of doing

so is through a BCP that models the motion of a particle in the Earth-Moon system including the gravitational effect of the Sun as a time-periodic perturbation. Therefore, the Sun-Earth-Moon BCP as we consider it, has a basic frequency that accounts for the relative motion between the Earth-Moon barycenter and the Sun. The vast majority of this thesis is developed within the framework of this model.

To a lesser extent, this dissertation also deals with systems subjected to several time-dependent perturbations. Like the Simplified Solar System Models (SSSM) introduced in [GMM02, Mon01], where the Earth-Moon system is considered to be subjected up to five basic frequencies that account for the gravitational effect of the Sun over the particle and the primaries (Earth and Moon), the lunar eccentricity, the inclination between the orbital plane of the Moon and the ecliptic plane, and also the inclination between the orbital and equatorial planes.

In the case in which a system is subjected to any $\tilde{d} \geq 1$ time-periodic perturbations, the dimension of the system as well as the dimension of the invariant objects on it, increases by $\tilde{d}$, meanwhile the frequencies of the perturbations are non-resonant.

The simplest invariant objects that one can find in these time-dependent systems have the same dimension as the vector of basic frequencies of the system. For example, in the BCP the simplest invariant objects are periodic orbits, meanwhile in the case of the SSSM with 5 basic frequencies, the simplest invariant object is a five-dimensional quasi-periodic solution. Nevertheless, it must be noticed that other invariant objects of higher dimension than the simplest ones can be also found on these systems.

The persistence of quasi-periodic solutions present on Hamiltonian autonomous systems when the perturbations are introduced is one of the main questions to which KAM theory is devoted. This theory was originated in the 50's by Kolmogorov [Kol54], and continued by Arnold [Arn63a, Arn63b] and Moser [Mos62]. The outcome of their works was that most of the quasi-periodic solutions survive under the perturbation. The reason why some of the quasi-periodic solutions do not survive is concerned to their basic frequency vectors, such that one or more of their components are resonant with one or more of the frequencies introduced by the perturbation. In this case, it is said that the quasi-periodic solution is destroyed, leaving a space where chaotic motion takes place.

A common way to treat time-periodic (or quasi-periodic) dynamical systems is to take recurrent temporal sections by application of stroboscopic maps. Stroboscopic maps are a kind of temporal Poincaré maps obtained by the evaluation of the flow of the system at a time equal to the period of one of the basic frequencies of the system. Consequently, a continuous dynamical system becomes a discrete dynamical system where the dimension of its phase space is reduced by one.

On the Poincaré map, a dynamical system like the BCP, that only has one basic frequency, becomes autonomous and the simplest invariant solution that can be found on it is a fixed point. As mentioned, higher dimensional objects can be found. In particular, we are interested in the two-dimensional quasi-periodic solutions (2D invariant tori) of the flow that are seen as one-dimensional invariant curves in the suitable defined stroboscopic map. Computing and analysing the stability of invariant curves on maps is a covered topic. There are different methods for doing so, we especially highlight the works [CJ00, GJ04], where a Newton method is applied to find the parametrization of the invariant curves in terms of Fourier series, and [Jor01] where the linearised normal behaviour around these objects is treated.

The methods introduced in those works are suitable for invariant curves or invariant tori of relatively low dimension, since they involve not-sparse linear systems of dimension proportional to the dimension of the phase space and to the number of harmonics used to approximate the invariant curve or torus. Therefore, as the dimension of the torus increases, also does the dimension of the systems to work with and hence, the computational effort, sometimes up to an unaffordable point.

When the dimension of the invariant torus is high we can rely on other methods. The thesis of E. Olmedo, [Olm07], is focused on obtaining invariant tori of stroboscopic maps of any dimension equal or higher than 1 along with their stability at the same time. The process presented there requires the torus to be reducible, such that the system we need to solve to find the high dimensional quasi-periodic solutions is a sparse linear system of large dimension, that can be decoupled into many independent small dimensional linear systems, what is very suitable for parallelising the computations.

Under generic conditions, if the invariant torus (or invariant curve) is hyperbolic, it has stable and unstable invariant manifolds associated. Stable manifolds approach the quasi-periodic solutions forward in time, meanwhile unstable manifolds do it backward in time. Therefore they constitute the skeleton for the dynamical transport phenomena that we are interested in analyse.

The linear approximation to the stable and unstable invariant manifolds of a quasi-periodic solution can be found as eigenfunctions of a suitable operator. For many scientific objectives, the linear approximation of these manifolds is enough, however sometimes it is necessary to resort to a higher order approximation. The parametrization method allows to write an approximation of invariant objects up to any order, however, this involves high order derivatives of the system, whose computation may suppose a delicate and burdensome task. In [GJJC$^+$21], J. Gimeno et al. develop an automatic differentiation method for computing the derivatives of a system on Poincaré maps leaning on the jet transport technique. They apply this tool to compute the parametrization of the stable/unstable invariant manifolds associated with fixed points of maps. In the present dissertation, we rely on the tool developed by these authors to introduce and carry out a computational method to obtain the high order parametrization of the invariant manifolds associated with invariant curves, as well as with reducible invariant tori of high dimension, that are approximated as formal Taylor-Fourier expansions.

As announced, most of the effort of the present work is addressed to the analysis of the Earth-Moon Bicircular Problem, where the system only has one perturbing frequency and where we focus on invariant curves of a stroboscopic autonomous map. Besides, following the results of [Olm07] we introduce a method to compute in parallel the high order parametrization of the stable/unstable invariant manifolds of reducible tori of high dimension. Therefore, in spite of most of the contents are devoted to a simpler case, we give the general basis of dynamical systems subjected to any number of forcing frequencies, since we will need it for the last part of the dissertation.

Then, in Chapter 1 we aim to introduce all the definitions needed for the analysis of the dynamical systems subjected to any number of quasi-periodic perturbations. It contains some basic definitions and properties of quasi-periodic systems, including the treatment of temporal Poincaré maps, the quasi-periodic solutions (or invariant tori) present on these maps and the high order parametrization of the stable/unstable invariant manifolds associated with those tori that are partially hyperbolic. This chapter finishes with the collection of all the computational details for finding invariant curves and their hyperbolic invariant manifolds in autonomous maps. In particular we introduce the idea of the *fundamental cylinders*, that are fundamental domains of the stable and unstable invariant manifolds associated with invariant curves. These manifolds, in the map, can be parametrized by only two parameters, what allows to visualise in a relatively simple way the general dynamics governed by these manifolds.

Chapter 2 is devoted to the description of the Bicircular Problem for the Earth-Moon system under the solar gravitational field perturbation. This model has been employed in previous works, then we will summarise what is done so far and what are some of the uncovered topics. More precisely, we have extensively treated the neighbourhood of the collinear unstable equilibrium point L_3. Then, in this chapter the horizontal and vertical families of quasi-periodic solutions around this point are presented. Besides, we will talk about the quasi-periodic solutions near the triangular points since we aim to extend the knowledge about them.

This general chapter about the Earth-Moon BCP also includes a detailed description of a non-autonomous change of coordinates to translate the coordinates of a particle in the BCP into a more

realistic model. This will be very useful when making comparisons between the simplified and realistic models.

The applications to the Earth-Moon BCP constitute the most extensive part of this dissertation and they are presented in the following three chapters.

Chapter 3 is focused on the dynamical transport that takes place in this model through L_3. It is found that diverse trajectories connecting the Earth, the Moon and the outside Earth-Moon system are governed by L_3 dynamics. Big attention is paid to the trajectories coming from the Moon towards the Earth, since they may give an insight of the travel that lunar meteorites perform before landing in our planet. These results have been translated and compared with those of a realistic model based on JPL (Jet Propulsion Laboratory) ephemeris. The comparisons indicate that the BCP is capable of reproducing to a good extent the dynamics of the more realistic system. Also, we have found the possible explanations of some appearing discrepancies between the results of the two models.

Chapter 4 is devoted to the study of the capture of a Near Earth Asteroid (NEA) using the stable invariant manifolds of the horizontal family of quasi-periodic orbits around L_3. A general strategy involving the high order parametrization of the stable/unstable invariant manifolds is defined. Then its application is carried out for the NEA 2006 RH120 arising promising results, including a possible capture manoeuvre of the order of 20 m/s.

In Chapter 5, we present two other contributions to the BCP. The first one has the objective of studying the unstable behaviour near the triangular points, meanwhile the second is devoted to a family of stable invariant curves around the Moon that are close to a resonance, what aids the appearance of chaotic motion. This chapter finishes our analysis in the framework of the BCP.

Chapter 6 is devoted to the study of dynamical systems under several time-periodic perturbations. Here we explain how to effectively compute in parallel the high order parametrization of the stable and unstable invariant manifolds associated with reducible invariant tori of any dimension. In addition, the methods presented in this chapter are combined with multiple shooting techniques to accurately compute highly unstable invariant objects. This chapter is a joint work with Dr. Gimeno and Dr. Olmedo.

Finally, some conclusions and further work are discussed.

Chapter 1

Invariant objects and stroboscopic maps

This chapter is devoted to the concepts and some theoretical aspects we need to analyse dynamical systems that depend on time in a quasi-periodic way. This kind of temporal dependence admits a reformulation of the dynamical system in terms of angular variables instead of in terms of the time.

Once the dynamical system is expressed in terms of angular variables, the period associated with one of them can be used to define a temporal Poincaré map that corresponds to a discretization of the dynamical system that depends on one angular variable less.

Then, Section 1.1 describes the steps towards the discretization of the dynamical system. Section 1.2 is focused on the quasi-periodic solutions, usually called invariant tori, that are present in those systems and how to analyse the linear behaviour around them. For those quasi-periodic solutions that are hyperbolic, the description of the high order parametrization of their stable and unstable invariant manifolds is given in Section 1.3. There we talk about a computational tool known as "jet transport", that is really helpful for obtaining the high order derivatives of the map, required by the computation of the high order parametrization.

Since most of the present dissertation concerns about two-dimensional invariant tori, that are seen as one-dimensional invariant curves in the temporal Poincaré map, Section 1.4 contains all the details for the computation of those quasi-periodic orbits as well as for their associated hyperbolic manifolds. This section is the basis for the computations and analysis presented in Chapters 2, 3, 4 and 5.

The computational details for the case of reducible invariant tori of any high dimension are presented at the end of the dissertation, in Chapter 6. For this reason, the first sections of the present chapter, that constitutes the theoretical basis for both situations are developed for the most general case, i.e. a dynamical system that depends on several angular variables.

1.1 Discretizing a quasi-periodic dynamical system

Let us consider a dynamical system defined by a differential equation,

$$\dot{x} = f(x, t), \tag{1.1}$$

where $t \in \mathbb{R}$ denotes the time, $x \in \mathbb{R}^n$ denotes a n-dimensional vector and

$$f : \mathbb{R}^n \times \mathbb{R} \mapsto \mathbb{R}^n, \tag{1.2}$$

is a smooth enough function.

Definition 1.1.1. *A function f as in (1.2), is said to be **quasi-periodic** if there exits a natural number $d \geq 0$ and a function $F(x, \theta)$ with $\theta \in \mathbb{T}^{d+1}$,*

$$F : \mathbb{R}^n \times \mathbb{T}^{d+1} \mapsto \mathbb{R}^n, \tag{1.3}$$

such that F is periodic on each angular variable θ_j, with $j = 0, ..., d$ and

$$f(x, t) = F(x, \omega t), \tag{1.4}$$

being $\omega = (\omega_0, ..., \omega_d) \in \mathbb{T}^{d+1}$ the vector of basic frequencies of the system, whose components are considered to be linearly independent over the rationals.

Then, assuming the function f to be quasi-periodic, the dynamical system can be expressed as

$$\begin{cases} \dot{x} = F(x, \theta), \\ \dot{\theta} = \omega, \end{cases} \tag{1.5}$$

where $\theta = (\theta_0, ..., \theta_d) \in \mathbb{T}^{d+1}$. The simplest quasi-periodic solutions present on a system like this are defined by the same frequencies than the vector of basic frequencies of the system, therefore they are of dimension $d + 1$. Moreover, other quasi-periodic solutions of dimension higher than $d + 1$ can be found on a dynamical system like this.

Let us consider a quasi-periodic solution of the continuous dynamical system with frequencies equal to those of the vector of basic frequencies of the system. Then, there exists a function $\Psi : \mathbb{T}^{d+1} \mapsto \mathbb{R}^n$ that is a quasi-periodic solution, or invariant torus, of the dynamical system (1.5) and that has $d + 1$ angular dimensions and basic frequency vector $\omega \in \mathbb{T}^{d+1}$. Then, it must satisfy

$$\phi_{t_0}^{t^*}(\Psi(\theta), \theta) = \Psi(\theta + (t^* - t_0)\omega), \tag{1.6}$$

where $\phi_{t_0}^{t^*}$ denotes the flow of the system (1.5) from time $t = t_0$ to $t = t^*$.

Since function F is periodic on each θ_j with $j = 0, ..., d$, one angular dimension can be reduced by imposition of a suitable temporal Poincaré map that makes one of these angular variables to be constant on the map. Then, applying this map as many times as we want to the continuous dynamical system, it allows to show a discrete dynamical system of one angular dimension less. These kind of temporal Poincaré maps are also known as stroboscopic maps.

Let $\tilde{P}$ be a diffeomorphism of an open set $\mathcal{U} \subset \mathbb{R}^n$,

$$\tilde{P} : \mathcal{U} \mapsto \mathcal{U}, \tag{1.7}$$

such that

$$\tilde{P}(x, \theta) := \phi_{t_0}^{t_0+\delta}(x, \theta),$$

also written as

$$\tilde{P}(x, \theta_0, ..., \theta_d) := \phi_{t_0}^{t_0+\delta}(x, \theta_0, ..., \theta_d), \tag{1.8}$$

where $\phi_{t_0}^{t_0+\delta}$ is the flow of the system (1.5) from time $t = t_0$ to time $t = t_0 + \delta$, being $\delta = \frac{2\pi}{\omega_0}$, that is the period of the angular variable θ_0. Then, when this map is applied to a quasi-periodic solution of the system (1.5), Ψ with $d + 1$ dimensions,

$$\tilde{P}(\Psi(\theta_0, ..., \theta_d), \theta_0, ..., \theta_d) = \Psi(\theta_0, \theta_1 + \rho_1, ..., \theta_d + \rho_d), \tag{1.9}$$

the solution Ψ is rotated a certain quantity, called rotation number $\rho_j = \frac{2\pi\omega_j}{\omega_0}$ for $j = 1, ..., d$, on each of its angular variables except on one, θ_0, that has become constant over the map.

Let $\varphi : \mathbb{T}^d \mapsto \mathbb{R}^n$ be a quasi-periodic solution on the map $\tilde{P}$. It has d dimensions since it does not depend on θ_0:

$$\varphi(\theta_1, ..., \theta_d) = \Psi(0, \theta_1, ..., \theta_d). \tag{1.10}$$

By defining a new map that also depends on an angle less

$$P(x, \theta_1, ..., \theta_d) := \tilde{P}(x, 0, \theta_1, ..., \theta_d), \tag{1.11}$$

and denoting with an upper bar ($\bar{}$) the image under P, the system in (1.5) can be written as the following discrete dynamical system

$$\begin{cases} \bar{x} = P(x, \theta), \\ \bar{\theta} = \theta + \rho, \end{cases} \tag{1.12}$$

where now $\theta = (\theta_1, ..., \theta_d) \in \mathbb{T}^d$ and ρ is also a d-dimensional vector where each component $j = 1, ..., d$, corresponds to $\rho_j = \frac{2\pi\omega_j}{\omega_0}$ and satisfies that $\langle \kappa, \rho \rangle \neq 2\pi k$ for $\kappa \neq 0$, where $\langle \cdot, \cdot \rangle$ denotes the scalar product, $\kappa \in \mathbb{Z}^d$ and $k \in \mathbb{Z}$.

1.2 Invariant tori

A quasi-periodic solution on the map (1.12), φ with dimension d, must satisfy the invariance condition over the map

$$\varphi(\theta + \rho) = P(\varphi(\theta), \theta). \tag{1.13}$$

If $d > 0$ no fixed points can be found in a system like (1.12), and then the simplest invariant set that can be found in that system is an invariant torus of dimension d, parametrized by the angle $\theta \in \mathbb{T}^d$ and that must satisfy invariant condition (1.13). Besides, as already mentioned, other invariant objects of dimension higher than d may be also found in this system.

Observation 1.2.1. *If $d = 0$, the case of a dynamical system (1.5) that only depends on one angular variable, the simplest solutions of the flow are one-dimensional (periodic orbits), that are seen as fixed points of the map P, that in this case becomes autonomous. Then, the system can be written as*

$$\bar{x} = P(x). \tag{1.14}$$

Note that apart from the periodic orbits, one can find in this system quasi-periodic solutions of higher dimension. For example, let us consider a two-dimensional torus of the flow, such that in the map P it is seen as an invariant curve, torus of dimension one, $\varphi : \mathbb{T} \mapsto \mathbb{R}^n$, that also must satisfy an invariance condition over the autonomous map

$$\varphi(\theta + \rho) = P(\varphi(\theta)), \tag{1.15}$$

with $\theta \in \mathbb{T}$ and $\rho \in \mathbb{T}$. This case is discussed in Section 1.4.

Let us continue with the exposition for the general case with $d \geq 0$. In order to study the linear behaviour around a quasi-periodic solution $\varphi : \mathbb{T}^d \mapsto \mathbb{R}^n$, it is usual to take a small displacement, $h \in \mathbb{R}^n$, from a point on the torus $\varphi(\theta)$ and apply the map:

$$P(\varphi(\theta) + h(\theta), \theta) = P(\varphi(\theta), \theta) + D_x P(\varphi(\theta), \theta) h(\theta) + \mathcal{O}(||h||^2), \tag{1.16}$$

where $P(\varphi(\theta),\theta) = \varphi(\theta+\rho)$ and $A(\theta) = D_x P(\varphi(\theta),\theta)$ is the Jacobian of the Poincaré map on φ, such that $h(\theta) \mapsto D_x P(\varphi(\theta),\theta)h(\theta)$.

Renaming h as x, the linear normal behaviour around the quasi-periodic solution can be expressed by the linear skew-product

$$\begin{cases} \bar{x} = A(\theta)x, \\ \bar{\theta} = \theta + \rho. \end{cases} \tag{1.17}$$

Definition 1.2.2. *The system (1.17) is said to be* ***reducible*** *if and only if there exists a continuous change of variables (real or complex) of the form $x = C(\theta)y$ such that (1.17) becomes*

$$\begin{cases} \bar{y} = By, \\ \bar{\theta} = \theta + \rho, \end{cases} \tag{1.18}$$

where the matrix

$$B = C^{-1}(\theta+\rho)A(\theta)C(\theta), \tag{1.19}$$

does not depend on θ. The matrix B is called the Floquet matrix and $x = C(\theta)y$ is the Floquet transformation.

Notice that the Floquet matrix B is a constant matrix that contains the dynamical information of the system in (1.17), and then, its eigenvalues give the linear stability around the quasi-periodic solution.

Remark 1.2.3. *Analogously, the linearisation of the system around the quasi-solution $\Psi : \mathbb{T}^{d+1} \mapsto \mathbb{R}^n$ is written as*

$$\dot{x} = \mathfrak{a}(\Psi,t)x \tag{1.20}$$

where $\mathfrak{a}(\Psi,t) = D_x f(\Psi(t),t)$. We will say that Ψ is a reducible quasi-periodic solution of (1.1) if there exists a change of variables $x(t) = \mathfrak{c}(\Psi,t)y(t)$ that transforms (1.20) into

$$\dot{y} = \mathfrak{b}y, \tag{1.21}$$

where $\mathfrak{b}$ is a constant matrix.

Then, Floquet matrix B for transforming the system (1.17) into (1.18) corresponds to

$$B = \exp\{\delta\mathfrak{b}\} \tag{1.22}$$

where δ denotes the time used to define the temporal section P and $\mathfrak{b}$ is the Floquet matrix for transforming (1.20) into (1.21).

In [Jor01] a characterisation of the reducibility is introduced. This characterisation is based on the analysis of the generalised eigenvalue problem to find couples of eigenvalue, λ, and eigenfunction, ψ, $(\lambda,\psi) \in \mathbb{C} \times (\mathcal{C}(\mathbb{T}^d,\mathbb{C}^n)/\ \{0\})$ that satisfy

$$A(\theta)\psi(\theta) = \lambda T_\rho \psi(\theta). \tag{1.23}$$

Definition 1.2.4. *T_ρ is an operator that applies a rotation corresponding to the rotation vector,*

$$T_\rho : \psi(\theta) \in \mathcal{C}(\mathbb{T}^d,\mathbb{C}^n) \mapsto \psi(\theta+\rho) \in \mathcal{C}(\mathbb{T}^d,\mathbb{C}^n).$$

It is said that two eigenvalues λ_1 and λ_2 of (1.23) are ρ-unrelated iff $\lambda_1 \neq \exp(i\kappa\rho)\lambda_2$, $\forall\kappa \in \mathbb{Z}^d$. Then, the statement made in [Jor01], and proved there, is the following: if there exits n ρ-unrelated

eigenvalues $\lambda_1, ..., \lambda_n$ for the generalised eigenvalue problem (1.23), then the system (1.17) can be reduced to (1.18), where the n eigenfunctions are used to construct the matrix for the Floquet change.

If the quasi-periodic solution is reducible, the system to find it can be written in a diagonal form, what makes it very suitable for its computational implementation in parallel, as it is described in [Olm07, JO09] and as we will summarise in Chapter 6.

If on the contrary, we do not wish to (or we can not) use the reducibility of the quasi-periodic solution, it is necessary to work with the system in (1.23) as a whole, that may or may not be of large dimension. This case will be explained in detail for invariant curves in Section 1.4.2.

Besides, it may happen that some part or parts of the system may be reducible meanwhile others may not. In this case it is possible to divide the system into different systems and apply the reducibility only when it is convenient to do so, see [HdlL06a, HdlL07].

In any case, given a particular torus of the map, the analysis of (1.23) leads to a set of n ρ-unrelated eigenvalues.

- If all the eigenvalues have modulus equal to 1, the torus is said to be totally elliptic.
- If all the eigenvalues have modulus different from 1 the torus is said to be totally hyperbolic.
- If some eigenvalues have modulus equal to 1 and others different from 1, the torus has centre parts and saddle parts, respectively.

This dissertation is focused on those tori that have one real saddle part, i.e. a pair of real eigenvalues $(\lambda_s,\ \lambda_u)$ such that $\lambda_s < 1$ is a stable eigenvalue and $\lambda_u > 1$ is an unstable eigenvalue. Besides, if the system is Hamiltonian, the relation $\lambda_s = \lambda_u^{-1}$ holds.

For these partially hyperbolic tori, a stable (and an unstable) invariant manifold grows from the torus in the stable (or unstable) eigendirection. They represent ways of approaching the invariant torus and of getting away from it, generating a structure to study the dynamical transport through those quasi-periodic solutions, what is of great interest for many applications.

1.3 High order parametrization of invariant manifolds

In this section we introduce the parametrization of stable and unstable invariant manifolds associated with invariant tori that have a saddle part. Stable invariant manifolds, W_s, are defined by the set of points that are sent towards the invariant tori forward in time, while unstable invariant manifolds, W_u, are defined by the set of points that are sent towards the tori backward in time.

The pairs of stable or unstable eigenvalue and eigenfunction $(\lambda_{s,u},\ \psi_{s,u})$ of (1.23) give the linear approximation of the stable or unstable invariant manifolds, respectively. For a given $\theta \in \mathbb{T}^d$, taking a small displacement $\sigma \in \mathbb{R}$ (positive or negative) from the point on the torus $\varphi(\theta)$,

$$(\theta, \sigma) \mapsto \varphi(\theta) + \sigma\psi_{s,u}(\theta), \tag{1.24}$$

gives the parametrization of the linearisation of the manifolds of the torus. This is an approximation of the true invariant manifolds with an error of the order of $|\sigma|^2$.

In order to improve the approximation of the invariant manifolds we make use of the well-known parametrization method. C. Simó used this method in the 80's to numerically compute approximation of the invariant manifolds of equilibrium points of ODEs and of fixed points of maps (see also [FR81]).

A salient feature of this method is that it can be used to prove the existence of invariant manifolds, as shown by X. Cabrè, E. Fontic and R. de la Llave [CFdlL03a, CFdlL03b, CFdlL05]. In [HdlL06b], authors consider the parametrization of stable and unstable invariant manifolds of an invariant curve on a quasi-periodic map. Recent book [HCL$^+$16] gives a very good exposition on the topic and collects the main results.

The particular interest in the present dissertation regarded to the parametrization method is focused on effective computation of the approximation of stable and unstable invariant manifolds associated with invariant tori on quasi-periodic maps. High order derivatives of the map are involved in this task, and to write their expressions by hand may not be feasible or at least, burdensome. To address this problem, we follow the ideas introduced in [GJJC$^+$21] developed an algorithm for the automatic differentiation of Poincaré maps based in the commonly called "jet transport technique" [BM98, AFJ$^+$08]. Some details about this tool are given at the end of this section, in Section 1.3.1. To stress the utility of the combination of the parametrization method with the jet transport, [GJJC$^+$21] includes some examples for the invariant manifolds of fixed points of maps.

For a better understanding of the subsequent explanations about the parametrization of invariant manifolds associated with invariant tori of stroboscopic maps, we briefly show the equivalent procedure for the case fixed points of maps. Remember that we can only find fixed points of stroboscopic maps in the case of autonomous maps (that is when $d = 0$), see Observation 1.2.1.

Invariant manifolds of fixed points of maps

Let us consider a hyperbolic fixed point, x_0, of an autonomous map, P. We assume that there exists a one-dimensional invariant manifold, that is C^∞, associated with this fixed point and that it can be written as a Taylor power expansion:

$$W(\sigma) = a_0 + a_1\sigma + a_2\sigma^2 + a_3\sigma^3 + ... = \sum_{k\geq 0} a_k\sigma^k, \tag{1.25}$$

where $\sigma \in \mathbb{R}$.

Notice that, the dimension of the parameter σ is given by the number the hyperbolic directions considered for the manifold. In this dissertation, only the case in which σ is one-dimensional is considered. The case of invariant manifolds with several hyperbolic directions associated with fixed points of Poincaré maps is detailed in [GJJC$^+$21]. Notice that in that case, k is a multi-index.

When applying P to the invariant manifold, it must satisfy the invariance condition:

$$P(W(\sigma)) = W(\lambda\sigma), \tag{1.26}$$

being λ a hyperbolic eigenvalue of x_0 to which eigenvector $v \in \mathbb{R}^n$ is associated.

Solving (1.26) order by order we find the expressions for the coefficients a_k:

- Order 0: being W_0 the truncated expansion up to order 0, we have that $P(W_0(\sigma)) = P(a_0) = a_0 + \mathcal{O}(\sigma)$ and $W_0(\lambda\sigma) = a_0$. Then a_0 corresponds to the fixed point, x_0.
- Order 1: being W_1 the truncated expansion up to order 1, we have that $P(W_1(\sigma)) = P(a_0 + a_1\sigma) = a_0 + D_xP(a_0)a_1\sigma + \mathcal{O}(\sigma^2)$ and $W_1(\lambda\sigma) = a_0 + a_1\lambda\sigma$.

  Neglecting high order terms, and taking into account the eigenvalue problem for a fixed point $D_xP(x_0)v = \lambda v$, then a_1 corresponds to the eigenvector of $D_xP(x_0)$ of eigenvalue λ.

Assuming $a_0, ..., a_{m-1}$ are known, we search for a_m. Then, being W_m the truncated expansion of the manifold up to order m,

$$W_m(\lambda\sigma) = W_{m-1}(\lambda\sigma) + a_m\lambda^m\sigma^m, \tag{1.27}$$

must be equal to

$$\begin{aligned} P(W_m(\sigma)) &= P(W_{m-1}(\sigma) + a_m\sigma^m) \\ &= P(W_{m-1}(\sigma)) + D_xP(W_{m-1}(\sigma))P(a_m\sigma^m) + \mathcal{O}(\sigma^{m+1}) \\ &= W_{m-1}(\lambda\sigma) + b_m\sigma^m + D_xP(a_0)a_m\sigma^m + \mathcal{O}(\sigma^{m+1}), \end{aligned}$$

where b_m is the coefficient of the term of order m that comes from the evaluation of manifold up to order $m-1$, W_{m-1}, over the map. Substituting this expression in (1.27) and neglecting terms of order higher than m, the function a_m that we are looking for must verify

$$(D_xP(a_0) - \lambda^m\mathrm{Id})a_m = -b_m. \tag{1.28}$$

This system has a solution meanwhile $\lambda^m \notin \mathrm{Spec}(D_xP(x_0))$.

Besides, in order to solve (1.28) it is necessary to know the vectors b_m, for each order $m \geq 2$. Here is where the jet transport technique plays a crucial role to provide their value through automatic differentiation of the map, see Section 1.3.1.

Invariant manifolds of invariant tori of maps

Now we want to extend these ideas to the parametrization of an invariant manifold (stable or unstable) of a d-dimensional invariant torus φ of a temporal Poincaré map P, that has associated a hyperbolic eigenvalue and eigenfunction pair (λ, ψ).

Therefore, let us write the parametrization of the invariant manifold of an invariant torus as a formal Taylor power expansion:

$$W(\theta, \sigma) = a_0(\theta) + a_1(\theta)\sigma + \sum_{k\geq 2} a_k(\theta)\sigma^k, \tag{1.29}$$

where a_k are the functions at order k that depend on the angles along the torus, $\theta \in \mathbb{T}^d$.

The invariant manifolds must satisfy an invariance condition under the map P:

$$P(W(\theta, \sigma), \theta) = W(\theta + \rho, \lambda\sigma). \tag{1.30}$$

It is clear that the Taylor expansion of the invariant manifold under the map application can be written as

$$W(\theta + \rho, \lambda\sigma) = a_0(\theta + \rho) + a_1(\theta + \rho)\lambda\sigma + \sum_{k\geq 2} a_k(\theta + \rho)(\lambda\sigma)^k.$$

Again, we obtain order by order the functions a_k that are given by imposing the invariance condition at each order k of the parametrization:

- Order 0: $W_0(\theta, \sigma) = a_0(\theta)$, when applying to it the map:

  $$P(W_0(\theta, \sigma), \theta) = P(a_0(\theta), \theta) = a_0(\theta + \rho) + \mathcal{O}(\sigma) = a_0(\theta + \rho) + \mathcal{O}(\sigma).$$

  On the other side of the equality (1.30):

  $$W_0(\theta + \rho, \lambda\sigma) = a_0(\theta + \rho).$$

  So it is clear that the parametrization function at order zero is the invariant curve itself, $a_0 = \varphi$.

- Order 1: $W_1(\theta, \sigma) = a_0(\theta) + a_1(\theta)\sigma$, when applying to it the map:

  $$P(W_1(\theta, \sigma), \theta) = P(a_0(\theta) + a_1(\theta)\sigma, \theta) = a_0(\theta + \rho) + D_xP(a_0(\theta), \theta)a_1(\theta)\sigma + \mathcal{O}(\sigma^2).$$

On the other side of the equality (1.30):

$$W_1(\theta+\rho,\lambda\sigma) = a_0(\theta+\rho) + a_1(\theta+\rho)\lambda\sigma.$$

Neglecting the terms of order higher than 1 in σ, we have that

$$D_xP(a_0(\theta),\theta)a_1(\theta) = \lambda T_\rho a_1(\theta),$$

where $T_\rho a_1(\theta) = a_1(\theta+\rho)$, recall Definition 1.2.4 for the operator T_ρ. Looking at the Equation (1.23) we have that the function of the parametrization at order one corresponds to the eigenfuntion: $a_1 = \psi$.

- Order 2: $W_2(\theta,\sigma) = a_0(\theta) + a_1(\theta)\sigma + a_2(\theta)\sigma^2$, when applying to it the map:

$$\begin{aligned} P(W_2(\theta,\sigma),\theta) &= P(a_0(\theta) + a_1(\theta)\sigma + a_2(\theta)\sigma^2, \theta) \\ &= P(a_0(\theta) + a_1(\theta)\sigma, \theta) + D_xP(a_0(\theta) + a_1(\theta)\sigma, \theta)a_2(\theta)\sigma^2 + \mathcal{O}(\sigma^3) \\ &= P(a_0(\theta),\theta) + D_xP(a_0(\theta),\theta)a_1(\theta)\sigma + b_2(\theta)\sigma^2 + D_xP(a_0(\theta),\theta)a_2(\theta)\sigma^2 + \mathcal{O}(\sigma^3) \\ &= a_0(\theta+\rho) + \lambda T_\rho a_1(\theta)\sigma + b_2(\theta)\sigma^2 + D_xP(a_0(\theta),\theta)a_2(\theta)\sigma^2 + \mathcal{O}(\sigma^3). \end{aligned}$$

where b_2 denotes a function of the term of order 2 appearing in the evaluation up to order 2 of the manifold at order 1, W_1, under the Poincaré map and that depends on the angle vector $\theta \in \mathbb{T}^d$. On the other side of the equality (1.30):

$$W_2(\theta+\rho,\lambda\sigma) = a_0(\theta+\rho) + a_1(\theta+\rho)\lambda\sigma + a_2(\theta+\rho)\lambda^2\sigma^2.$$

Neglecting the terms of order higher than 2 in σ, we have that

$$b_2(\theta) + D_xP(a_0(\theta),\theta)a_2(\theta) = \lambda^2 T_\rho a_2(\theta).$$

So, function a_2 satisfies the following system:

$$(D_xP(a_0(\theta),\theta) - \lambda^2 T_\rho)a_2(\theta) = -b_2(\theta).$$

Now, let us assume that we know the parametrization up to order $m-1$, W_{m-1}, i.e. we assume we know the functions a_0,...,a_{m-1}, we look for the function a_m involved in W_m

$$W_m(\theta,\sigma) = W_{m-1}(\theta,\sigma) + a_m(\theta,\sigma)\sigma^m.$$

For this, we apply the Poincaré map to W_m

$$\begin{aligned} P(W_m(\theta,\sigma),\theta) &= P(W_{m-1}(\theta,\sigma),\theta) + D_xP(W_{m-1}(\theta,\sigma),\theta)a_m(\theta)\sigma^m + \mathcal{O}(\sigma^{m+1}) \\ &= P(W_{m-1}(\theta,\sigma),\theta) + D_xP(a_0(\theta),\theta)a_m(\theta)\sigma^m + \mathcal{O}(\sigma^{m+1}) \end{aligned} \tag{1.31}$$

The Taylor expansion of the invariant manifold W_{m-1} under the Poincaré map is

$$P(W_{m-1}(\theta,\sigma),\theta) = W_{m-1}(\theta+\rho,\lambda\sigma) + b_m(\theta)\sigma^m + \mathcal{O}(\sigma^{m+1}), \tag{1.32}$$

where b_m is a θ-dependent function at order m that comes from the image under P of the invariant manifold at order $m-1$. Now we insert this expression in (1.31) and impose invariance condition (1.30) at order m:

$$b_m(\theta)\sigma^m + D_xP(a_0(\theta),\theta)a_m(\theta)\sigma^m = a_m(\theta+\rho)\lambda^m\sigma^m, \tag{1.33}$$

or equivalently,

$$(D_xP(a_0(\theta),\theta) - \lambda^m T_\rho)a_m(\theta) = -b_m(\theta). \tag{1.34}$$

This is an equation that, under generic conditions of non-resonance, uniquely determines the function a_m.

If the dimension of the torus is low, functions a_k can be found by solving a (may be large dimensional) linear system in which the matrix $D_x P(a_0(\theta), \theta)$ is involved. However, as the dimension of the torus is higher, solving this system as a whole may not be feasible.

For this reason, when the dimension of torus is high it is very convenient to use the reducibility of the system in order to look for expressions of the parametrization functions in terms of the constant Floquet matrix B. We will show in Chapter 6 that once the system (1.34) is written in terms of B, it offers a high degree of parallelism in its computational implementation.

1.3.1 Jet transport

Jet transport is a computational technique to compute high order derivatives of the flow of an ODE with respect to initial data and/or parameters ([BM98, AFJ+08, AFJ+09, ADLBZB10, WZ12]). It is based on using automatic differentiation [Gri00] on a numerical integrator of ODEs.

The main idea is to replace the basic arithmetic of the integrator by an arithmetic of (truncated) formal power series in several variables. The formal power series codifies the value of a function, that corresponds to the constant term, and their derivatives, that correspond to the coefficients of each monomial up to the truncation order of the series. In [GJJC+21] it is shown that the propagation of these power series through the numerical integration produces exactly the same results as the integration of the corresponding high order variational equations of the ODE.

Since we aim to use this technique to obtain the high order derivatives of the stroboscopic map applied to the invariant manifolds, that we express as truncated Taylor series

$$W(\theta, \sigma) = \sum_{k \geq 0} a_k(\theta) \sigma^k, \quad \theta \in \mathbb{T}^d,$$

we need to compute $P(W)$ also as a truncated Taylor series,

$$P(W(\theta, \sigma), \theta) = \sum_{k \geq 0} b_k(\theta) \sigma^k, \quad \theta \in \mathbb{T}^d.$$

Then, to handle with a_k and b_k, we make use of the equivalence between trigonometric polynomials and tables of values.

Notice that we will work at a prescribed order. For example, if we have the truncated invariant manifold W_{m-1} and we apply the jet transport up to order m, the algorithm computes the terms b_k up to order m.

Different numerical integrators can be modified to operate on power series and construct this computational tool. In particular, in this dissertation we make use of the numerical integrators implemented by the authors of [GJJC+21], that used two basic integrators; the Taylor method [JZ05] and the Runge-Kutta-Verner 8(9) [Ver78]. To be more precise, the Taylor integrator with the jet transport is used in Chapters 4, 5 and 6 and the Runge-Kutta-Verner 8(9) with the jet transport is employed in Chapter 6.

1.4 Computations in an autonomous map

This section is devoted to the case referred in Observation 1.2.1, that is, when the time dependence of the system can be written in terms of just one angular variable and the system becomes autonomous in the stroboscopic map P. This case usually corresponds to a time-periodic perturbation of an autonomous system. Let us assume this is the situation. Then, the simplest invariant object of the

flow that one can find is a periodic orbit that comes from an equilibrium point of the unperturbed system. In particular, we are specially interested in the two-dimensional tori of the perturbed flow that come from periodic orbits of the flow of the unperturbed dynamical system.

One of the two frequencies of the 2D-torus is used to define the stroboscopic map, P, such that under it the invariant torus is seen as an one-dimensional invariant curve that satisfies the invariance condition

$$\varphi(\theta + \rho) = P(\varphi(\theta)), \qquad \theta \in \mathbb{T},$$

as pointed in Observation 1.2.1.

This section starts with the explanations about the numerical methods followed for the computation of invariant curves of stroboscopic maps and of the normal modes that give the linear stability around them, Sections 1.4.1 and 1.4.2, respectively. This is a topic already covered in many works, hence there are several procedures for these aims. In this dissertation we follow the ideas presented in [CJ00, Jor01, GJ04], since the methods presented there do not require any particular property of the invariant curve for their implementation; nor to belong to a Hamiltonian system, neither to satisfy any symmetry, for example. Then we think they are robust enough to be implemented in the search for any invariant curve.

In Section 1.4.3, we introduce the computation of a high order parametrization of hyperbolic invariant manifolds associated with invariant curves of a stroboscopic map. In the stroboscopic map, these manifolds are seen as two-dimensional invariant objects, since in this case $\theta \in \mathbb{T}$ and we consider σ to be one-dimensional. With these two parameters (θ, σ) a fundamental domain of the invariant manifold can be defined. These domains are cylinder shaped for which we refer to them as Fundamental Cylinders (FC). An interesting property of the FC is that they allow to give a generic view of the dynamics governed by these manifolds in a relatively simple way, as we will explain in Section 1.4.4 and for this reason, they will be extensively used in the applications presented in this dissertation.

Finally, Section 1.4.5 is devoted to give some tests to check that the computations carried out are correct and an analysis of the validity of the approximations.

Notice that for many steps of the computations presented here, the evaluation of the Poincaré map is required, what is done by means of numerical integration. In particular, the computations in autonomous maps presented here have been performed by means of a Taylor method [JZ05].

1.4.1 Invariant curves

Here we assume that the stroboscopic map has a smooth invariant curve, φ, parametrized by an angle θ as $\theta \in \mathbb{T} \mapsto \varphi(\theta) \in \mathbb{R}^n$ and that satisfies the invariance equation (1.15). For this, the function φ must be discretized. There is not an unique way of doing this, in the references we follow, this discretization is done by means of a real (truncated) Fourier series in terms of the angle $\theta \in [0, 2\pi]$,

$$\varphi(\theta) \approx \varphi^{(0)} + \sum_{\kappa=1}^{N} \varphi_\kappa^{(c)} \cos(\kappa\theta) + \varphi_\kappa^{(s)} \sin(\kappa\theta), \tag{1.35}$$

being $\varphi^{(0)}$, $\varphi_\kappa^{(c)}$, $\varphi_\kappa^{(s)}$ with $\kappa = 1, ..., N$ the Fourier modes and N is the order of truncation of the series, such that $2N + 1$ is the total number of Fourier coefficients considered for each of the n dimensions of the phase space.

Let us now define the function F as

$$F = P(\varphi(\theta)) - \varphi(\theta + \rho) \equiv 0, \tag{1.36}$$

and we look for the set of coefficients $\varphi^{(0)}$, $\varphi_\kappa^{(c)}$, $\varphi_\kappa^{(s)}$ of φ that verifies this expression. This is done by application of a Newton method.

Known rotation number

As a first case, we assume that we know the rotation number of the invariant curve we want to compute. Then, we have $m = (2N+1)n$ unknowns corresponding to the Fourier coefficients, $2N+1$, needed for each of the n coordinates, and hence, we need m equations to find the unknowns. For this, we evaluate each of the n dimensions of the equation (1.36) in a mesh of $2N+1$ angles,

$$\theta_s = \frac{2\pi s}{2N+1}, \qquad \text{with } s = 0, ..., 2N, \tag{1.37}$$

such that, without loss of generality, the function F is considered to be the set of evaluations of (1.36) on θ_s with $s = 0, ..., 2N$, this is $F = \{F_s\}$. Therefore it has dimension m and its Jacobian DF is an $m \times m$ matrix that contains the derivatives of the function F with respect to the Fourier coefficients

$$\begin{aligned}
\frac{\partial F_s}{\partial \varphi^{(0)}} &= D_x P(\varphi(\theta_s)) \frac{\partial \varphi(\theta_s)}{\partial \varphi^{(0)}} - \frac{\partial \varphi(\theta_s + \rho)}{\partial \varphi^{(0)}} = D_x P(\varphi(\theta_s)) - \mathrm{Id}, \\
\frac{\partial F_s}{\partial \varphi_\kappa^{(c)}} &= D_x P(\varphi(\theta_s)) \frac{\partial \varphi(\theta_s)}{\partial \varphi_\kappa^{(c)}} - \frac{\partial \varphi(\theta_s + \rho)}{\partial \varphi_\kappa^{(c)}} = D_x P(\varphi(\theta_s)) \cos(\kappa\theta_s) - \mathrm{Id} \cos(\kappa(\theta_s + \rho)), \\
\frac{\partial F_s}{\partial \varphi_\kappa^{(s)}} &= D_x P(\varphi(\theta_s)) \frac{\partial \varphi(\theta_s)}{\partial \varphi_\kappa^{(s)}} - \frac{\partial \varphi(\theta_s + \rho)}{\partial \varphi_\kappa^{(s)}} = D_x P(\varphi(\theta_s)) \sin(\kappa\theta_s) - \mathrm{Id} \sin(\kappa(\theta_s + \rho)),
\end{aligned} \tag{1.38}$$

where Id is the identity matrix of dimension $n \times n$.

Observation 1.4.1. *Notice that here we have a problem of* ***lack of uniqueness****, since given a particular parametrization $\varphi(\theta)$ of an invariant curve, and being α any angle, $\varphi(\theta + \alpha)$ is also a parametrization of the same curve.*

A way to avoid this lack of uniqueness situation is to fix the value of one component of φ at a specific angle $\theta \in [0, 2\pi]$. For this, we add an extra equation to the system, that is typically set for $\theta = 0$, such that the Fourier series discretizing the curve is reduced to

$$\varphi(\theta = 0) = \varphi^{(0)} + \sum_{\kappa=1}^{N} \varphi_\kappa^{(c)},$$

and their derivatives with respect to the Fourier coefficients (1.38) are as simple as ones and zeros.

Note that this extra equation implies that the linear system to solve is rectangular, of dimensions $(m+1) \times m$, instead of square. In other words, we have one more equation than unknowns. To solve this system we use Gaussian elimination with partial pivoting. Therefore, the last (extra) equation should be redundant so it is ignored for the backward substitution process.

Unknown rotation number

In the case the rotation number is unknown, the number of unknowns is increased by one, $m+1$, and we need the derivatives of F with respect to ρ:

$$\frac{\partial F}{\partial \rho} = -\frac{\partial \varphi(\theta + \rho)}{\partial \rho} = \sum_{\kappa=1}^{N} \left[\varphi_\kappa^{(c)} \kappa \sin(\kappa(\theta + \rho)) - \varphi_\kappa^{(s)} \kappa \cos(\kappa(\theta + \rho)) \right]. \tag{1.39}$$

To solve the lack of uniqueness here, it is necessary to add another extra equation, typically one that fixes the value of another component of φ at some angle θ.

In this case, the dimensions of the system are $(m+2) \times (m+1)$, since it is composed by the m equations for F_s plus the two equations devoted to fix two coordinates, and the number of unknowns is $m+1$. Notice that the derivatives of the extra equations are needed, not only with respect to the Fourier coefficients but also with respect to the rotation number.

Seed for the Newton method

In order to start the numerical method we need some approximate values of the Fourier coefficients $(\varphi^{(0)}, \varphi_\kappa^{(c)}, \varphi_\kappa^{(s)})$ for $\kappa = 1, ..., N$ that discretize the invariant curve and an approximate value of ρ if it is not known.

Here, we distinguish between two situations:

- When the invariant curve grows from an elliptical fixed point p of the map P, we use the point p and its elliptical eigenvector, $v_r + \mathrm{i}v_i$ with i being the imaginary unit, to give the seed for φ as

$$\varphi(\theta) = p + \delta(v_r \cos\theta + v_i \sin\theta), \tag{1.40}$$

  where δ is a small value corresponding to the distance from the point p to the invariant curve. In this case, the approximation to the rotation number, if needed, is given by the argument of the elliptical eigenvalue.

- If we aim to compute an invariant curve coming from a periodic orbit in the unperturbed system, we can use the discretization of the periodic orbit as seed for the invariant curve and take its frequency as the frequency of the invariant curve, that needs to be scaled according to the temporal Poincaré map defined. Sometimes the perturbation acts so strongly on this invariant curve that we can not go directly from the unperturbed system to the perturbed one, and then we make a continuation between both systems, as we will see in Section 5.2.

Continuation of the family of invariant curves

When the dynamical system is Hamiltonian, it is usual that the quasi-periodic solutions present on them appear in families. In this case, it may be of interest to compute the family of invariant solutions and for this, a continuation method is usually employed.

Again, there is not a unique way of performing the continuation of the family of invariant curves. The procedure we have follow consists on using the aforementioned methods to obtain the parametrizations of two close invariant curves, and employ them to compute by linear extrapolation a precise seed for the parametrization of a new invariant curve. If the rotation number is unknown, the seed for the new one is obtained likewise. Let us assume it is not known in order to describe a more generic procedure.

As usual in a continuation scheme, we refer to each single curve as a point in the family of invariant curves. Then, in order to have a uniform distribution of points in the continuation curve, we ask to the new point in the continuation curve, φ_j, to be at some distance δ of the previous point, φ_{j-1},

$$\begin{aligned}\delta^2 &= ||\varphi_j - \varphi_{j-1}||^2 + (\rho_j - \rho_{j-1})^2 \\ &= |\varphi_j^{(0)} - \varphi_{j-1}^{(0)}|^2 + \sum_{\kappa=1}^{N} \left(|\varphi_{\kappa,j}^{(c)} - \varphi_{\kappa,j-1}^{(c)}|^2 + |\varphi_{\kappa,j}^{(s)} - \varphi_{\kappa,j-1}^{(s)}|^2 \right) + (\rho_j - \rho_{j-1})^2.\end{aligned} \tag{1.41}$$

This condition replaces one of the extra equations used for fixing one component of φ, so that the dimensions of the linear system do not vary for the continuation problem. Notice that if the rotation number of the invariant curve is known, the term corresponding to the difference between rotation numbers is not needed in Equation (1.41).

Then, with the seed and the set of equations $m + 2$ for $m + 1$ unknowns (or $m + 1$ for m unknowns), we look for zeros of Equation (1.36) and the extra equations added. If more than 3 or 4 steps of Newton method are required to achieve a certain tolerance, for example 10^{-12} or 10^{-10}, the step of continuation δ is decreased.

Every time a new invariant curve is obtained, the error of its parametrization as a Fourier series is estimated by checking the invariance condition (1.15) on a much finer mesh, say 20 or 100 times finer than the mesh used to solve (1.36). The maximum difference gives an estimation of the error of the computed curve,

$$E(\varphi, \rho) = \max_{\theta \in \mathbb{T}} |\varphi(\theta + \rho) - P(\varphi(\theta))|.$$

If this value is bigger than a prescribed threshold, again something like 10^{-12} or 10^{-10}, the number of Fourier modes (i.e., the value of N) is increased and the invariant curve is computed again.

1.4.2 Stability of invariant curves

Once we have an approximation of an invariant curve, we want to compute an approximation of its normal modes. As explained in Section 1.2, this is done by looking for pairs of eigenvalue and eigenfunction $(\lambda, \psi) \in \mathbb{C} \times (\mathcal{C}(\mathbb{T}, \mathbb{C}^n)/\ \{0\})$ that satisfy the generalised eigenvalue problem (1.23). For the numerical resolution of said problem, it is rewritten as

$$T_{-\rho} A(\theta) \psi(\theta) = \lambda \psi(\theta), \tag{1.42}$$

where in this case of an autonomous map, $A(\theta) = D_x P(\varphi(\theta))$, and $T_{-\rho}$ is the inverse of the operator T_ρ, that is, it applies a rotation equal to $-\rho$, see Definition 1.2.4. Therefore, in order to study the linear behaviour around the invariant curve, we have to analyse the spectrum of the matrix $T_{-\rho} A(\theta)$.

Remember that the invariant curve is approximated by a Fourier series, and notice that the eigenvalue problem can be also solved in terms of the Fourier coefficients, so that the obtained eigenfunctions are also approximated by Fourier series truncated at order N.

The discretization of the matrix A has dimensions $m \times m$, recall that $m = n(2N+1)$, and it corresponds to the derivative of the following composition:

$$\begin{pmatrix} \varphi^{(0)} \\ \varphi_1^{(c)} \\ \varphi_1^{(s)} \\ \vdots \\ \varphi_N^{(c)} \\ \varphi_N^{(s)} \end{pmatrix} \xrightarrow{M} \begin{pmatrix} \varphi(\theta_0) \\ \varphi(\theta_1) \\ \varphi(\theta_2) \\ \vdots \\ \varphi(\theta_{2N-1}) \\ \varphi(\theta_{2N}) \end{pmatrix} \xrightarrow{P} \begin{pmatrix} P(\varphi(\theta_0)) \\ P(\varphi(\theta_1)) \\ P(\varphi(\theta_2)) \\ \vdots \\ P(\varphi(\theta_{2N-1})) \\ P(\varphi(\theta_{2N})) \end{pmatrix} \xrightarrow{M^{-1}} \begin{pmatrix} \bar{\varphi}^{(0)} \\ \bar{\varphi}_1^{(c)} \\ \bar{\varphi}_1^{(s)} \\ \vdots \\ \bar{\varphi}_N^{(c)} \\ \bar{\varphi}_N^{(s)} \end{pmatrix}. \tag{1.43}$$

Such that, in the practice, $A = DM^{-1} \cdot D_x P \cdot DM$, where M denotes the evaluation of the parametrization of the invariant curve on a mesh of angles θ_s like (1.37), and M^{-1} the inverse Fourier transformation.

Notice that following the same discretization for the operator T_ρ, Definition 1.2.4, it can be written as a block diagonal matrix where each block, $(T_\rho)_\kappa$, is just a 2×2 matrix whose role is to apply a rotation equal to ρ to each pair of coefficients $(\varphi_\kappa^{(c)}, \varphi_\kappa^{(s)})$,

$$(T_\rho)_\kappa = \begin{pmatrix} \cos(\kappa\rho) & \sin(\kappa\rho) \\ -\sin(\kappa\rho) & \cos(\kappa\rho) \end{pmatrix}. \tag{1.44}$$

Since T_ρ is orthonormal, its inverse (involved in (1.42)) corresponds to its transpose.

Generally, one-dimensional invariant curves do not involve very large linear systems, since the dimensions of these systems just depend on the dimension of the phase space n and the number of Fourier coefficients, $2N + 1$. For this reason, it is feasible to look directly for the normal modes of the matrix $T_{-\rho} A$. The solution of this system involve m eigenfunctions associated with m eigenvalues, that are disposed in concentric circles around the origin in the complex plane.

On the accuracy of the normal modes

The m pairs of eigenvalue and eigenfunction $(\lambda_j,\ \psi_j)$ with $j = 1, ..., m$ obtained from the resolution of (1.42) in terms of Fourier series, do not have the same accuracy. In fact there is a maximum of n pairs of accurate eigenvalues and eigenfunctions and the rest of the pairs correspond to rotations of accurate ones. As a result of this, the m obtained eigenvalues are disposed in at most n concentric circles with centre at the origin of the complex plane.

Let us write the eigenfunction ψ of the eigenvalue λ like $\psi(\theta)$ to stress its dependence on the angle θ. As shown in [Jor01], $\exp(-\mathrm{i}\kappa\theta)\psi(\theta)$ is also an eigenfunction of eigenvalue $\exp(\mathrm{i}\kappa\rho)\lambda$ of the same system, being i the complex unit. Then, considering ψ to be the set of m *possible versions* of the same eigenfunction $\psi(\theta) = \sum_j \psi_j \exp(\mathrm{i}j\theta)$, the p-norm $||\cdot||^{(\mathrm{p})}$

$$||\psi||^{(\mathrm{p})} = \sum_{j\in\mathbb{Z}} |\psi_j||j|^{\mathrm{p}}, \tag{1.45}$$

seems to be a good indicator of the decay of the Fourier series for some $\mathrm{p} \in \mathbb{N}$, typically $\mathrm{p} = 1$ or $\mathrm{p} = 2$.

Since the last terms (or tails) of a Fourier series gives an estimation of the error in the discretization of a function, we can use this norm to study the tails of the m eigenfunctions obtained as truncated Fourier series and with this, we can identify the most accurate eigenpairs.

1.4.3 Invariant manifolds

As introduced in Section 1.3, the approximation of the hyperbolic invariant manifold associated with a torus, in this case with an invariant curve, can be written as a truncated formal Taylor expansion:

$$W_K(\theta,\sigma) \approx \sum_{k=0}^{K} a_k(\theta)\sigma^k, \tag{1.46}$$

where K denotes the maximum order considered for the parametrization. Therefore, the error in the approximation of the invariant manifold written this way depends on the first term neglected, *i.e.* it is of the order of $|\sigma|^{K+1}$.

Observation 1.4.2. *Notice that, for the* ***linear approximation*** *of the invariant manifold, $K = 1$, only the invariant curve and its associated eigenfunction are needed:*

$$W_1(\theta,\sigma) \approx \varphi(\theta) + \sigma\psi(\theta), \tag{1.47}$$

since $a_0 = \varphi$ and $a_1 = \psi$. Then, given a small value of σ, positive or negative, this expression leads to an approximation of the invariant manifold with an error of order $|\sigma|^2$.

The practical interest of the high order approximation of these manifolds is that, the higher is the order K, the larger may be the value chosen for σ that ensures a good enough approximation of the manifold. Consequently, the globalisation of the invariant manifolds through numerical integration can start further away from the torus, reducing significantly the integration time.

Therefore, if we are interested in computing the approximation of an invariant manifold up to any order $K \geq 2$, and assuming that the approximations to the invariant curve and to its eigenfunctions are known, the parametrization functions a_k for $2 \leq k \leq K$ have to be computed. In Section 1.3 we reach the following expression to find a_k assuming the functions $a_0, ..., a_{k-1}$ are known

$$b_k(\theta)\sigma^k + D_x P(a_0(\theta))a_k(\theta)\sigma^k = a_k(\theta+\rho)\lambda^k\sigma^k,$$

which can be rewritten as

$$(D_x P(a_0(\theta)) - \lambda^k T_\rho) a_k(\theta) = -b_k(\theta). \tag{1.48}$$

We recall that the θ-dependent function b_k corresponds to a term of order k that arises from the evaluation under the Poincaré map of the invariant manifold up to order $k-1$. Then this function is unknown and must be computed in order to find the corresponding function a_k.

The jet transport algorithm applied to an invariant manifold up to order $k-1$ gives the coefficients of order equal and higher than k. Therefore, we will use this tool to numerically compute each function b_k at order k and once we have it, we face a linear system that can be again discretized and solved in terms of the Fourier coefficients, so that each function a_k is approximated by a real truncated Fourier series. For this reason, we refer sometimes to expansion (1.46) as truncated formal Taylor-Fourier expansion.

Since this particular technique to compute the high order approximations of the invariant manifolds of invariant curves of a Poincaré map is a new procedure, we give the details of the numerical algorithm.

Our algorithm for computing the parametrization functions a_k for $k \geq 2$ of an invariant manifold of an invariant curve up to order K starts by defining a mesh of angles along the curve: $\theta_j = 2\pi j/\ell$, being ℓ the number of points of the mesh such that $j \in [0, \ell]$ and $\theta_j \in [0, 2\pi]$, and to apply the jet transport to each of these points in order to obtain the values $b_k(\theta_j)$. Notice that, the jet transport algorithm applied to an invariant manifold up to order $k-1$ could give the coefficients of order equal and higher than k, but only order k is of interest at each application.

Once we have the table of values $(b_k(\theta_j), \theta_j)$, we compute the corresponding Fourier series for the b_k function, and solve one linear system (1.48) in terms of Fourier coefficients to find a_k as Fourier series.

For convenience we start the computations with $\ell = 2N+1$, so that functions b_k and a_k are approximated using the same number of modes than for discretizing the invariant curve and its eigenfunction. However, it may happen that this number, that is good enough for approximating the invariant curve and the eigenfunction, does not approximate accurately some of the a_k for $k \geq 2$, and therefore it is necessary to add modes to the Fourier series in order to improve the approximation of the invariant manifold.

To avoid solving the linear system that gives the function a_k with low precision, we note that the accuracy of each a_k is related to the accuracy of corresponding b_k. Then, when we compute the Fourier series of b_k we check the euclidean norm of its last two modes to be below some tolerance. If it is not, we re-compute the table of values $(b_k(\theta_j), \theta_j)$ for a larger number of points (higher value of ℓ) such that the number of modes employed in the approximation of b_k is increased, as well as the number of modes employed in the approximation of a_k.

Let us now summarise our numerical implementation. The starting point is a truncated Fourier series that approximates the invariant curve (φ) and a truncated Fourier series that approximates the eigenfunction (ψ), a_0 and a_1, respectively, what gives the linear approximation to the manifold. Moreover, we need the $(2N+1)n \times (2N+1)n$ matrix that contains the matrix flow $D_x P(a_0)$ (this is the same matrix that appears in the Newton method and in the stability computation (1.23)). As before, $2N+1$ is the number of Fourier coefficients and n the dimension of the dynamical system.

Note that at each step we have to evaluate $P(W_m)$, where W_m is a Taylor-Fourier series truncated at order m. As the jet transport technique only allows to evaluate P on power series, we compute $\{W(\theta_j, \sigma)\}_j$ being θ_j a suitable equispaced mesh of values of θ. Each $W(\theta_j, \sigma)$ is now a power series so we can compute $P(W(\theta_j, \sigma))$ and, using a Fourier transform, we obtain $P(W_m)$.

The computation of the coefficients a_k, $k \geq 2$, is done recurrently order by order. Let us assume that we know W_{m-1} and we want to compute W_m. Also, assuming that we have computed and stored the matrix (of size $(2N+1)n \times (2N+1)n$) $D_x P(a_0(\theta))$, we summarise the algorithm in a schematic way:

Algorithm 1.4.3 (High order parametrization of the invariant manifold of an invariant curve)**.**

1. *Evaluate $W_{m-1}(\theta_j, \sigma)$ on a mesh $\{\theta_j\}_{j=0}^{\ell-1}$ of ℓ points ($\theta_j = 2\pi j/\ell$, $\ell = 2N+1$), to obtain ℓ polynomials of degree $m-1$.*
2. *Apply the jet transport algorithm (working with polynomials of degree up to m) to each of the ℓ polynomials $W_{m-1}(\theta_j, \sigma)$ to obtain the table of values (θ_j, $b_m(\theta_j)$) from the function of degree m.*
3. *Apply a Fourier transformation to obtain b_m. We use as an estimate of the error the size of the last terms of these Fourier coefficients. If this estimate is not small enough, we repeat steps 1 and 2 with a larger value of ℓ.*
4. *Solve the linear system in (1.48) to obtain a_m, and then $W_m = W_{m-1} + a_m \sigma^m$.*

These steps are applied up to the desired degree for the invariant manifold.

Stable invariant manifold computation

This algorithm is valid for computing both stable and unstable invariant manifolds. However, it must be taken into account that when the stroboscopic map is applied forward in time to a stable manifold, it approaches the invariant curve and also the unstable invariant manifold, affecting the accuracy of its computation. Then, in order to minimise the error propagation in the computation of the approximation of the stable invariant manifold, it is convenient to find its parametrization functions by application of the inverse map P^{-1}.

The reason for this better numerical behaviour is that the stable manifold is a repelling manifold under the stroboscopic map applied forward in time, P, but it is not repelling under its application backward in time P^{-1}. Likewise, the unstable manifold is repelling under P^{-1} and not repelling under P.

The procedure to find the parametrizating functions a_k of the stable manifold when applying the inverse Poincaré map is basically the same as the one already explained. In this case, we impose that invariant manifolds satisfy the invariance condition under P^{-1}:

$$P^{-1}(W(\theta, \sigma)) = W(\theta - \rho, \frac{\sigma}{\lambda}), \tag{1.49}$$

at each order k.

Obviously, order zero of the parametrization is, as before, the invariant curve and the order one corresponds to the stable eigenfunction. In general, assuming that we already know the functions up to order $m-1$, we look for the function $a_m(\theta)$ that satisfies the system given by:

$$(D_x P^{-1}(a_0(\theta)) - \lambda^{-m} T_{-\rho}) a_m(\theta) = -b_m^-(\theta) \qquad m \geq 2, \tag{1.50}$$

where $D_x P^{-1}(a_0)$ is the Jacobian matrix corresponding to apply the inverse of the Poincaré map to the invariant curve and b_m^- denotes the function at order m of the evaluation of the manifold up to order $m-1$ under the inverse Poincaré map, that is obtained through the jet transport technique as in the previous case.

The whole algorithm to follow is exactly the same as the detailed in previous section, but now integrations backwards in time, the operator $T_{-\rho}$ and Equation (1.50) are involved instead of the integrations forward in time, T_ρ and Equation (1.48).

1.4.4 Fundamental cylinders

Invariant manifolds are composed by trajectories that may behave differently, although they belong to the same invariant object. This happens with the invariant manifolds associated with fixed points, periodic orbits or invariant tori. For this reason, it is usual to use a fundamental domain for the invariant manifolds in order to have a complete representation of the manifold.

Due to their nature, an invariant manifold associated with an invariant curve can be seen as a cylinder, parametrized by the same angle as the invariant curve (θ) and a parameter to move along the manifold (σ). Looking at these parameters, the dynamics on this cylinder is very simple: the point corresponding to the parameter values (θ, σ) is mapped to $(\theta + \rho, \lambda\sigma)$ through P. Therefore, we can define a fundamental domain of the approximation of the invariant manifold as the image of $\mathbb{T} \times [\sigma_0, \lambda\sigma_0]$, such that the parametrization of the manifold that generates, under iteration of the map P, the complete manifold. We refer to such set as Fundamental Cylinder (FC).

Remark 1.4.4. *For sake of reducing numerical errors, the FC corresponding to the unstable invariant manifold is defined by application of the direct map P, covering values for $\sigma \in [\sigma_0, \lambda_u\sigma_0]$. Meanwhile, for the stable invariant manifold, we consider that the point with parameter values (θ, σ) is mapped to $(\theta - \rho, \lambda^{-1}\sigma)$ through P^{-1}, so that, for the definition of the FC of the stable manifold, we impose $\sigma \in [\sigma_0, \lambda_s^{-1}\sigma_0]$*

For simplicity, we continue the discussion focusing ourselves on the unstable manifold. An approximation for a curve of the fundamental cylinder is given by $W_K(\theta, \sigma_0)$, where K is the order of the approximation and σ_0 is a sufficiently small value. If we choose this curve as the "lower part" of the cylinder, then the "upper part" is given by $W_K(\theta, \lambda_u\sigma_0)$. Note that neglecting the rotation of the angle for the upper curve does not affect to the definition of the fundamental domain. We write the parametrization of the fundamental cylinder for the unstable invariant manifold,

$$W_K^u(\theta, \sigma) = \sum_{k=0}^{K} a_k^u(\theta)\sigma^k,$$

as the following expression:

$$(\theta, \tau) \in [0, 2\pi] \times [0, 1] \quad \mapsto \quad \mathcal{Z}^u(\theta, \tau) = \sum_{k=0}^{K} a_k^u(\theta)((1 + \tau(\lambda_u - 1))\sigma_0)^k, \tag{1.51}$$

where $\tau \in [0, 1]$ is a parameter such that when $\tau = 0$, $\mathcal{Z}^u(\theta, \tau)$ parametrizes the lower curve, $W_K^u(\theta, \sigma_0)$, and when $\tau = 1$, it parametrizes the upper curve, $W_K^u(\theta, \lambda_u\sigma_0)$.

The FC is used as starting place for the numerical integrations used to extend the manifold as much as needed. The points in the FC of the unstable manifolds are globalized by numerical integration forward in time meanwhile the points in the FC of the stable manifolds are globalized by numerical integration backward in time.

Note that the value σ_0 has to be chosen small enough such that this representation of the FC is accurate, but large enough to minimise the integration time needed to extend the manifold by numerical integration. The choice of σ_0 is discussed in the next section.

For the fundamental cylinder of the stable invariant manifold,

$$W_K^s(\theta, \sigma) = \sum_{k=0}^{K} a_k^s(\theta)\sigma^k,$$

we use

$$(\theta, \tau) \in [0, 2\pi] \times [0, 1] \quad \mapsto \quad \mathcal{Z}^s(\theta, \tau) = \sum_{k=0}^{K} a_k^s(\theta)((1 + \tau(1/\lambda_s - 1))\sigma_0)^k. \tag{1.52}$$

Again, $\mathcal{Z}^s(\theta,\tau)$ parametrizes the lower curve, $W^s_K(\theta,\sigma_0)$, when $\tau=0$, and when $\tau=1$ it parametrizes the upper curve, $W^s_K(\theta,\lambda_s^{-1}\sigma_0)$.

Once we have the parametrization of the fundamental cylinders in terms of the two parameters, we can make plots of meshes on (θ,τ) and colour each point according to some magnitude of interest. For example, according to their fate. This allows to visualise in an easy way the origin of the trajectories in the stable FC before approaching the invariant curve, of the destination of the trajectories in the unstable FC after leaving that same curve. This idea will be very helpful in Chapters 3, 4 and 5.

1.4.5 Accuracy and tests

In this section we discuss about the estimation of the domain of validity of the computed parametrization for a given the degree K, and about a test used to check the correctness of the results. We recall that, applying the Algorithm 1.4.3 we approximate the functions a_k, up to some order K, as a truncated Fourier series,

$$a_k(\theta) \approx a_k^{(0)} + \sum_{\kappa=1}^{N} a_{k,\kappa}^{(c)} \cos(\kappa\theta) + a_{k,\kappa}^{(s)} \sin(\kappa\theta),$$

where $a_k^{(0)}$, $a_{k,\kappa}^{(c)}$ and $a_{k,\kappa}^{(s)}$ with $\kappa = 1,...,N$ denote the Fourier coefficients of the parametrization function at order k, a_k.

As a general rule, we have that the higher the degree of the parametrization K and the number of Fourier modes N, the more accurate is the approximation of the parametrization of the invariant manifold $W(\theta,\sigma)=\sum_{k=0}^{K} a_k(\theta)\sigma^k$. However, when K is large enough, the gain of domain of validity provided by a new degree $K+1$ of the parametrization does not compensate the computational cost needed to obtain this new degree.

To fix the discussion, let us focus on the unstable manifold (a similar discussion is valid for the stable one), and let us also assume that the value N has already been chosen to have the required accuracy, may be depending on K (see the discussion in Section 1.4.3). A fast error estimate for the truncated expansion of the manifold follows from the size of the last computed term (the one of degree K),

$$||a_K||_1\,|\sigma|^K \approx \varepsilon, \qquad ||a_K||_1 = |a_K^{(0)}| + \sum_{\kappa=1}^{N} |a_{K,\kappa}^{(c)}| + |a_{K,\kappa}^{(s)}|.$$

We have to choose a value $\sigma_0 > 0$ such that the parametrization of a fundamental domain as in (1.51) is accurate up to $\lambda_u\sigma_0$. Hence, from the previous formula we obtain that

$$\bar{\sigma}_0 \approx \frac{1}{\lambda_u}\left(\frac{\varepsilon}{||a_K||_1}\right)^{1/K}. \tag{1.53}$$

Therefore, given an accuracy ε, we compute the value of $\bar{\sigma}_0$ and use some $\sigma_0 \le \bar{\sigma}_0$ for computing the approximation to the FC. Notice that, in the presence of symmetries, checking only the last order of the parametrization may cause problems since it could vanish depending on its parity. In this case the last two terms of the expansion have to be used.

In order to check the final accuracy of the approximation of the invariant manifold we compare the error of the invariance condition for the parametrization of the invariant manifold, $W(\theta,\sigma)$, at a given angle θ, but at two different values of σ, say σ_1 and $\sigma_2=\sigma_1/2$. Obviously, if the parametrization of the manifold has been computed up to order K, the truncation error depends on the power $K+1$ of the parameter σ. Then, for σ_i with $i=1,2$, we would have that

$$\epsilon_i = |P(W_K(\theta,\sigma_i)) - W_K(\theta+\omega,\lambda\sigma_i)| \approx c\sigma_i^{K+1},$$

where c denotes a constant. The relation between the two errors is

$$\frac{\epsilon_1}{\epsilon_2} \approx \frac{\sigma_1^{K+1}}{(\frac{\sigma_1}{2})^{K+1}} \approx 2^{K+1}.$$

Therefore, we compute the quantity

$$\frac{\log(\epsilon_1/\epsilon_2)}{\log(2)},$$

and check that the result is close to $K+1$. This test has been passed for the manifolds used in this dissertation.

Chapter 2

The Bicircular Problem

The main objective of this dissertation is to contribute to the study of the motion of a particle in the Earth-Moon system and to develop tools for its proper understanding. As explained in the Introduction, there are several simplified models for describing the motion of a small particle in an astrodynamical system, being the most extended one the Restricted Three-Body Problem (RTBP). This model describes the motion of an infinitesimal particle subjected to the gravitational fields of two punctual massive bodies, called the primaries, that are assumed to revolve in circular motion.

Among the modifications of this simplified model, we are interested in the Bicircular Problem (BCP). This model assumes that there is a third punctual massive body revolving in circular motion around the original set up of the RTBP, such that the gravitational field of this third body affects the motion of the particle but not the motion of the primaries. For this, the BCP can be understood as a time-periodic perturbation of the RTBP.

As far as we are concerned, in the neighbourhood of the Earth-Moon system the gravitational effect of the Sun is too important to be negligible. For this reason we want to take this effect into account and probably the easiest way of doing so is through a BCP that considers the Earth and Moon as primaries and the Sun as the forcing body.

Besides, a typical issue with any simplified model is the reliance on them to know if the insight about the dynamics they provide is close enough to the dynamics in real systems. Here, we have particular interest in making comparisons between the simplified model that we use and a realistic one. Then, we must notice an interesting peculiarity of the Sun-Earth-Moon BCP as we consider it. Its dependence on time gives a relation between the relative positions of the three massive bodies at any particular epoch, as we will detail. Since we are going to implement a non-autonomous change of coordinates, the BCP time-dependence will help us to choose the right epoch at which to apply the change.

Before delving into the BCP, let us give some preliminary concepts and general information about the RTBP in order to make the explanations clearer. It is well-known that in the RTBP there are five equilibrium points L_i with $i = 1, ..., 5$, where in a few words, collinear points L_1 and L_2 are highly unstable, collinear point L_3 is moderately unstable and the triangular points, L_4 and L_5, are linearly stable for the Earth-Moon mass parameter.

Stable invariant objects in dynamical systems always attracts lots of attention because of the proper and simple interest on the dynamics around them and also because of the stable regions that are usually found in their vicinities, that are target for many applications. In particular, the stable regions around the triangular points in the RTBP have been studied in different works, we highlight [GDF$^+$89, Sim89, CG91]. Under the perturbation introduced by the solar gravity field of the Earth-

Moon BCP, L_4 and L_5 become slightly unstable, [SGJM95], as we will see. In spite of this, [Jor00] showed how effective stable regions can still be found in their neighbourhoods and also how these regions can also be found in a realistic model based on JPL (Jet Propulsion Laboratory) ephemeris.

Unstable invariant objects are of great interest too, since their stable and unstable invariant manifolds suppose mechanisms for approaching these objects and getting away from them. Due to its strong instability and low energy level, the dynamics in the neighbourhoods of L_1 and L_2 have been objective of many research works since in the frame of the RTBP, only an object with such low energy levels can enter or leave the system, see the structure of the forbidden regions in Section 4.7 in [Sze67]. Therefore, many studies have pointed out the role of L_1 and L_2 and their associated invariant manifolds to explain the behaviour of Near Earth Objects (NEOs), or Asteroids (NEAs). Hou et al. explain in [HXSW15] that the typical way for a NEO to enter the Earth-Moon system is first through Sun-Earth L_1 and L_2, and secondly, through Earth-Moon L_1 and L_2 for low energy trajectories, or directly without passing through any equilibrium point for high energy trajectories. Many other authors have also analysed these two collinear points for this purpose, for example, [LRMG14, SNU18]. However, as far as we know, none of them have pointed to L_3, in spite of having the same kind of stability. It is known that the L_3 equilibrium point in the RTBP has stable and unstable manifolds associated that approach the small primary giving rise to a horseshoe structure [BO06]. In [BMO09] the homoclinic connections of Lyapunov orbits around L_3 are computed numerically. Concerning to this family of Lyapunov periodic orbits around L_3, it was proved that their related invariant manifolds have transversal intersections, see [SSST13] for more details.

In the frame of the BCP Earth-Moon system, collinear equilibrium points L_1 and L_2 have also been extensively studied. For the case of L_1 we remark [JJCR20] and for the case of L_2, due to the appearance of a 2:1 resonance between the natural frequency of Lyapunov orbits around L_2 and the frequency of the Sun, it was required a major effort to understand its dynamics in the BCP so we can find many references, from the earlier works of M.A. Andreu [And98, And02] to recent ones [JCFJ18, RJJC21]. Nevertheless, no major attention has been paid to L_3 dynamics in the Earth-Moon BCP frame until now. Therefore, this dissertation is mainly focused on the L_3 dynamical role in the Earth-Moon system under the gravitational effect of the Sun. In addition, some other contributions to the BCP devoted to analyse the instability of the triangular points and a family of stable quasi-periodic solutions around the Moon are also presented in this dissertation.

The structure of this chapter is as follows, Section 2.1 describes the Restricted Three-Body Problem, applied to the Earth-Moon system, that introduces the basis for the Earth-Moon Sun-perturbed Bicircular Problem, detailed in Section 2.2. Section 2.3 and 2.4 are devoted to the dynamical substitutes of L_3 and of the triangular equilibrium points in the BCP, as well as to the families of quasi-periodic solutions around them, respectively. Finally, Section 2.5 is focused on the translation of time and coordinates between the BCP and the real system.

2.1 Restricted Three-Body Problem

In the Restricted Three-Body Problem (RTBP), the primaries are considered to move in circular motion around their common centre of masses, where the origin is set. The assumption of the circular motion leads to the distance between the primaries to be constant. It is usual to take this distance, 3.8440×10^5 km in the Earth-Moon system, as the unit of length, the sum of the masses of the primaries, 6.0457×10^{24} kg, as the unit of mass and to normalise their period of revolution, 27.321577 days, to 2π, so that the gravitational constant is 1. Another common consideration is to define a rotational (synodic) reference frame, such that the x-axis is set on the line connecting the primaries, the z-axis is set on the direction of their angular momentum and the y-axis is taken such that the system is positively oriented, [Sze67].

In this reference frame, the primaries are seen as fixed, the Earth, with mass $1-\mu$, placed at $(x, y, z) = (\mu, 0, 0)$ and the Moon, with mass μ, placed at $(x, y, z) = (\mu - 1, 0, 0)$. Being $\mu = \frac{m_M}{m_M+m_E} \approx 0.01215$ the mass parameter of the Earth-Moon system and m_E and m_M the masses of the Earth and the Moon respectively.

Then, the equations of motion for a massless particle in the Earth-Moon RTBP synodical reference frame are:

$$\begin{cases} \ddot{x} = 2\dot{y} + x - \frac{1-\mu}{r_{PE}^3}(x-\mu) - \frac{\mu}{r_{PM}^3}(x-\mu+1), \\ \ddot{y} = -2\dot{x} + y - \frac{1-\mu}{r_{PE}^3}y - \frac{\mu}{r_{PM}^3}y, \\ \ddot{z} = -\frac{1-\mu}{r_{PE}^3}z - \frac{\mu}{r_{PM}^3}z, \end{cases} \tag{2.1}$$

where $(\dot{x}, \dot{y}, \dot{z})$ are the velocities of the particle, $(\ddot{x}, \ddot{y}, \ddot{z})$ its accelerations and $r_{PE} = ((x-\mu)^2 + y^2 + z^2)^{1/2}$ and $r_{PM} = ((x-\mu+1)^2 + y^2 + z^2)^{1/2}$ are the distances from the Earth and from the Moon to the particle, respectively.

This system can be written in the Hamiltonian formalism as

$$H_{RTBP} = \frac{1}{2}(p_x^2 + p_y^2 + p_z^2) + yp_x - xp_y - \frac{1-\mu}{r_{PE}} - \frac{\mu}{r_{PM}}, \tag{2.2}$$

being $(p_x, p_y, p_z) = (\dot{x} - y, \dot{y} + x, \dot{z})$ the momenta of the particle.

The RTBP is an autonomous Hamiltonian system, with three degrees of freedom and for which the energy is conserved. The existence of this integral of motion is very convenient, since it enables to identify regions where the movement of the infinitesimal particle is allowed or forbidden, [Sze67]. In addition, this conserved quantity is commonly used to reduce one degree of freedom in the analysis of the system.

The equations of the motion included in (2.1) satisfy the following symmetries when inverting the sense of the time,

$$\begin{aligned} (t, x, y, z, p_x, p_y, p_z) &\to (-t, x, -y, -z, -p_x, p_y, p_z), \\ (t, x, y, z, p_x, p_y, p_z) &\to (-t, x, -y, z, -p_x, p_y, -p_z). \end{aligned} \tag{2.3}$$

This means that if the set of coordinates on the left of these expressions is a particular solution of the system, also is the set of coordinates on the right.

Another well-known characteristic of the RTBP is that, in synodical coordinates, it presents five equilibrium points, also known as Lagrangian points. Three of them, called collinear points (L_1, L_2 and L_3), are disposed along the horizontal axis and the other two are called equilateral or triangular points (L_4 and L_5) and are located in the third vertex of the two equilateral triangles formed by taking the primaries as vertices, see Figure 2.1.

Collinear points are unstable while triangular equilibrium points are linearly stable for values of the mass parameter smaller than the critical Routh mass $\mu_R = \frac{1}{2}\left(1 - \sqrt{\frac{23}{27}}\right) \approx 0.0385$, as it happens for the Earth-Moon mass parameter. According to the classical Lyapunov Centre Theorem, see for example [MHO09], under generic non-resonance and non-degeneracy conditions, from each linearly stable direction of an elliptic equilibrium point of a Hamiltonian system, a one-parametric family of periodic orbits emerges.

In particular, the collinear points are unstable of the form centre $\times$ centre $\times$ saddle, such that, in the vicinity of each of them, there is a family of periodic orbits tangent to the (z, p_z) plane, known as vertical family, and another one inside the (x, y, p_x, p_y) plane, known as horizontal family. Due to the saddle part, each of these periodic orbits has stable and unstable invariant manifolds that grow

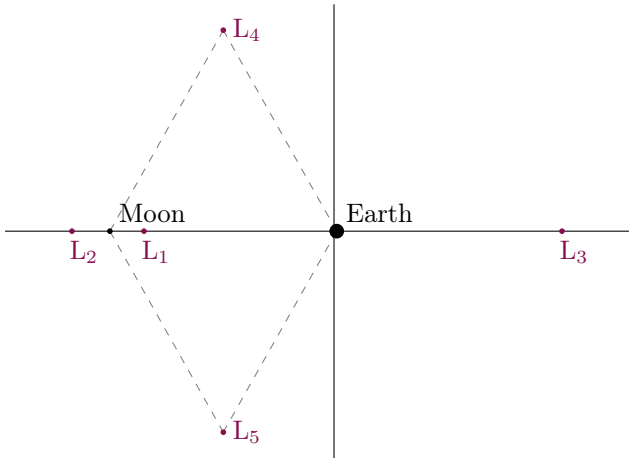

Figure 2.1: Schematic of the Earth-Moon Restricted Three-Body Problem, including the positions of the equilibrium points.

tangent to their hyperbolic eigendirections. Concerning the triangular equilibrium points for the mass parameter of the Earth-Moon system, they are linearly stable of the form centre × centre × centre.

These families of periodic orbits have been computed extensively in the literature due to their interest in space science for plenty of examples. For the Earth-Moon system it is remarkable the early work of R. Broucke [Bro68].

2.2 The effect of the Sun's gravity

As mentioned at the beginning of this chapter, the Bicircular Problem (BCP) is a modification of the circular Restricted Three-Body Problem (RTBP) in which the gravitational effect of a fourth body (three punctual massive bodies in total) is introduced as a time-periodic perturbation, [Hua60, CRR64]. Therefore the initial set up, units and reference frame is the same one as in the RTBP, detailed in previous section.

In our particular case, we consider the Earth-Moon system as in the RTBP and assume its barycentre to be rotating in circular motion around the Sun, that plays the role of the additional perturbative massive body. Since the origin of coordinates is placed at the Earth-Moon barycentre and the reference frame is such that rotates with Earth and Moon, the Sun is seen as moving around the Earth-Moon system, see Figure 2.2.

The equations of motion for the massless particle in the Earth-Moon Sun-perturbed BCP in the synodical reference frame are written as:

$$\begin{cases} \ddot{x} = 2\dot{y} + x - \frac{1-\mu}{r_{PE}^3}(x-\mu) - \frac{\mu}{r_{PM}^3}(x-\mu+1) - \frac{m_s}{r_{PS}^3}(x - a_s\cos\vartheta) - \frac{m_s}{a_s^2}\cos\vartheta, \\ \ddot{y} = -2\dot{x} + y - \frac{1-\mu}{r_{PE}^3}y - \frac{\mu}{r_{PM}^3}y - \frac{m_s}{r_{PS}^3}(y + a_s\sin\vartheta) + \frac{m_s}{a_s^2}\sin\vartheta, \\ \ddot{z} = -\frac{1-\mu}{r_{PE}^3}z - \frac{\mu}{r_{PM}^3}z - \frac{m_s}{r_{PS}^3}z, \end{cases} \tag{2.4}$$

where m_s is the mass of the Sun, r_{PS} is the distance from the Sun to the particle such that

$$r_{PS}^2 = (x - a_s\cos\vartheta)^2 + (y - a_s\sin\vartheta)^2 + z^2,$$

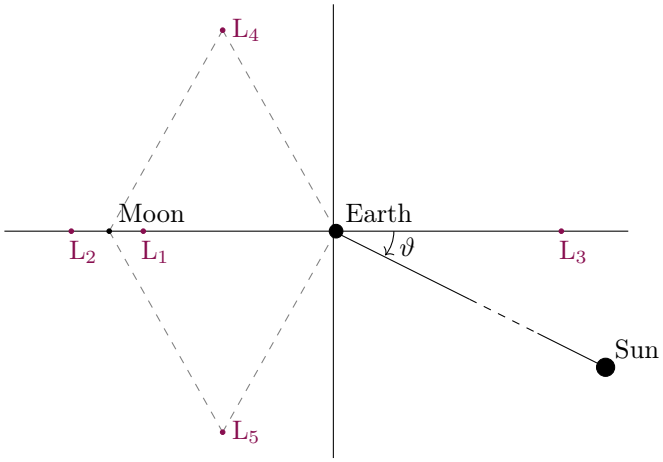

Figure 2.2: Schematic of the Bicircular Problem. Note that distance to Sun is not in scale.

μ	m_s	ω_s	a_s
0.012150582	328900.55	0.925195985	388.811143023

Table 2.1: Parameters of the Bicircular model for the Earth-Moon system, in RTBP units.

and a_s is the distance from the Sun to the origin, set in the Earth-Moon barycentre, and that responds to Kepler's third law of planetary motion

$$1 + m_s = n_s^2 a_s^3, \tag{2.5}$$

being n_s the angular velocity of the Sun, such that $\omega_s = 1 - n_s$ is the angular velocity of the Sun with respect to the angular velocity of the Earth-Moon system, that has been normalised to 1. The angle

$$\vartheta = \omega_s t + \vartheta_0, \tag{2.6}$$

specifies the position of the Sun at each time t in the BCP synodic reference frame, see Figure 2.2. The angle ϑ_0 denotes a possible initial phase for the position of the Sun, that it is usually taken as 0.

Table 2.1 contains the values of the parameters for Earth-Moon-Sun BCP in the RTBP units. Notice that, in the Earth-Moon BCP model, the period of revolution of the Sun with respect to the Earth-Moon system, $T = 2\pi/\omega_s$, corresponds to the synodic period of the Moon in the real system (about 29.53 days).

The BCP also admits to be written in Hamiltonian formalism, but now the Hamiltonian function is non-autonomous, since it depends on time. It can be expressed in two parts

$$H_{BCP} = H_{RTBP} + \widehat{H}_{BCP}, \tag{2.7}$$

where H_{RTBP} is the Hamiltonian function of the RTBP, see (2.2), and $\widehat{H}_{BCP}$ contains the terms due to the gravitational effect of the Sun on the massless particle,

$$\hat{H}_{BCP} = -\frac{m_s}{r_{PS}} - \frac{m_s}{a_s^2}(y \sin\vartheta - x\cos\vartheta), \tag{2.8}$$

consisting in a gravitational potential term and a Coriolis one.

Remark 2.2.1. *It is worth to mention that, in spite of the perturbation, the Hamiltonian function (2.7) preserves the same* ***symmetries*** *when inverting the sense of the time as in the RTBP, (2.3). These symmetries are helpful in the analysis of the system as we will see.*

Looking at the perturbative part of the Hamiltonian, expression in (2.8) or at the equations of motion (2.4), it is clear that BCP is not coherent since the third massive body acts only on the infinitesimal particle, but not on the primaries. This might seem a weak point of the model, however it has been proved to give a good insight of the real dynamics of the Earth-Moon system, [SGJM95]. It is remarkable that some results obtained using the BCP model have been checked successfully using a realistic model based on the JPL ephemeris [GLMS01, Jor00], and as we will see in Chapter 3 of the present dissertation.

A system like the one described by the BCP in which the variation in time is regarded to a simple angular variable, ϑ, corresponds to the case of the Observation 1.2.1 made in the first chapter. Then, the time dependence can be removed by imposition of a temporal Poincaré map at time T, let us call it P, transforming the system in an autonomous map.

Due to the perturbation, no fixed points may appear in the flow of the BCP as they do in the RTBP. Under generic conditions, the equilibrium points of the RTBP are replaced by periodic orbits in the BCP, with the same period as the period of the perturbation, T. They are usually called dynamical substitutes. In particular, for the Earth-Moon system under solar perturbation, each of the three collinear points, L_1, L_2[1] and L_3, is replaced by one unstable periodic orbit and each of the triangular equilibrium points, L_4 and L_5 (that are linearly stable in the RTBP) is replaced by three periodic orbits; two of them stable and the other one, linearly unstable, see [SGJM95, Jor00]. In those works, authors named the unstable periodic orbit as *PO1* and the two linearly stable ones as *PO2* and *PO3*.

Regarding to the families of Lyapunov periodic orbits present in the RTBP, under a periodic perturbation and meanwhile non-degeneracy and non-resonance conditions hold, each periodic solution increases its dimension becoming a quasi-periodic solution with two basic frequencies; one frequency comes from the unperturbed system and the other one from the perturbation. From a geometrical point of view, each of these quasi-periodic solutions fills densely a torus of dimension two, that is the reason why they are commonly called two-dimensional invariant tori. If the frequency of one periodic orbit in the RTBP is nearly resonant with the frequency of the perturbation, i.e. it does not satisfy the corresponding Diophantine condition, it is destroyed and it can not be found in the perturbed system, leaving gaps in the family of surviving quasi-periodic solutions. Therefore, in each of the centre directions of each of the dynamical substitutes, a one-parametric Cantorian family of quasi-periodic motion emanates, [JV97b]. The gaps in these Cantorian families of tori appear due to the resonances and their size was proved to be exponentially small with the distance to the unperturbed invariant object they come from. In particular, in the BCP, the size of the possible gaps is so small that they are not detected when working with double precision and consequently the families of quasi-periodic orbits can be considered as effectively continuous.

Since the periodic orbits substituting the collinear points in the BCP, as well as the periodic orbit *PO1*, are linearly unstable, of centre $\times$ centre $\times$ saddle type, in each of the centre directions of each of these dynamical substitutes, there is a one-parametric family of quasi-periodic orbits with hyperbolic behaviour, [JV97a]. This means that there is one horizontal family and one vertical family of quasi-periodic orbits emanating from each dynamical substitute, where each quasi-periodic solution has a stable and an unstable invariant manifold associated. The invariant manifold that belongs to a two-dimensional torus is of dimension three. Taking into account the effective continuity of the family, the union of the (stable or unstable) invariant manifolds of one family of invariant tori constitutes a four-dimensional invariant object.

The analysis of the horizontal families of invariant tori, contained in the plane (x, y, p_x, p_y), can be performed in the planar BCP, where the dimension of the phase space is $n = 4$ (since $z = 0$ and $p_z = 0$) plus the dependence on time. Therefore, the aforementioned four-dimensional object separates the fifth dimensional phase space of the planar BCP and hence, it organises the flow around the invariant object that creates the family.

[1] At the begining of this chapter we briefly talked about the special case of L_2.

This is different in the case of the vertical families of invariant tori, two-dimensional tori tangent to the (z, p_z) plane, since the analysis needs to be done in the spatial BCP, that involves a seven-dimensional phase space.

In order to compute the invariant objects around these equilibrium points we make use of the aforementioned temporal Poincaré map at time T, such that the dynamical substitutes of the equilibrium points are seen as fixed points in the map and the two-dimensional tori are seen as one-dimensional invariant curves, therefore we will rely on the explanations and details presented in Section 1.4 for their numerical computation and analysis.

As introduced at the beginning of this chapter, our main concern is on the dynamics related with the invariant objects in the neighbourhood of L_3. In addition, we are also interested in showing the unstable behaviour near the triangular points. Then, the following two sections are devoted to the invariant objects that are found in their vicinities.

2.3 L_3 collinear point in the BCP

First of all, we need to find the dynamical substitute of L_3 equilibrium point in the BCP. For this, it is usual to apply a continuation method in terms of a parameter, let us call it ε, that is added to (2.7) allowing to move from the RTBP when $\varepsilon = 0$ to the BCP when $\varepsilon = 1$,

$$H_\varepsilon = H_{RTBP} + \varepsilon \hat{H}_{BPC}. \tag{2.9}$$

Let us denote by P_ε the Poincaré map defined by the flow at time T, the period of the BCP, for this ε-dependent Hamiltonian function H_ε. It is clear that the L_3 point of the RTBP is a fixed point of the map P_ε for $\varepsilon = 0$. We continue this fixed point of the map P_ε for ε going from 0 to 1, and no bifurcations occur, see the plot on the left of Figure 2.3. On the right of the same figure, the resulting periodic orbit for $\varepsilon = 1$ is shown, this is the dynamical substitute of L_3 in the BCP. Note that the dynamical substitute of L_3 in the map P is seen as a point, let us call it p_{L_3}, whose coordinates (x, y, z, p_x, p_y, p_z) are

$$p_{L_3} = (0.997186694046419,\ 0,\ 0,\ 0,\ 1.015787603690979,\ 0). \tag{2.10}$$

In order to understand why the dynamical substitute of L_3, at the right of Figure 2.3, goes around twice we can write the Taylor expansion of the solar gravitational potential as the authors did in [JCFJ18], it starts as

$$\frac{1}{a_s}\left(1 + \frac{x\cos\vartheta - y\sin\vartheta}{a_s}\right), \tag{2.11}$$

and then, they realised that the Coriolis acceleration is compensated by the linear order of the gravitational potential of the Sun. With this, the first non-autonomous contributing term is of order 2, for this reason, it is at second time that the periodic orbit crosses in positions that it closes.

It is important to mention that the reason for performing the continuation was to clarify that no bifurcation of the periodic orbit takes place, as it happens for L_4 and L_5, [SGJM95, JCFJ18] and we will see in Section 2.4. Actually, in the case of L_3 the computation of its dynamical substitute in the BCP could have been simply performed by directly imposing $\varepsilon = 1$ in (2.9) and looking for the fixed point of the Poincaré map by means of a Newton method.

The type of stability of the orbit remains the same as for the equilibrium point L_3 in the RTBP, centre $\times$ centre $\times$ saddle. Where one centre belongs to the (x, y, p_x, p_y) plane and the other is tangent to the (z, p_z) plane, referred as `Horizontal centre` and `Vertical centre`, respectively, in Table 2.2. This

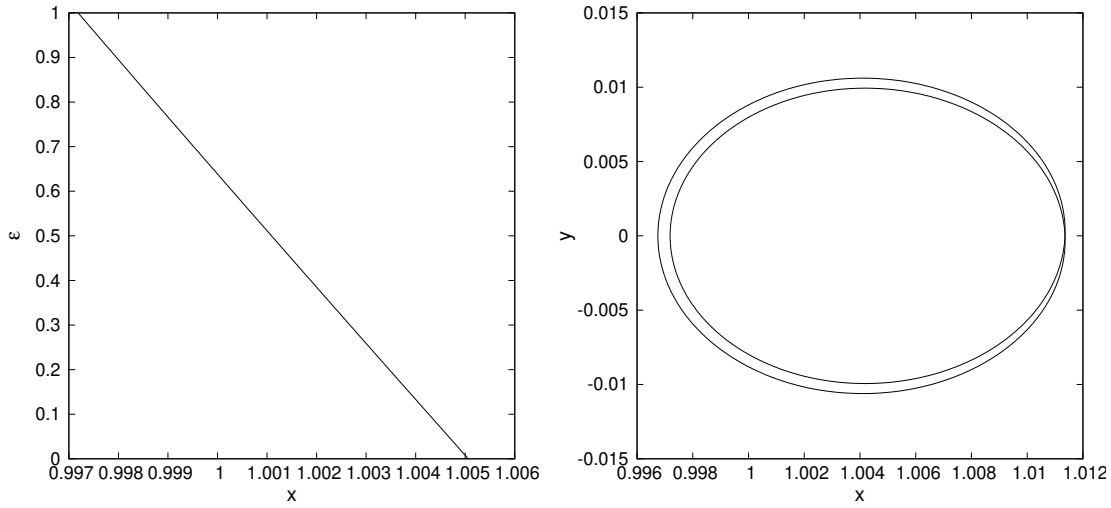

Figure 2.3: Left, continuation of the fixed point of L_3 on P_ε in terms of ε. Right, periodic orbit replacing L_3 in the BCP, i.e. when $\varepsilon = 1$.

	Re(λ)	Im(λ)	modulus	argument
Horizontal centre	0.863703727358484	0.503999872368095	1.0000	0.5282236213808816
Vertical centre	0.841136691142219	0.540822583491406	1.0000	0.5714147449967407
	λ_u	λ_s		
Saddle	3.372815841682823	0.296488170993962		

Table 2.2: Eigenvalues of the dynamical substitute of L_3 in the BCP. The two centres are imaginary of modulus one and the hyperbolic pair corresponding to the saddle part is real and satisfies $\lambda_u = \lambda_s^{-1}$ due to the Hamiltonian structure.

table includes the eigenvalues of the two centres, that are imaginary and have modulus equal to 1. Also their arguments are shown since they will be used in the computation of the families of invariant curves. In the last row, the table contains the hyperbolic eigenvalues corresponding to the Saddle part, that are real, where λ_u denotes the unstable eigenvalue and λ_s the stable one. Note that, due to the Hamiltonian structure $\lambda_u = \lambda_s^{-1}$.

2.3.1 Horizontal family of quasi-periodic orbits

The horizontal family of quasi-periodic orbits growing from L_3 is contained in the (x, y, p_x, p_y) plane, therefore their computation and analysis can be performed in the planar BCP, i.e. taking $z = 0$ and $p_z = 0$ in (2.7). Besides, in order to reduce the angular dimension introduced by the perturbation of the solar gravitational field, we make use of the temporal Poincaré map defined at time T, P. With this, the dimension of the phase space to work with in this section is $n = 4$.

As announced, the BCP corresponds to the case in which the Poincaré map becomes autonomous (Observation 1.2.1). Therefore, we follow the steps detailed in Section 1.4 for the computation of the invariant objects in the BCP.

The first thing we need to do is to compute an invariant curve very close to the point that occupies the periodic orbit L_3 in the map, p_{L_3}. Following Section 1.4.1, to find this curve, φ, we discretize it in terms of Fourier series, see (1.35), in this case with $N = 25$ Fourier modes, and look for zeros of the invariance condition (1.36),

$$F = P(\varphi(\theta)) - \varphi(\theta + \rho) \equiv 0,$$

by means of Newton method.

In this case the rotation number of the invariant curve, ρ, is not known, therefore the linear system to solve is composed by $m+2$ equations for $m+1$ unknowns, recall that $m = n(2N+1)$. Consequently, we need to fix two coordinates to have a unique solution. In particular, we fix the components x and y of φ when $\theta = 0$,

$$\begin{aligned} \varphi_x(\theta = 0) &= p_{L_3,x} - \delta, \\ \varphi_y(\theta = 0) &= 0, \end{aligned} \tag{2.12}$$

where $p_{L_3,x}$ denotes the x component of the point that L_3 occupies in the map P, p_{L_3} in (2.10). Note that $p_{L_3,y} = 0$.

The value of δ is the same as in the circle equation given in (1.40). We use that equation for the seed of the Fourier coefficients, starting with $\delta = 10^{-3}$. As seed for the rotation number we use the argument of the complex eigenvalue associated to the centre in the horizontal plane shown in Table 2.2.

Solving the system described in Section 1.4.1 with this information we obtain an invariant curve at a distance of 10^{-3} from p_{L_3}. Repeating the same procedure for some other small value of δ, for example $\delta = 2 \times 10^{-3}$, we compute another invariant curve. With these to invariant curves we proceed to the continuation of the family of invariant curves growing from L_3 using the sphere equation (1.41), as detailed at the end of Section 1.4.1.

Note that with an imposition like (2.12), the invariant curves are parametrized such that they always cut the x-axis at the left of point occupied by L_3 in the map when $\theta = 0$, given by p_{L_3} in (2.10). Therefore let us introduce the following definition.

Definition 2.3.1. *We call **distance to L_3** to the distance between the x component of the point L_3 in the map, p_{L_3} in (2.10), and the x component of the invariant curve at $\theta = 0$.*

The computed family of invariant curves around L_3 in the horizontal plane is shown in Figure 2.4. We have computed the continuation until a distance to L_3 of 0.8, that corresponds to a distance of around 0.2 from the centre of the Earth, quite close to the Earth. For this reason the invariant curves, that are, roughly speaking, circular close to p_{L_3}, start to deform when approaching the Earth. Consequently more and more Fourier modes are needed for their computations, see Figure 2.5, requiring $N = 211$ modes for the last computed curve. Recall that the number of Fourier modes is increased according with the error estimates introduced in Section 1.4.1. Then, for our purposes we have not continued the family of these invariant curves further from 0.8, since it already covers a considerable area and the increasingly number of Fourier modes difficult its numerical computation. Nevertheless, if there is an interest in the future for continuing this family as it approaches the Earth, this can be done by applying the reducibility (and parallelization) methods introduced in [JO09] that we will use at the final part of this dissertation.

As the invariant curves grow far away from L_3 their rotation number varies, in Figure 2.6 the variation of this magnitude along the family is shown. Note that a maximum in the rotation number is achieved, therefore at this point of the family the twist condition is not satisfied and the curve that occupies that position is a degenerated curve, sometimes called "meandering" curves [Sim98].

Normal behaviour of the family

Once computed the family of invariant curves, we analyze their linear behaviour. To accomplish this task we follow Section 1.4.2 and look for pairs of eigenvalue and eigenfunction (λ, ψ) that satisfy (1.42).

As explained in that section, for each curve $m = 4(2N+1)$ pairs of eigenvalue and eigenfunction

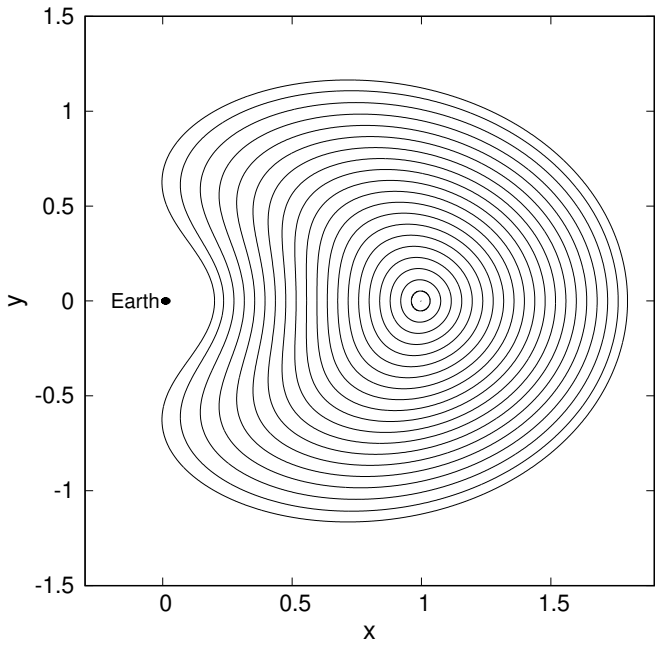

Figure 2.4: Horizontal family of invariant curves growing from L_3 dynamical substitute in the map P and projected in the (x, y) plane.

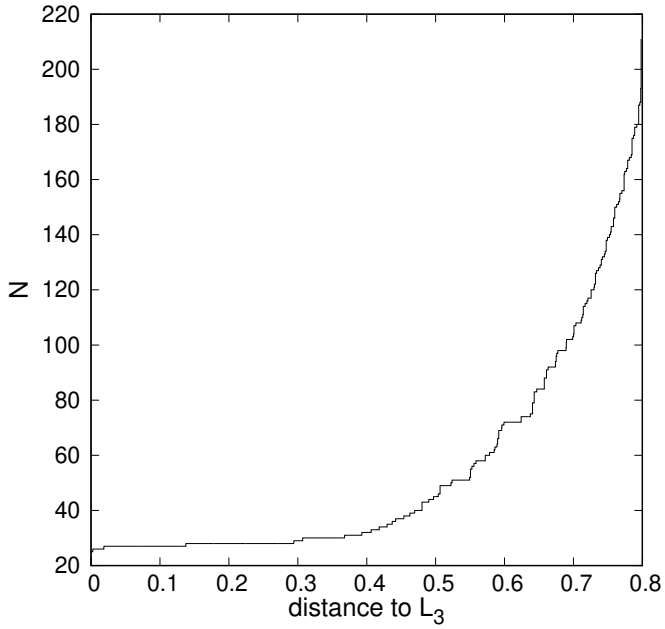

Figure 2.5: Variation of the number of Fourier modes needed to compute the invariant curves as their distance to L_3 increases.

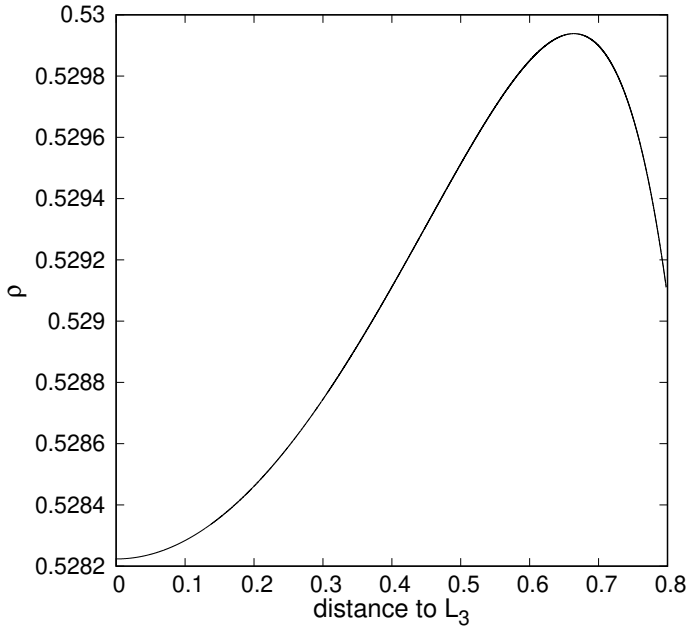

Figure 2.6: Variation of the rotation number as the distance of the invariant curves to L_3 increases.

are found. The eigenvalues are disposed in the complex plane in circles of radius $\{\lambda_s, 1, \lambda_u\}$, where the subindex s means stable and u, unstable. Again, due to the Hamiltonian structure, we have that $\lambda_s = \lambda_u^{-1}$. See some examples in Figure 2.7, where the eigenvalues of some of the invariant curves are plotted along with three circles of radius equal to the eigenvalues of the dynamical substitute of L_3, see Table 2.2.

It was also mentioned in Section 1.4.2 that not all the eigenvalues are equally accurate, therefore we must keep the most accurate ones basing our search on the expression of the p-norm introduced for the eigenfunctions, (1.45), in particular we use p = 2.

It is clear that the most accurate hyperbolic eigenvalues should be those that lie on the real axis, see Figure 2.7. Looking at these images, it is also clear that as further is the invariant curve to p_{L_3}, its hyperbolic eigenvalues get apart from those associated to the dynamical substitute of L_3. The variation of these stable and unstable eigenvalues associated to each invariant curve according to the distance to L_3 is shown in Figure 2.8. It is appreciated how the instability of the family becomes weaker as the distance to L_3 increases.

2.3.2 Vertical family of quasi-periodic orbits

The procedure is almost the same as in the previous section but now the family of invariant curves is tangent to the (z, p_z) plane and consequently, its computation and analysis require to work in the spatial phase space, $n = 6$.

Now we use the stability information of the `Vertical centre` in Table 2.2 and impose conditions on the z and p_z coordinates to compute the first two curves of this family. Analogously to (2.12), for the vertical family we impose

$$\begin{aligned} \varphi_z(\theta = 0) &= -\delta, \\ \varphi_{p_z}(\theta = 0) &= 0, \end{aligned} \tag{2.13}$$

Note that the z and p_z coordinates of p_{L_3} are zero, see (2.10). Then with the imposition above, the

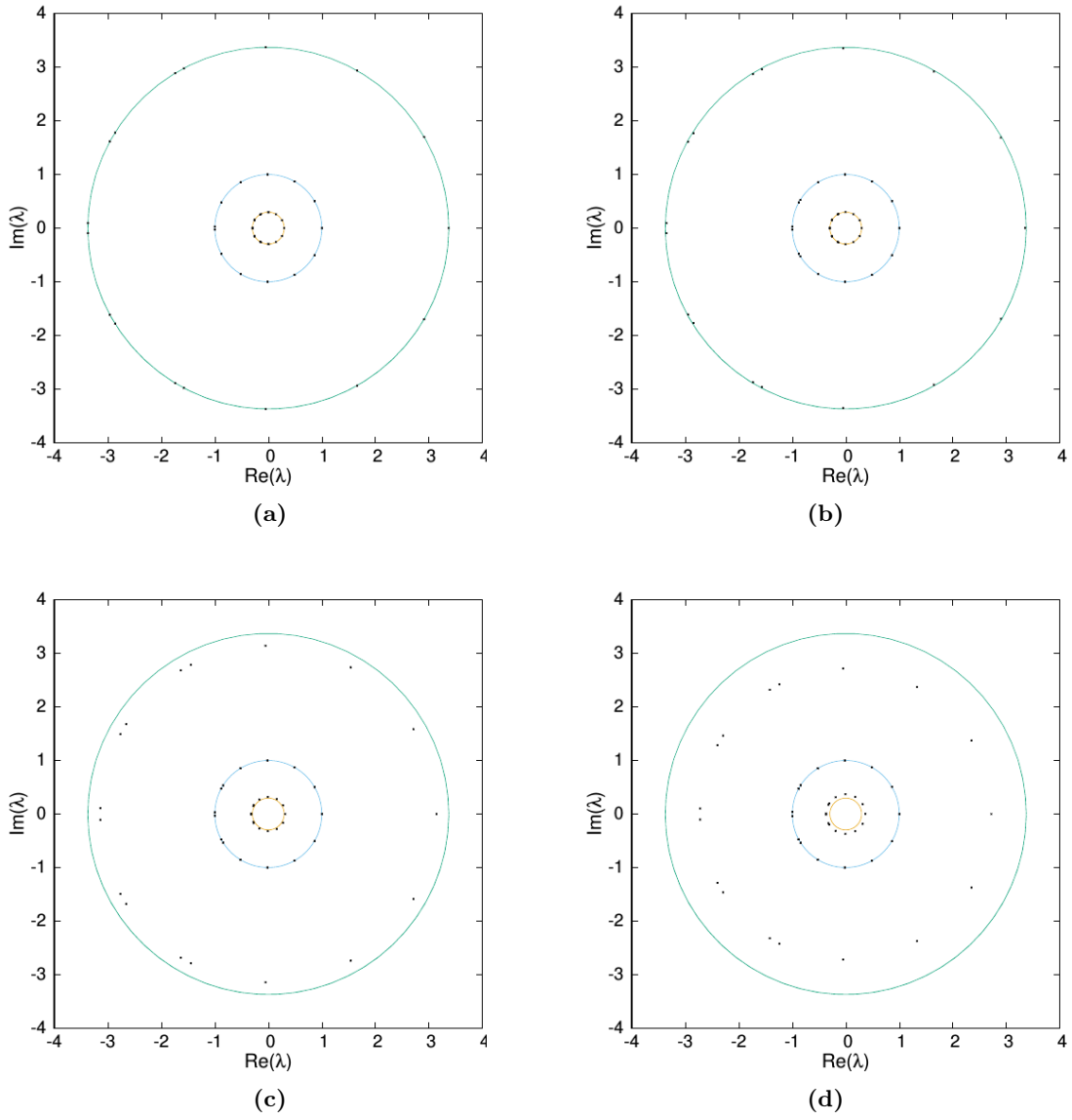

Figure 2.7: Graphs of the eigenvalues obtained from solving the generalised eigenvalue problem (1.42) for four invariant curves at distances to L_3 equal to 6.0505×10^{-3} (a), 1.3073×10^{-1} (b), 4.3616×10^{-1} (c) and 6.8953×10^{-1} (d). The eigenvalues of the invariant curves are plotted as black stars along with three circles of radius corresponding to the eigenvalues $(\lambda_u, 1, \lambda_s)$ of the dynamical substitute of L_3 appearing in Table 2.2; in particular, the circle in green has radius equal to λ_u, the one in blue equal to 1 and the one in orange has radius equal to λ_s.

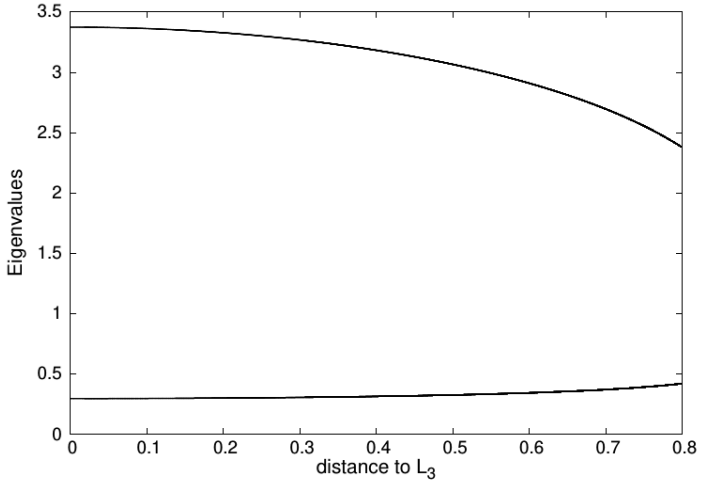

Figure 2.8: Variation of the hyperbolic eigenvalues, stable ($\lambda_s < 1$) and unstable ($\lambda_u > 1$), as the distance of the invariant curves of the horizontal family to L_3 increases.

curves are parametrized such that at angle $\theta = 0$ they have zero vertical momentum and cut the z-axis on the negative part according to the value of δ.

Definition 2.3.2. *We call* ***vertical distance to L_3*** *to the distance between the z component of the point L_3 in the map, p_{L_3} in (2.10), and the z component of the invariant curve at $\theta = 0$.*

It is worth to mention that, since there is no massive body or any other invariant object significantly close to this family, its growth is easily continued up to high values of the vertical amplitudes, see the plot at the left of Figure 2.9. In fact we compute invariant curves up to almost a vertical distance of 1 from p_{L_3} (more precisely up to $z \approx 0.9663$) using only $N = 25$ Fourier modes for each curve all over the family. Reaching a vertical distance of 1 has not been feasible. The reason may be in the bifurcations that the vertical family of periodic orbits around L_3 suffers in the Earth-Moon RTBP, see [GM01]. It is known that it suffers three bifurcations, where the third one implies the termination of the family into a planar orbit that surrounds the two primaries and the three collinear equilibrium points. Since the vertical family of invariant curves around L_3 in the BCP comes from the one of periodic orbits in the RTBP, the bifurcation in latter may explain the termination of the former. In the BCP case the last invariant curve obtained does not surround the two primaries, but it approaches the Earth, as it is shown in the plot at the right of Figure 2.9, that corresponds to the projection in the (x, y) plane of the family of invariant curves in the Poincaré map.

In Figure 2.10 a spatial view of the family, in (x, y, z) coordinates, is given. It is clear the symmetry between the solutions passing through positive or negative values of z, one of the symmetries presented in Equation (2.3). It is also appreciated that, as the value of z gets apart from zero, be it positive or negative, these invariant curves approach the position of the Earth in the x coordinate.

The variation of the rotation number of the invariant curves in the vertical family with respect to the vertical distance to L_3 does not present any maximum or minimum, see Figure 2.11 left.

Once we have the invariant curves, we study their linear behaviour as explained in Section 1.4.2. We find that the invariant curves in the vertical family growing from L_3 are also hyperbolic, as the curves in the horizontal family, with real eigenvalues for each torus shown in Figure 2.11 right. As it happens in the horizontal family, here we can also observe how the instability of the family becomes weaker as the distance to L_3 increases.

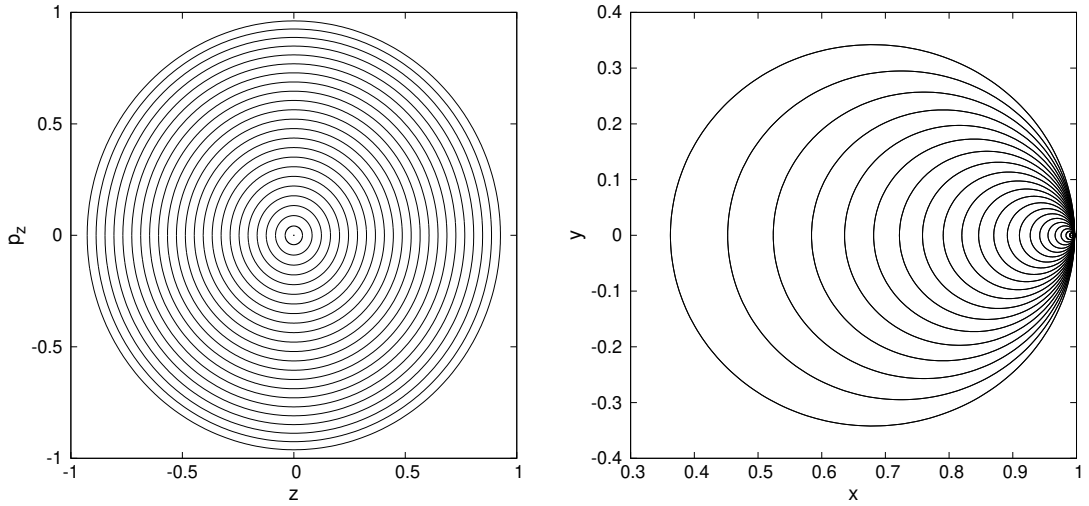

Figure 2.9: Vertical family of invariant curves growing from L_3 dynamical substitute in the map P. Left, projected in the (z, p_z) plane. Right, projected in the (x, y) plane.

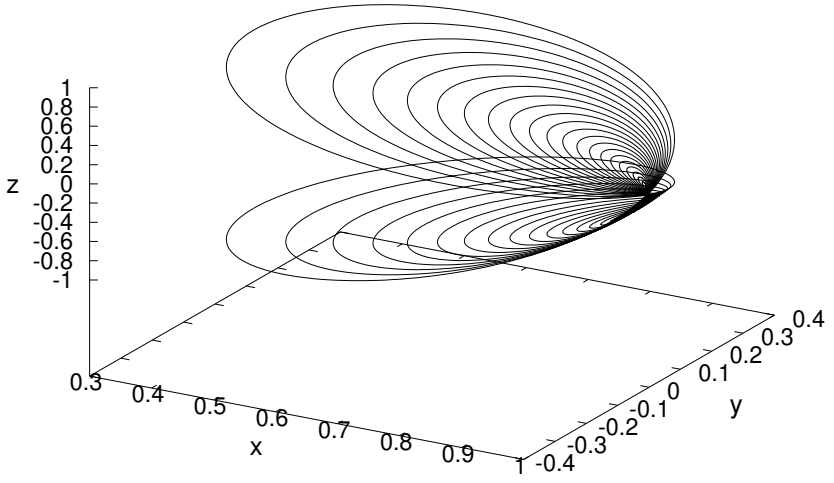

Figure 2.10: Spatial view, in (x, y, z) coordinates, of the vertical family of invariant curves growing from L_3 dynamical substitute in the map P.

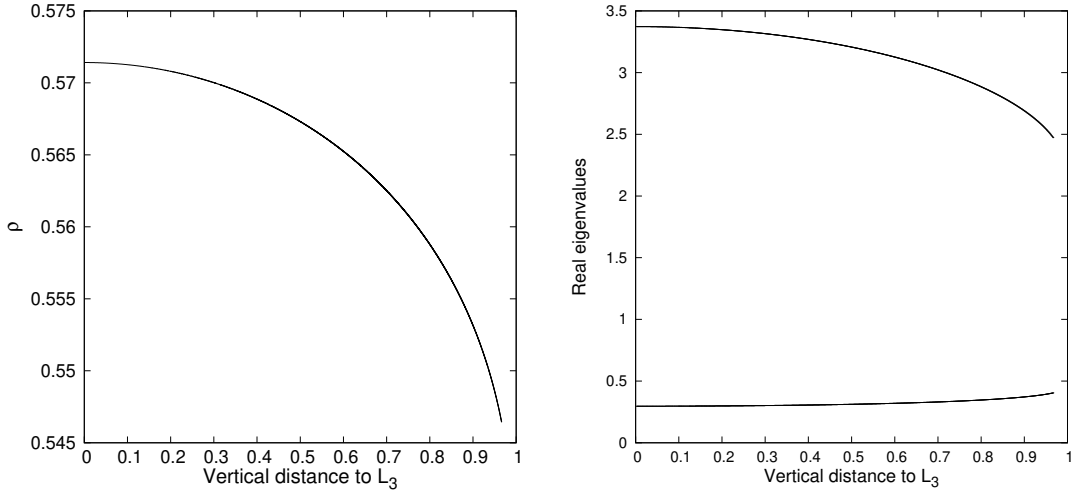

Figure 2.11: Left, variation of the rotation number as the vertical distance of the invariant curves to L_3 increases. Right, variation of the real eigenvalues of the invariant curves.

2.4 Triangular points in the BCP

In this section we talk about the family of quasi-periodic orbits around one of the dynamical substitutes of the triangular points. The study of these dynamical substitutes in the BCP for the case of the solar-perturbed Earth-Moon system has been the target of many works [SGJM95, JCFJ18] and the families of invariant curves at their neighbourhoods can be found in [Cas03]. In this dissertation we have repeated some of these computations with the aim of extending the knowledge about the unstable behaviour around them, this will be presented in Chapter 5.

It is well-known that in the case of triangular points, for the system we are treating, there exists a bifurcation when performing the continuation of the L_4 point from the RTBP to the BCP, a detailed analysis of this bifurcation can be found in [JCFJ18]. The process for the continuation is like the one performed in the previous section for L_3 with the Equation (2.9). Said bifurcation gives rise to three dynamical substitutes for each of the triangular points; three periodic orbits with the period of the perturbation, two of them linearly stable and one unstable. This is detailed in [SGJM95], in which authors gave the names *PO1* to the unstable periodic orbit and *PO2* and *PO3* to the two stable ones. The variation of the fixed point in P_ε according to the value of ε for L_4 can be found in the plot on the left of Figure 2.12. On the right of same figure we show the three periodic orbits substituting L_4 in the BCP, i.e. when $\varepsilon = 1$. It is clear that by the symmetry (2.3), also present in the BCP, the same bifurcation occurs for L_5.

These three periodic orbits near L_4 are seen as fixed points in the temporal Poincaré map P. Let us denote them, abusing notation, by p_{PO1}, p_{PO2} and p_{PO3}, with coordinates (x, y, z, p_x, p_y, p_z),

$$\begin{aligned}
p_{PO1} &= (-0.489747046956582,\ 0.870531584107967,\ 0,\\
&\qquad -0.854843586317783,\ -0.489868573136372,\ 0),\\
p_{PO2} &= (-0.718951017967613,\ 0.816712731336547,\ 0,\\
&\qquad -0.744398375648738,\ -0.517371635492186,\ 0),\\
p_{PO3} &= (-0.090233783126090,\ 0.947699209500149,\ 0,\\
&\qquad -0.998675985923189,\ -0.262665745802195,\ 0).
\end{aligned} \tag{2.14}$$

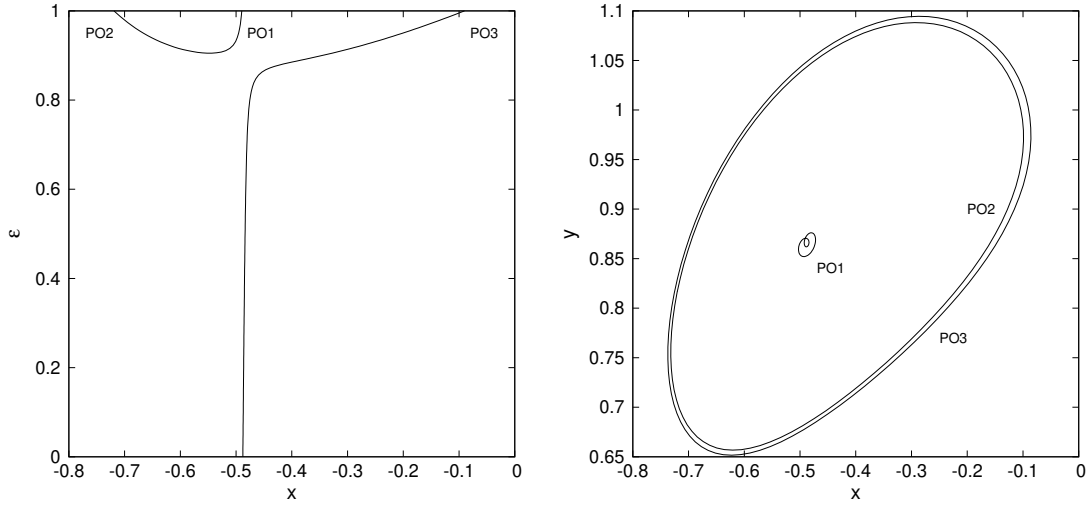

Figure 2.12: Left, continuation of the fixed point of L_4 on P_ε in terms of ε. Right, periodic orbits replacing L_4 in the BCP, i.e. when $\varepsilon = 1$.

	Re(λ)	Im(λ)	modulus	argument
Horizontal centre	-0.4528721303074714	0.8915754783475778	1.0000	2.040780450260600
Vertical centre	0.8601576454180473	0.5100282590493204	1.0000	0.535217643292990
	λ_u	λ_s		
Saddle	1.098639944378693	0.9102163134670177		

Table 2.3: Eigenvalues of *PO1*, the unstable dynamical substitute of L_4 in the BCP. The two centres are imaginary of modulus one and the hyperbolic pair corresponding to the saddle part is real and satisfies $\lambda_u = \lambda_s^{-1}$ due to the Hamiltonian structure.

Periodic orbit *PO1* is of type centre × centre × saddle, therefore from the point it occupies in the plane P, there emanates a family of invariant curves in the horizontal plane and another family tangent to the vertical one. Associated eigenvalues are shown in Table 2.3.

In spite of the appearance of an unstable periodic orbit, and since its instability is very weak (see its hyperbolic eigenvalues, λ_u and λ_s, in Table 2.3), regions of effective stability around L_4 can be still found in the Bicircular Earth-Moon system, [Jor00], specially when the vertical coordinate is different from zero. In that work the stable regions were translated to a realistic model, based on JPL ephemeris, to verify that they are still present when the gravitational effect of the rest of the planets of the solar system are also considered.

Most of the works devoted to the study of the triangular points are centred on the stable behaviour since it is the dominant one in their regions and it is of interest for many applications. However, our interest is focused on the unstable behaviour, more precisely the study of the periodic orbit *PO1*, the families of invariant quasi-periodic orbits around it and in the stable and unstable invariant manifolds associated to them.

2.4.1 Horizontal family of quasi-periodic orbits around *PO1*

The way to proceed is the same as in Section 2.3.1. Recall that for the horizontal families we work with $n = 4$ dimensions of the phase space. Again, we follow the steps detailed in Section 1.4.1 for computing the invariant curves. In this case we use the argument of the `Horizontal centre` in

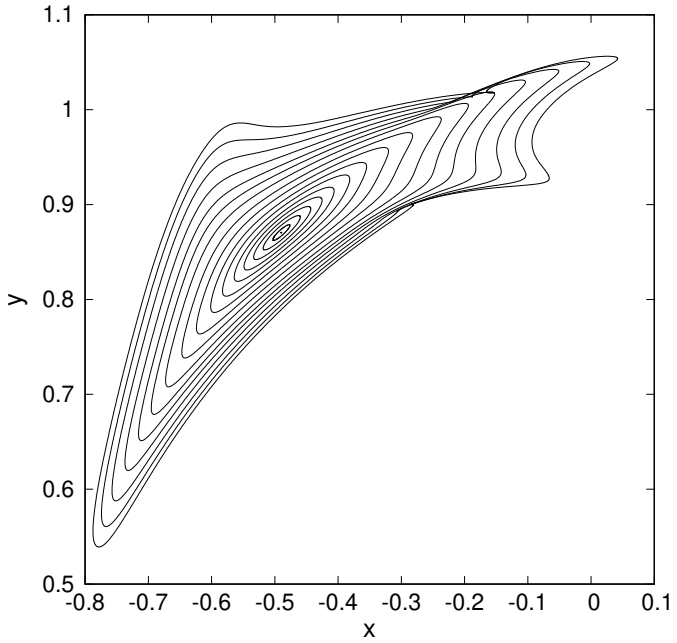

Figure 2.13: Horizontal family of invariant curves growing from the *PO1* dynamical substitute of L_4 in the map P and projected in the xy-plane.

Table 2.3 and impose the following conditions:

$$\begin{aligned} \varphi_x(\theta = 0) &= p_{PO1,x}, \\ \varphi_y(\theta = 0) &= p_{PO1,y} - \delta, \end{aligned} \tag{2.15}$$

where $p_{PO1,x}$ and $p_{PO1,y}$ denote the x and y components of the dynamical substitute *PO1* of L_4 in P, where it is seen as a point, see (2.14). With these conditions, each curve is parametrized such that at $\theta = 0$ they cut the line $x = p_{PO1,x}$ at different values of y.

Definition 2.4.1. *We call* ***distance to PO1 of*** L_4 *to the distance between the y component of the point PO1 of* L_4 *in the map P, (2.14), and the y component of the invariant curve at* $\theta = 0$.

The family of invariant curves growing from *PO1* in the map is shown in Figure 2.13. The limitation of the growth of this family and the wrinkle shape of these invariant curves is due to the effect the families of invariant curves around *PO2* and *PO3*. As the invariant curves are further away from the *PO1* of L_4 more difficult is to compute them and more Fourier modes are needed for their parametrization, see Figure 2.14, where it is easily observed how quickly increase the number of modes as the curves grow further from the dynamical substitute.

Figure 2.15 shows the variation of the rotation number of these curves as they grow far away from *PO1* of L_4 and the variation of their real eigenvalues. We can observe that although the invariant curves around the *PO1* of L_4 are hyperbolic, its instability is extremely weak, specially close to the periodic orbit *PO1*.

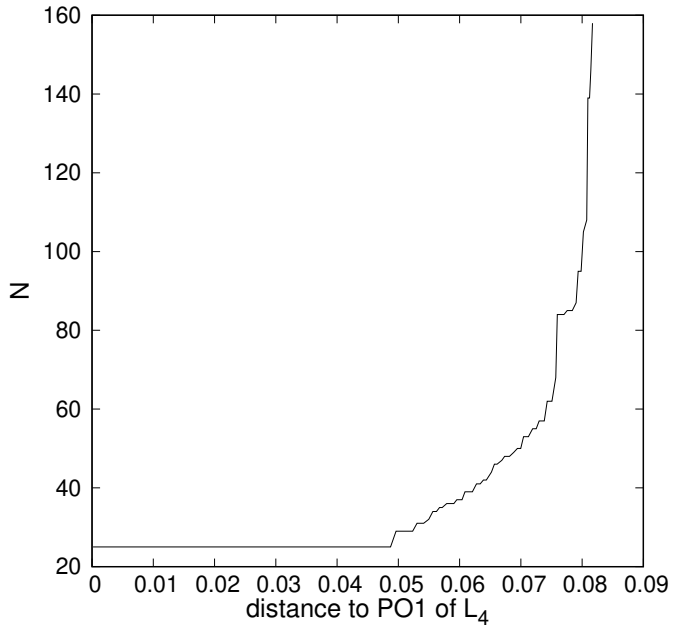

Figure 2.14: Variation of the number of Fourier modes needed to compute the invariant curves as their distance to the *PO1* of L_4 increases.

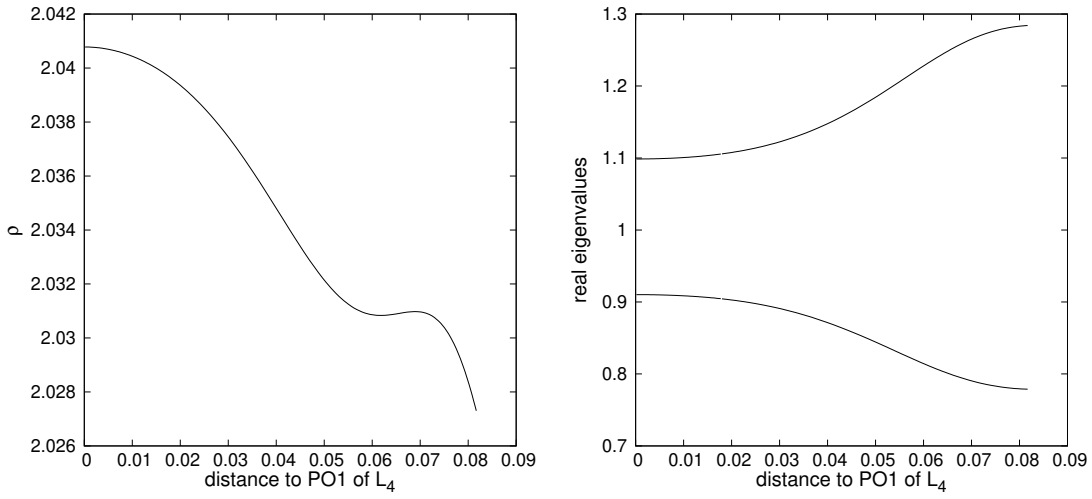

Figure 2.15: Left, variation of the rotation number as the distance of the invariant curves to *PO1* of L_4 increases. Right, variation of the real eigenvalues of the invariant curves.

2.5 Change of coordinates and time

To finish this chapter about the Bicircular Problem, we include a section about the change of coordinates and time needed to make comparisons between this simplified model and a realistic one.

The fact that the Bicircular Problem is a time-dependent model implies somehow a relation between this simplified model and the real one, that allows to look for a correspondence between epochs in the two different models and for a suitable change of coordinates involving the information of the bodies, Sun, Earth and Moon, in the real system at the proper time.

First, the correspondence between times in the two models is introduced, Section 2.5.1. The change is a little bit different depending on the sense of the translation, however both are based on the same features of the model. Then, the translation of coordinates, positions and velocities, of an infinitesimal particle is detailed in Section 2.5.2.

2.5.1 Time

The statement about the relation between the epochs in the BCP model and a real one is based on two properties of the BCP. The first one is that, at time $t = 0$, the three massive bodies are placed on the x-axis, see Figure 2.2, such that their relative positions correspond to a lunar eclipse. The second property relies on the fact that time is a periodic variable in the BCP, as a result, at every period T, the Earth, the Moon and the Sun come back to their initial positions.

Time from BCP to real system

Due to the periodicity of time in the BCP, it is clear that any possible value for time, $t \in \mathbb{R}$, in this model can be re-scaled to $t \in [0, T]$ (or $t \in [-T, 0]$ when the sense of time is inverted). Also, any adimensional time can be measured in days, $\tilde{t}$, with the conversion unit of time,

$$\tilde{t} = t\frac{27.321577}{2\pi}.$$

Since at $t = 0$ the massive bodies describe the set up of a lunar eclipse, it is easy to identify a real lunar eclipse, such that $t = 0$ in the BCP is translated to the time of the eclipse, $T_{ECLIPSE}$ in Julian days. Therefore, any other adimensional time after (or before) $t = 0$ corresponds to some days after (or before) the eclipse:

$$t \text{ (adimensional time)} \to T_{ECLIPSE} + \tilde{t} \text{ (Julian days)}. \tag{2.16}$$

Time from real system to BCP

The basis is the same, but now the set of times to be translated is much wider. We can establish the origin of time in the real system as

$$t_0 = T_{ECLIPSE} + S_T\tilde{T}, \quad \text{with} \quad S_T \in [0, 1), \tag{2.17}$$

where

$$\tilde{T} = T\frac{27.321577}{2\pi}$$

is the period of the Sun with respect to the Earth-Moon system in days, since $T = \frac{2\pi}{\omega_s}$ is defined in adimensional RTBP units. Then, S_T denotes the fraction of period after the lunar eclipse, what corresponds to the temporal section $t = S_T T$ in the BCP.

Let N_T be an integer number that accounts for the number of lunar periods after the origin of time. Since time is a periodic variable in the BCP, any Julian epoch of the form

$$t = t_0 + N_T \tilde{T}, \tag{2.18}$$

corresponds to the same temporal section in the BCP. In a schematic way

$$t \text{ like in (2.18) (Julian days)} \rightarrow S_T T \text{ (adimensional time)}. \tag{2.19}$$

Note that, S_T can be also defined with negative values, $S_T \in (-1, 0)$, such that it would denote the fraction of period before the lunar eclipse. Likewise, subtracting $N_T \tilde{T}$ to t_0, we have a set of Julian epochs that corresponds to the same BCP temporal section.

2.5.2 Positions and velocities

As usual, there is not a unique change of coordinates for translating the positions and velocities of an infinitesimal particle between a simplified model and a realistic one. The change of coordinates that we detail here and will be used in Chapters 3 and 4 is a non-autonomous change of coordinates that was introduced in [GLMS85] and afterwards employed in some other works devoted as to the RTBP as to the BCP, for example [GLMS01]. Concerning to its application to the BCP, we find [Jor00], where the translation was performed at the time of an eclipse or [GJMS01], where the change was employed covering a time span what lead the authors to observe that, in spite of the general good agreement found in the comparison between BCP and realistic model, the goodness of the change of coordinates depends on the epoch at which it is performed. This effect will be also observed in Section 3.2 where we will give some explanations about its appearance.

The reference frame of the BCP consists on an adimensional synodical frame, with the origin of coordinates placed at the Earth-Moon barycentre and where the distances between the three massive bodies are taken as constant. Meanwhile the reference frame of the real system consists on an ecliptical inertial one, with the origin placed at the solar system barycenter and where the distances between the bodies are continuously changing.

Therefore, it is necessary to know the positions and velocities of the primaries and the Sun at the time at which the change of coordinates is performed. For this, an ephemerides database is used. In particular, we use the Jet Propulsion Laboratory (JPL) ephemeris, file DE405, that provides the orbital information of the bodies by interpolating polynomials.

In the case of the change of coordinates, the translation between the systems is given by the same expressions regardless the sense of the translation. Then, let us explain the change of coordinates from the adimensional synodic reference frame of the BCP to the ecliptical inertial one.

Let a be the positions of an infinitesimal particle in the adimensional synodic reference frame of the Bicircular model, and let e be its positions in the real ecliptic one. The relation between them is given by a scale factor to change the unit of length, an ortoghonal matrix to move from a rotating frame to a non-rotating one and a translation to the origin of coordinates of the ecliptic system:

$$e = kCa + b, \tag{2.20}$$

where $k = ||R_E - R_M||$ is the scale factor, with $||\cdot||$ denoting the euclidean norm, and R_E and R_M being the positions of the Earth and Moon in the ecliptic frame. Then, k is the instantaneous distance between the primaries at the time of the conversion. The vector b points to the position of the Earth-Moon barycentre from the barycentre of the solar system, see Figure 2.16.

Matrix C is an orthonormal matrix composed by three unitary column vectors,

$$c_1 = \frac{R_E - R_M}{||R_E - R_M||}, \qquad c_3 = \frac{(R_M - R_E) \wedge (V_M - V_E)}{||(R_M - R_E) \wedge (V_M - V_E)||}, \qquad c_2 = c_3 \wedge c_1,$$

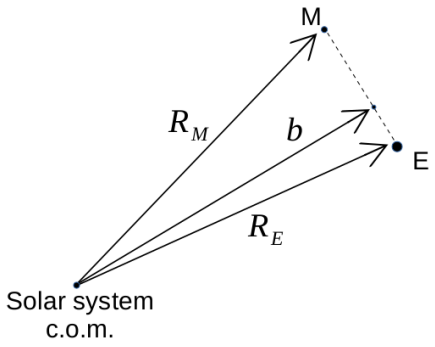

Figure 2.16: Scheme of the vectors R_E, R_M and b pointing to the Earth (E), the Moon (M) and their barycenter from the solar system centre of mass in the ecliptic system.

where V_E and V_M are the velocities of the Earth and Moon in the ecliptic frame. This matrix is in charge of changing between rotating and non-rotating reference frames, but it also includes the modification of the relative positions of the primaries, that in the BCP are suppose to be coplanar and separated by a constant distance at all times. Then, it is important to observe that the first vector, c_1, marks the direction between the two primaries, the expression of the third one, c_3, is the normalised angular momentum for their relative motion, so that it is positively oriented, and the second one, c_2, is positively defined perpendicular to the other two.

Be $R = R_M - R_E$ and $V = V_M - V_E$, the position and the velocity of the Moon with respect to the Earth. So, column vectors of matrix C are rewritten as:

$$c_1 = \frac{-R}{k}, \qquad c_3 = \frac{R \wedge V}{||R \wedge V||}, \qquad c_2 = c_3 \wedge c_1. \tag{2.21}$$

The relation between the velocities in the adimensional system, $\dot{a}$, and the ones in the ecliptic system, $\dot{e}$, is also needed. For getting it, it is necessary to derive expression (2.20) with respect to time:

$$\dot{e} = \dot{k}Ca + k\dot{C}a + kC\dot{a} + \dot{b}, \tag{2.22}$$

where $\dot{b}$ is the velocity of the barycenter and $\dot{k} = \frac{RV}{k}$ is the derivative of the scale factor.

Rotational matrix derivative is performed by deriving the three column vectors with respect to time:

$$\dot{c}_1 = \frac{-kV + \dot{k}R}{k^2}, \qquad \dot{c}_3 = \frac{W(R \wedge A) - \dot{W}(R \wedge V)}{W^2}, \qquad \dot{c}_2 = \dot{c}_3 \wedge c_1 + c_3 \wedge \dot{c}_1, \tag{2.23}$$

where $A = A_M - A_E$ is the relative acceleration of the Moon with respect to the Earth, and $W = ||R \wedge V||$, so $\dot{W} = W^{-1}(R \wedge V)(R \wedge A)$.

Notice that, R_E, R_M, V_E, V_M and b are provided by the ephemeris database at the specific time of the conversion. Equivalently to how the change of positions between the two systems involves the velocities of the primaries, their accelerations are involved in the change of velocities. A_E and A_M are not provided by the ephemeris database we use, but they are easily computed by with a $\mathcal{N}$ body problem, making the balance of forces of all the planets of the solar system, the Sun and the Moon, acting on them (application of Newton's second law); whose positions and velocities are provided by the ephemeris database.

In particular, the JPL database provides these magnitudes in dimensional units; astronomical unit for length and day for time. Special attention must be paid to $\dot{a}$ in Equation (2.22), since this

quantity refers to the derivative with respect to the dimensional time of the adimensional position of the particle. Therefore, it is necessary to multiply the velocities of the particle in the adimensional system by $2\pi/27.321577$ before introducing it into the expression (2.22). Also, let us remember that in a synodic system, velocities and momenta do not coincide, then if we work with momenta in the BCP, it is necessary to change to velocities before performing the change of coordinates:

$$\dot{a} = \{\dot{a}_x, \dot{a}_y, \dot{a}_z\} = \frac{2\pi}{27.321577}\{\dot{x}, \dot{y}, \dot{z}\} = \frac{2\pi}{27.321577}\{p_x + y, p_y - x, p_z\}.$$

Finally in this section, let us briefly comment that the change of coordinates from the ecliptical reference frame to the synodic adimensional one, given by the same expressions (2.20) and (2.22), involve the inverse of the matrix C. Since this matrix is orthonormal, $C^{-1} = C^T$, and there is no need of computing the inverse.

Chapter 3

Transport through L_3 in the BCP

In Section 2.3 we show that there are two families of two-dimensional quasi-periodic orbits growing from L_3 in the BCP. These orbits are seen geometrically as tori defined by two frequencies, one coming from the unperturbed system and the other one corresponding to the perturbation. In the stroboscopic map, P, defined by the evaluation of the flow at time equal to the period of the solar perturbation, $T = 2\pi/\omega_s$, each of these families is seen as a family of one-dimensional invariant curves, one family in the horizontal plane and the other one tangent to the vertical plane, all details about these families, computation and stability are found in Section 2.3.1 and Section 2.3.2, respectively.

We have also seen that the quasi-periodic orbits that constitute these families are partially hyperbolic, therefore, each of them has a stable and an unstable invariant manifolds associated. Stable manifold approaches the torus forward in time, while the unstable one gets apart from it. Consequently, they represent a skeleton for connections through the invariant torus. Then, this chapter is focused on the transport due to the families of Lyapunov quasi-periodic orbits around L_3 in the BCP.

Recall that all conceptual and numerical details about hyperbolic invariant manifolds were introduced in the first chapter. More precisely, in Sections 1.4.3 and 1.4.4 for the case of manifolds associated with invariant curves in autonomous stroboscopic maps, that is the case of the present chapter. Therefore, now we limit ourselves to brief comments on the theoretical aspects and focus on the application.

The invariant manifolds associated with two-dimensional quasi-periodic orbits have three dimensions, two dimensions of the torus plus the hyperbolic direction. Therefore in the map P these manifolds are two-dimensional and they can be defined through two parameters, the angle along the curve θ and a parameter σ to move in the direction of the stable/unstable eigenfunction.

Taking into account that the stability of the families of invariant curves around L_3 is hyperbolic but neither very strong nor very weak (see Figure 2.8 and 2.11), the analysis of the transport given by the linear approximation of the related invariant manifolds is enough for understanding their role. We recall that such approximation of the manifolds of an invariant curve is given by the curve itself (φ) and its stable and unstable eigenfunctions ($\psi_{s,u}$), see (1.47) in Section 1.4.3,

$$(\theta, \sigma) \mapsto \varphi + \sigma\psi_{s,u}(\theta). \tag{3.1}$$

By evaluating last expression on a mesh of values for $\theta \in [0, 2\pi]$ and for $\sigma \in [\sigma_0, \sigma_0\lambda_u]$ (for the unstable manifold) or $\sigma \in [\sigma_0, \sigma_0\lambda_s^{-1}]$ (for the stable manifold), it generates a set of curves, displaced from the invariant one in the direction of the eigenfunctions. Said set of curves constitutes a fundamental domain of the manifold that we have called fundamental cylinder (FC), detailed in Section 1.4.4, that by iteration under P (or P^{-1}) spans the whole unstable (or stable) manifold. Recall the comments about the convenience of using application of the stroboscopic map forward in time for the unstable

manifolds and the backward in time for the stable ones, Remark 1.4.4.

When working with the linear approximation of the invariant manifolds the value of the displacement σ_0 must be small enough for the approximation to be accurate. In particular we have used $\sigma_0 = 10^{-5}$. Note that, in order to have both "sides" of the manifold, parameter σ_0 must also take a negative value. Then, in order to globalise the manifold, we have defined an equispaced mesh of M_1 values of θ, and mesh of M_2 equispaced values of σ to construct a mesh of $M_1 M_2$ points on the manifold that we propagate forward to span the unstable manifold and backwards to span the stable manifold.

During the propagation of the orbits in the manifolds, we check at every step of the numerical integration (that is performed again by means of a Taylor method [JZ05]) if they have reached some of the primaries or if they have left the system. Leaving the system has been defined as being at a distance from the Earth-Moon barycentre larger than 10 Earth-Moon distances, since at this distance we consider the particle to be orbiting around the Sun. At the moment that some orbit reaches the Earth or Moon, a Newton method is applied to refine the coordinates at which the orbit reaches their surfaces. Throughout the text we talk about lunar and terrestrial surfaces for simplicity, however keep in mind that when we study the planar case, trajectories that reach the primaries are analysed at their equators.

Before following with the invariant manifolds, let us give a scheme of this chapter. In Section 3.1 we show the results and general behaviour found for the invariant manifolds associated with the invariant curves of the horizontal family. Special attention is paid to the behaviour of trajectories that may explain the travel of lunar meteorites towards the Earth, the analysis of this phenomenon and its translation to a realistic model are collected in Section 3.2. These first two sections are mostly presented in [JN20]. Section 3.3 is devoted to some comments about the trajectories that starting at a parking orbit of the Earth can reach some other locations of interest, like the Moon or the vicinities of other Lagrangian points. This section contains a summary of the joint work with Dr. Yuying Liang, [LNJ21], devoted to the design of a transfer to L_4 from a low orbit of the Earth, passing through that same horizontal family of L_3. Finally, in Section 3.4 we present the invariant manifolds associated with the vertical family of invariant curves around L_3.

This chapter is developed using the linear approximation of the invariant manifolds, we will present in the next chapter the high order approximation of these manifolds, that is needed to purposes in which a higher accuracy on the fundamental domain is required.

3.1 Transport through the horizontal family

It is well known that the invariant manifolds of L_3 in the RTBP approach the small primary giving rise to horseshoe-like motions [BO06, SSST13]. As we will see, in the BCP the invariant manifolds of the tori near L_3 display a shape that reminds that of the RTBP, but with important differences. In particular, in the BCP the motion is not restricted to an energy level so that the manifolds fill a larger region of configuration space and even they move far away from the Earth-Moon system.

In Figure 3.1, invariant manifolds corresponding to two invariant tori (one at distance 1.3974×10^{-3} from L_3, and another one at 5.5857×10^{-3}) are shown together to illustrate the shape of the manifolds for different tori. The "distance to L_3" is given according to Definition 2.3.1. As natural, the trajectories correspond to the flow, not to the Poincaré map. For reference, Earth and Moon are also included in the figure as black circles of proportional radius.

As expected, it takes some Earth-Moon revolutions to leave L_3 neighbourhood. This is shown in Figure 3.2, where the manifolds of the curve at 1.3974×10^{-3} from L_3 are plotted for different integration times. Images on the right column are the same as those on the left, but making a zoom

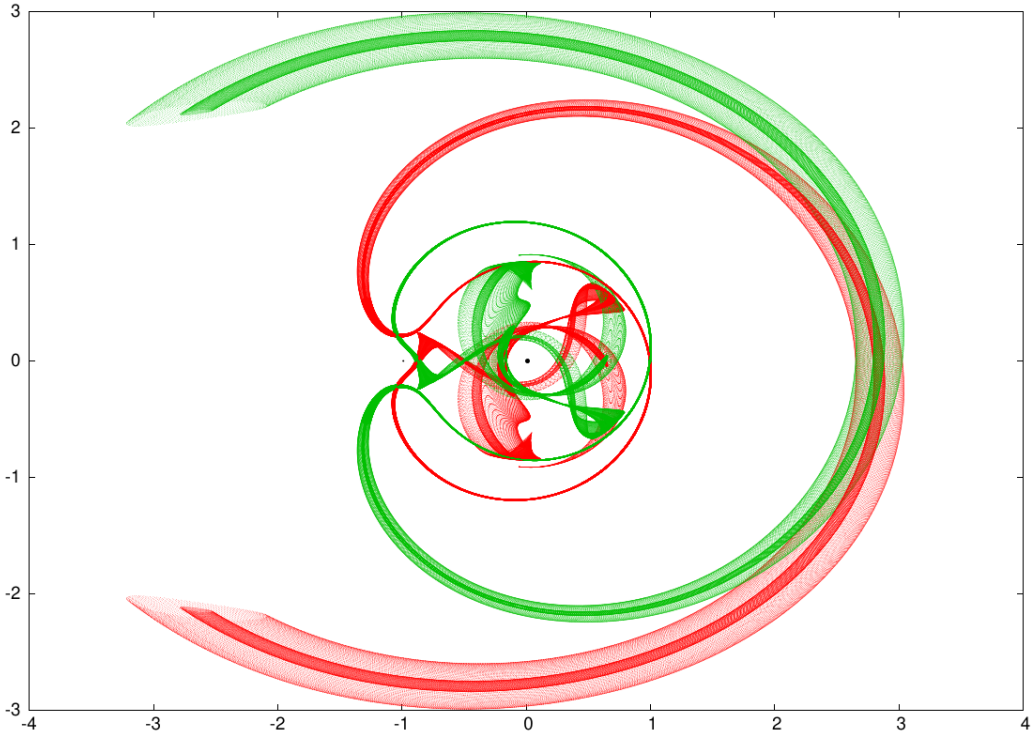

Figure 3.1: Stable (green) and unstable (red) invariant manifolds corresponding to two invariant curves, in the xy-plane. See the text for more details.

around the primaries in order to show how some of the orbits reach them. The integration time for the first (upper) image is meaningless since it depends on the initial distance to the invariant torus. The following images are separated in time just by one Earth-Moon revolution. Note that the manifolds reach not only the Moon, but also the Earth. As a side comment, the reversing symmetry of the BCP mentioned in Section 2.2, see Remark 2.2.1, is now easy to observe: therefore, the stable manifold can be obtained from the unstable one by changing y by $-y$ and p_x by $-p_x$.

Next we perform massive numerical simulations to explore the evolution of the invariant manifolds for the computed family of invariant tori. The results show that most of the computed trajectories on the unstable manifolds (43.27%) leave the Earth-Moon system, a big amount of them (21.69%) collide with the Moon and a smaller number (2.67%) collide with the Earth. Due to the reversing symmetry, a 43.27% of trajectories on the stable manifold come from outside the Earth-Moon system, a 21.69% come from the Moon and a 2.67% come from the Earth. The remaining trajectories keep moving around the system without colliding with the primaries or escaping for the whole simulation.

In order to display the rich dynamics given by these invariant manifolds, we use the fundamental cylinders introduced. In particular, we have used a mesh of $M1 = 1000$ equispaced points on $[0, 2\pi]$ and $M2 = 1000$ equispaced points on $[\sigma_0, \lambda_u \sigma_0]$ to produce 10^6 initial conditions for each piece of each unstable manifold (and similarly for the stable manifolds). We have coloured each couple (θ_i, σ_j) according to the fate of the orbit that they generate: yellow colour corresponds to escaping the Earth-Moon system, purple to collision with the Earth, red to collision with the Moon and black to those trajectories that move along the system without neither crashing nor escaping during the simulation time. Horizontal axis is taken as the angle along the curve $\theta \in [0, 2\pi]$ and the vertical one corresponds to the height of the fundamental domain, that is different for each curve, so we have scaled it to $\tau \in [0, 1]$, see Section 1.4.4.

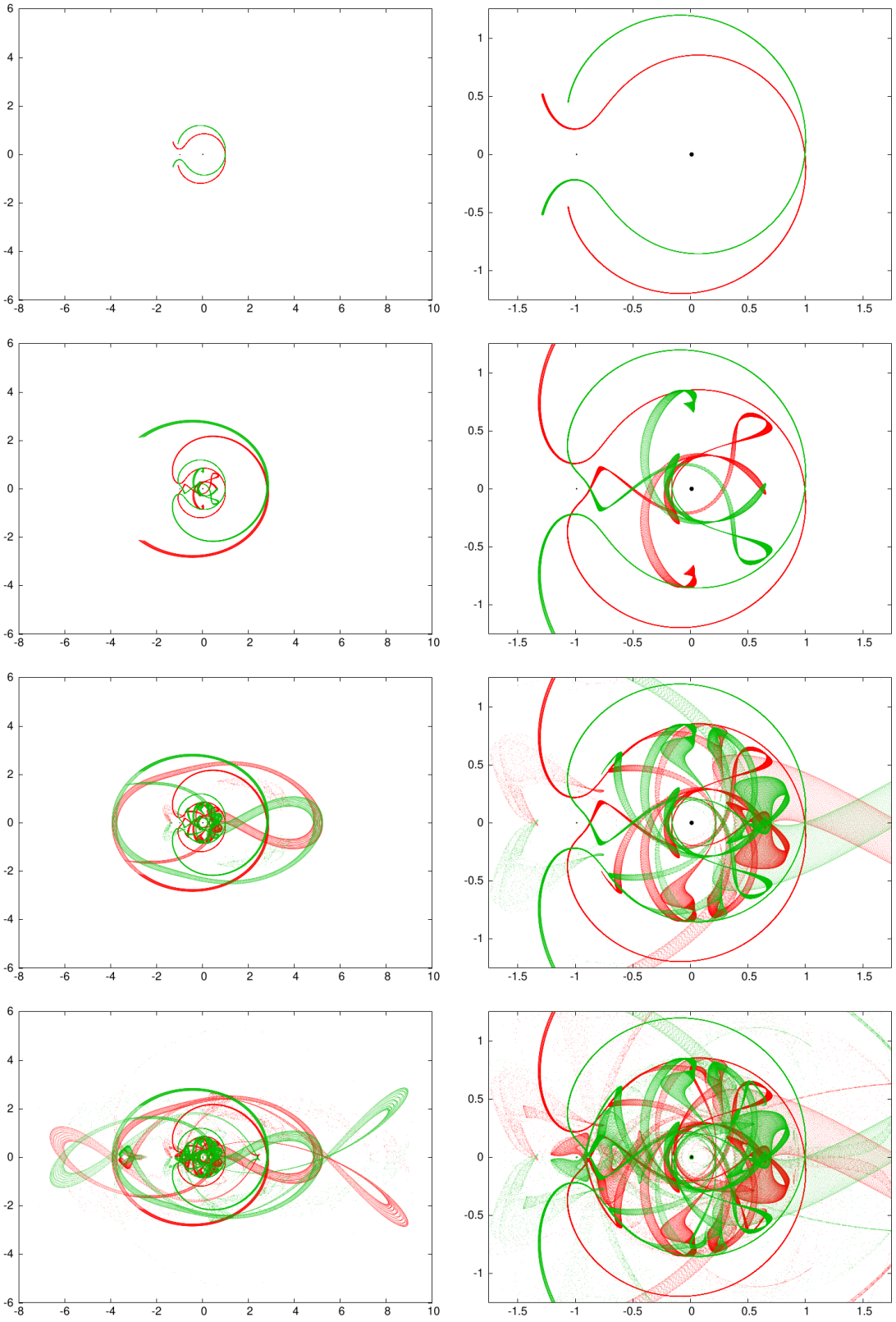

Figure 3.2: Invariant manifolds in the xy-plane of the curve at 1.3974×10^{-3} from L_3 for different times.

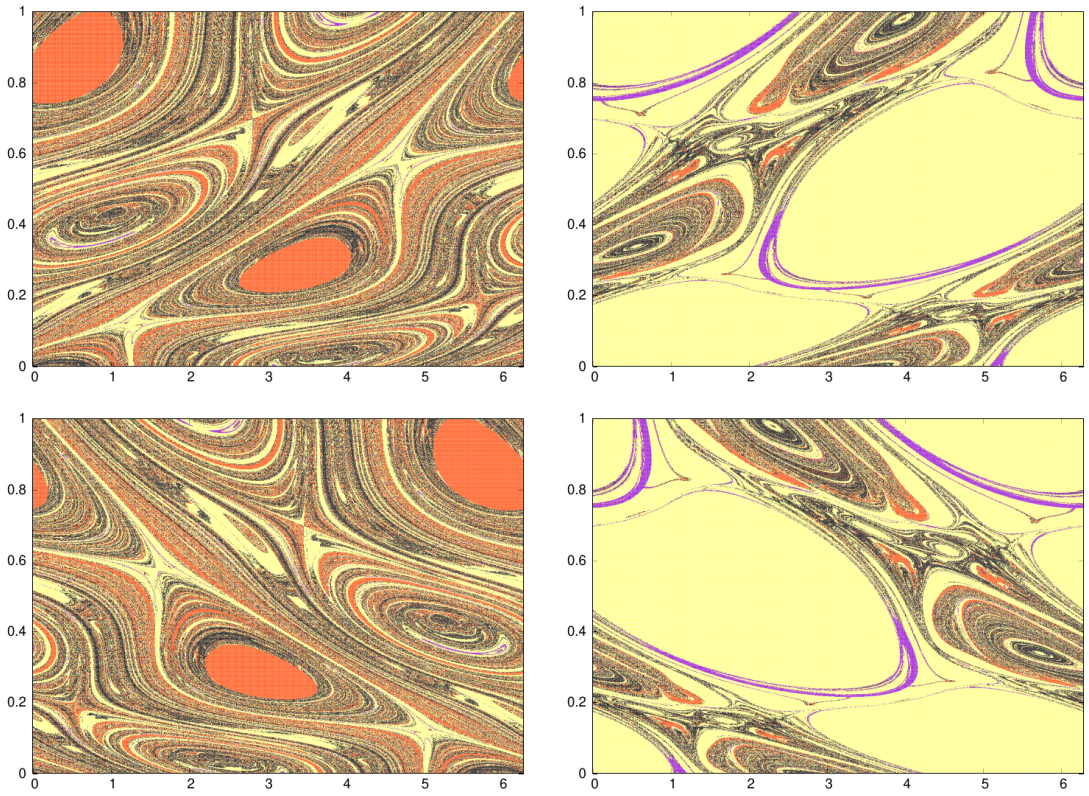

Figure 3.3: Fundamental cylinder of the invariant manifolds for an invariant curve at a distance 3.3351×10^{-2} from L_3. Up, unstable manifolds. Down, stable manifolds. Left, positive piece. Right, negative piece. See text for more details.

Figure 3.3 shows the colour maps of the fundamental cylinders corresponding to the four pieces of the manifolds of an invariant curve close to L_3 (at 3.3351×10^{-2} from L_3). The existence of the symmetry when inverting the time is easily recognisable, which means that from now on we will only plot, say, unstable invariant manifolds. Figures 3.4, 3.5, 3.6 and 3.7 show colour maps for several invariant curves at different distances from L_3. Note that the left side of each plot coincides with the right side, due to the periodicity of θ. The upper side of the fundamental cylinder is the result of applying the Poincaré map to the bottom side, so they coincide except for a shift equal to the rotation number of the invariant curve (ρ).

Looking at Figures from 3.3 to 3.7 we can see how the aspect of the colour maps evolves with the invariant curve. In general, in the first images, red and yellow colours seem to predominate, while for the last images quantity of purple and black colours has clearly increased; except for those curves very close to L_3 (see Figures 3.3 and 3.4), where purple regions are well defined. This means that it is more likely for the Earth to be origin or destiny of the trajectories passing close to the invariant curves near L_3, or far away from it, than for intermediate curves. The opposite effect is observed for the Moon. However, both primaries have connections with invariant curves at any distance from L_3. In order to give quantitative support to this qualitative explanation drawn from the colours of the maps, for each of the curves we have counted how many initial conditions on the fundamental cylinder reach the Earth, the Moon, escape the system, or none of these. The results are summarised in Table 3.1 for the unstable manifolds, where the two columns in each category correspond to the two sides of the manifold ($\sigma_0 > 0$ and $\sigma_0 < 0$). Due to the symmetries mentioned before, an identical table is obtained for the stable manifold. It is clear that there is a large piece of the manifolds that enters/leaves the system and a significant number of trajectories connecting the two bodies.

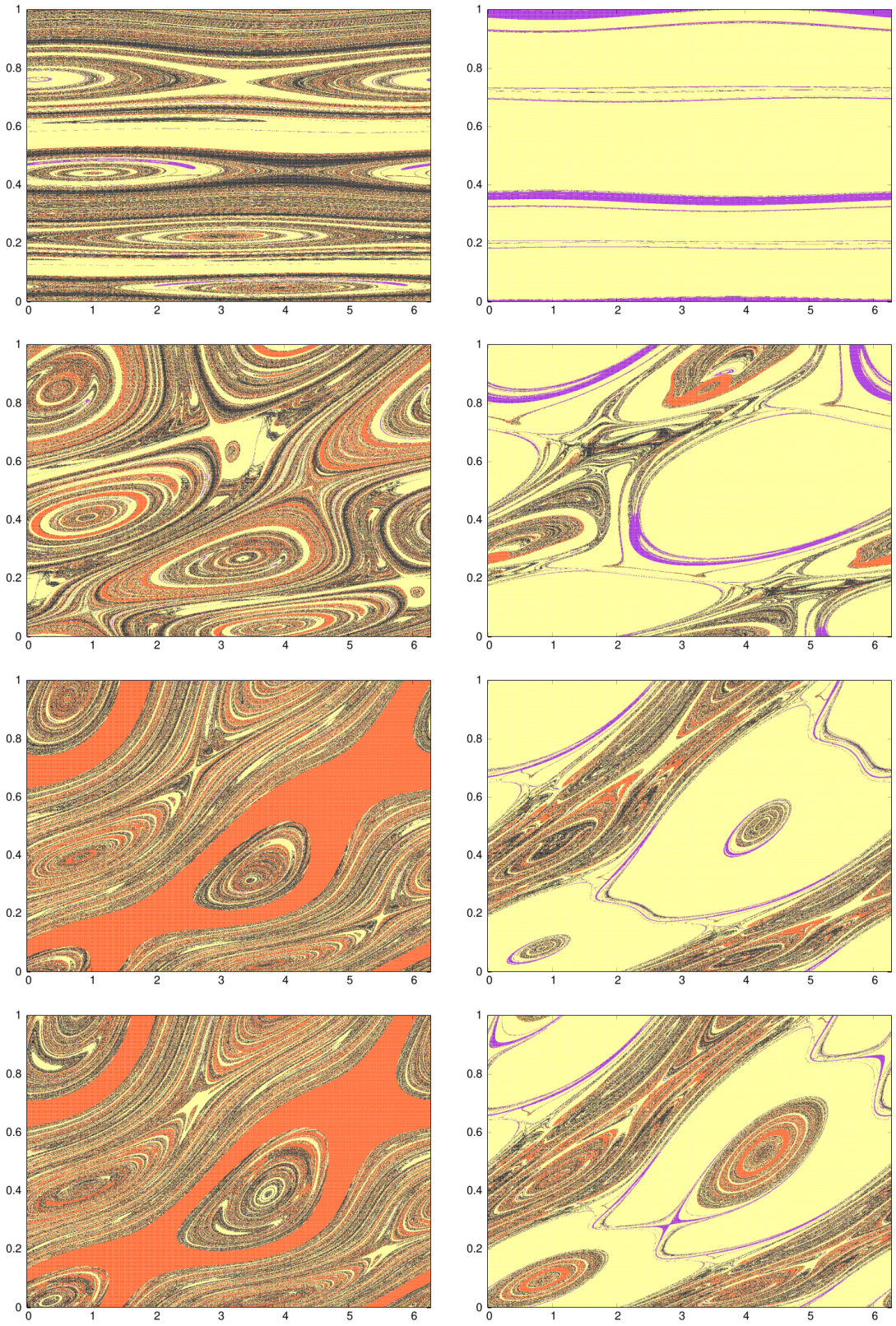

Figure 3.4: Fundamental cylinders for the two directions of the unstable manifolds of curves at distances to L_3, from up to down, 1.3974×10^{-3}, 2.1585×10^{-2}, 6.9987×10^{-2} and 8.2112×10^{-2}. Notice that cylinders in Figure 3.3 fit between the second and third row.

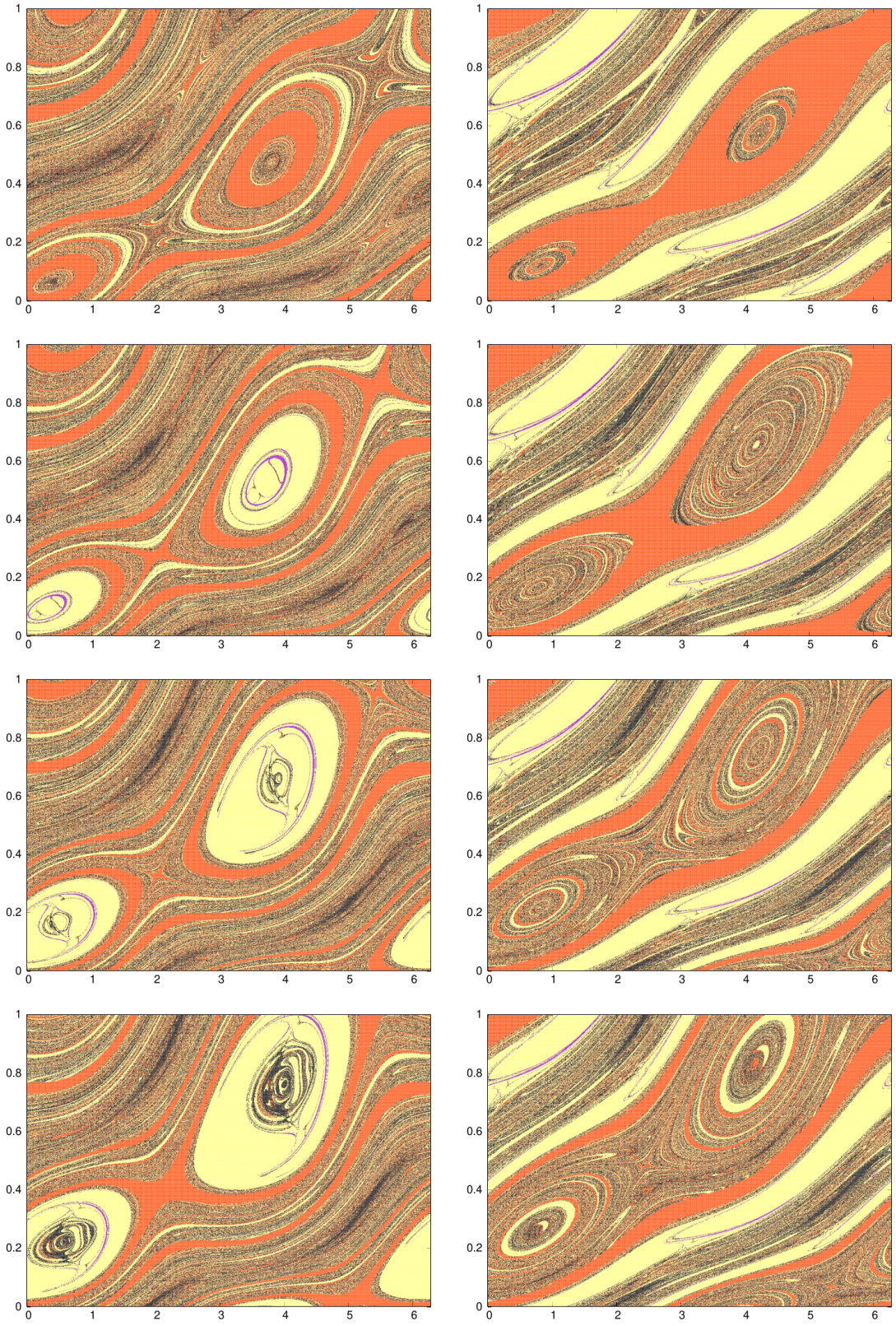

Figure 3.5: Fundamental cylinders for the two directions of the unstable manifolds of curves at distances to L_3, from up to down, 1.3079×10^{-1}, 1.6494×10^{-1}, 1.9607×10^{-1} and 2.2528×10^{-1}.

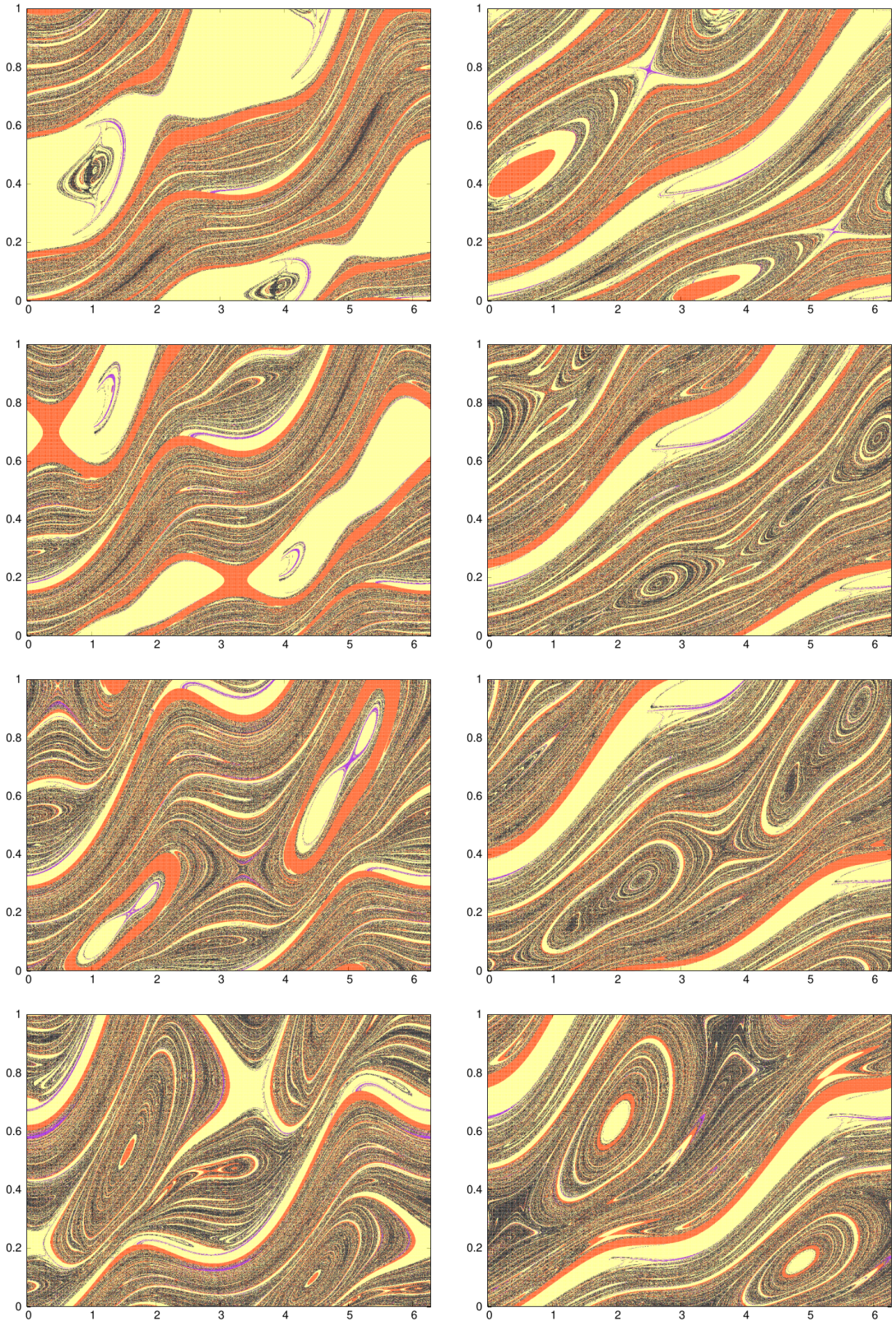

Figure 3.6: Fundamental cylinders for the two directions of the unstable manifolds of curves at distances to L_3, from up to down, 3.0902×10^{-1}, 3.9200×10^{-1}, 4.3616×10^{-1} and 4.9936×10^{-1}.

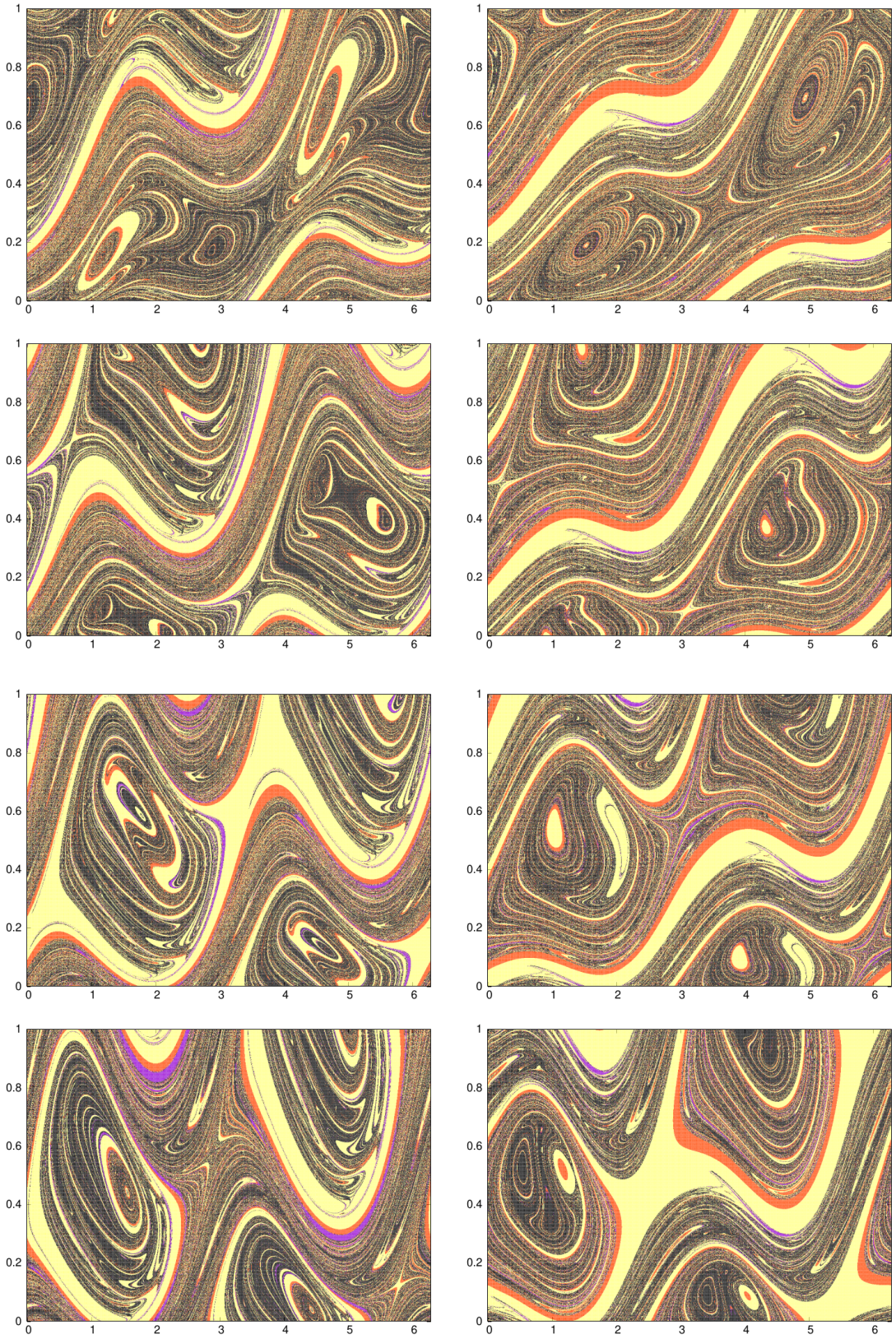

Figure 3.7: Fundamental cylinders for the two directions of the unstable manifolds of curves at distances to L_3, from up to down, 5.7020×10^{-1}, 6.4418×10^{-1}, 6.8953×10^{-1} and 7.4214×10^{-1}.

Distance to L_3	Earth (%)		Moon (%)		Exterior (%)		Neither (%)	
1.3974×10^{-3}	1.93	6.93	12.17	0.19	49.63	92.20	36.27	0.68
1.3036×10^{-2}	1.72	5.81	19.19	1.10	42.40	85.77	36.69	7.32
2.1585×10^{-2}	1.73	4.62	21.27	4.14	42.85	80.02	34.14	11.22
3.3351×10^{-2}	1.73	3.75	26.85	5.09	39.11	77.23	32.30	13.93
4.5581×10^{-2}	1.41	2.99	36.81	5.97	33.99	75.17	27.78	15.87
6.9987×10^{-2}	1.14	2.55	43.27	7.25	28.96	75.06	26.63	15.15
8.2112×10^{-2}	1.14	2.88	41.63	10.93	29.58	69.37	27.66	16.82
9.4396×10^{-2}	1.22	2.30	39.81	14.84	32.10	63.36	26.87	19.51
1.0661×10^{-1}	1.27	2.04	37.14	22.73	33.29	56.10	28.30	19.13
1.3079×10^{-1}	1.23	1.72	39.25	34.08	30.93	46.17	28.59	18.03
1.6494×10^{-1}	1.59	1.70	35.53	32.74	36.25	42.70	26.63	22.86
1.9607×10^{-1}	1.68	1.76	31.19	29.08	41.72	43.54	25.42	25.63
2.2528×10^{-1}	1.56	1.70	28.46	27.54	44.47	44.09	25.51	26.68
3.0902×10^{-1}	1.50	1.92	22.35	24.25	53.50	45.68	22.65	28.16
3.5299×10^{-1}	1.83	1.86	21.95	20.78	52.21	45.62	24.01	31.73
3.9200×10^{-1}	2.03	1.84	25.02	20.22	44.84	43.07	28.12	34.87
4.1505×10^{-1}	2.19	1.89	24.98	19.78	39.83	43.53	33.00	34.80
4.3616×10^{-1}	2.66	1.99	25.02	19.34	36.26	42.33	36.06	36.34
4.8488×10^{-1}	2.32	2.02	20.53	19.94	36.70	40.93	40.45	37.11
4.9936×10^{-1}	2.55	1.88	18.71	20.04	39.04	39.19	39.71	38.89
5.3657×10^{-1}	2.80	2.19	16.82	18.45	36.76	39.07	43.62	40.28
5.7020×10^{-1}	2.57	2.19	15.42	18.78	36.20	37.93	45.82	41.10
6.1431×10^{-1}	3.12	2.50	14.00	19.11	37.31	38.26	45.57	40.12
6.4418×10^{-1}	3.46	3.11	13.44	18.22	38.95	37.99	44.15	40.68
6.6872×10^{-1}	3.88	3.39	12.54	17.97	40.87	37.22	42.72	41.41
6.8953×10^{-1}	4.21	3.84	13.46	16.91	41.56	38.07	40.78	41.17
7.1879×10^{-1}	4.94	3.83	13.87	17.91	36.89	36.75	44.30	41.52
7.4214×10^{-1}	5.61	3.89	12.56	14.71	35.52	39.53	46.31	41.87
7.7146×10^{-1}	6.87	4.99	10.60	14.53	32.76	35.49	49.77	44.99
7.9720×10^{-1}	8.79	6.89	10.04	12.93	30.38	31.29	50.80	48.89

Table 3.1: Percentages of the trajectories starting at fundamental cylinders that go to the Earth, Moon, outside system or neither, through the two directions of the unstable invariant manifolds for some invariant curves.

The mix of colours in the maps in Figure 3.3 shows that a single invariant curve can be reached from several places and, starting at this quasi-periodic orbit, there are several possible destinations. These manifolds are the skeleton that organises the dynamics near L_3, and they provide multiple connections between Earth and Moon, and also allow to enter and exit the Earth-Moon system. In particular, it is remarkable that an asteroid entering the Earth-Moon system near these manifolds has more chances to impact on the Moon than on the Earth.

3.1.1 Leaving/entering trajectories

Due to Sun gravitational attraction, when a particle reaches a distance far enough from the Earth-Moon barycentre, it is captured by the Solar gravitational field. Consequently, unstable manifolds that overcome this distance are said to leave the Earth-Moon system, and stable ones, are said to enter in the system, both led by L_3 dynamics. To analyse the kind of trajectories that enter and leave the system, their orbital elements with respect to the Sun are computed. As the trajectories considered here belong to manifolds of the horizontal family, they are treated in the planar BCP and then only semi-major axis and eccentricity are obtained. Before computing the orbital elements,

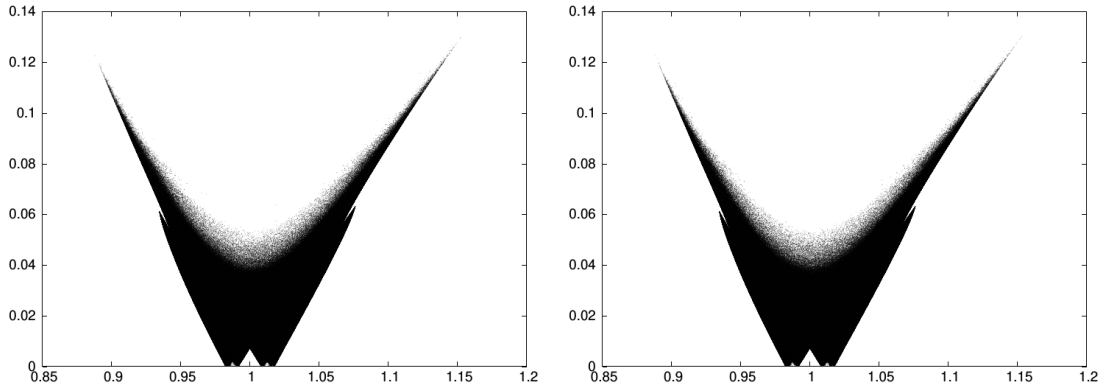

Figure 3.8: Horizontal axis corresponds to semi-major axis (in astronomical units), and vertical to eccentricity. Orbital elements for orbits entering (left) and leaving (right) the Earth-Moon system.

synodic coordinates are translated to inertial ones, with the origin set at Sun position.

In Figure 3.8 semi-major axis and eccentricity are shown. Due to the time reversibility of the system, it is quite natural that the orbital elements corresponding to trajectories that escape the Earth-Moon system are similar to those corresponding to trajectories that enter the system. Notice that in this model, the Earth-Moon system describes a circular trajectory with respect to the Sun, therefore its orbital elements are semi-major axis equal to $1AU$ and zero eccentricity. Then, considering that the trajectories enter or leave the system when they are at a distance of 10 Earth-Moon distances from their barycentre leads to the well-defined "peak" shape of the graph for very low values of the eccentricity.

Granvik et al., [GVJ12], computed the capture probability for NEOs according to their orbital elements. If we compare their results with the orbital elements obtained with the Bicircular Problem, we check that the graphs of the orbital elements (semi-major axis vs. eccentricity) presented in [GVJ12] display the same shape and range values that the ones obtained through L_3 in the planar BCP, shown in Figure 3.8. Therefore, it seems that trajectories entering and leaving the Earth-Moon system described by BCP, are probably to happen in the real system. We will rely on these results to partially motivate our analysis for the capture of an asteroid via L_3 in Chapter 4.

Our results show that these entering manifolds connect, near L_3, with manifolds that go towards the Moon or the Earth, and viceversa. Moreover, we have observed trajectories that enter in the Earth-Moon system after orbiting the Sun in an orbit outer than the one of the Earth (i.e., with semi-major axis larger than $1AU$) and then leave the system to orbit around the Sun in an inner orbit than the Earth (semi-major axis smaller than $1AU$). In the same way, the opposite transfer (from an inner orbit around the Sun to an outer one) can be led by L_3 dynamics. This behaviour reminds that of the quasi-satellites except for the fact here there is no inclination for the trajectories, [MIW$^+$06].

3.1.2 On the existence of heteroclinic connections

We would like to show a phenomenon we have observed among the trajectories on the manifolds of the invariant curves belonging to the horizontal family of L_3. It seems that there exist intersections among manifolds of different quasi-periodic orbits near L_3. In Figure 3.9 (left) we can see an orbit that goes from the Moon surface to the outside system through a torus close to L_3, but it also seems to spin around a second torus. In Figure 3.9 (right), we can observe the opposite effect, for an orbit that goes from the Moon to the Earth. The study of these connections is left for another work.

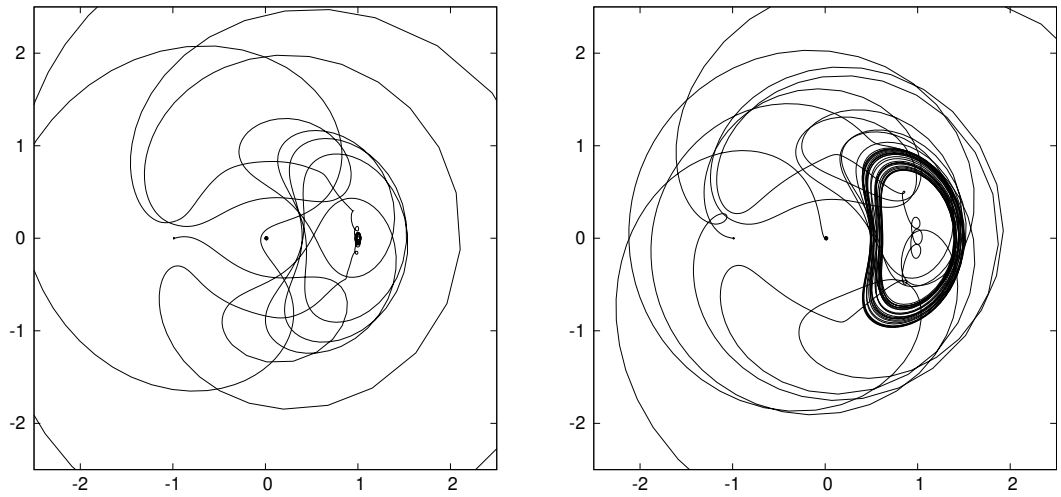

Figure 3.9: Trajectories that suggest intersections between the manifolds of different invariant curves. A zoom of the trajectories has been done in order to show the behaviour around L_3.

3.2 Lunar Meteorites

Lunar meteorites are meteorites originated on the Moon that are thought to have their origin in the impacts that the Moon suffers every year. When an object impacts on the Moon surface with enough energy, a crater is produced. If the velocity of the crater ejecta is higher than the lunar escape velocity (≈ 2.38 km/s), they get free from the Moon gravity and become lunar meteorites travelling through space, being able to reach the Earth. In [GBDL95], Gladman et al. perform numerical simulations of a big number of initial conditions at the Moon surface for velocities in the range $[2.3, 3.5]$ km. There, they argue that a four body problem needs to be implemented to integrate initial conditions, due to the important effect that Sun has on them.

Concerning how lunar meteorites reach the Earth, there are clear ideas of how they leave the Moon, and numerical computations supporting these ideas can be found in [GBD$^+$96]. There are also reliable physical procedures to analyse the time they have spent in space. However, the geometrical mechanism behind this transport is not fully understood. As far as we know, no invariant object in the Earth-Moon vicinity is known to play a crucial role in their behaviour.

In Section 3.1 we mentioned that among the connections found to be organized by the invariant manifolds of the horizontal family of invariant curves around L_3, connections between Earth and Moon were present. Therefore, in this chapter we study whether the invariant manifolds of the previous section can "guide" lunar meteorites to reach the Earth. The skeleton for these connections is defined by the subsets of the stable invariant manifolds that connect the Moon surface with a quasi-periodic orbit near L_3 whose unstable manifold reaches the Earth surface.

Let us start by computing the points (positions and velocities) at which stable manifolds reach the Moon surface, and the points at which unstable manifolds reach the Earth surface. In Figure 3.10 some histograms for the initial and the final data of these trajectories are included. Left panels show data corresponding to the starting point on Moon surface: initial phase of the Sun, point along the surface and velocity. Right panels show data corresponding to the final destination of these trajectories on the Earth surface: phase of the Sun, point along the surface and velocity. Notice that the phase of the Sun is parametrized on $[0, T]$, and the surface of the primaries is assumed to be circular and parametrized by an angle in $[0, 2\pi]$. It is remarkable that there is not a preferred Sun phase or point on the Moon surface for these orbits to start or on the Earth surface for them to end. So, transport

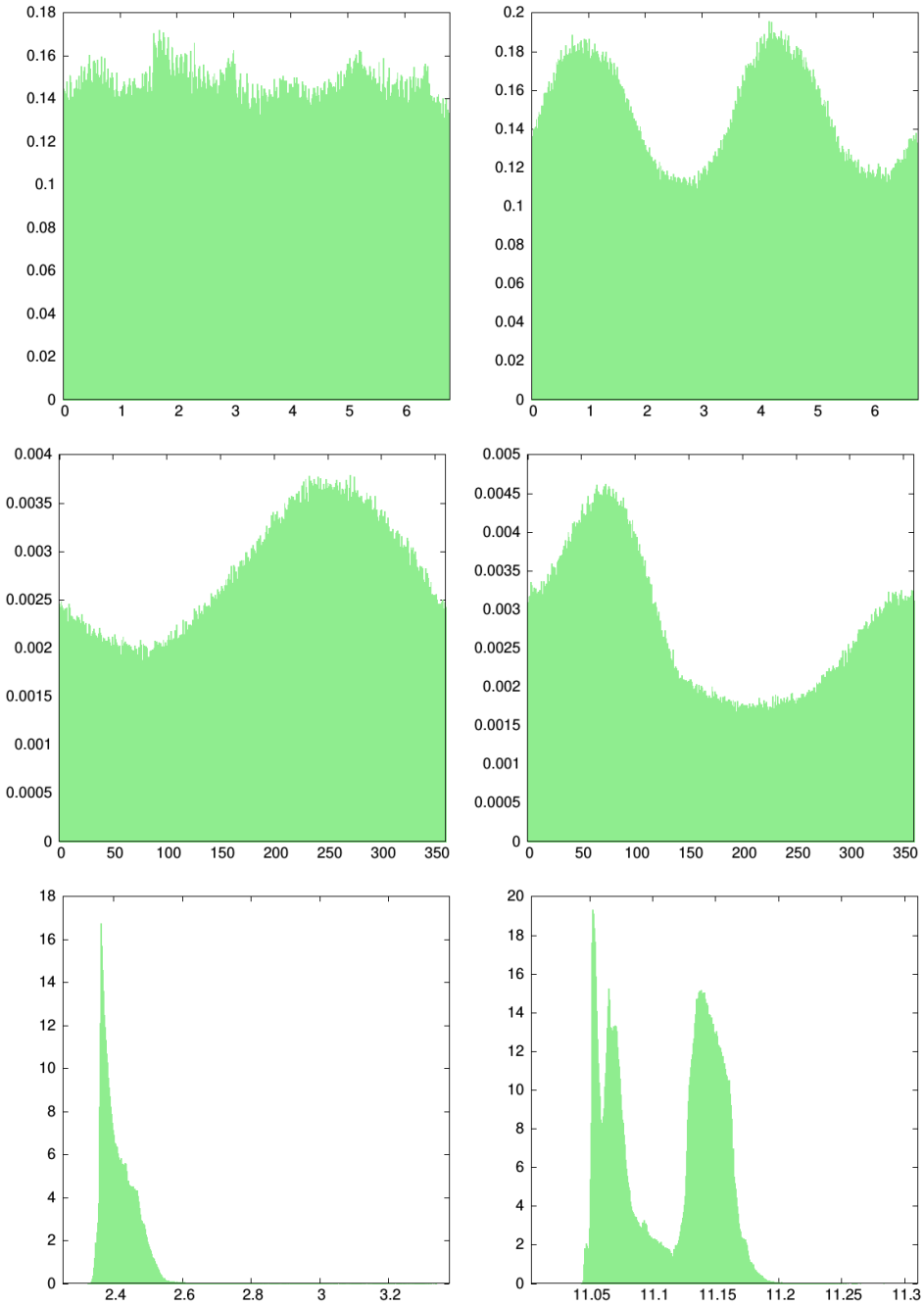

Figure 3.10: Left column contains histograms for the Moon; from up to down they show the time leaving the primary, the point of the surface at which it happens, and escape velocity. Right column contains similar histograms but for the Earth. See the text for more details.

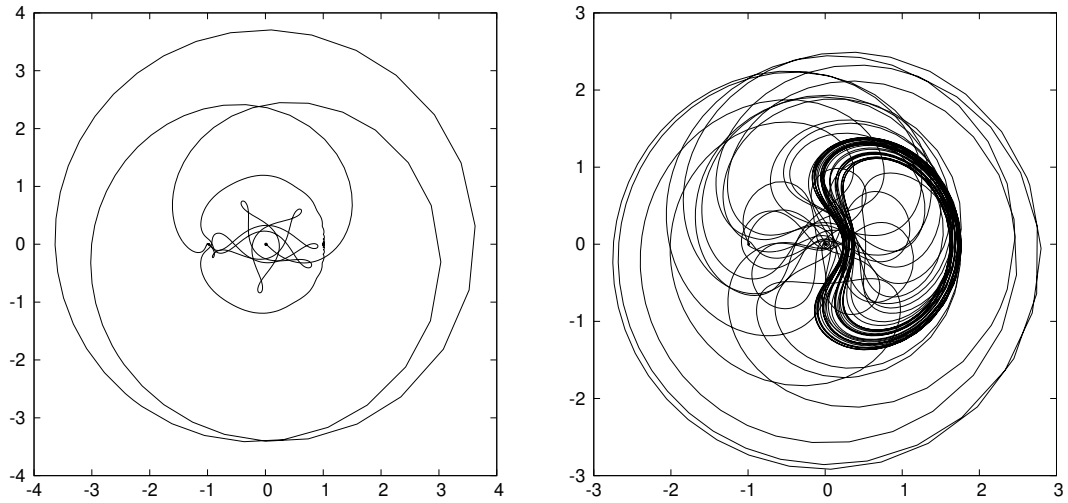

Figure 3.11: Two trajectories, in the xy-plane, connecting the Moon with the Earth. See the text for details.

between Earth and Moon takes place in a generic way, in the sense that it is not necessary to be in any specific location on the bodies or to have an specific phase for the Sun. Ranges for velocities of the trajectories leaving the Moon are in $[2.25, 3.38]$ km/s, while for the velocities when they reach the Earth surface (neglecting atmosphere effects) is in the range $[11.00, 11.31]$ km/s. For velocities we do find some ranges that are preferred, or have higher possibilities; they correspond to values close to the Moon and Earth escape velocities, respectively, what seems to be a natural result. Vertical axis have been scaled such that they correspond to the probability percentage for each of the 500 bins.

Trajectories going from the Moon to the Earth can have very different shapes, depending on the invariant curve they approach during their journey. In Figure 3.11 two trajectories connecting Moon and Earth are shown; the left one is close to the invariant manifolds of a quasi-periodic orbit close to L_3 and the right one is close to the invariant manifolds of a quasi-periodic orbit far from L_3.

To see how likely is for a Moon ejecta to follow these trajectories we have performed a series of numerical simulations. To this end, for each intersection point of the stable manifolds with the Moon surface, we have modified the corresponding velocity module and direction maintaining its x and y coordinates, as well as the initial time (we recall that the BCP depends on time). A mesh of modules and angle directions for the velocities is created from the values of the trajectory.

The mesh is formed by 10^3 points in each direction (modulus and angle of the velocity vector) for a total of 10^6 points. Each of these points gives an initial condition that is integrated during a maximum of 55 Earth-Moon revolutions; depending on their final destination a colour is assigned to them, see Figure 3.12. As in the colour maps from Section 3.1, yellow corresponds to trajectories that leave the Earth-Moon system, purple to those that reach the Earth and red colour to those that come back to the Moon. There are also a few trajectories in black colour that neither crash nor leave the system. The trajectory at the left of each colour map corresponds to an orbit which is extremely close to the invariant manifold and reaches the Earth (we note that, in a perfect computation with no errors, an orbit exactly on the manifold will accumulate to the quasi-periodic orbit without going anywhere else). Note that the plot axes have been adjusted differently for each trajectory.

In these maps we find a large variety of destinations for each of the trajectories starting on the Moon surface and near the stable manifold. We can see that only for higher velocities big areas of initial conditions leading to the Earth from the Moon are found. Also, it is quite visible that three of the four maps have a vertical red band on the left of the plot, the reason for this to happen is that

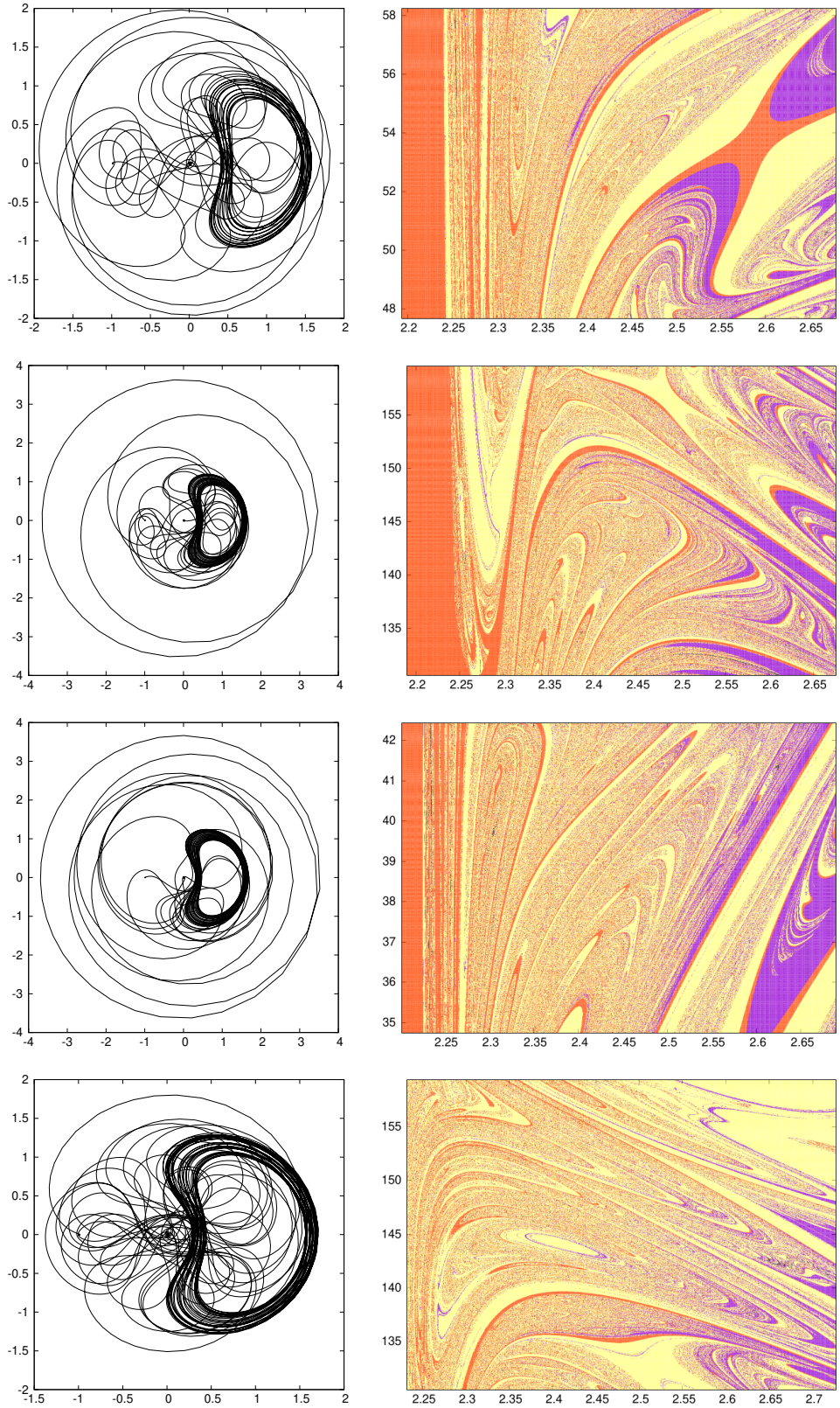

Figure 3.12: Left, trajectories connecting the Moon with the Earth, in the xy-plane. Right, destination colour maps when modifying trajectories velocities; horizontal axis corresponds to the velocity module (km/s) and vertical to the angle direction (degrees). The trajectory on the left corresponds to the centre point of the map at the right. See the text for more details.

those are trajectories with velocities below the Moon velocity escape, consequently they tend to fall again against the lunar surface. However, in the last map this red vertical band is not present, the reason may be the relative position of the Sun when the trajectory starts, that helps to escape Moon's gravity. In Table 3.2 the initial angular position of the Sun (ϑ_0, see (2.6) and Figure 2.2) for the four trajectories are shown. Notice that for the last trajectory, the initial position of the Sun is almost vertically above the primaries.

Trajectory	1st	2nd	3rd	4th
ϑ_0	132.917506118	225.259626325	298.729423247	263.209360181

Table 3.2: Initial angular position of the Sun with respect to the Earth-Moon barycentre (ϑ_0) in degrees, for the trajectories in Figure 3.12.

3.2.1 Comparison with a realistic model

The results concerning to the transport between Earth and Moon that we have obtained by analysing L_3 in the Bicircular Problem may explain the behaviour of lunar meteorites travelling to the Earth. Now we want to check these results in a more realistic model. To this end, we consider the Solar system as an $\mathcal{N}$-body problem containing Sun, Earth, Moon and all the planets, with initial conditions provided by the JPL ephemeris DE405. The initial conditions for the particles are obtained by means of a change of coordinates from BCP to the the ecliptic system of reference, whose origin is placed at the Solar system centre of mass. Once the change is performed, we integrate every particle jointly with the Solar system as a restricted $(\mathcal{N}+1)$-body problem.

Every initial condition of the maps in Figure 3.12 has been translated to the ecliptical system by applying the change of coordinates detailed in Section 2.5. Notice that our coordinates in the planar BCP are four-dimensional, so initial vertical position and velocity in the adimensional system are zero. Also, each colour map corresponds to a different starting time (the angles in Table 3.2), that needs to be translated to modified Julian days (the time in the JPL ephemeris is measured in Julian days). Since time zero for BCP model corresponds to a lunar eclipse we have chosen as origin of time in the real system the first lunar eclipse of year 2000, which corresponds to the modified Julian day 20.1978749133 (day 0.0 corresponds to year 2000.0). Since time at which the trajectories on the stable invariant manifolds intersect the surface of the Moon, is negative (since these manifolds are propagated backward in time), all these trajectories occur some time (lower than a solar period T) before the eclipse. Taking all this into account, we obtain the initial data for each point of the colour maps with the same units as in the JPL ephemeris.

The initial numerical simulations, with the same mesh of initial conditions as in the BCP, showed similar patterns but sometimes with a shift, mainly in velocities, and different in each case. For this reason we have enlarged the mesh to cover a larger set of initial data. The results are shown in Figure 3.13. An explanation of these shifts, different for each map (i.e. for each different time) may be given by the relative positions and velocities of the Earth and Moon at each time. This implies a different scale factor that can be translated into higher or lower velocities for the initial conditions, see Table 3.3. The last column in this table, $\sigma_{\mathrm{v}} = ||\dot{e} - V_M|| - ||\dot{a}||$ (in km/s), is a comparison of the initial velocities with respect to the Moon in the two reference frames. Note that value of σ_{v} is correlated with the shift in velocities when comparing the colour maps in Figures 3.12 and 3.13. It is remarkable that for the time of the fourth map the relative positions of Earth, Moon and Sun are close enough to the (planar) BCP configuration so that we have not needed to widen the mesh to find the same patterns.

As a last check, the trajectories that leave the Earth-Moon system in those integrations (yellow colour in the maps), are characterised in terms of their orbital elements. Again, for the planar Bicircular model, only semi-major axis and eccentricity can be computed. For the realistic model, all the orbital

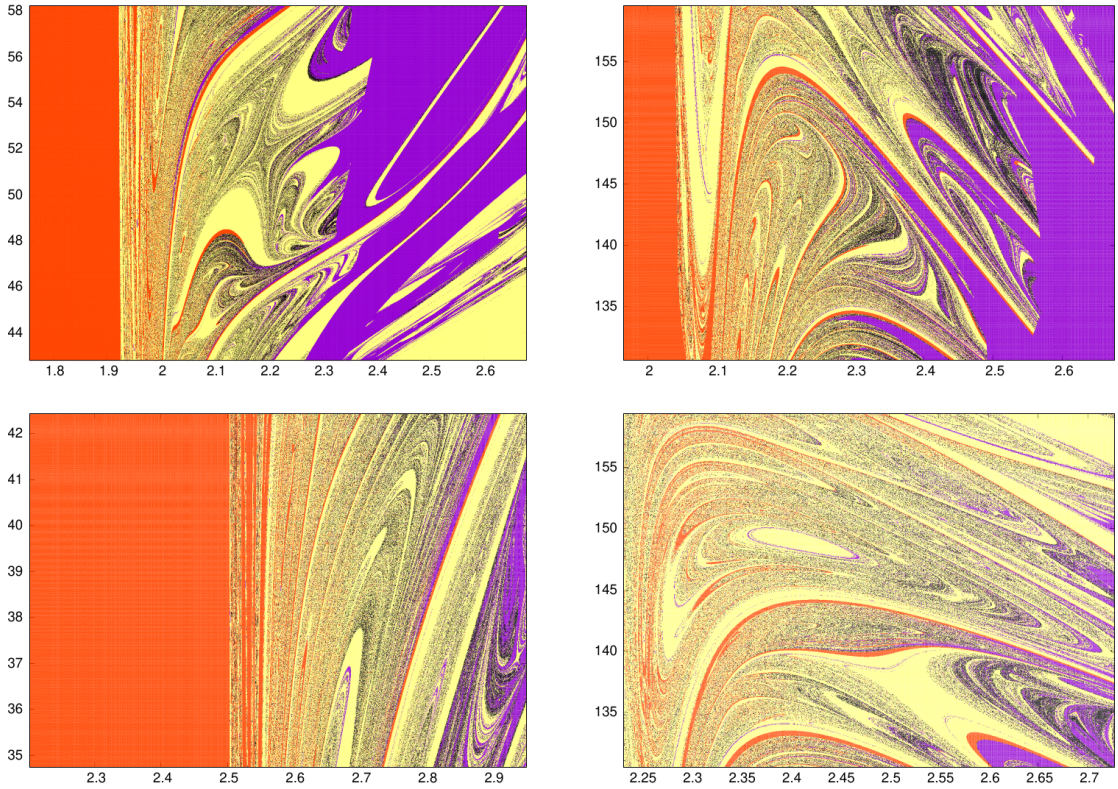

Figure 3.13: JPL results for the destination colour maps when modifying trajectories velocities; horizontal axis corresponds to the velocity module (km/s) and vertical to the angle direction (degrees). See the text for more details.

Trajectory	k (km)	V_{EM} (km/s)	ω_{EM} (1/s)	e_z (km)	σ_{v} (km/s)
1st	404835.4469	0.9702	2.3964×10^{-6}	64623.3917	1.4039×10^{-1}
2nd	396750.5357	0.9923	2.5012×10^{-6}	16469.0752	6.2282×10^{-2}
3rd	369879.1465	1.0594	2.8641×10^{-6}	-2390.8644	-1.0638×10^{-1}
4th	384247.7345	1.0195	2.6533×10^{-6}	-517.1608	-1.3396×10^{-2}
BCP	384400.0000	1.0236	2.6628×10^{-6}	0.0000	----

Table 3.3: Scale factor, relative Earth-Moon linear and angular velocities and vertical coordinate in the ecliptic system and BCP for the initial data of the four trajectories of Figure 3.12. Last row corresponds to the difference in the ecliptical velocity module for the particle relative to the adimensional one.

elements have been computed. Here we only include the semi-major axis, eccentricity and inclination values for the four maps, see Figure 3.14. Again, the plots for the BCP and for the real model are in good agreement.

Finally, it is worth to mention that the simulations in a realistic model have been also performed taking other considerations. In particular, we repeated these simulations using the coordinates of the planets, Sun and Moon given by the ephemeris database at each time step instead of integrating each of the massive bodies with a $\mathcal{N}$-body that only accounts for gravitational effects. The colour maps did not present any difference, at least from a qualitative point of view. Also, we repeated these simulations taking only into account three massive bodies, the Earth, the Moon and the Sun. Again, no representative differences were appreciated.

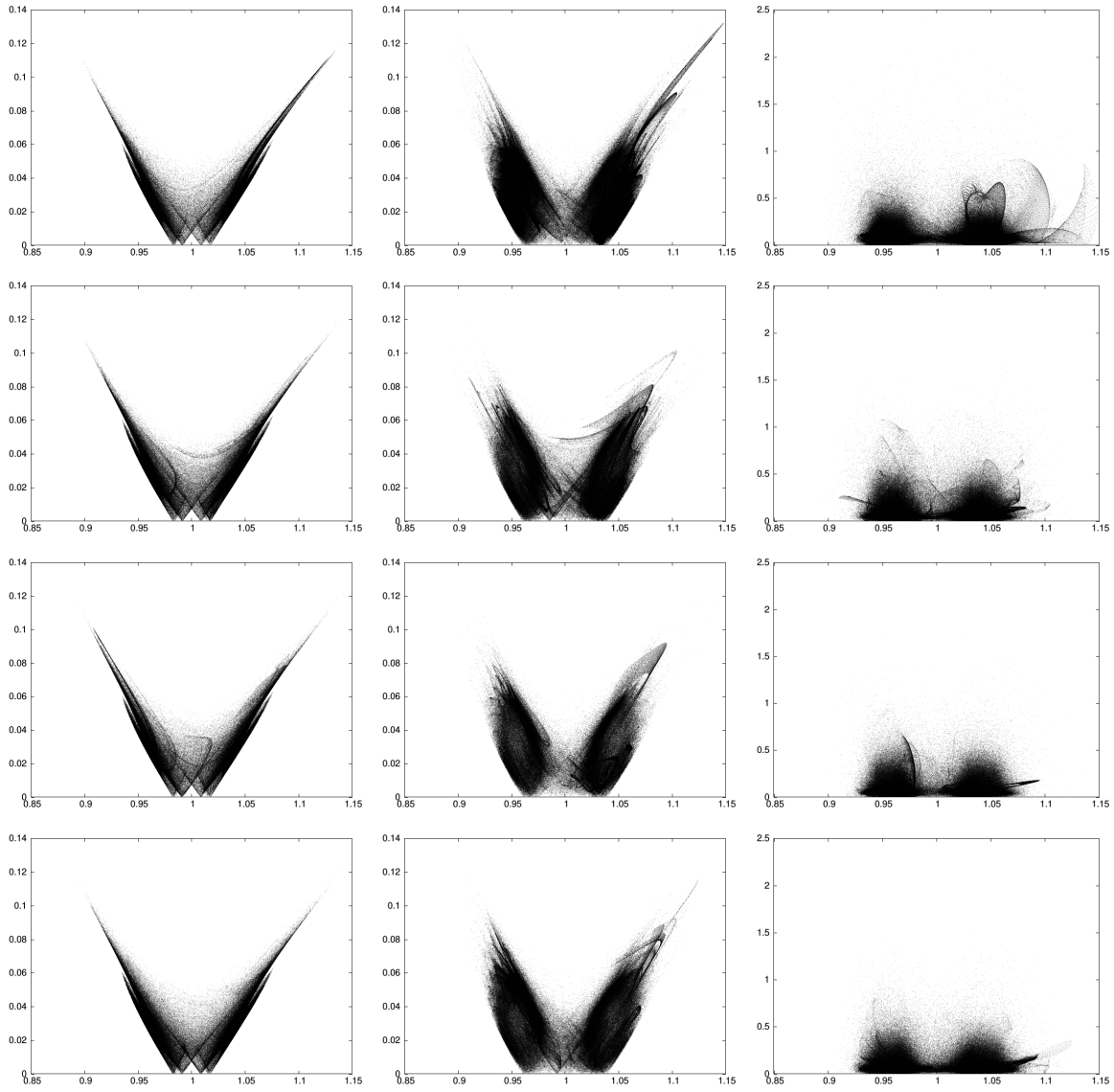

Figure 3.14: Orbital elements for the trajectories that leave the Earth-Moon system, corresponding to the four maps of initial conditions shown in Figure 3.12 (from up to down), integrating them in the BCP (first column) and in a realistic restricted $(\mathcal{N}+1)$-body problem (other two). First two columns of graphs show eccentricity versus semi-major axis (astronomical units), and the last one the inclination (in degrees) versus semi-major axis.

3.3 Transfers from a Parking Orbit of the Earth

Similarly to how we have analysed the trajectories that go from the Moon to the Earth passing through a quasi-periodic orbit around L_3, it is possible to look for connections starting in the surroundings of the Earth to go towards the Moon or some other destination.

In this case, we can not consider the ejecta travelling directly from the Earth surface to the Moon since the friction of Earth's atmosphere would ask for extremely high speeds. Instead, we can analyse the transfer from a low orbit around the Earth, what has undoubtedly astronautical interest. Therefore, we can use the same strategy as in previous section but starting at some distance from the Earth surface, for instance at some parking orbit. If a quasi-periodic orbit has trajectories in the stable invariant manifold crossing a parking orbit and trajectories in the unstable manifold colliding with the Moon we can use this geometrical structure to go from the surrounding of the Earth to the Moon by means of a single manoeuvre, which is a change of velocity Δv at the crossing point (in configuration space) between the parking orbit and the stable manifold.

We have done some estimations on the Δv costs for transferring to L_3 stable manifolds from a parking orbit defined at an altitude of 200 km from the Earth surface, and they show that the minimum cost for some spaceship to make this manoeuvre is of 3.17 km/s; value near typical costs for leaving a parking orbit at this distance. After this, the trajectory in the stable manifold goes towards the quasi-periodic orbit near L_3 where it will connect with a trajectory in the unstable manifold that may go to the Moon, to the outside system or to some other destination.

Encouraged by these results, we started a collaboration with Dr. Liang for constructing a transfer from parking orbits around the Earth to the vicinity of the triangular point L_4 passing through a selected quasi-periodic orbit around L_3. There, the costs for using the stable manifolds of a torus around L_3 are carefully analysed, looking for the selection of the most convenient parking orbit and solar phase (i.e. time). This collaboration resulted in a publication, [LNJ21] that we will briefly summarise.

Leveraging L_3 to transfer to L_4:

The strategy developed in [LNJ21] is based in three steps. The first one is to look for the trajectories in the unstable manifold of a selected quasi-periodic orbit around L_3 that intersect the family of quasi-periodic orbits around the $PO1$ of L_4; this family is studied in Section 2.4. The intersections are sought at ten different temporal Poincaré sections: at times equal to $T, 0.1T, 0.2T, ..., 0.9T$. The trajectories of interest are saved in a set called U_1 and the times of flight (TOF) for these trajectories are found to be around the 55-69 days.

The second step is to study the stable manifolds associated with the trajectories in the set U_1 and look for intersections between the trajectories in those stable manifolds with parking orbits covering altitudes from low Earth orbits at 167 km to geostationary orbits. Therefore the set of trajectories of interest is narrowed, we call it U_2. It is clear that, as a general rule, the higher is the altitude of the considered parking orbit, the lower is the cost in Δv for leaving it. In particular, the costs found for the trajectories in this new set, U_2, to leave the parking orbits are around 1-2.85 km/s and the TOFs for going from the neighbourhood of the Earth to the quasi-periodic orbit around L_3 undertake about 300-1000 days. These TOFs are quite long due to time spent in the neighbourhood of L_3.

The third step is to confirm that the whole trajectory connects from the parking orbit to the vicinity of L_4, passing through L_3. At this step we compute the quasi-periodic orbit around the $PO1$ of L_4 that intersects exactly with the trajectory coming from the quasi-periodic orbit around L_3 at the right temporal section. For refining this invariant curve, we make a sweep between the tori presented in Section 2.4.1, evaluating each curve in a fine mesh of angles $\theta \in [0, 2\pi]$. Then, we save the information of the invariant curve that is closer to that intersection point and the angle $\tilde{\theta}$ at which this happens.

Transfer	total TOF (days)	Δv at parking orbit (m/s)	Δv for patching method (m/s)	time of the intersection near L_4	Δv around L_4 (m/s)	total Δv (m/s)
Figure 3.15	175.98	1494.85	69.51	0.7T	124.05	1688.41
				0.8T	118.92	1683.28
				0.9T	150.00	1714.36
Figure 3.16	192.62	1013.15	75.00	T	102.48	1190.63
				0.1T	153.31	1241.46
				0.9T	132.54	1220.69
Figure 3.17	177.37	1271.80	69.45	0.2T	173.70	1514.95
				0.3T	111.86	1453.11
				0.4T	150.45	1491.70

Table 3.4: TOF and fuel costs for three possible transfers for going from parking orbits around the Earth to a quasi-periodic orbit around L_4, using stable and unstable manifolds of a quasi-periodic orbit around L_3.

That curve is used as seed for the Newton method explained in Section 1.4.1 and the angle $\tilde{\theta}$ is used to fix that the coordinates x and y of the curve at that angle are equal to those of the trajectory coming from L_3. Notice that, in this case we may need to compute the invariant curve at a temporal section different from a time 0, then the value of the initial phase $\vartheta_0 \neq 0$ in (2.6). The cost of the injection of the analysed trajectories in quasi-periodic orbits near L_4 are of less than 300 m/s.

Once we have some trajectories going from the parking orbit of the Earth to the vicinity of L_4, a patching method based on multiple shooting method is implemented with the aim of reducing the TOF in the vicinity of L_3. The manoeuvre for this patch is of the order of 60-80 m/s. Therefore, the principal cost of the whole connection is paid when leaving the parking orbit.

To sum up the results, we obtain trajectories that can be used to reach the triangular points passing through L_3 from a parking orbit of the Earth, that would undertake less than 200 days and total costs in Δv about 1.2-2 km/s. Notice that following this construction scheme for the transfer, even the lowest time of flight obtained may be large due to the passage close to L_3. In order to overcome this situation, a second construction in using solely stable manifolds to transfer from a parking orbit to a quasi-periodic solution near L_4 is explored through a similar selection scheme developed for the first construction. A large decrement in the total TOF is obtained and the lowest TOF is 60.86 days. However, the results also demonstrate that this second construction leads to much less transfer opportunities in the sense of number of transfer trajectories and launch opportunities from the Earth parking orbits and no advantage in the total fuel consumption is found.

In Table 3.4, the general information for three possible transfers following the first scheme construction (i.e. passing through L_3) is collected. The table includes the total TOF for the transfer and the total fuel consumption, that is the sum of the costs for leaving the parking orbit, the cost of the patching method for reducing the time spent close to L_3 and the cost for the intersection of the trajectory into a torus around L_4, that can take place at different temporal sections for the same trajectory.

The trajectories of the transfers in Table 3.4 are shown in Figures 3.15, 3.16 and 3.17, where the piece going from the parking orbit to the quasi-periodic orbit around L_3 is plotted in black colour and the piece going from that location to the quasi-periodic orbit around L_4 is in blue colour. The red squares denote the intersection points between the trajectories in the stable manifolds of L_3 and the parking orbits of the Earth and the green squares denote the intersection points between the trajectories in the unstable manifolds of L_3 and the quasi-periodic orbits around L_4. In these images the plots at the left correspond to the original trajectory and the one at the right (centre in the case of Figure 3.15) correspond to the trajectory after the patching method is performed.

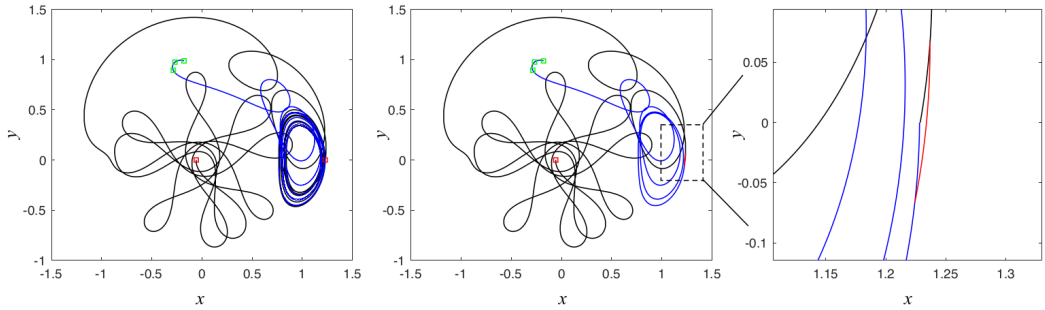

Figure 3.15: Possible transfer from a parking orbit of the Earth to a torus around L_4, passing through L_3. Left, original transfer. Centre, after the patching method. Right, a zoom where the patching method is implemented.

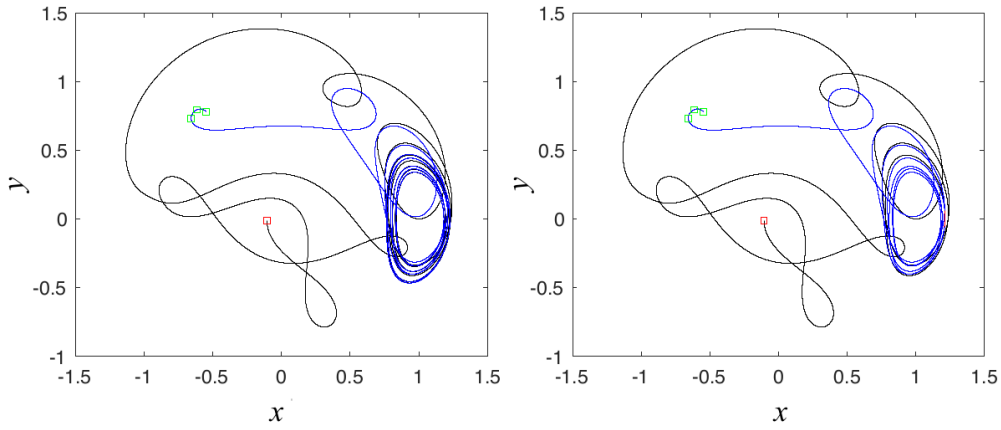

Figure 3.16: Possible transfer from a parking orbit of the Earth to a torus around L_4, passing through L_3. Left, original transfer. Right, after the patching method.

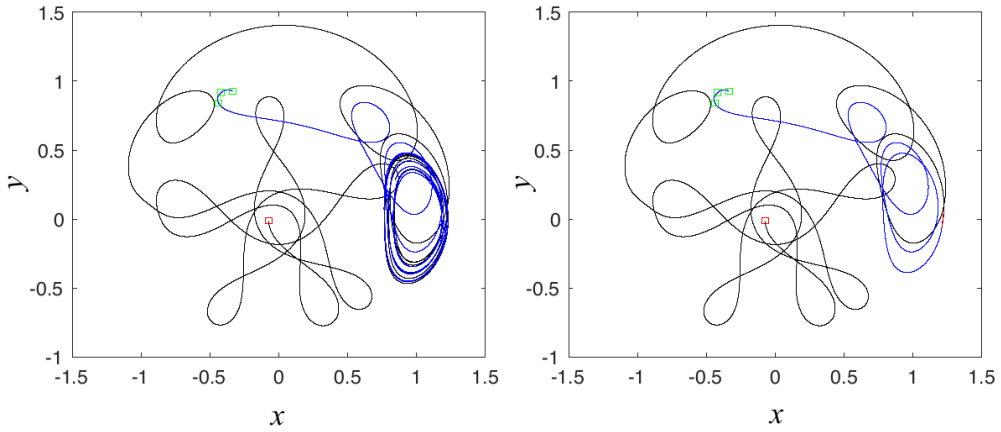

Figure 3.17: Possible transfer from a parking orbit of the Earth to a torus around L_4, passing through L_3. Left, original transfer. Right, after the patching method.

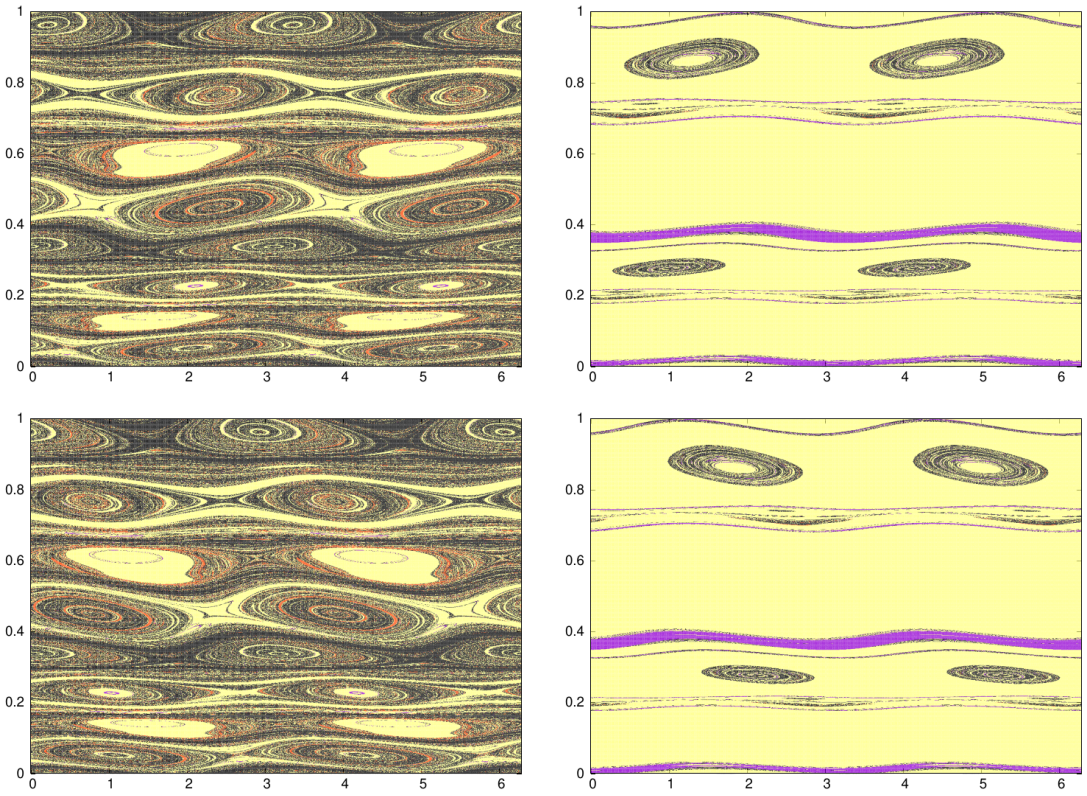

Figure 3.18: Fundamental cylinder of the invariant manifolds for an invariant curve of the vertical family at a vertical distance 5.8942×10^{-2} from L_3. Up, unstable manifolds. Down, stable manifolds. Left, positive piece. Right, negative piece. See text for more details.

Therefore, we have found trajectories that go from parking orbits of the Earth to the vicinity of L_4 governed by invariant manifolds of a quasi-periodic orbit around L_3. These trajectories involve affordable fuel costs but the time of flight is still long. Note that this analysis could be extended to include more possibilities than only the ones provided by just one quasi-periodic orbit around L_3, looking specially for a reduction of the time spent in the vicinity of L_3. Finally, just to mention that a similar strategy could be used to reach the Moon or some other location of interest.

3.4 Transport through the vertical family

This section is aimed to give an insight about the dynamics governed by the vertical family of invariant tori around L_3. The computation of this family and the analysis of its stability have been presented in Section 2.3.2.

There it is explained that the vertical family of invariant tori around L_3 is composed by two-dimensional tori that are seen as one-dimensional curves in the temporal Poincaré map corresponding to the period of the Sun P, as it happens with the horizontal family of invariant tori around L_3. We also showed how these invariant curves have associated stable and unstable invariant manifolds since they are hyperbolic, as it happens with the horizontal family.

Then, in spite of the fact that the analysis of the vertical family requires to work in a six-dimensional phase space, the invariant manifolds associated with the invariant curves in the map are two dimen-

sional. Consequently, we can proceed as in Section 3.1 and define fundamental cylinders that allow to know the behaviour of the connections given by the vertical family of invariant tori around L_3 in the BCP.

The size of the meshes used to parametrize these fundamental cylinders in $\theta \in [0, 2\pi]$ and $\sigma \in [\sigma_0, \lambda_u \sigma_0]$ (for the unstable manifolds) and $\sigma \in [\sigma_0, \lambda_s^{-1} \sigma_0]$ (for the stable ones) are the same as those used in Section 3.1, $M_1 = 1000$ and $M_2 = 1000$. Then, each point in the fundamental cylinders of the stable and unstable invariant manifolds is computed following (3.1) using $\sigma_0 = 10^{-5}$ since we work again with the linear approximation of the invariant manifolds. The initial conditions in the fundamental cylinders are propagated during the same time span as in Section 3.1 in order to make comparisons between the transport mechanisms that both families suppose.

Figure 3.18 shows the four fundamental cylinders of the stable and unstable invariant manifolds (two branches for each manifold) associated with an invariant curve at a vertical distance of 5.8942×10^{-2} from L_3, see Definition 2.3.2. The two images above correspond to the unstable invariant manifolds and the two below to the stable ones. The colour scale is again: purple for reaching the Earth, red for reaching the Moon, yellow for reaching the outside system (*i.e.* being at more than 10 Earth-Moon distances from the Earth-Moon barycentre) and black for those trajectories that during the considered propagation time have not reached neither the primaries nor leaving the system. It is clear that trajectories in both manifolds of this invariant curve reach the Earth, the Moon and leave the system, suggesting that the vertical family of invariant tori around L_3 is also a mechanism of transport arising many possibilities. From these images the symmetry between stable and unstable invariant manifolds is appreciated.

In Figures 3.19 and 3.20 the fundamental cylinders of the two branches of the unstable invariant manifolds for invariant curves in the vertical family of L_3 are shown. Notice that the fundamental cylinders for small vertical distance to L_3 remain a little to those close to L_3 in the horizontal family (see Figure 3.4); in one of the branches colours yellow and black with a little of red are dominant, meanwhile in the other branch the dominant colours are yellow and purple. It is clear that the connections involving the primaries are relevant when the vertical distance to L_3 is small, and as it increases the majority of the trajectories just travel around the system without reaching any of the primaries nor leaving the system (what corresponds to the black colour). Another comment is that there are not so many trajectories in the stable and unstable manifolds of the curves in the vertical family that reach the Moon, as it happens in the case of the horizontal family. And finally, it is remarkable that for invariant curves corresponding to high values of the z component ($\gtrsim 0.8$) a clear relation with the Earth appears again (in other words, the purple colour is again appreciable). This effect may be related with the shape of the invariant curves in this family, see Figure 2.10. In that plot, one can appreciate that as the z coordinate gets apart from zero, the invariant curves approach the position of the Earth.

In Table 3.5 the percentages of the trajectories in the unstable manifolds that reach the Earth, the Moon, the outside system or just travel around the Earth-Moon system during the propagation time are shown. Notice that the same percentages are found for the trajectories in the stable manifolds due to the symmetry.

Those trajectories in the hyperbolic invariant manifolds that reach distances far away enough from the Earth-Moon barycentre, are trapped by the solar gravitational field and their orbital elements with respect to the Sun are computed. Since now we are working in the spatial phase space we can analyse all the heliocentric orbital elements of interest. Due to the symmetry, the elements of the trajectories that leave the Earth-Moon system through the unstable invariant manifolds and those of the trajectories that enter the system through the stable invariant manifolds correspond to the same ranges of values. Therefore, we only show the orbital elements corresponding to the stable manifolds. In Figure 3.21 some graphs corresponding to the semi-major axis, eccentricity, inclination are shown. Again the shape and the range of values of these graphs of the orbital elements coincide with those presented in [GVJ12].

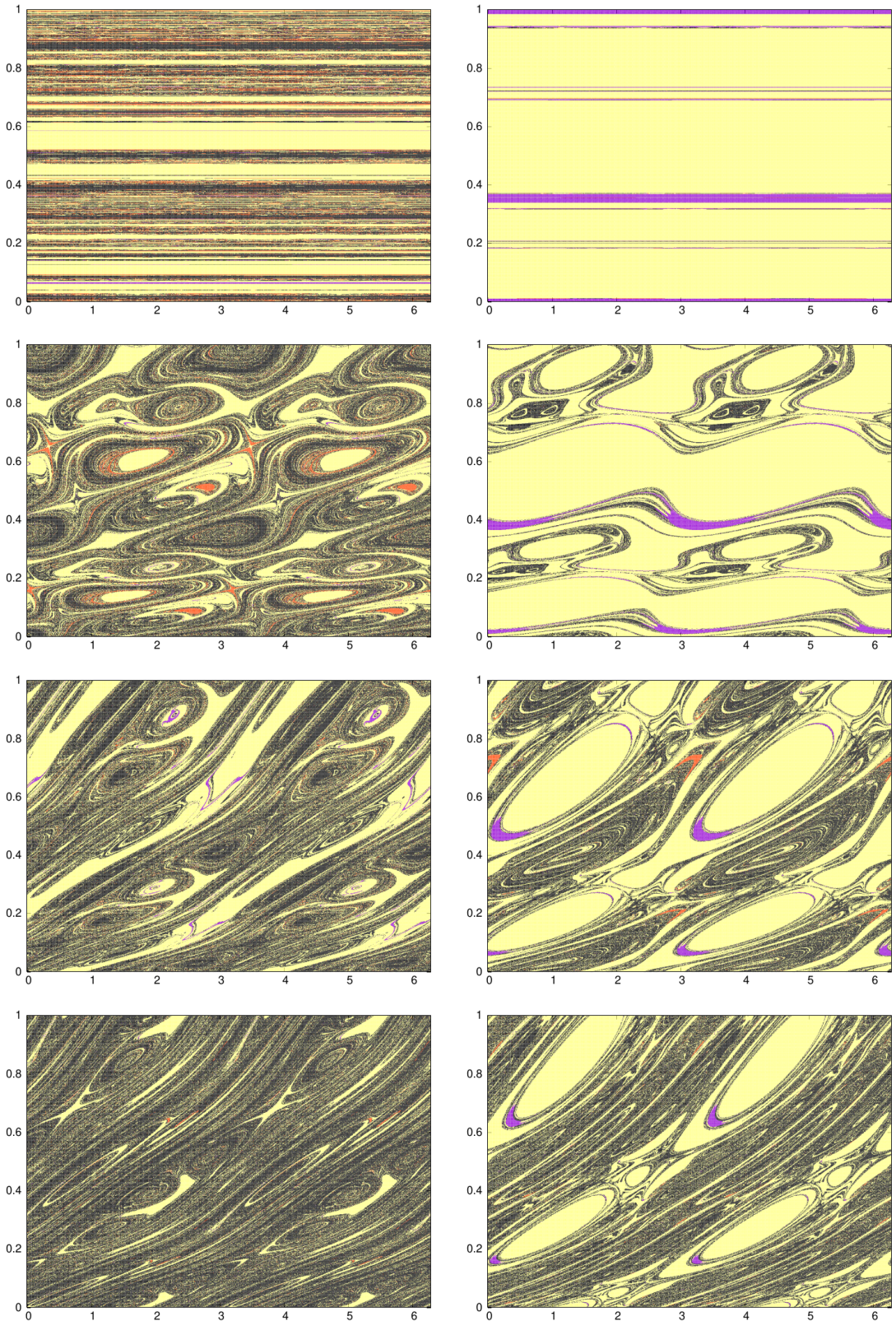

Figure 3.19: Fundamental cylinders for the two directions of the unstable manifolds of curves at vertical distances to L_3, from up to down, 2.0385×10^{-3}, 1.0090×10^{-1}, 2.0103×10^{-1} and 3.0013×10^{-1}. Notice that cylinders in Figure 3.18 fit between the first and the second rows.

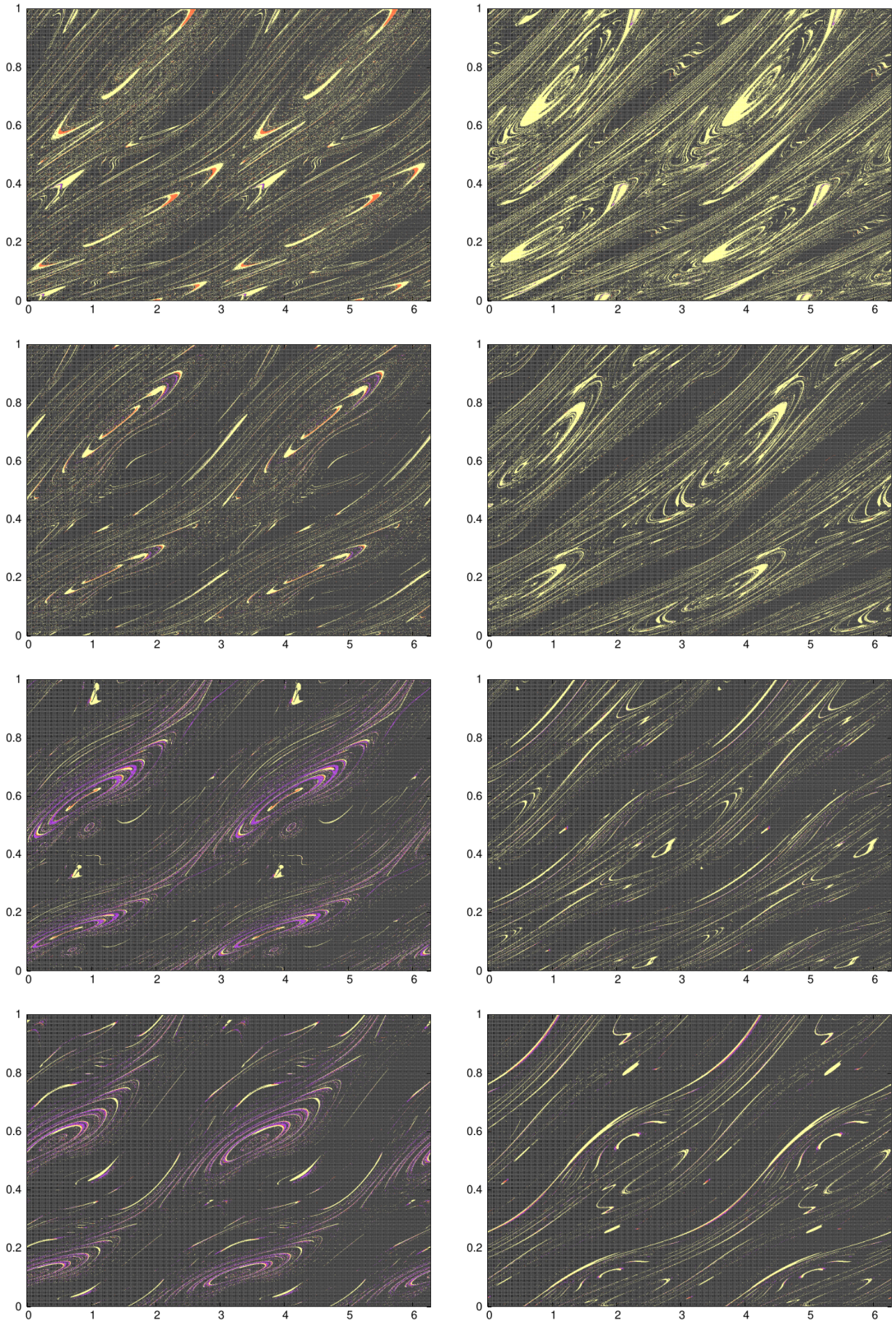

Figure 3.20: Fundamental cylinders for the two directions of the unstable manifolds of curves at vertical distances to L_3, from up to down, 5.0057×10^{-1}, 6.3333×10^{-1}, 8.0081×10^{-1} and 9.0097×10^{-1}.

Vertical distance to L_3	Earth (%)		Moon (%)		Exterior (%)		Neither (%)	
2.0385×10^{-3}	1.49	6.79	11.25	0.37	50.75	91.72	36.52	1.12
5.8942×10^{-2}	0.94	4.99	6.49	0.15	39.95	89.13	52.62	5.73
1.0090×10^{-1}	0.77	2.93	4.93	0.16	42.46	82.65	51.84	14.25
1.5064×10^{-1}	0.76	1.85	3.11	0.54	39.67	70.89	56.46	26.71
2.0103×10^{-1}	1.05	1.34	2.09	1.12	43.69	60.24	53.17	37.31
3.0013×10^{-1}	0.44	0.73	1.80	0.87	26.38	49.02	71.38	49.38
4.0035×10^{-1}	0.42	0.31	2.55	1.12	23.55	39.99	73.48	58.58
5.0057×10^{-1}	0.23	0.24	1.56	0.44	12.64	23.74	85.57	75.58
6.0019×10^{-1}	0.35	0.16	1.01	0.28	8.16	14.07	90.48	85.49
6.3334×10^{-1}	0.39	0.13	0.91	0.29	6.66	12.08	92.04	87.50
7.0056×10^{-1}	0.58	0.15	0.80	0.27	5.09	9.22	93.53	90.36
8.0081×10^{-1}	3.46	0.46	0.66	0.22	3.74	6.16	92.13	93.16
9.0097×10^{-1}	2.82	0.71	0.57	0.39	3.11	4.63	93.50	94.26
9.6602×10^{-1}	0.49	0.41	0.30	0.47	1.12	3.11	98.09	96.01

Table 3.5: Percentages of the trajectories starting at fundamental cylinders that go to the Earth, Moon, outside system or neither, through the two directions of the unstable invariant manifolds for some invariant curves of the vertical family around L_3.

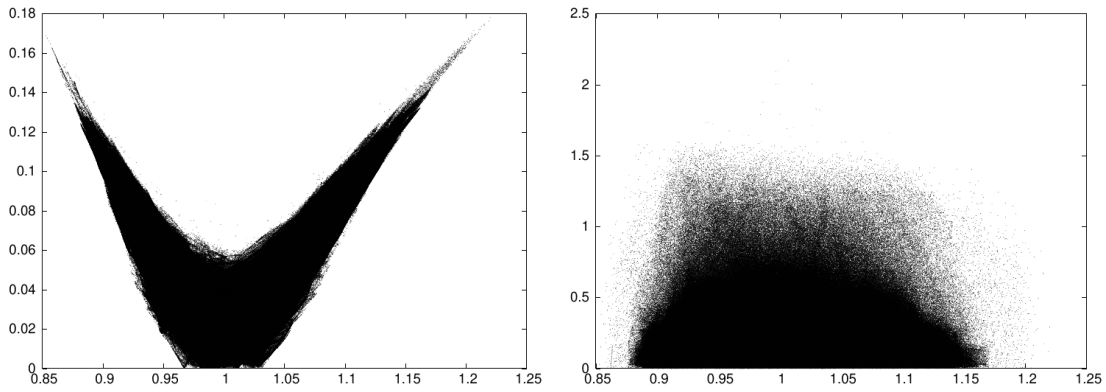

Figure 3.21: Orbital elements for orbits entering the Earth-Moon system through the stable invariant manifolds associated with the vertical family of tori around L_3. Horizontal axis corresponds to semi-major axis (in astronomical units) in both plots. The vertical to eccentricity, in the plot on the left, and to inclination (in degrees) in the plot on the right.

Chapter 4

Capture of an asteroid through L_3 in the BCP

Nowadays, several space agencies and private companies are considering the exploitation of raw materials from asteroids, e.g., gold, iridium and platinum [MMBM15, ABB+15, VMC20]. Metals such as gold or platinum could be transported to Earth, while more common metals could be used for construction in space [O'L77]. Different options have been pointed out to obtain these materials from asteroids. One option is to send a robotic probe to visit an asteroid, collect such materials and bring them back to Earth. A second option is to attach a propulsion system to the asteroid and, by means of a small manoeuvre, capture it into a suitable orbit of the Earth-Moon system. This last technique, although difficult to carry out, allows for a much simpler mining strategy once the asteroid is inside the Earth-Moon system. In this context, Near Earth Asteroids (NEAs) offer very suitable targets.

There are several works in the literature that analyse the capture near the L_1 and L_2 collinear points (for a recent review, see [SNU18]). For instance, [SGYAM12] studies the capture opportunities for a selection of NEAs targeting Lyapunov and Halo orbits of the Earth-Sun Circular Restricted Three-Body Problem (RTBP). The capture of NEAs targeting L_2 Lyapunov and Halo orbits in the Earth-Moon RTBP is discussed in [TMC17]. In both works, the case of asteroid 2006 RH120 is analysed, resulting in costs between 58 m/s and 298 m/s in the first case (Earth-Sun RTBP) and less than 500 m/s in the second (Earth-Moon RTBP). The attention paid to the collinear points L_1 and L_2 is due to their strong instability and low energy level, that aids to a rapid dynamics to enter and leave the system passing close to the small primary, either the Moon in the Earth-Moon system or the Earth in the Sun-Earth system. However this advantage to have a fast approach is also a disadvantage to control it, since high fuel costs have to be employed to avoid the asteroid to leave this region with the same facility as it is approached. Not to mention the risks of a crash into the Moon or the Earth. Other works suggest the capture of an asteroid without targeting any particular orbit, for example, in [USB+14], the authors analyse the lengthening of the time that the asteroid 2006 RH120 was orbiting the Earth in its last approach in 2006, by sweeping a three dimensional mesh on the parameters that define a low thrust manoeuvre. Among their results, a manoeuvre of total Δv of only 32 m/s is found to have been able to extend this time another five years.

In this chapter we analyse the neighbourhood of the L_3 point of the Earth-Moon system as one of the potential destinations for a captured asteroid. One of the advantages of this region is a very mild instability that allows for an extremely cheap control to keep the asteroid there: the station keeping manoeuvres to remain in the neighbourhood of L_3 are of just some cm/s per year [FV04]. So, it is very cheap to keep the asteroid in that region, in order to perform a mining process or just waiting for the right moment to send it towards to some other region. Another advantage of this region is that, as we commented in Section 3.1.1, there are invariant manifolds connecting the vicinity of L_3

with the typical trajectories of NEAs.

The model we have used in this study of the capture of an asteroid is the planar Bicircular model. In this model, when the infinitesimal particle is at some distance from Earth and Moon it follows a nearly-Keplerian orbit around the Sun, see Section 3.1.1, while when it enters the Earth-Moon system it follows the dynamics of a Restricted Three-Body Problem with a perturbation coming from the Sun. Hence, it seems a natural initial model to study the capture of a NEA.

The idea is to use the stable invariant manifolds associated with the invariant curves around L_3 in the horizontal plane to capture the asteroid. When working with the linear approximation of the invariant manifolds the numerical integrations have to start very close to the torus in order to have a good level of accuracy and, hence, a *long* integration time is needed to move away from the neighbourhood of L_3. This long integration time introduces some numerical difficulties (as we will see in Section 4.1) and, for this reason, we have implemented the parametrization method to compute these invariant manifolds up to high order. As these computations are done in a Poincaré map, the parametrization method is combined by a jet transport technique to propagate the high order derivatives needed in the parametrization method [GJJC$^+$21]. The last step of the process is to refine trajectories on the stable manifold that arrive at some given position at a given time; the position and time of the asteroid. The difference in their velocities gives the value of the impulse manoeuvre, Δv, required to insert the NEA into the stable manifold.

As a test example, we have considered the capture of the asteroid 2006 RH120. This is a small asteroid (3.3 ± 0.4 meters in size [KKP$^+$09]) that makes close approaches to the Earth-Moon system. In fact, in its last approach it was orbiting the Earth from September 2006 to June 2007. We have selected the 2006 approach to show a strategy to capture it near the L_3 point of the Earth-Moon system. We show that there are many options to capture it using a Δv in the range 100-300 m/s, and some other options to capture it with a Δv below 100 m/s. Remarkably, there is one option with a Δv as low as 20 m/s.

The chapter is structured as follows. Section 4.1 discusses the use of the high order approximation of the stable invariant manifolds to construct a capturing strategy, and Section 4.2 shows the results of applying the previous strategy to the capture of the asteroid 2006 RH120. Finally, Section 4.3 is devoted to the conclusions and future work regarding to the use of manifolds for capturing an asteroid. The analysis and results of the present chapter are collected in [JN21].

4.1 Computational strategy

The previous chapter has shown how parts of the invariant manifolds of the quasi-periodic orbits near L_3 move around the Earth-Moon system, while other parts escape and orbit the Sun. The main idea to capture a NEA in the vicinity of L_3 is to propagate, backward in time, the stable invariant manifold of a quasi-periodic orbit near L_3 looking for encounters in positions with the target object. The difference in velocities at this "meeting point" gives the manoeuvre to inject the NEA in the manifold so that the natural dynamics of the problem sends the asteroid to the neighbourhood of L_3. As mentioned, the advantages of using L_3 are mainly a very low cost for the station keeping there, the possibilities offered to reach a different region from there and the low risk of crashing during the transfer.

It is worth mentioning that a preliminary exploration of the possibilities of L_3 for the capture has been done using the linear approximation of the invariant manifolds of the invariant curves shown in Figure 2.4. However we do not aim just to find an invariant manifold that passes close to the position of an asteroid to justify the capture, but to be able to find the initial condition on the fundamental domain of a torus that is sent (by the backwards flow of the BCP) to the position of the asteroid

at the right time. Notice that, when using the linear approximation of the invariant manifolds the fundamental domain, or fundamental cylinder (FC) detailed in Section 1.4.4, needs to be defined very close to the invariant curve (for $\sigma_0 \leq 10^{-5}$), therefore the globalisation of those initial conditions requires numerical integration of trajectories that spend a significant amount of time just closely following the quasi-periodic orbit, increasing the numerical errors and making more difficult to find the initial condition that corresponds exactly with the position of the asteroid. This difficulty is solved using a high order parametrization method for the invariant manifolds.

The computational strategy for the capture that we present here is based on three steps. First of all, the positions and velocities of the asteroid are obtained from the JPL Horizons system [JPL] in the ecliptic reference frame at some Julian epochs. Therefore, a change of positions, velocities and time is needed to transfer the information on the location of the asteroid to the Bicircular model. We use the change of coordinates detailed in Section 2.5 and the particular case of the chosen asteroid is presented in Section 4.1.1. The second step is to define the fundamental cylinders of the stable invariant manifolds of tori around L_3 using the high order parametrization, globalise them backward in time, see Section 4.1.2, and then compare the position of the trajectories in the manifold with that of the asteroid. This allows to identify sets of initial conditions on the FC that approach the asteroid. Finally, in Section 4.1.3, we explain a Newton method used to compute the initial condition on the FC that arrives, backward in time, to the location (positions and time) of the asteroid.

As the BCP is a periodically time-dependent model, we can look for encounters NEA-manifolds at different times. If we use the Poincaré map P then we only look for encounters at time $t = 0 \mod T$ (that is, after an integer number of periods of the BCP). In our analysis of the capture we define different temporal sections, corresponding to an integer number of periods, to a quarter, to a half and to three quarter of the period. This has two effects; on the one hand, the relative position of the Earth-Moon system with respect to the Sun changes and this can aid (or difficult) the capture, and on the other hand, the positions of the asteroid itself are also different.

Finally, we want to emphasise that this work studies, as an example, the capture of the asteroid 2006 RH120 in its last approach to the Earth, but it is easy to see that the whole strategy described here can be used to study the capture of any other asteroid or object of interest.

4.1.1 Bringing a real asteroid to the BCP

We take the coordinates of asteroid 2006 RH120 from the JPL data base at different times corresponding to times equal to

$$t = S_T T \qquad S_T = \left\{0, \frac{1}{4}, \frac{1}{2}, \frac{3}{4}\right\} \tag{4.1}$$

in the Bicircular reference frame. That correspond to times

$$t = T_{ECLIPSE} + N_T \tilde{T} + S_T \tilde{T} \qquad S_T = \left\{0, \frac{1}{4}, \frac{1}{2}, \frac{3}{4}\right\} \tag{4.2}$$

in Julian days, see Section 2.5.1, in particular Equation (2.19).

The database gives the coordinates of the asteroid at those selected temporal sections in the ecliptical reference frame. In order to have the coordinates in the reference frame of the BCP, we apply the change of coordinates detailed in Section 2.5.2. Two observations need to be done. First one, as we want to translate the positions provided by the JPL database to the BCP frame, we have to apply the inverse change of coordinates. And second one, since we consider the planar BCP, we project the positions and corresponding velocities in the adimensional reference frame to the xy-plane.

In our example, we study the cost to capture the asteroid 2006 RH120 near L_3. This NEA was naturally captured by the Earth from September 2006 to June 2007. We analyse the possibilities

of capture at different epochs that verify (4.2), such that all these epochs correspond to the same temporal section in the BCP for a given S_T. The selected epochs go from April 2006 and May 2007, some months before and along the time of the natural capture. The reasons for choosing this time span are the following: at these epochs the vertical coordinate is lower than in previous epochs, the change of coordinates (2.20) is more precise close to (or inside) the Earth-Moon system, and finally, considering positions close to the system, the propagation time of the invariant manifolds is quite low, so that we can guarantee a certain level of control on the numerical errors.

The exact epochs and coordinates of the asteroid in the planar BCP at a temporal section corresponding to integer number of solar periods ($S_T = 0$ in (4.2) and taking $T_{ECLIPSE} = 2451564.69787$ Julian Days) for the selected time span, are shown in Table 4.1. First column designates an identity number to each epoch.

it	Epoch in Julian Day	x	y	p_x	p_y
1	2453838.55277 (2006-Apr-13)	8.49569856e+00	5.32382756e+00	-1.32303889e+00	6.39230591e-01
2	2453868.08336 (2006-May-12)	4.30485868e+00	2.69869849e+00	-5.98173604e-01	4.69696447e-01
3	2453897.61394 (2006-Jun-11)	2.20409179e+00	3.15215977e+00	-2.31495071e-01	4.09922742e-01
4	2453927.14452 (2006-Jul-10)	1.79617205e+00	3.52278287e+00	4.88502390e-02	5.27242305e-02
5	2453956.67511 (2006-Aug-09)	8.44580321e-01	1.94256864e+00	-1.83258282e-01	-2.87989646e-01
6	2453986.20569 (2006-Sep-07)	-2.03317473e+00	3.96100179e-01	-3.27669077e-01	3.32987066e-02
7	2454015.73627 (2006-Oct-07)	-1.77595242e+00	-6.00168179e-01	1.34571469e-01	-5.87429182e-02
8	2454045.26686 (2006-Nov-05)	-1.59983939e+00	-1.84351841e+00	-1.29626305e-01	1.68008169e-02
9	2454074.79744 (2006-Dec-05)	-2.52446813e+00	-1.45236080e+00	4.97133752e-02	2.81586255e-01
10	2454104.32802 (2007-Jan-03)	5.36966985e-01	1.89106392e-01	9.19935708e-01	-1.16359612e-01
11	2454133.85861 (2007-Feb-02)	1.01383428e+00	-1.06799662e+00	-2.12516151e-01	1.87709985e-01
12	2454163.38919 (2007-Mar-03)	-5.50357733e-01	4.66104142e-01	-1.47342869e-01	2.34743158e-01
13	2454192.91977 (2007-Apr-02)	1.55999311e-01	-1.47760228e+00	1.76720970e-01	-6.54112731e-01
14	2454222.45036 (2007-May-01)	-1.05304516e+00	-1.90933922e+00	1.94206705e-01	1.00575691e-01
15	2454251.98094 (2007-May-31)	-3.67319092e-01	5.92231168e-01	2.52078533e-01	2.49872133e-01

Table 4.1: Fifteen epochs corresponding to time 0 or $N_T T$ in the BCP, and the coordinates of the asteroid 2006 RH120 in the planar BCP at these epochs.

4.1.2 High order parametrization of L_3 invariant manifolds

In Section 1.3 we explained that the high order parametrization of hyperbolic invariant manifolds of a torus can be written as a formal Taylor-Fourier expansion in terms of two parameters, σ and the angle vector $\theta \in \mathbb{T}^d$:

$$W(\theta, \sigma) = a_0(\theta) + a_1(\theta)\sigma + \sum_{k \geq 2} a_k(\theta)\sigma^k,$$

where a_k are the functions parametrizing the manifold at order k that depend on the angles along the torus. In particular, in this chapter we are studying the manifolds associated with invariant curves of a stroboscopic map, therefore there is only one angular variable, $\theta \in [0, 2\pi]$. Then we follow the steps given in Section 1.4.3 to compute the stable and unstable invariant manifolds associated with invariant curves in a temporal Poincaré map.

Let us write the parametrization of the stable invariant manifold (W^s) and of the unstable invariant manifold (W^u) associated with an invariant curve as:

$$\begin{aligned} W^s(\theta, \sigma) &= \sum_{k \geq 0} a_k^s(\theta)\sigma^k, \\ W^u(\theta, \sigma) &= \sum_{k \geq 0} a_k^u(\theta)\sigma^k, \end{aligned} \tag{4.3}$$

where a_k^s (a_k^u) denotes each function of the parametrization of the stable (unstable) invariant manifold at order k. Now, we must remember that the Bicircular Problem, as many other classical mechanical

systems, presents a symmetry when inverting the time (see Equation (2.3)); *i.e.* if (x, y, p_x, p_y, t) is a particular solution of the system, also is $(x, -y, -p_x, p_y, -t)$. Since the computed invariant curves near L_3 cut symmetrically the x-axis, they are symmetric to themselves (self-symmetric), and their stable and unstable manifolds associated are also symmetric between them. Also, in our frame of the BCP, $\lambda_u = \lambda_s^{-1}$ due to the Hamiltonian structure. Therefore, we can compute only one invariant manifold (either the stable or the unstable) and have both, since

$$W^s(\theta, \sigma)\{x, y, p_x, p_y\} = W^u(\theta, \sigma)\{x, -y, -p_x, p_y\}. \tag{4.4}$$

In fact, for this application we have computed the unstable manifolds and we have used the symmetry to obtain the stable one.

The family of invariant curves around L_3 covers a wide area of the Earth-Moon system, see Figure 2.4. However, as these curves grow far away from L_3, they approach the Earth. This makes the curves in the outer part of the family to be considered inconvenient for being used in the capture, since the closer they pass to the Earth the risk of a crash increases. Also, if the asteroid is captured using an inner curve of the family it remains orbiting in a small zone, that is easy to control and where the risk of any crash is not relevant. Therefore, not all the invariant curves in the family are of interest for this application, and then we decide to focus on those at a maximum distance of 0.65 adimensional units from L_3, recall Definition 2.3.1 for the distance to L_3. Within this distance the parametrization method is applied to a subset of curves separately by, approximately, 10^{-3} adimensional length units, to obtain a total of 614 invariant curves.

Recall that the orders 0 and 1 of the parametrization of the invariant manifolds correspond to the invariant curve and to the hyperbolic eigenfunction, respectively, that we have already computed and used in previous chapters. For computing the orders $k \geq 2$ of the parametrization of the invariant manifolds of these 614 invariant curves, we follow the Algorithm 1.4.3, described in Section 1.4.3, up to order $K = 16$.

Looking at Figure 2.4 it is clear that each invariant curve in the family has different shape and different eigenvalues as their distance to L_3 increases. This is why each of them is discretized by a different number of Fourier modes. Moreover, the number of Fourier modes is not kept constant during the computation of the manifold: as it has been explained in Algorithm 1.4.3, the number of modes is increased from one order of the parametrization to the next when needed. Notice that each order of the parametrization, m, is computed tentatively with the same number of Fourier modes as the coefficient of the previous order, $m - 1$. The criteria we have followed to increase this number is for the Euclidean norm of the last two terms of b_m to be below some tolerance that also depends on the order of the parametrization, being $tol_2 = 10^{-10}$ at order 2 and $tol_m = 2tol_{m-1}$ for $m > 2$. When this tolerance is reached, the number of modes is increased by 20. The reason for this criteria is that the requirement of accuracy can be decreased for higher order terms without loss of accuracy for the manifold. The full computation of the parametrizations of the invariant manifolds for the 614 invariant curves following the procedure explained in Algorithm 1.4.3 takes less than 1.5 hours in a computer with 16 processors.

Table 4.2 shows the number of Fourier modes for the coefficients of the parametrization at order 0 (a_0, the invariant curve), $N_{k=0}$, and the number of modes needed for the parametrization function at order 15 (a_{15}), $N_{k=15}$ and at order 16 (a_{16}), $N_{k=16}$, for curves at different distances from L_3 in order to illustrate how the size of the discretizing series increases according to the shape of the invariant curve and to the degree of the parametrization.

Once we have the parametrizations of the invariant manifolds for the computed curves, we check up to which distance from the invariant curve each of the parametrizations can be trusted. Following the criteria defined by (1.53),

$$\bar{\sigma}_0 \approx \frac{1}{\lambda_u}\left(\frac{\varepsilon}{||a_K||_1}\right)^{1/K},$$

Invariant Curves			Invariant Manifolds			
distance to L_3	λ_u	$N_{k=0}$	$N_{k=15}$	$\bar{\sigma}_0$ from (1.53)	$N_{k=16}$	$\bar{\sigma}_0$ from (1.53)
10^{-3}	3.37281360	25	25	1.17×10^{-1}	25	1.34×10^{-1}
0.1	3.36135224	27	27	8.08×10^{-2}	27	9.28×10^{-2}
0.2	3.32665559	28	48	6.25×10^{-2}	48	7.20×10^{-2}
0.3	3.26751807	29	69	5.10×10^{-2}	69	5.86×10^{-2}
0.4	3.18166131	32	92	4.37×10^{-2}	92	5.02×10^{-2}
0.5	3.06474188	45	125	3.87×10^{-2}	125	4.45×10^{-2}
0.6	2.90843912	72	192	3.52×10^{-2}	332	4.04×10^{-2}
0.65	2.79811097	84	364	3.52×10^{-2}	424	3.86×10^{-2}

Table 4.2: Values of the unstable eigenvalue (λ_u), the number of Fourier modes needed for the orders of the parametrizations 0 ($N_{k=0}$), 15 ($N_{k=15}$) and 16 ($N_{k=16}$) and the $\bar{\sigma}_0$ parameter such that the error of the parametrization up to order $k = 15$ and $k = 16$ is below 10^{-14}, for invariant curves at different distances from L_3.

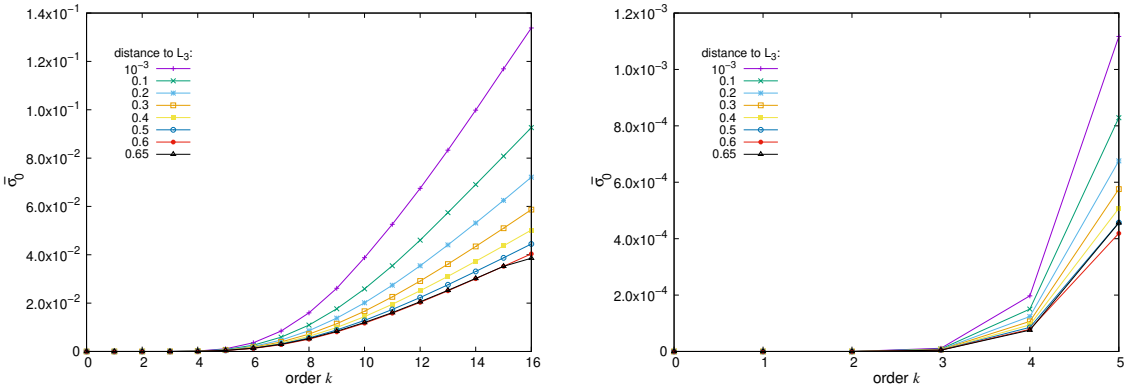

Figure 4.1: Growth of the value of $\bar{\sigma}_0$, for the approximation to be trusted with an error below 10^{-14}, according with the order of the parametrization (k). It is shown for the manifolds of the eight invariant curves in Table 4.2. Left, for the maximum order considered, $K = 16$. Right, a zoom including only up to order 5.

in the Section 1.4.5, we see that for the parametrizations at the maximum considered order, $K = 16$, to satisfy an error ε below 10^{-14}, the values of $\bar{\sigma}_0$ must be between 1.34×10^{-1} for the inner invariant curves of the family and 3.86×10^{-2} for the outer ones, see Table 4.2. This supposes a big improvement with respect to the value $\sigma_0 \approx 10^{-5}$ needed for accurately approximate the manifold using the linear approximation. The values of $\bar{\sigma}_0$ at the parametrization order $k = 15$ are also included in the table to illustrate that the gain of domain of validity from order 15 to 16 is not significant, and therefore considering parametrization order higher than 16 seems to be not necessary.

In order to make this improvement more visual, in Figure 4.1, the variation of the computed value $\bar{\sigma}_0$ with respect to the order of the parametrization is shown. The plot on the left shows this variation up to the maximum order considered ($K = 16$) and the plot on the right shows a zoom of the first orders. As it is natural, the first orders of the approximation allow to increase the value of $\bar{\sigma}_0$ more easily than for the higher orders.

Now we have the information needed to define fundamental domains for the stable invariant manifolds following expression (1.52), as explained in Section 1.4.3. These domains are cylinder shaped and they

distances to L_3	$\lvert\sigma_0\rvert$ considered	divisions in θ	divisions in τ
10^{-3} - 0.1	5.00×10^{-2}	1000	500
0.1 - 0.3	5.00×10^{-2}	2000	500
0.3 - 0.4	5.00×10^{-2}	2500	400
0.4 - 0.65	2.50×10^{-2}	5000	200

Table 4.3: Values of σ_0 and the number of divisions taken for the mesh of (θ,τ) to define the fundamental cylinders for the invariant curves depending on their distance to L_3.

are parametrized by two parameters, θ and τ,

$$(\theta,\tau)\in[0,2\pi]\times[0,1] \quad \mapsto \quad \mathcal{Z}^s(\theta,\tau)=\sum_{k=0}^{K} a_k^s(\theta)((1+\tau(1/\lambda_s-1))\sigma_0)^k.$$

Notice that σ_0 must take positive and negative values, in order to parametrize the two branches of the stable invariant manifold. Therefore, to analyse the fundamental domains, first, we need to specify a value for σ_0 and to make a mesh on the two parameters, such that every point in the fundamental cylinder, (θ,τ), is an initial condition on the stable invariant manifold. For each invariant curve we need to specify the value of σ and of the number of divisions taken along the angle θ and in parameter τ to define the mesh of its fundamental cylinder. The selected values are taken attending to the differences observed between the parametrizations of the manifolds for curves at different distances to L_3. Table 4.3 collects the values considered depending on the range of distance at which the curve is placed. This way, the mean distance between each two points in the mesh of any of the FC is of the order of 5×10^{-4} adimensional units, around 200 km.

Each of the points in the mesh, i.e. initial condition on the FC, is integrated backward in time for a maximum of 15 solar periods, by means of a Taylor method [JZ05]. After each period of the BCP, we compute the distance to each of the fifteen positions of the asteroid given in Table 4.1 and we store the minimum of this distance, jointly with the differences in velocities between the point of minimum distance and the asteroid (we will refer to this difference as Δv).

If, during the integration, a trajectory in the stable manifold crashes with the Earth or the Moon the integration is stopped and we keep the information of the closest approach to the asteroid before the crash. We also compute the growth of the derivative of the trajectory with respect to the initial condition (this is the typical computation done to estimate Lyapunov exponents) to have an idea of the error propagation due to the instabilities of the problem. If this increasing factor grows more than 10^9, we proceed as in the crash case, in order to discard those trajectories with significant error accumulated.

4.1.3 Refining an initial confition on the FC

In this section we present a Newton method to refine an initial condition on the FC, identified by two values θ and τ, that arrives to the position of the asteroid, at a specific time. The seed for the Newton method is given by the first approximation obtained in the previous section. The FC is parametrized according to (1.52) as

$$\mathcal{Z}^s(\theta,\tau)=\sum_{k}^{K} a_k^s(\theta)((1+\tau(\lambda_s^{-1}-1))\sigma_0)^k,$$

where $\mathcal{Z}^s(\theta,\tau)$ is a four-dimensional vector, ($\mathcal{Z}^s=\{x,y,p_x,p_y\}$). Therefore, what we want is to find parameters (θ,τ) such that the trajectory starting at this point reaches, at some time t_f, the position

of the asteroid. This condition is written as

$$F(\theta,\tau) = \{x(\theta,\tau), y(\theta,\tau)\}_{t_f} - \{x_{asteroid}, y_{asteroid}\} = 0.$$

This is the equation we will solve using a Newton method. The derivatives of F with respect to θ and to τ follow from the chain rule,

$$\begin{aligned}
\frac{\partial F}{\partial \theta}(\theta,\tau) &= D_x P(\mathcal{Z}^s(\theta,\tau))_{t_f} \sum_{k=0}^{K} \frac{\partial a_k^s(\theta)}{\partial \theta} \left[\sigma_0(1+\tau(\lambda_s^{-1}-1))\right]^k, \\
\frac{\partial F}{\partial \tau}(\theta,\tau) &= D_x P(\mathcal{Z}^s(\theta,\tau))_{t_f} \sum_{k=1}^{K} a_k^s(\theta)\sigma_0^k k[1+\tau(\lambda_s^{-1}-1)]^{k-1}(\lambda_s^{-1}-1),
\end{aligned}$$

being $D_x P(\mathcal{Z}^s(\theta,\tau))_{t_f}$ a 4×4 matrix that contains the derivative of the flow at the final time, t_f. Notice that for $k=0$, the derivative of $F(\theta,\tau)$ with respect to τ is zero, since at this order, the parametrization corresponds just to the invariant curve, that does not depend on τ. Also, note that these expressions involve four dimensions, but we are only interested on the first two components, since we want to refine the values of (θ,τ) that give the desired values for the (x,y) coordinates at the final time.

4.2 Results for the asteroid 2006 RH12O

The strategy explained in the previous section has been applied to four different temporal sections, that is four Poincaré maps defined at times corresponding to an integer number of solar periods (T), to a quarter ($T/4$), to a half ($T/2$) and to three quarter ($3T/4$) of solar periods, see Equation (4.2).

In the time span considered, we have found several trajectories that approach different positions of the asteroid, and requiring a low Δv for the capture at any of the four temporal sections. Since we want to compute the trajectory in the stable manifold that arrives exactly to the position of the asteroid at the right time, we look for areas in the fundamental domain of the invariant curves that show clearly a minimum of the distance to the position of the asteroid, what we have called "minimum distance areas" for short.

In order to visualise the results of globalising the invariant manifolds, we make use of colour maps corresponding to fundamental cylinders, such that the horizontal axis corresponds to $\theta \in [0, 2\pi]$, the vertical one to $\tau \in [0,1]$. Therefore, every point $(\theta,\ \tau)$ is an initial condition on the FC, that is integrated backward in time and coloured according to some magnitude. Details about the meshes used and how to compute these trajectories in the stable manifolds are presented in Section 4.1.2.

Each point of the FC is coloured according to the minimum distance of the trajectory starting at this point to the asteroid, making easy to identify sets of trajectories, covering some area of the FC, that approach significantly the asteroid. In order to reduce the possibilities to the most convenient ones, we add two restrictions for the coloured maps. The first one is regarding to the distance to the asteroid and the second one to the maximum affordable Δv. Only trajectories that get closer than 10^5 km to the asteroid with a difference in velocities below 1 km/s, are included in the maps. Note that these are not strong restrictions, the reason for them is only to make easy to recognise the minimum distance areas and to have an idea of the Δv that may be involved. Actually, between all the suitable trajectories that have been found, only some of those requiring a Δv below 500 m/s are presented. Also, once the minimum distance areas are identified, we use the method explained in Section 4.1.3 to refine a trajectory nearby that arrives to the asteroid position. The accuracy imposed to the Newton method is for the trajectory in the manifold to lay as close as 10^{-10} adimensional units ($\approx$ 3.8 cm) to the asteroid position at the right time; this tolerance is achieved with just three or four Newton iterations.

The way to present and interpret the results is the same for any of the temporal sections, so an extended examination of the results corresponding to the temporal section at times "0" or $N_T T$ are first given in Section 4.2.1, and some of the results for the other three temporal sections are collected, in a more schematic way, in Section 4.2.2.

At the end of Section 4.2.1, we also give a brief explanation about the continuity in time of the minimum distance areas, and its effect on the Δv, in order to express the robustness of the trajectories susceptible to be used for the capture and to point out the possibility of implementing optimisation algorithms.

4.2.1 Temporal Poincaré sections at time T

The first results show that stable invariant manifolds of tori close to L_3 (that are also the most unstable ones) reach the positions of the NEA before the asteroid enters the Earth-Moon system (epochs it=1, 2 and 3 of the Table 4.1), with a low difference in velocities. Once the asteroid has entered the Earth-Moon system there are many initial conditions in the fundamental cylinders that approach the asteroid, specially for stable invariant manifolds of tori in the middle of the family, not very close to L_3. However, the difference in velocities when the asteroid is in the region close to the Earth and Moon is higher than when the asteroid is far away from any massive body, as expected according to some results found in the literature [SGYAM12, TMC17]. Finally, when the asteroid is leaving the system, the stable manifolds reach its position with a smaller difference in the velocities than when it is inside. In order to support these comments, three epochs are analysed in detail; it=2, it=7, and it=14. Since the procedure to obtain and present the results is the same for the three cases, we give a more detailed explanation for the first one, and limit ourselves to a brief version for the other two, again to avoid being repetitive.

it=2, (2006-May-12)

In Figure 4.2, colour maps of the FC of different tori, covering distances to L_3 from 0.01257 to 0.05784 (a length of $\sim$ 17400.33 km) are shown. The first six maps, in the first two rows, are coloured according to the minimum distance, in km, reached between the trajectory in the stable manifold and the position of the asteroid at epoch it=2. Belonging the first colour map to the invariant curve that is closer to L_3 and the following ones, to invariant curves increasingly further away from L_3. The last six maps in Figure 4.2 correspond to the same fundamental cylinders as the first two rows, this time coloured according to the instantaneous Δv in km/s, needed for the insertion of the asteroid in those trajectories belonging to stable manifolds. Remember that only trajectories that approach that position at least at 10^5 km and require a Δv of less than 1 km/s are included in the maps.

Recalling the effective continuity of the family of quasi-periodic orbits, we can compute any invariant curve between those shown in Figure 4.2 and observe a similar dynamics for the invariant manifolds than that of their neighbour curves, including presenting similar minimum distance areas. Altogether, considering the union of all these tori that present some clear zones of minimum distance, there exists some three dimensional regions of significant size where there are points that allow the capture of the asteroid with a single manoeuvre.

Now, we analyse the maps in Figure 4.2 separately. It is clear that for the first FC, two minimum distance areas are identified, very close one to the other, for values of θ between 3 and 4, and for some τ around 0.6. Let us call the minimum distance area on the left Minimum 1, and Minimum 2 to the one on the right. We can see these two minimum distance areas on the FC of the manifolds of nearby invariant curves that are further away from L_3. These minima start moving away and two other minimum distance areas appear for the FC in the second colour maps, named Minimum 3 (the one on the left) and 4 (the one of the right). For the FC in the third map of the first row another two minima are already found, Minimum 5 and 6. In the following maps these six minima can be

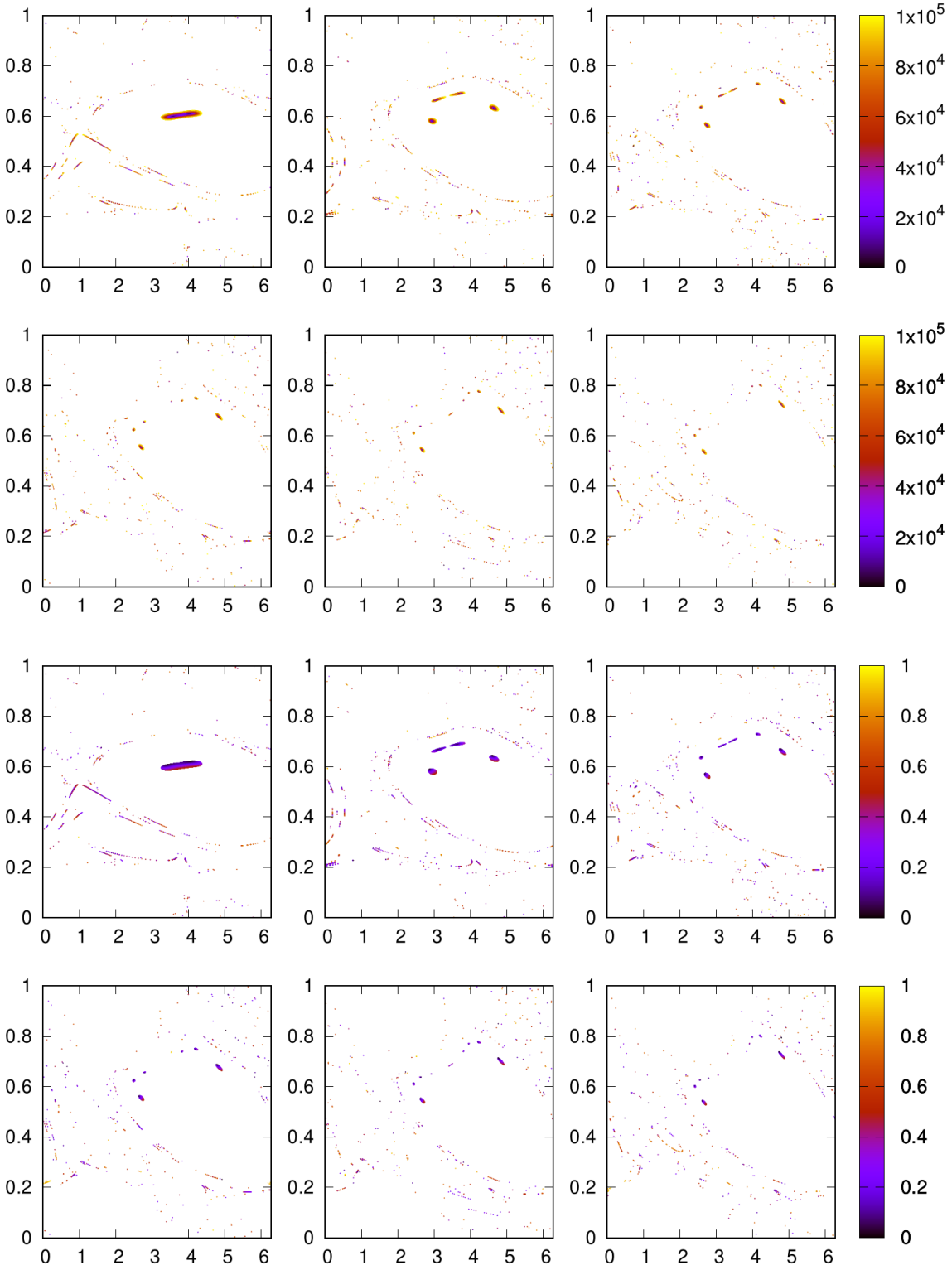

Figure 4.2: Six fundamental cylinders of tori at different distances from L_3 between 0.01257 and 0.05784. Plots in the first two rows show the FCs coloured according to the distance to the asteroid at position it=2, in km. Plots in the last two rows show the same FCs this time coloured according to the instantaneous Δv in km/s.

	Min 1				Min 2			
dist to L_3	N_T	θ	τ	Δv (m/s)	N_T	θ	τ	Δv (m/s)
0.01257	5	3.589	0.600	254.159	5	4.029	0.609	254.188
0.02043	5	2.953	0.580	254.098	5	4.654	0.632	254.260
0.03213	5	2.755	0.564	254.045	5	4.826	0.659	254.341
0.03947	5	2.709	0.555	254.018	5	4.849	0.676	254.392
0.04926	5	2.681	0.545	253.986	5	4.839	0.701	254.464
0.05784	5	2.672	0.537	253.962	5	4.805	0.725	254.529
	Min 3				Min 4			
dist to L_3	N_T	θ	τ	Δv (m/s)	N_T	θ	τ	Δv (m/s)
0.01257								
0.02043	6	3.065	0.664	114.391	6	3.702	0.690	114.414
0.03213	6	2.591	0.636	114.346	6	4.149	0.729	114.426
0.03947	6	2.501	0.624	114.320	6	4.216	0.749	114.425
0.04926	6	2.442	0.611	114.283	6	4.237	0.776	114.416
0.05784	6	2.419	0.601	114.248	6	4.222	0.801	114.403
	Min 5				Min 6			
dist to L_3	N_T	θ	τ	Δv (m/s)	N_T	θ	τ	Δv (m/s)
0.01257								
0.02043								
0.03213	7	3.132	0.681	131.324	7	3.506	0.707	131.301
0.03947	7	2.791	0.656	131.348	7	3.827	0.740	131.272
0.04926	7	2.628	0.638	131.366	7	3.958	0.771	131.247
0.05784	7	2.556	0.626	131.379	7	3.997	0.797	131.228

Table 4.4: Values of θ and τ corresponding to the initial conditions in the fundamental cylinders in Figure 4.2, that lay on the position of the asteroid at May 12, 2006, (it=2) after N_T BCP periods, and the Δv required for each of them.

easily identified. Looking at same maps in last two rows of Figure 4.2, it is clear that these minimum distance areas correspond to low values of Δv. It is worth mentioning that these maps are very similar for epochs it=1 and it=3.

For each of the six minimum distance areas, and for different tori, we have computed the trajectory that exactly arrives to the asteroid position at epoch it=2, with the Newton method introduced in Section 4.1.3. Table 4.4 collects the results for the initial condition in the fundamental cylinder, θ and τ, along with the number of solar periods, N_T, that this trajectory needs to reach the position of the asteroid and the amount of Δv required for the transfer. The trajectories in the stable manifold that reach the asteroid corresponding to the first bigger two minima need five solar periods to reach the position of interest and the Δv to take advantage of their dynamics is around 254 m/s. For the next two minima, smaller in size than the previous ones, six solar periods are required and the Δv is of less than 115 m/s. Finally, for the last two, even smaller in size, another extra solar period is needed in the propagation of the trajectories and the costs are of less than 132 m/s.

Now, we perform the simulation of the capture of asteroid 2006 RH120. For this, we consider as starting point the coordinates of the asteroid at epoch it=2, add the corresponding velocity impulse, the Δv included in the Table 4.4, and integrate forward in time in the planar BCP, making sure that the asteroid is trapped by the stable invariant manifolds of L_3, and lead to the neighbourhood of L_3, where it remains, just spinning around the corresponding torus for long time.

In Figure 4.3, we show the trajectories corresponding to the six minima present in the fifth colour map of Figure 4.2. It is clear that the trajectories of the first two minima almost overlap, specially when they are far from the Earth-Moon system. Similar effect is observed with the trajectories of

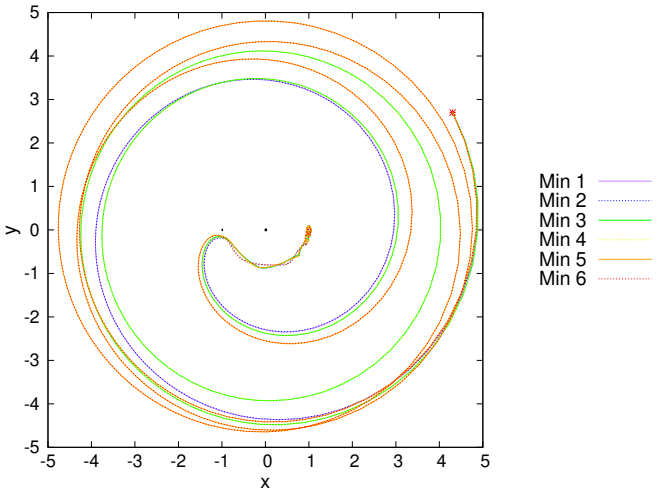

Figure 4.3: Simulation of the capture of the asteroid at May 12, 2006, through the trajectories in the stable manifold of the fifth FC of Figure 4.2 when applying the obtained Δv, Table 4.4. The Earth and the Moon are included as black circles of corresponding radius, and the initial position of the asteroid as a red star.

the second two minima, and with the ones of the third two minima. It is clear also the reason for the different values of the number of solar periods needed for each of the trajectories. Finally, these trajectories do not approach much neither of the massive bodies, although they pass at a distance of less than sixty thousand kilometres from the Moon, which makes that the norm of the derivative of the actual position w.r.t. the initial conditions be in the range between 10^3 and 10^4. This is a moderate error increasing factor.

it=7, (2006-Oct-07)

In this case, we consider the capture in an epoch in which the asteroid has already entered the Earth-Moon system. Figure 4.4 contains colour maps of the FC of different tori, covering distances to L_3 from 0.53075 to 0.60047 (a length of about 26800.76 km). Again, the first six maps are coloured according to the minimum distance, in km, reached between the trajectory in the stable manifold and the position of the asteroid, this time at epoch it=7. And the last six maps in Figure 4.4 correspond to the same fundamental cylinders but coloured according to the instantaneous Δv in km/s.

In the first fundamental cylinder of Figure 4.4 only one minimum distance area is identified, lets call it Minimum 1. However, as we consider fundamental domains of curves increasingly distant to L_3, this minimum is split into two different minimum distance areas. Let us call Minimum 2 to the minimum distance area at higher value of τ. In the third colour map, the first two minima are moving apart and a third one appears for low values of τ, Minimum 3. If we keep on examining fundamental domains of invariant curves further away from L_3, we observe that the third minimum splits into two, naming Minimum 4 the one at lower value of τ. In the fifth colour map, the four minimum distance areas are clearly identified, and for the last colour map Minimum 2 passes to be at the lower part of the fundamental domain. Keep in mind that this is a normal phenomenon since there is a continuity between the boundaries of these maps. The fact that this minimum passes from the upper part of the fundamental domain to the lower part makes necessary to integrate an extra period, see Table 4.5, since now this initial condition is closer to the invariant curve and it requires more time to approximate the asteroid. Minimum 1 and Minimum 3 come closer as moving through the family of invariant curves of L_3, until they join and then disappear. Concerning to Minimum 2 and Minimum 4, they have been tracked through more invariant curves, further to L_3 that the six fundamental

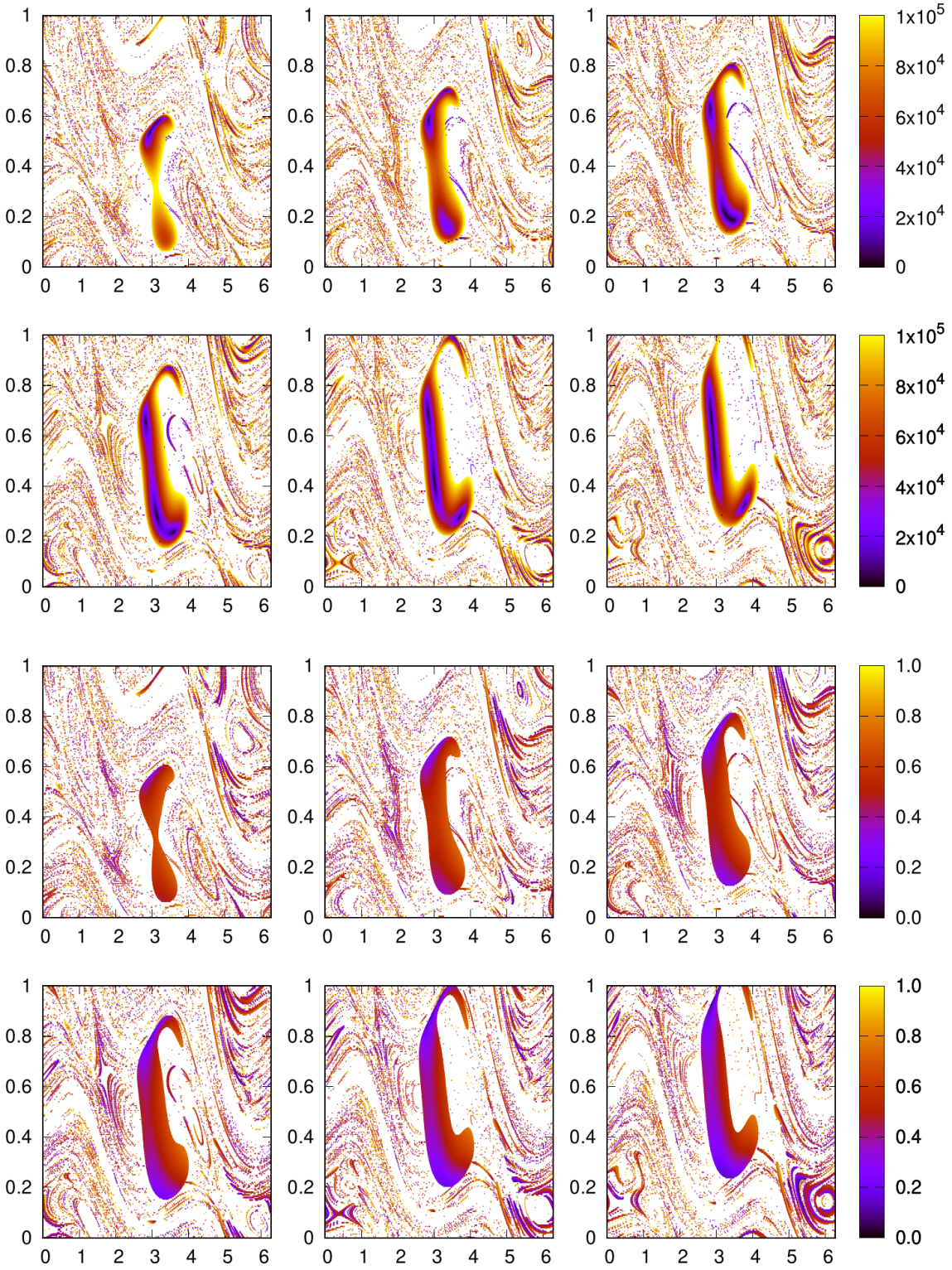

Figure 4.4: Six fundamental cylinders of tori at different distances from L_3 between 0.53075 and 0.60047. Plots in the first two rows show the FCs coloured according to the distance to the asteroid at position it=7, in km. Plots in the last two rows show the same FCs this time coloured according to the instantaneous Δv in km/s.

	Min 1				Min 2			
dist to L_3	N_T	θ	τ	Δv (m/s)	N_T	θ	τ	Δv (m/s)
0.53075	6	2.970	0.539	402.596				
0.55281	6	2.867	0.585	388.037	6	3.358	0.702	427.682
0.56617	6	2.844	0.628	379.142	6	3.451	0.800	433.318
0.57624	6	2.840	0.656	373.419	6	3.506	0.870	436.837
0.59139	6	2.850	0.691	365.138	6	3.584	0.985	442.115
0.60047	6	2.872	0.691	360.775	7	4.158	0.021	445.375
	Min 3				Min 4			
dist to L_3	N_T	θ	τ	Δv (m/s)	N_T	θ	τ	Δv (m/s)
0.53075								
0.55281								
0.56617	6	3.307	0.204	406.799				
0.57624	6	3.146	0.285	389.217	6	3.600	0.216	434.045
0.59139	6	3.027	0.420	373.829	6	3.737	0.280	446.723
0.60047	6	2.964	0.533	365.323	6	3.802	0.326	452.982

Table 4.5: Values of θ and τ corresponding to the initial conditions in the fundamental cylinders in Figure 4.4, that lay on the position of the asteroid at the October 7, 2006, (it=7) after N_T BCP periods and the Δv required for each of them.

domain included here, however the Δv needed for using them in a capture increases, see the last map in Figure 4.4. Therefore, we only focus on the results of the fundamental cylinders included in the Figure 4.4.

As in the previous case, we use a Newton method to find the initial condition (θ and τ on the FC) that arrives to the asteroid 2006 RH120 at epoch it=7. The results are collected in Table 4.5. It can be observed that the Δv required for the trajectories corresponding to the minimum distance areas 1 and 3 decreases as the curve they belong to is further away from L_3. The opposite effect happens with the trajectories of the minima 2 and 4.

Finally, we take the coordinates of the asteroid at epoch it=7, we add the velocity impulse of Table 4.5 and we integrate these trajectories forward in time in the planar BCP to check that the asteroid is lead towards L_3 (this is also a final test of correctness of all the computations). In Figure 4.5 the trajectories corresponding to the four minimum distance areas of the fifth fundamental cylinder in Figure 4.4 are shown. They correspond to an invariant curve for which Minimum 1 and 3 have not yet come together, but it can be appreciated how their trajectories are approaching. For trajectories of Minima 1 and 3 the expansion factor for the error is only of the order 10^2, because they do not approach much any massive body and because of the short integration time. This factor is of the order of 10^3 for the trajectory of Minimum 4, and increases to 10^4 for Minimum 2, due to the fact that the trajectory approaches the Moon.

it=14, (2007-May-01)

In this last example of temporal section corresponding to time $t = 0 \mod T$ (or $t = N_T T$), we show the results for the capture of 2006 RH120 when it is starting to leave the Earth-Moon system. As the evolution of the minimum distance areas between different tori has been detailed in previous cases, from now on the results are presented in a short version. Figure 4.6 shows the fundamental cylinders for tori at distances to L_3 from 0.52061 to 0.59139 (a length of $\sim$ 27207.85 km). In the first three FCs, each initial condition is coloured according to the minimum distance, in km, to the position of the asteroid at epoch it=14, and in the last three, they are coloured according to the difference in velocities between the trajectories in the stable manifolds and those of the asteroid, in km/s.

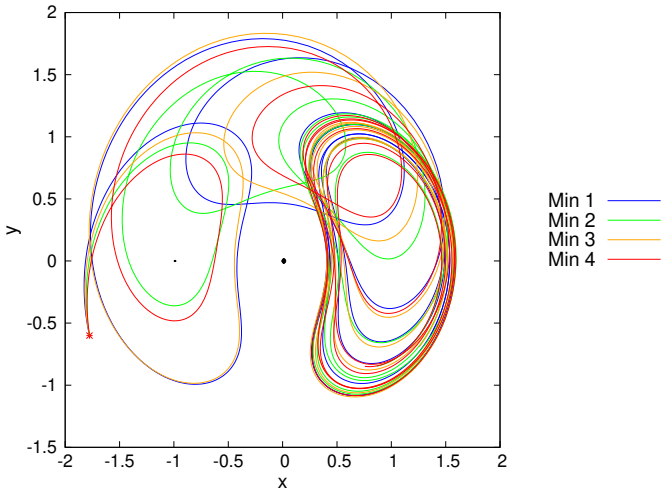

Figure 4.5: Simulation of the capture of the asteroid at October 7, 2006, through the trajectories in the stable manifold of the fifth FC of Figure 4.4 when applying the obtained Δv, Table 4.5. The Earth and the Moon are included as black circles of corresponding radius, and the initial position of the asteroid as a red star.

In the first colour map of Figure 4.6 a curved minimum distance area seems to appear for high values of τ (if we zoom that region we realise that there are actually two very close minima). As we examine the colour maps corresponding to invariant curves increasingly further away from L_3, the distance between these two separated minima increases: note that they move toward higher values of τ until they appear in the lower part of the fundamental cylinders. When this happens, the trajectories corresponding to those that lay on the exact position of the asteroid, obtained as in the previous cases and collected in Figure 4.7 (left), require an extra period of integration. At the right in the same Figure, the trajectories described by the asteroid, starting at epoch it=14 and propagated forward in time after adding the computed Δv for the two minima of the third fundamental cylinder are presented. In this case, the two trajectories approach a little the position of the Moon, specially the red one, for this reason the expansion factor for the error is between $10^3 - 10^4$. Nevertheless, an expansion factor of this value is acceptable.

Temporal continuity

We have performed some computations in order to analyse how the minimum distance area evolve at different time sections, close in time to the temporal section treated in the previous examples. The asteroid was considered twelve hours before and another twelve hours after the three epochs such that the time spans cover one day and are centered in each of the three cases.

For the first case, twelve hours before it=2, the Δv of minima 1, 2, 3 and 4 increases about 10 m/s, however for the minima 5 and 6 it decreases to $\approx$ 120 m/s. When we study these minima twelve hours later than it=2, we see that the difference in velocities has increased for the six trajectories; about 30 m/s for Minimum 1 and 2, $\approx$ 70 m/s for Minimum 3 and 4 and more than 100 m/s for Minimum 5 and 6.

In the second case, twelve hours before it=7, the Δv grows of the order of a couple of tens of m/s for the four minima. And, twelve hours after it=7, the minimum distance areas do not appear well defined for the first five invariant curves, but the first two minima appear in the fundamental domain corresponding to the last one, requiring less Δv for both; about 20 m/s less for Minimum 1 and about 40 m/s less for Minimum 2.

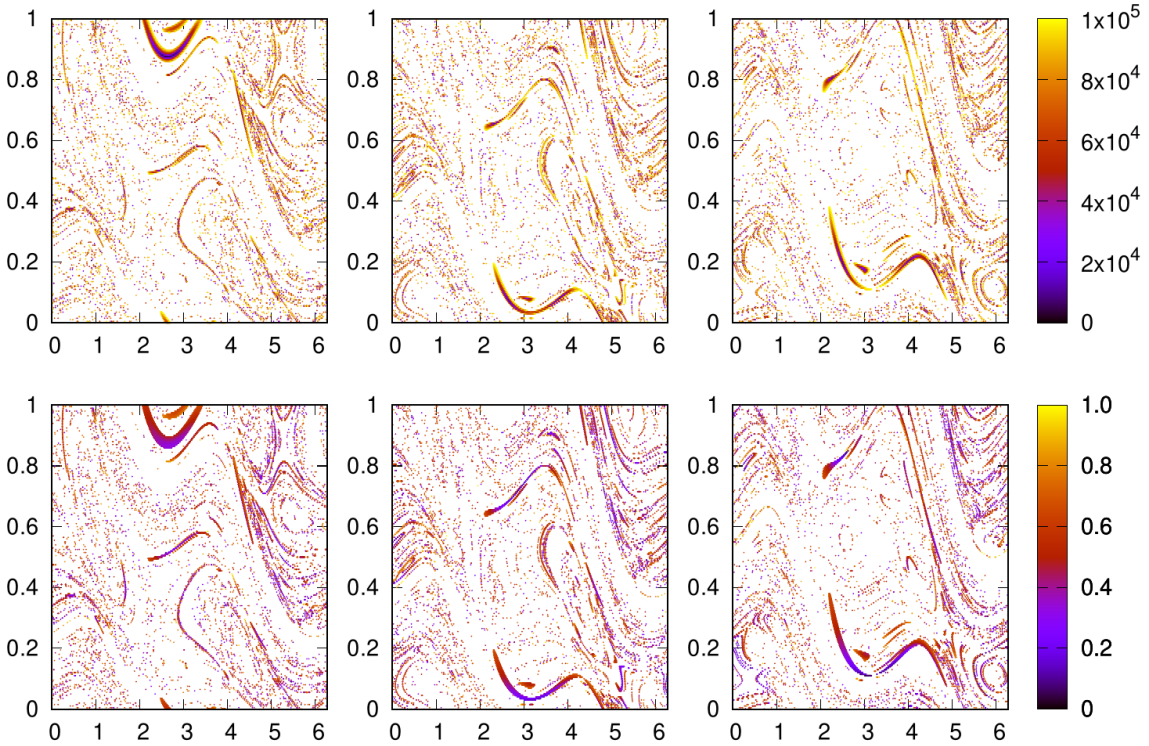

Figure 4.6: Three fundamental cylinders of tori at different distances from L_3 between 0.52061 and 0.59139. Plots in the first row show the FCs coloured according to the distance to the asteroid at position it=14, in km. Plots in the last row show the same FCs this time coloured according to the instantaneous Δv in km/s.

Finally, for the last case the differences are more homogeneous. Roughly speaking, twelve hours before it=14 the Δv needed is about 20 m/s lower than the one obtained for the two minima studied, and twelve hour after it=14, it increases more or less the same quantity.

Therefore, the same minimum distance areas that are found at a specific temporal section, appear at different close temporal sections, varying a little the difference between the velocities of the trajectories in the stable manifolds and those of the asteroid. This can be used to look for the optimal time (less Δv required) to perform the capture, or to use all these minima, continuous in time, to perform a low thrust. This is left for future work.

4.2.2 Temporal Poincaré sections at times $T/4$, $T/2$ and $3T/4$

Looking at the variety of possible trajectories for the capture of asteroid 2006 RH120 offered by the stable manifolds of the invariant curves of L_3, it is expected that many other possibilities appear when applying the same strategy for the capture at temporal Poincaré sections corresponding to $T/4$, $T/2$ and $3T/4$.

Actually, several new minimum distance areas have been found for any of these three temporal sections and for the different epochs of the asteroid. We do not aim to present neither all the possibilities nor different cases for any of the temporal sections, but to give some representative results in a qualitative way and to explain, quantitatively, a couple of examples.

	Min 1			
dist to L_3	N_T	θ	τ	Δv (m/s)
0.52061	5	2.551	0.878	362.771
0.56111	6	2.674	0.072	359.814
0.59139	6	2.516	0.197	361.850
	Min 2			
dist to L_3	N_T	θ	τ	Δv (m/s)
0.52061	5	2.845	0.885	370.471
0.52061	6	3.822	0.080	391.813
0.52061	6	4.039	0.205	407.460

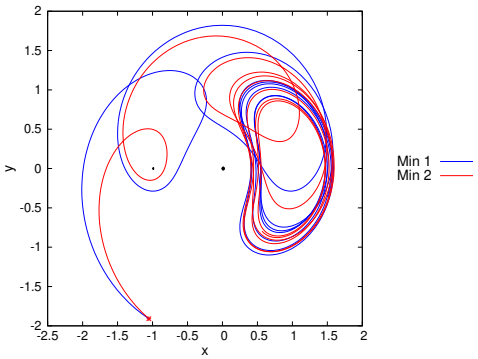

Figure 4.7: Left, values of the initial conditions in the FCs of Figure 4.6, that after N_T BCP periods lay on the position of the asteroid at May 1, 2007, (it=14), and the Δv required for each of them. Right, simulation of the capture of the asteroid by the trajectories in the minimum distance areas of the third FC when applying the obtained Δv. The Earth is included as a black circle of corresponding radius, and the initial position of the asteroid as a red star.

First, we discuss the situation where the asteroid has not still entered the Earth-Moon system. Regardless of the temporal section applied, the obtained colour maps corresponding to fundamental cylinders of the inner tori in the family, are very similar to those presented in Figure 4.2, with some variations in the required Δv. This is in good agreement with the temporal continuity of the minimum distance areas exposed in Section 4.2.1.

Notice that the fact that these minimum distance areas are present in the fundamental cylinders of inner tori covering a time span of more than three months and different temporal section, implies a long continuity in time of these possibilities of capture, which is good. The reason for this to happen is that the trajectories in the stable invariant manifolds that are far from the Earth and the Moon, are orbiting the Earth-Moon system while approaching it, the same behaviour is shown by the asteroid before entering the system. Therefore, the trajectory of the asteroid and the trajectories on the stable manifolds of L_3 are continually meeting before finally entering the system, where they may behave differently.

In fact, such a long temporal continuity is not found for any of the other minimum distance areas corresponding to epochs in which the asteroid is inside the system. What we have observed for these epochs is a decrease in the required Δv, being in many cases even lower than 200 m/s. However, for these new temporal sections, less possibilities are available for the epochs in with the asteroid is leaving the system.

Finally, we present two cases, the first one concerns to the lowest Δv found for the epochs in which the asteroid has not entered yet the system, and the second one is devoted to an example of relative low Δv when the asteroid is already inside the system.

A very cheap transfer

If we look closely to the maps in Figure 4.2, we can observe that in the minimum distance areas, the trajectory corresponding to the one that lays on the position of the asteroid is placed, roughly speaking, in the centre of zone, however, when we look at the same colour maps coloured according to the Δv, we see that the minimum value of Δv for those areas is not placed at their centres. It happens that half a period after epoch it=3, the minimum in distance and the minimum in Δv more or less overlap for the first two minima of the six observed, leading to trajectories that require less than 20 m/s for the capture.

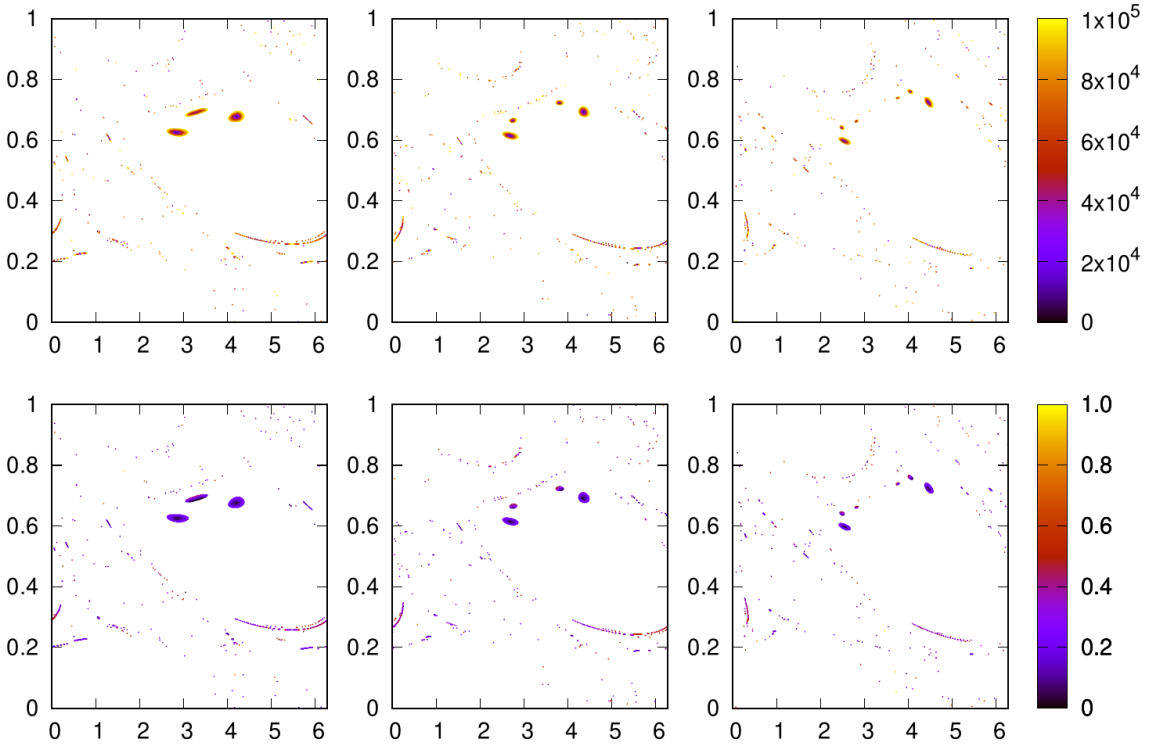

Figure 4.8: Three fundamental cylinders of tori at different distances from L_3 between 0.02159 and 0.03947. Plots in the first row show the FCs coloured according to the distance to the asteroid $T/2$ after position it=3, in km. Plots in the last row show the same FCs this time coloured according to the instantaneous Δv in km/s.

	Min 1			
dist to L_3	N_T	θ	τ	Δv (m/s)
0.02159	4	2.856	0.626	19.398
0.02738	4	2.693	0.615	19.386
0.03947	4	2.555	0.597	19.338
	Min 2			
dist to L_3	N_T	θ	τ	Δv (m/s)
0.02159	4	4.224	0.678	19.338
0.02738	4	4.373	0.693	19.293
0.03947	4	4.472	0.725	19.176

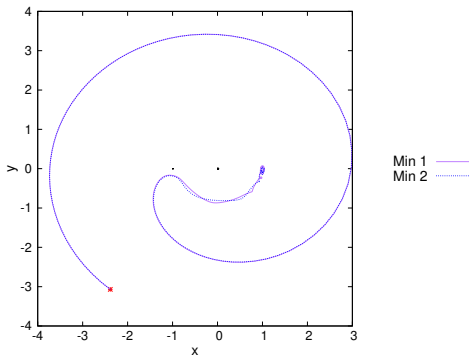

Figure 4.9: Left, values of the initial conditions in the FCs of Figure 4.8, that after N_T BCP periods lay on the position of the asteroid at June 25, 2006, (half a period after it=3) and the Δv required for each of them. Right, simulation of the capture of the asteroid by the trajectories in the two bigger minimum distance areas on the third FC when applying the obtained Δv. The Earth and the Moon are included as black circles of corresponding radius, and the initial position of the asteroid as a red star.

In Figure 4.8 we show some fundamental cylinders of tori close to L_3, at distances from 0.02159 to 0.03947. The first three maps are coloured according to the distance between the position of the asteroid at the 25 of June of 2006 (half a period after epoch it=3) and the trajectories in the stable manifolds at the temporal section $T/2$; the other three colour maps are coloured according to the difference between velocities. It is easy to observe that the required Δv has decreased significantly for the first bigger minima, but not for the other four. Figure 4.9 (left) contains the table with the data for the initial conditions in the FCs, corresponding to those two minima, that leads to the trajectories laying on the position of the asteroid, together with the trajectories described by the asteroid, forward in time, after adding the velocity impulse of the third presented fundamental cylinder. These trajectories not only require a very low Δv but also do not come close to any of the primaries, suggesting a safe and very cheap journey for the asteroid.

A last example

Figure 4.10 shows some fundamental cylinders for tori at distances from L_3 between 0.44160 and 0.53075. In the first three plots, the initial conditions are coloured according to the distance between the position of the asteroid at the 14 of October of 2006 (a quarter of period after epoch it=7) and the trajectories in the stable manifolds at temporal section $T/4$; the other three maps correspond to the same FCs, now coloured according to the difference between their velocities. Two minima are found, for one of them, the Δv increases with the distance to L_3, and for the other one, it decreases. As before, we have refined trajectories near these minima that arrive exactly to the asteroid, the results are collected in Figure 4.11, left. At the right of this figure, the trajectories corresponding to the integration of the asteroid forward in time, after adding a velocity impulse to reach the third fundamental domain are also included. In this last example, the asteroid is so close to the family of tori around L_3 that the trajectories are pretty short.

4.3 Conclusions about the capture

This chapter presents a strategy for capturing a NEA in a neighbourhood of the L_3 point of the Earth-Moon system. It is based on the use of stable invariant manifolds of invariant tori around L_3 of the planar Bicircular Earth-Moon system. To compute the manifolds we first obtain a high order approximation to them by combining jet transport and the parametrization method, and then we globalise them by means of numerical integration. This shows that a part of these manifolds exits the Earth-Moon system and then orbits the Sun in a trajectory close to that of the Earth around the Sun, which intersects the region of motion of NEAs. When these manifolds intersect with the position of a NEA, the difference between their velocities (Δv) gives the necessary manoeuvre to inject the NEA in the manifold so that it travels to the neighbourhood of L_3. For a NEA following an orbit similar to that of the Earth, this difference of velocities should not be very large.

We have applied this procedure to study the capture of the asteroid 2006 RH120. In general, several possibilities for the capture have been found, for the different positions of the asteroid and for the different temporal Poincaré maps applied to the stable manifolds. As expected, the Δv varies depending on the relative position of the asteroid with respect to the massive bodies in the system, being higher when the asteroid is inside the Earth-Moon system and significantly lower when it is still outside. In fact, one option for the capture that only requires a manoeuvre of less than 20 m/s has been analysed.

In addition, it has been observed that the possibilities for the capture vary continuously between nearby tori in the family and also depend continuously in time. This suggest that the dynamics below these opportunities is robust. Moreover, these continuities can be exploited to perform optimisation methods and reduce, even more, the required Δv.

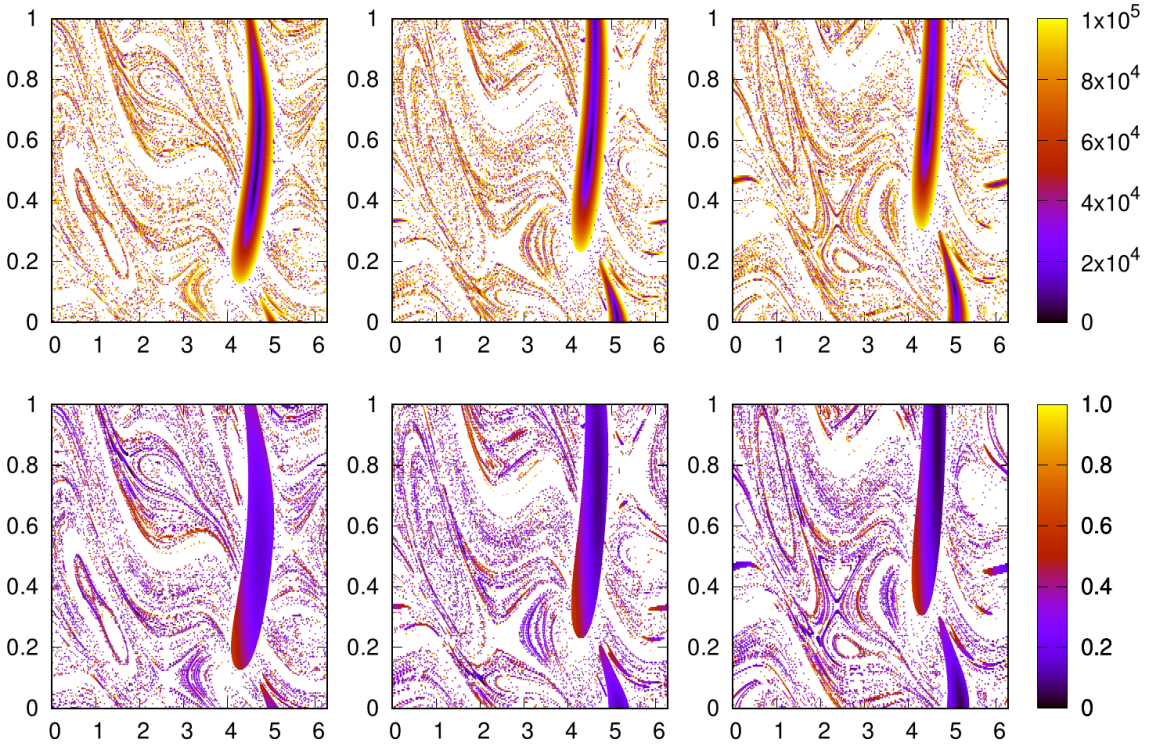

Figure 4.10: Three fundamental cylinders of tori at different distances from L_3 between 0.44160 and 0.53075. Plots in the first row show the FCs coloured according to the distance to the asteroid $T/4$ after position it=7, in km. Plots in the last row show the same FCs this time coloured according to the instantaneous Δv in km/s.

	Min 1			
dist to L_3	N_T	θ	τ	Δv (m/s)
0.44160	4	4.645	0.453	186.195
0.50037	4	4.517	0.560	204.122
0.53075	4	4.481	0.666	213.989
	Min 2			
dist to L_3	N_T	θ	τ	Δv (m/s)
0.44160	4	4.743	0.635	170.133
0.50037	5	5.137	0.026	148.754
0.53075	5	5.067	0.116	144.139

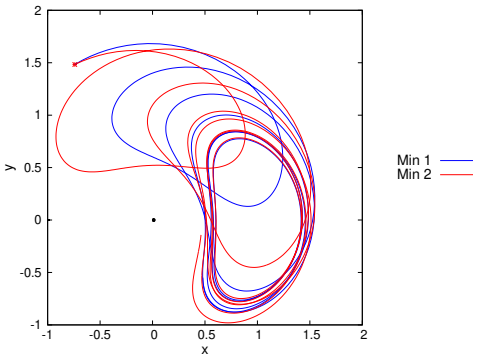

Figure 4.11: Left, values of the initial conditions in the FCs of Figure 4.10, that after N_T BCP periods lay on the position of the asteroid at October 14, 2006, (a quarter of period after it=7), and the Δv required for each of them. Right, simulation of the capture of the asteroid by the trajectories in the minimum distance areas on the third FC when applying the obtained Δv. The Earth is included as a black circle of corresponding radius, and the initial position of the asteroid as a red star.

We want to emphasise that this machinery is valid for studying the capture of any other asteroid or space debris with an orbit close to that of the Earth. It is also possible to use other families of quasi-periodic orbits as a target destination for the captured object, and it may also be a tool to analyse the deflection of NEAs (with an orbit close to that of the Earth) that pose a collision threat to the Earth.

It is worth to mention that some analysis have been done using the manifolds associated with the vertical family of quasi-periodic orbits around L_3 in the BCP, Section 3.4. In that case, we need to match the three positions of the asteroid (x, y, z) at the right time, however those manifolds are defined by just two parameters. Then, a way of overcome this difficulty is to add another condition, as for example, a third parameter that allows to move along the family to find the suitable torus for the capture. We saw that the possibilities for capture are given for those invariant curves with low z amplitude, as expected from Section 3.4, and we found that it is more difficult to recognise the areas of minimum distance since in this 3D system, many possible approaches turned out to be tangent to the position of the asteroid, and therefore, not useful for out purpose. For those reasons we do not include the results for that family in this dissertation.

Finally, let us comment on some extensions of this work. The next natural steps are to use three-dimensional quasi-periodic orbits of the 3D Bicircular model, to refine the transfer trajectory and the destination orbit near L_3 to a realistic model (for instance, based on the JPL ephemeris), and to consider the use of a low thrust propulsion system for the transfer manoeuvre.

Chapter 5

Some other contributions to BCP

This chapter is devoted to other two contributions to the Earth-Moon-Sun Bicircular problem we have carried out. First one is focused on the analysis of the unstable behaviour around the triangular points and the second one is about a family of stable invariant tori around the Moon.

As explained in Chapter 2, more particularly in Section 2.4, the triangular equilibrium points, L_4 and L_5 of the Earth-Moon RTBP, are replaced by three periodic orbits when the solar gravitational field is introduced as a time periodic perturbation of the Earth-Moon system. Two of the three periodic orbits are stable (*PO2* and *PO3*) and the other one is unstable (*PO1*). In Section 2.4.1, we show the family of invariant tori around *PO1*, see Figure 2.13, and their partially hyperbolic behaviour. Since, their instability is extremely weak ($\lambda_u < 1.3$ for the invariant tori in the family, see Figure 2.15), globalising their hyperbolic invariant manifolds using the standard linear approximation is not a feasible task. Recall that when we use the linear approximation for the invariant manifolds, their numerical propagation must start very close to the invariant curve and then, the integration time may be too long. In this particular case, the integration time of the trajectories in the manifolds when they are in the vicinity of the invariant curve is so long that the numerical errors start to accumulate before they leave this region. For this reason, in Section 5.1 we present the high order parametrization of the stable/unstable invariant manifolds associated with the invariant tori around *PO1* of L_4, what allows to start their globalisation far away from the family, showing their behaviour when leaving the L_4 vicinity. Notice that, due to the symmetries between L_4 and L_5, the analysis performed for L_4 can be extrapolated to the L_5 case.

The second section of this chapter, Section 5.2, concerns about stable invariant tori around the Moon in the BCP. They come from a family of stable periodic orbits around the Moon that can be found in the Earth-Moon RTBP. Their stability can be of interest for many purposes, like studying the lunar surface or to be used as parking orbits where to keep materials reservoirs for lunar missions or where to capture an asteroid. However, we will see that in the BCP this family is close to a resonance that favours the appearance of chaotic motion.

5.1 Unstable behaviour around triangular points

Most of the works focused on the study of the triangular points and their neighbourhood rely on their stability for many applications, regardless of whether these works are developed in the RTBP framework or in the BCP one. It must be noticed that stable behaviour is still dominant in the vicinity of these points in the BCP, where effectively stable regions are still found in spite of the appearance of an unstable dynamical substitute, see [Jor00]. In addition, due to the very mild instability of the

Invariant Curves			Invariant Manifolds			
			Stable		Unstable	
distance to $PO1$ of L_4	λ_u	$N_{k=0}$	$N_{k=16}$	$\bar{\sigma}_0$ from (1.53)	$N_{k=16}$	$\bar{\sigma}_0$ from (1.53)
4.93×10^{-4}	1.09864459	25	25	7.46×10^{-2}	25	8.77×10^{-2}
5.26×10^{-3}	1.09917517	25	25	7.00×10^{-2}	25	8.48×10^{-2}
0.011	1.10111040	25	25	6.63×10^{-2}	25	8.22×10^{-2}
0.014	1.10285521	25	65	6.46×10^{-2}	25	8.12×10^{-2}
0.019	1.10623723	25	65	6.22×10^{-2}	45	7.96×10^{-2}
0.029	1.12080462	25	65	4.58×10^{-2}	65	5.81×10^{-2}
0.054	1.20217907	31	91	4.02×10^{-2}	71	5.10×10^{-2}
0.066	1.25240803	46	86	4.51×10^{-2}	86	5.62×10^{-2}
0.073	1.27176712	55	115	4.84×10^{-2}	115	5.89×10^{-2}
0.078	1.28174818	85	145	4.98×10^{-2}	125	5.89×10^{-2}
0.081	1.28394365	146	226	5.00×10^{-2}	186	5.85×10^{-2}

Table 5.1: Values of the unstable eigenvalue (λ_u), the number of Fourier modes needed for the orders of the parametrizations 0 ($N_{k=0}$) and 16 ($N_{k=16}$) and the σ parameter such that the error of the parametrization of the stable and unstable invariant manifolds up to order $K = 16$ is below 10^{-14}, for invariant curves at different distances from the *PO1* of L_4.

invariant objects associated with *PO1*, it is not possible to study their hyperbolic behaviour using the standard linear approximation of the invariant manifolds, according to the explanation given at the beginning of this chapter.

In this dissertation we have presented how to compute the high order parametrization of stable and unstable invariant manifolds associated with invariant curves, therefore we have the knowledge and tools to overcome the main difficulty of studying the unstable behaviour around the triangular points and consequently, the present section is devoted to this aim.

The whole procedure to compute them is detailed in Section 1.4.3 and its application to the invariant manifolds of the horizontal family of invariant tori around L_3 is presented in Section 4.1.2. Therefore, here we limit ourselves to a brief exposition of the parametrization of the family of tori around *PO1* of L_4, since our aim is only to give a general view of the dynamics in this vicinity. Notice that the conclusions about the behaviour around *PO1* of L_4 can be extrapolated to the behaviour of the *PO1* of L_5, due to the symmetry that exists between them.

In this case, there is not a symmetry between the stable and unstable invariant manifolds of the same invariant object, as it occurs in the case of L_3. In fact, the stable (unstable) invariant manifolds of the invariant tori around the *PO1* of L_4 give us by the symmetry, the unstable (stable) invariant manifolds of the invariant tori around the *PO1* of L_5.

We compute the high order parametrization of the stable and unstable invariant manifolds of the invariant curves around *PO1* shown in Figure 2.13. The maximum order considered for the parametrization is again $K = 16$, as for the case of the manifolds associated with L_3, see the comments about the maximum considered order given in Section 4.1.2. Recall that the order 0 and order 1 correspond to the invariant curve and eigenfunction, respectively. Then, we start the computation of the parametrizing functions a_k for $2 \leq k \leq K$ following the Algorithm 1.4.3 and using the same number of Fourier modes than the number used for the computation of the invariant curves and its eigenfunctions. Again, we increase this number according to the criteria established in Section 4.1.2; if the Euclidean norm of the last two terms of b_2 are below a tolerance $tol_2 = 10^{-10}$ we increase the number of Fourier modes by 20, then this tolerance varies as $tol_m = 2tol_{m-1}$ for $m > 2$.

In Table 5.1, we show the number of Fourier modes that are needed to discretize the parametrizing

distances to to $PO1$ of L_4	$\|\sigma_0\|$ considered	divisions in θ	divisions in τ
10^{-4} - 6.5×10^{-3}	5.00×10^{-2}	500	200
6.5×10^{-3} - 0.011	5.00×10^{-2}	1000	200
0.011 - 0.014	5.00×10^{-2}	2000	200
0.014 - 0.029	2.50×10^{-2}	2500	200
0.029 -0.082	2.50×10^{-2}	5000	200

Table 5.2: Values of σ_0 and the number of divisions taken for the mesh of (θ,τ) to define the fundamental cylinders for the invariant curves depending on their distance to *PO1* of L_4.

function at order 16, a_{16}, of the stable and unstable manifolds of the family of invariant curves around *PO1*, and the value of $\bar{\sigma}_0$ from Equation (1.53), that corresponds to the maximum distance from the invariant curve at which we can consider that the error of the computed parametrization is below 10^{-14}. These values vary along the family of invariant curves, in order to identify the region of the family we use the distance to the *PO1* of L_4 introduced in Definition 2.4.1.

Notice that in general the parametrization of the unstable invariant manifolds require less Fourier modes than the parametrization of the stable ones. Also, the value of $\bar{\sigma}_0$ up to which we consider the approximation to be accurate enough is higher for the unstable than for the stable invariant manifolds parametrization. This suggests that the unstable manifolds suffer less wrinkling than the stable ones, as we will see.

The value of $|\sigma_0|$ that we have considered for the definition of the fundamental cylinders, of the stable and unstable manifolds, as well as the number of divisions taken along the angle $\theta \in [0, 2\pi]$ and the parameter $\tau \in [0, 1]$ are collected in Table 5.2. The selected values vary according to the distance to the *PO1* of L_4.

Once we define the fundamental cylinders we propagate a mesh of points on them, forward in time for those in the unstable manifolds, and backward in time for those in the stable manifolds. It is important to remember that the closer the invariant curves are to the *PO1* of L_4, the weaker is its instability, see Figure 2.15. This affects to the invariant manifolds, making that for those associated with invariant curves closer to the *PO1* of L_4, it takes more time to go far away from the vicinity of L_4. For this reason we use again the the growth of the derivative of the trajectory w.r.t. the initial condition, sometimes called expansion factor, to have an idea of the error propagation due to the instabilities of the problem, as we did in Chapter 4. Then, we show the behaviour of the manifolds when this factor for the trajectories in their fundamental domains is lower than 10^9.

In Figure 5.1 the stable and unstable invariant manifolds, along with the invariant curve they belong to, are shown projected in the xy-plane. The invariant curve in that figure is at a distance to the *PO1* of L_4 of 3.7202×10^{-3} (corresponding to an unstable eigenvalue $\lambda_u = 1.09890577$). In spite of using the high order approximation of the invariant manifolds, that allows to start their globalisation far from the invariant curve ($|\sigma_0| = 5.00 \times 10^{-2}$), it takes tens of Earth-Moon revolutions to make them grow as they are shown in the first image of the figure. The three images are separated in time five Earth-Moon revolutions. It is easy to see that as time evolves, the invariant manifolds (stable and unstable) come back towards the invariant curve. It seems like the stable and unstable invariant manifolds connect, suggesting homoclinic connections, however, we must keep in mind that these images correspond to a projection in two dimensions of four-dimensional trajectories, plus the time dependence.

Figure 5.2 is similar to the previous one, now for an invariant curve at a distance of 8.2050×10^{-3} to the *PO1* of L_4 (at which corresponds an unstable eigenvalue of 1.09996271). In this case we can see how the invariant manifolds start to take a shape different from the shape of the invariant curve as they grow far away from it.

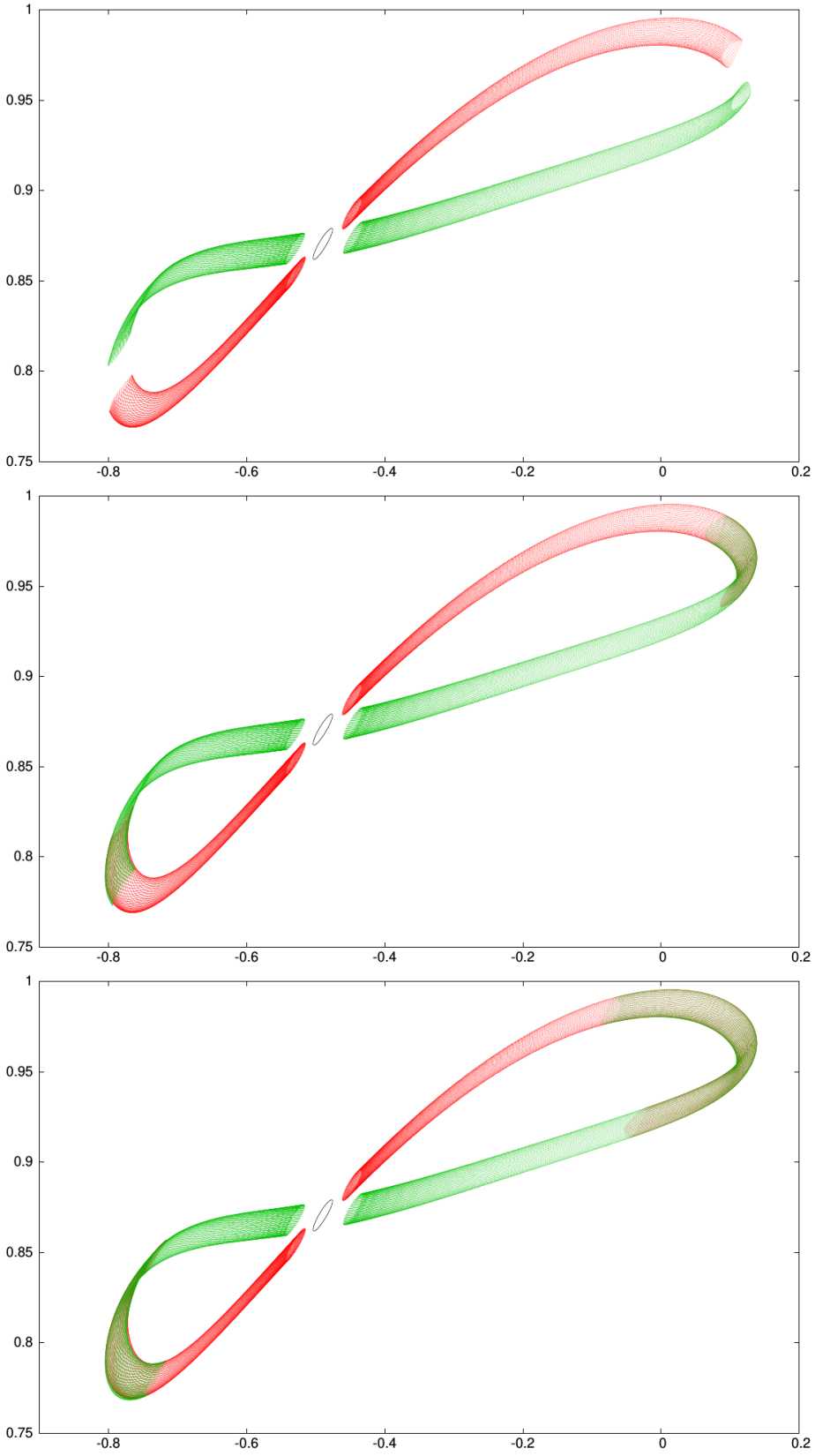

Figure 5.1: Invariant manifolds in the xy-plane of the curve at a distance to the *PO1* of L_4 of 3.7202×10^{-3} at different times. Stable manifolds in green, unstable in red. The curve is also included in black.

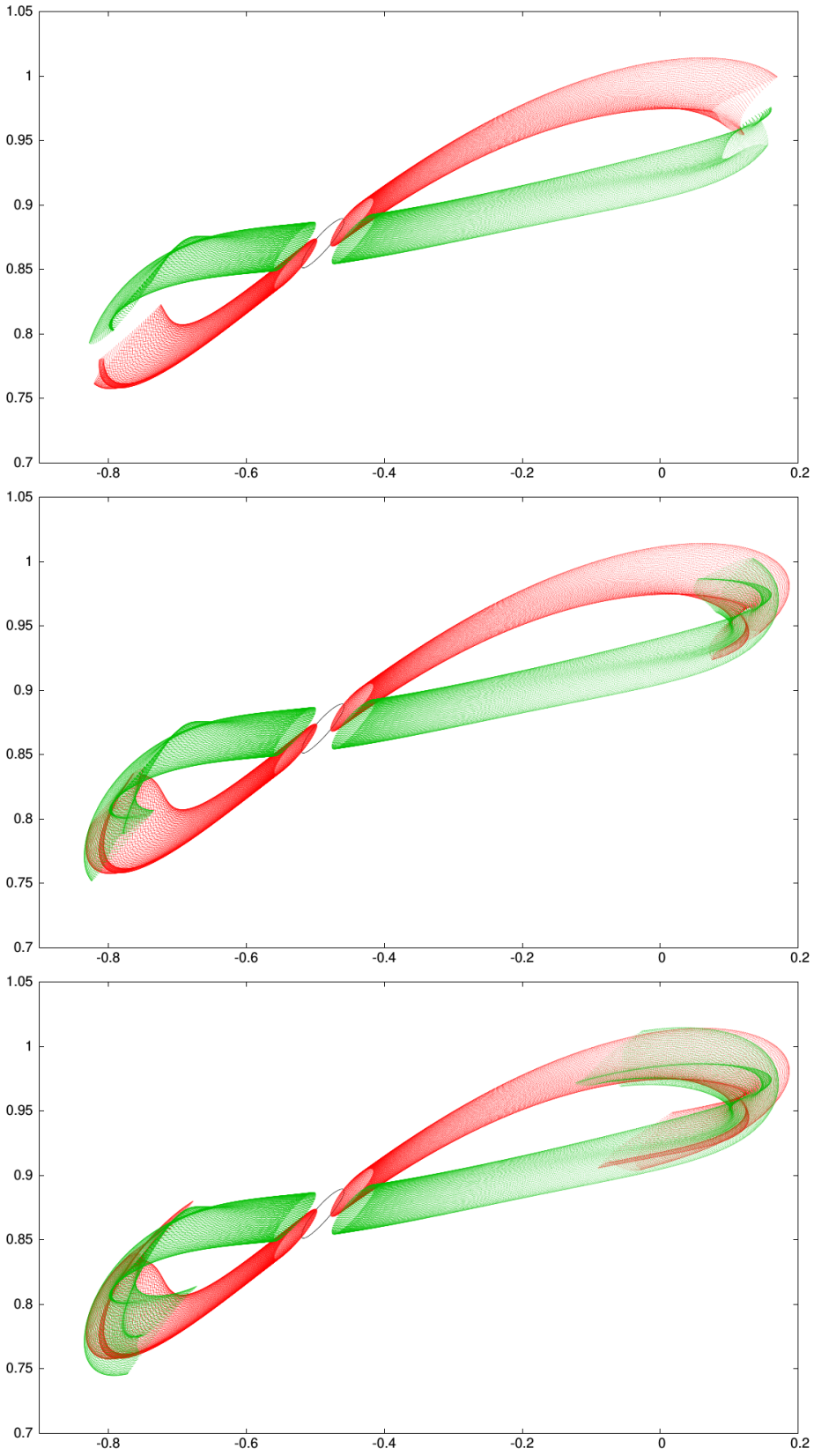

Figure 5.2: Invariant manifolds in the xy-plane of the curve at a distance to the *PO1* of L_4 of 8.2050×10^{-3} at different times. Stable manifolds in green, unstable in red. The curve is also included in black.

As the distance to the *PO1* of L_4 increases, also does the instability of the invariant curves and escaping the vicinity of L_4 becomes easier. In Figure 5.3 we present two images corresponding to the invariant manifolds associated with an invariant curve at a distance of 1.2579×10^{-2} (corresponding to $\lambda_u = 1.10187690$). The first image shows the propagation of the manifolds, and in the image below we show a cut of those manifolds, corresponding to the curves at $\tau = 1$ in the fundamental cylinder after the same propagation time, so the plots are closed curves, one for each manifold. This image is included in order to stress how the shape of these manifolds changes. This shape starts being close to a circle and it deforms appearing some "peaks" that correspond to the trajectories that are able to leave the region of L_4. Notice that the peaks of the stable manifolds are more pronounced than those of the unstable ones. This is related to the wrinkle effect mentioned above.

In fact, if we now analyse the colour maps corresponding to fundamental cylinders of the same invariant manifolds shown in Figure 5.3, and colour each initial condition according to their fate for a globalisation of the manifolds satisfying that the expansion factor is small enough, we see that none of the trajectories in the unstable invariant manifolds associated with that invariant curve is able to leave the vicinity of L_4, meanwhile some of the trajectories in the stable manifolds are. In Figure 5.4 we include the fundamental cylinders of those stable manifolds, coloured according to their origin. The meaning of the colours is the same as in previous chapters, purple for reaching the Earth, red for reaching the Moon, yellow for reaching the outside system (that is, being at more than 10 Earth-Moon lengths from the origin). Now the trajectories that do not reach any primary nor escape the system are not included, since they constitute the vast majority of the possible trajectories and it would not be convenient to colour them in black as we did for the L_3 case.

We see in Figure 5.4 that there are sets of trajectories in the stable manifolds that reach the Moon (red colour). They are disposed in "V" shape, in agreement with the plots in Figure 5.3. However, colouring the trajectories according to their fate does not allow to distinguish all the trajectories in those FC that are able to leave the L_4 vicinity. That is, we observe that most of the trajectories in the manifolds do not reach any of the primaries nor the outside system, but this does not mean that these trajectories remain in the vicinity of L_4. In order to identify all the trajectories that leave this vicinity, regardless their fate, we colour the trajectories in those CF according to the number of crosses to the x-axis they perform, see Figure 5.5. Note that only those trajectories that cross at least once the x-axis are included.

For those trajectories that leave the vicinity of L_4 but do not reach any primary nor escape, we find different behaviours, among them it is interesting the kind of trajectory like the one shown at the left of Figure 5.6. Its behaviour recalls to that of the Hilda asteroids in the Sun-Jupiter system [DBDO05], with the difference that in this case the primaries are the Earth and Moon. The trajectory on the right of that figure, shows a trajectory that leaves the vicinity of L_4 through a stable manifold, surrounds the vicinity of L_3 and then reaches the Moon.

Since the invariant curves around *PO1* of L_4 are more unstable as they are further from this periodic orbit, for invariant curves disposed further than the one corresponding to Figure 5.4, it is feasible to show the fundamental cylinders of both, the stable and unstable invariant manifolds coloured according to their fate; origin for the stable manifolds and destination for the unstable ones. In Figures 5.7 and 5.8 we show colour maps for curves at different distances from the *PO1* of L_4.

It is clear that most of the trajectories in these manifolds describe motions in which no primary is reached and only some of them are able to reach the Moon and the outside system, but in general they do not reach the Earth.

To finish this section, it is worth to mention that due to the shape of these manifolds, specially when they leave the vicinity of L_4, to use them for the capture of an asteroid as we did in Chapter 4 using the manifolds of tori around L_3, is not convenient. In fact, we followed the strategy presented in Section 4.1, however, when the sets of trajectories in the FC that approach the position of the asteroid were identified, we found that the Newton method used to compute the trajectory that lies

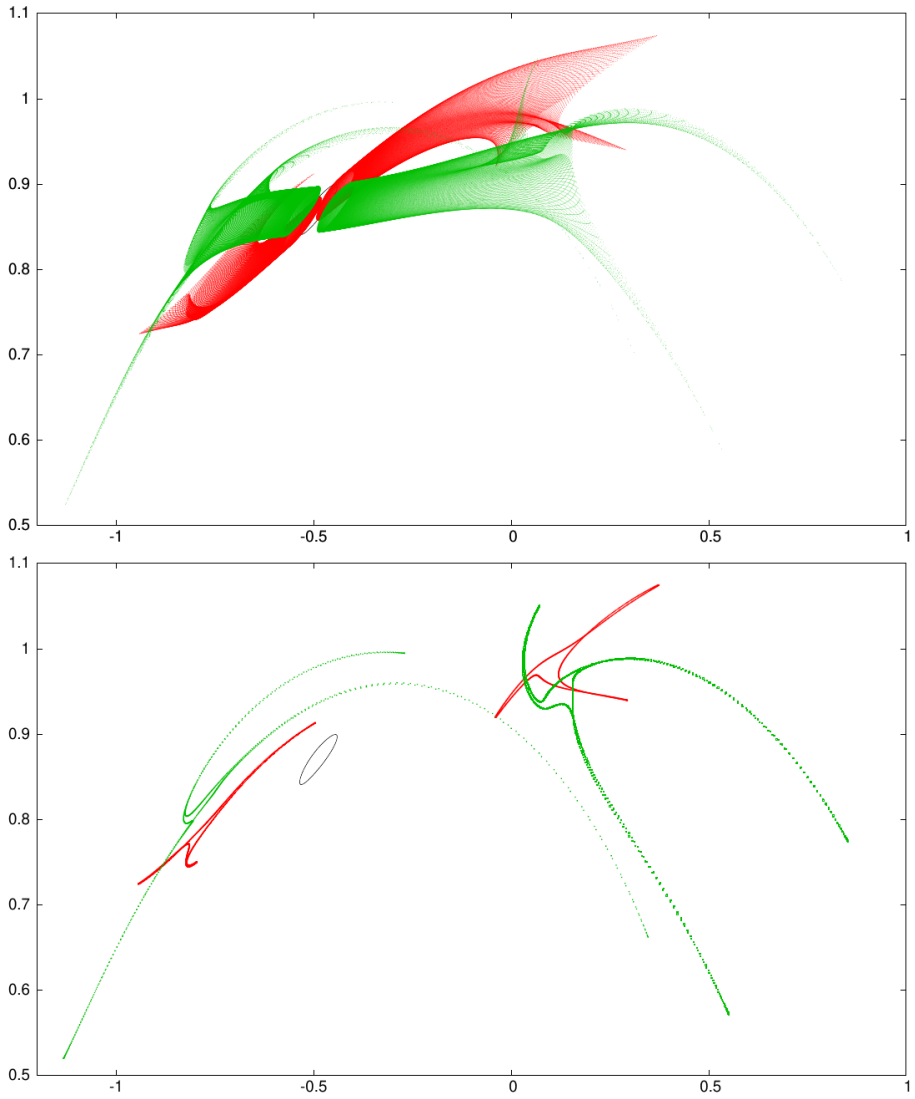

Figure 5.3: Invariant manifolds in the xy-plane of the curve at a distance to the *PO1* of L_4 of 1.2579×10^{-2}. Above, the propagation of the manifolds up to a certain time. Below, a cut on the manifolds corresponding to $\tau = 1$ after the same propagation time as above. Stable manifolds in green, unstable in red. The curve is also included in black.

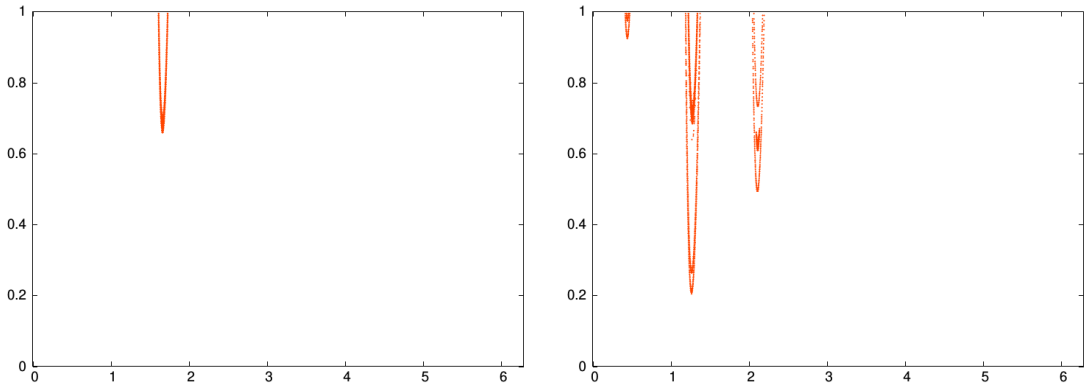

Figure 5.4: Fundamental cylinders of the stable invariant manifolds for an invariant curve of the horizontal family at a distance to the *PO1* of L_4 of 1.2579×10^{-2}, coloured according to their origin. See the text for more details.

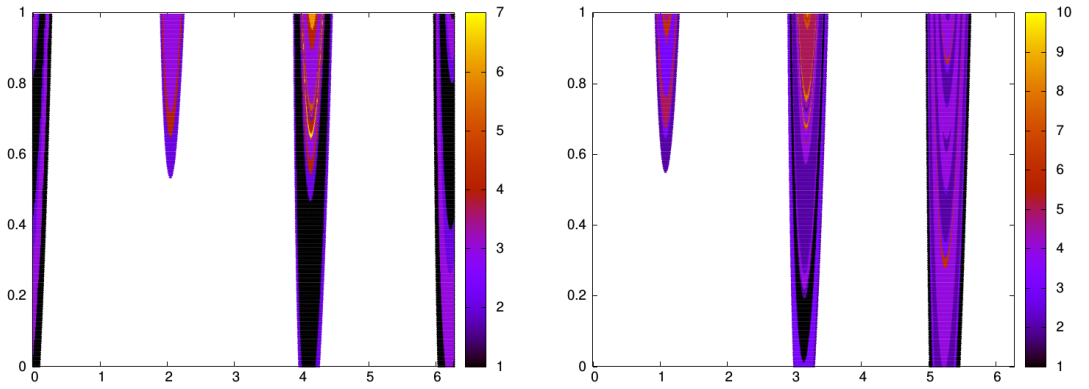

Figure 5.5: Same fundamental cylinders than in Figure 5.4, now coloured according to the number of crosses to the x-axis they perform. Only those trajectories that cross the x-axis at least once are included.

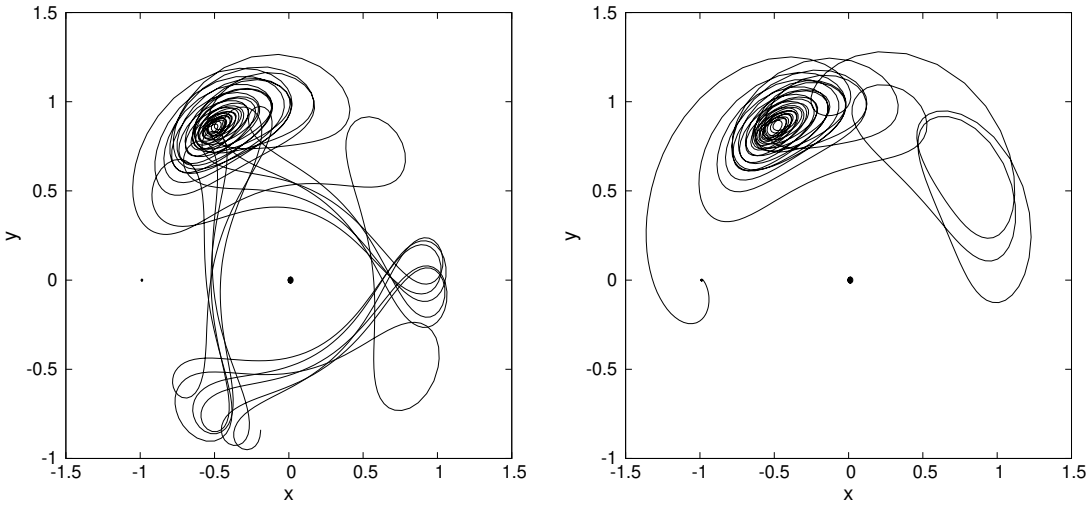

Figure 5.6: Two trajectories governed by quasi-periodic solutions near the *PO1* of L_4

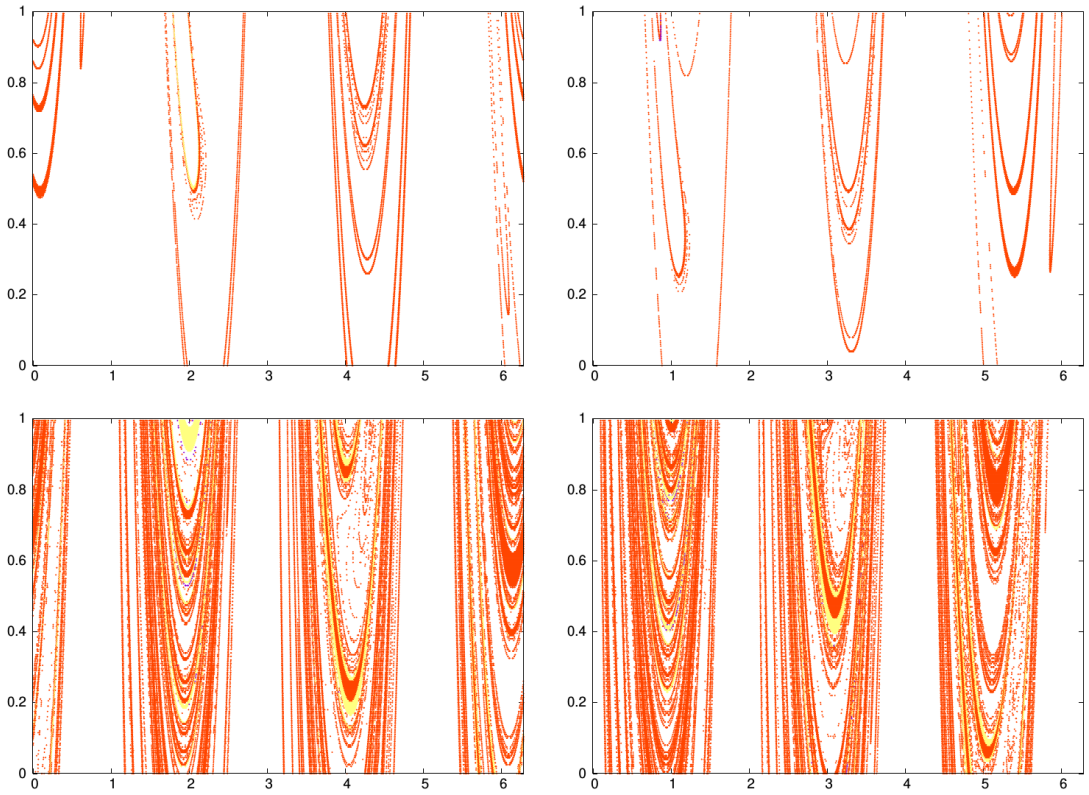

Figure 5.7: Fundamental cylinders of the invariant manifolds for an invariant curve of the horizontal family at a distance to the *PO1* of L_4 of 4.4071×10^{-2}, coloured according to their fate. Up, the unstable manifolds, down, the stable ones.

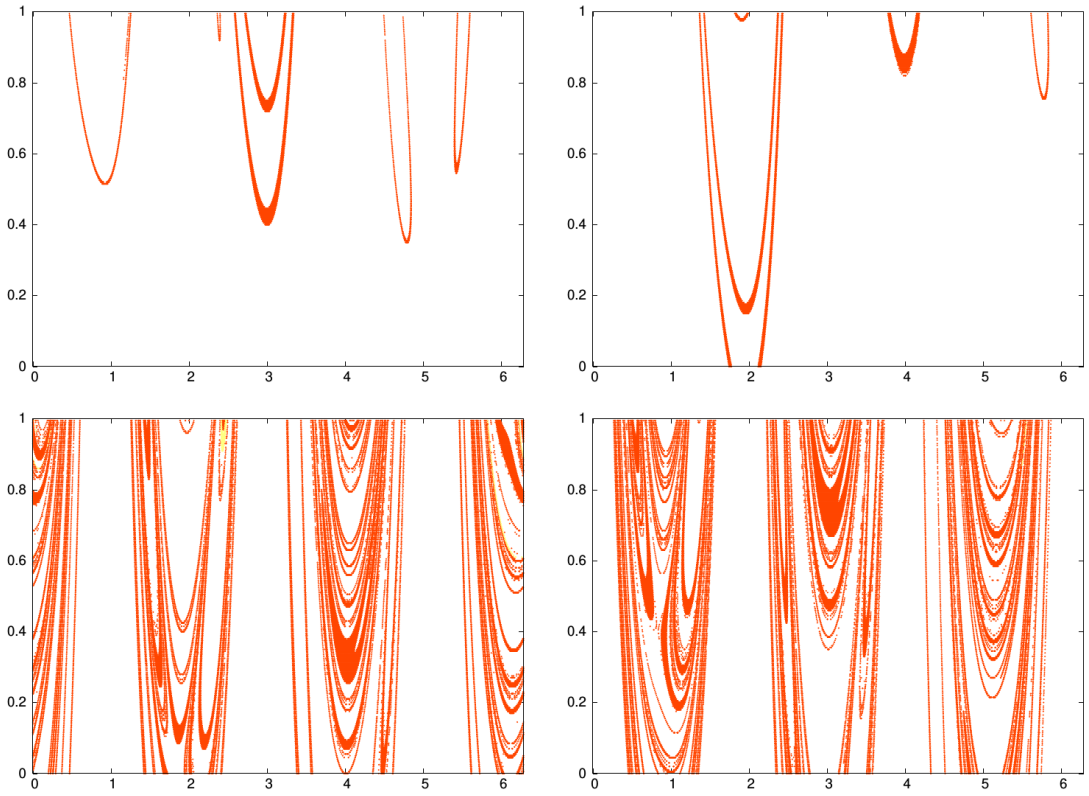

Figure 5.8: Fundamental cylinders of the invariant manifolds for an invariant curve of the horizontal family at a distance to the *PO1* of L_4 of 6.0390×10^{-2}, coloured according to their fate. Up, the unstable manifolds, down, the stable ones.

at the exact position and time of the asteroid did not converge in the vast majority of the cases. The reason is that the trajectories in the FC of tori around the *OP1* of L_4 that approximate the position of the asteroid, do it in a tangent way, not surrounding the position of the asteroid. Consequently, there is not a trajectory in those sets that approaches as much as we want the position of the asteroid allowing the capture.

5.2 Invariant tori around the Moon

In the RTBP many families of periodic orbits are found. Be them around the equilibrium points, around one of the primaries or around the two primaries. In particular, there is a family of retrograde periodic orbits around the Moon, contained in the horizontal plane, that in the bibliography is usually called *Family C of retrograde periodic orbits*, [Bro68]. This family is stable, what makes it suitable for many purposes like performing physical measurements or just to be employed as lunar parking orbits where to capture an asteroid or to keep materials for some mission in the Moon.

When adding the time-periodic perturbation due to the gravitational field of the Sun, these periodic orbits become two-dimensional invariant tori meanwhile generic non-resonance and non-degeneracy conditions are satisfied. Then, in this section we are interested in the analysis of the invariant tori around the Moon in the Earth-Moon BCP under the gravitational effect of the Sun. To this end, we first obtain the family of periodic orbits around the Moon in the Earth-Moon RTBP, and then we continue them to the BCP model through the parameter ε, that allows to introduce little by little the

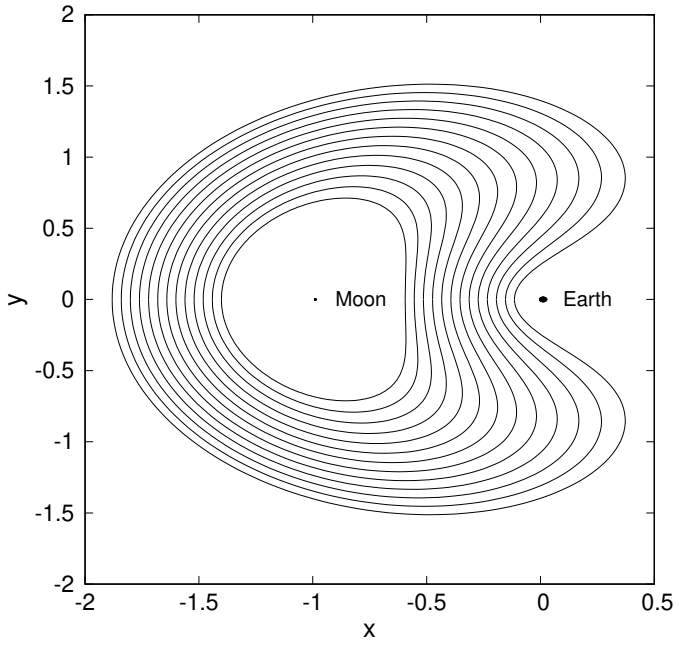

Figure 5.9: Family of retrograde periodic orbits around the Moon in the Earth-Moon RTBP.

gravitational effect of the Sun,

$$H_\varepsilon = H_{RTBP} + \varepsilon \hat{H}_{BCP}, \tag{5.1}$$

similarly as what we did to find the dynamical equivalents of the equilibrium points in the BCP in Chapter 2.

In Figure 5.9 the *family C* around the Moon in the RTBP is shown. Each of these periodic orbits is identified by an energy level and by a frequency, that we denote by ω_{RTBP}. As natural, for inner periodic orbits, this frequency is larger, see Figure 5.10. In order to compute the invariant tori that come from these periodic orbits when the time-periodic perturbation is added, we use again the temporal Poincaré map, P, corresponding to the period of the Sun in the BCP and look for the resulting invariant curve in the map to satisfy the invariance condition, see Section 1.4.1. For these reason in Figure 5.10 we add the value of the rotation number that the periodic orbits have if we look at them in the map P,

$$\rho = 2\pi \left(\frac{\omega_{RTBP}}{\omega_s} - 1 \right). \tag{5.2}$$

Notice that we subtract 2π to the typical expression of the rotation number (see Chapter 1) in order to avoid have values of ρ larger than 2π. Also, note that the rotation numbers shown in Figure 5.10 cross the value equal to 1, what indicates that there is a resonance between these orbits and the natural frequency of the problem.

Then, we use the periodic orbits in the unperturbed system and their frequencies to find the corresponding invariant tori in the BCP by computing invariant curves of the Poincaré map P as ε in Equation (5.1) goes from zero to one. Here, we must realise that the periodic orbit of the RTBP, i.e. when $\varepsilon = 0$, is also seen as an invariant curve in the Poincaré map P. For the computations we discretise the invariant curves of the RTBP in terms of Fourier series and follow the procedure explained in Section 1.4.1.

In this particular case the continuation of these invariant objects of the RTBP to the BCP presents difficulties, probably due to the fact of being so close to a resonance. Moreover, we will see that the shape of the resulting invariant curves in the BCP is significantly different from the shape of the

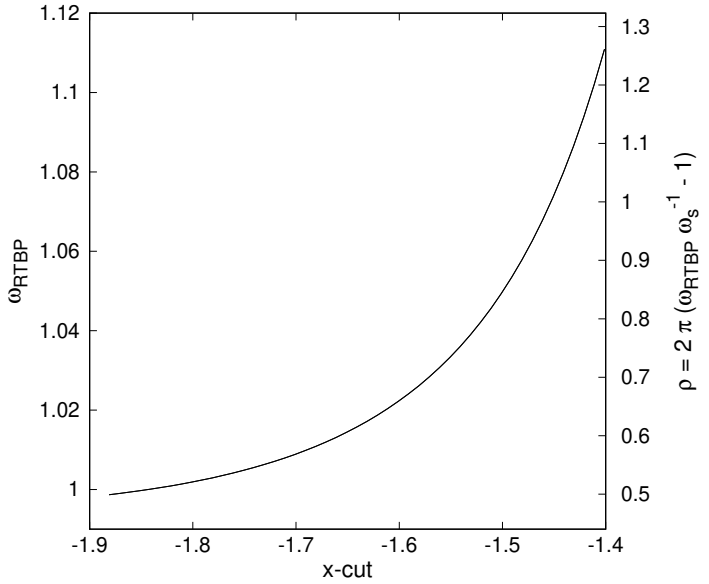

Figure 5.10: Variation of the frequency of the periodic orbits of the *Family C* in the Earth-Moon RTBP, ω_{RTBP}, according to the cut on the x-axis the periodic orbits in Figure 5.9 perform at the left of the Moon. The second vertical axis corresponds to the rotation number they have in the Poincaré map P.

periodic orbits they come from. Then, the continuation in ε of one periodic orbit to the corresponding invariant curve in the BCP needs to be performed using a small step of continuation and giving good enough seeds for the Newton method defined in Section 1.4.1. In this case we keep the value of ρ fixed, therefore the rotation number is not an unknown of the linear system we need to solve and we only need to add one extra equation to have uniqueness of solution. We have force the y coordinate of the curve to be zero when the angle θ is zero,

$$\varphi_y(\theta = 0) = 0.$$

To be more precise, we use the Fourier series of the invariant curve corresponding to the periodic orbit of the map P in the RTBP ($\varepsilon = 0$) to find the invariant curve at $\varepsilon = 0.01$. Then, we use this two curves to give a precise seed to compute the invariant curve at $\varepsilon = 0.02$, and with these three we compute the corresponding invariant curve at $\varepsilon = 0.03$. From that value we perform the continuation in ε with a step of 0.01 using the discretizations of the previous four invariant curves up to obtain the one in the BCP model ($\varepsilon = 1$). The periodic orbits are approximated by Fourier series with $N = 57$ Fourier modes. As the value of ε increases, the number of modes is also increased when needed as we have done previously.

In Figure 5.11 we show some of these invariant tori in the BCP in the stroboscopic map P, i.e. the invariant curves, along with the periodic orbits of the RTBP they come from. It is clear that the shape of the curves is affected by the perturbation due to the Sun gravitational field, making them to approach the Earth. In Table 5.3 more information about these tori, identified by the colour, is given. In particular, their rotation number and the value of the x coordinate when $y = 0$ at the right of the Moon. The number of Fourier modes needed to discretize the periodic orbit ($N_{\varepsilon=0}$) and the corresponding the invariant torus in the BCP ($N_{\varepsilon=1}$) are also included to show that about the double of modes are needed for the tori. Looking at the values of ρ and the x-cut, we can say that the inner curves of the ones presented approach the resonance and that the outer curves approach the Earth. For these reasons the continuation of these invariant tori becomes really sensitive.

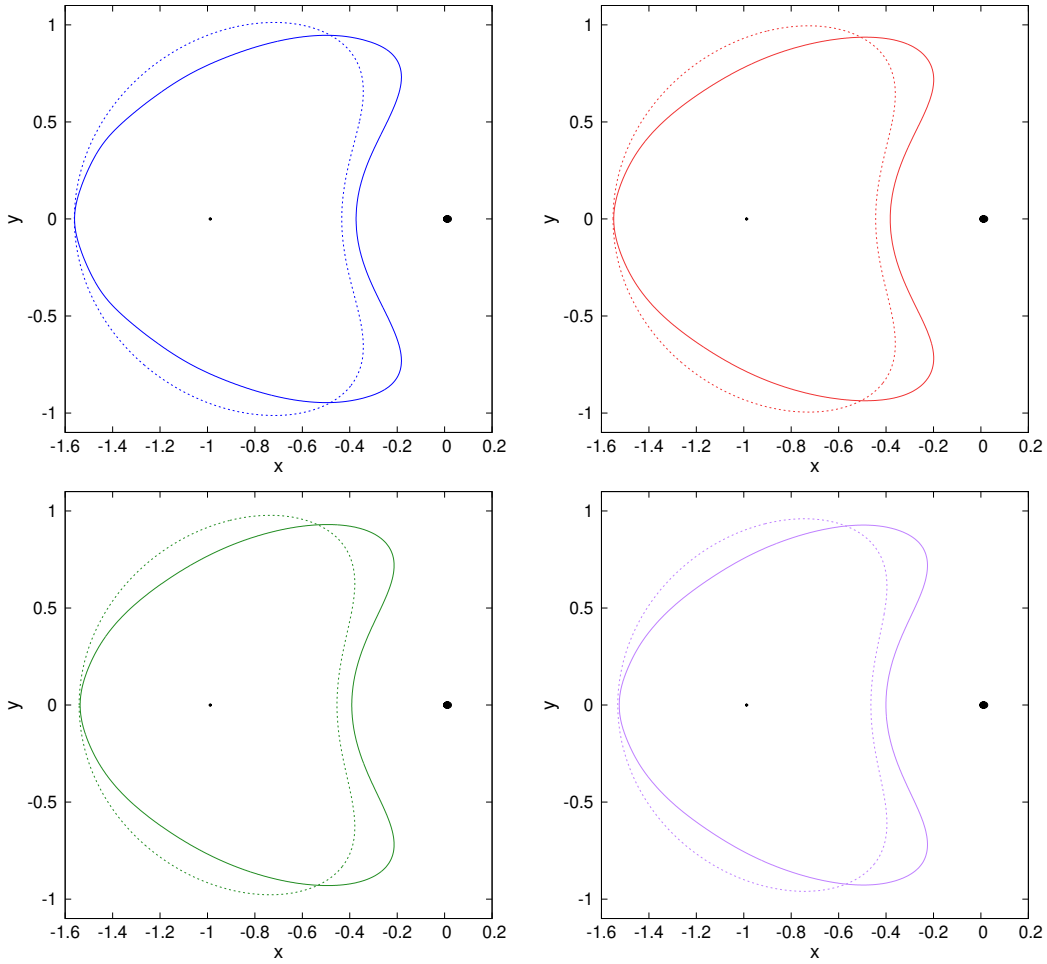

Figure 5.11: In dashed line, some periodic orbits of the RTBP ($\varepsilon = 0$). In continuous line, the resulting invariant curves in P in the BCP ($\varepsilon = 1$). The colour identifies each periodic orbit with the corresponding invariant curve. The Earth and Moon are included as black circles of corresponding radius.

	PO	Invariant curve		
				x-cut between
colour	$N_{\varepsilon=0}$	$N_{\varepsilon=1}$	ρ	Earth and Moon
blue	57	136	0.71636	-0.3732997
red	57	107	0.73368	-0.3824480
green	57	117	0.75236	-0.3914972
purple	57	98	0.77251	-0.4005613

Table 5.3: Values of the number of Fourier modes used to approximate the periodic orbits, PO, ($N_{\varepsilon=0}$) and the corresponding invariant curves ($N_{\varepsilon=1}$), along with the values of the rotation number (ρ) and the cut of over the x coordinate at the right of the Moon, i.e. between Earth and Moon. These values correspond to the periodic orbits and tori shown in Figure 5.11, identified by the colour.

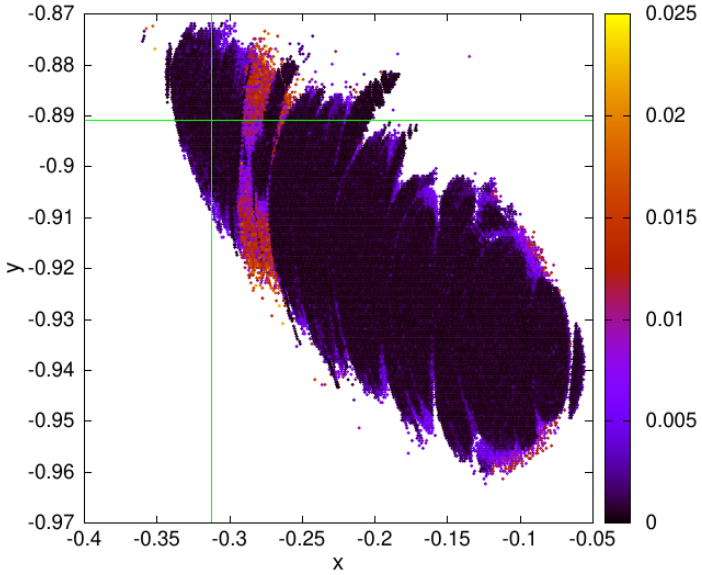

Figure 5.12: A neighbourhood of the invariant tori around the Moon coloured according to their Lyapunov exponent. In green, two lines to illustrate where the selected point on the curve is.

In order to illustrate that around these invariant curves there exits chaotic motion we analyse the Lyapunov exponent in a neighbourhood of one of them. More precisely, we take a point in the invariant curve of the map P plotted in green in Figure 5.11, and define a mesh of initial conditions around it, varying the x and y coordinates and maintaining p_x and p_y. The selected point on the curve, p_c, has coordinates (x, y, p_x, p_y):

$$p_c = (-0.312226578560269, -0.890844722802814, 0.645880857474948, -0.826791414257056).$$

Let us denote by x_0 and y_0 the x and y coordinates of this point. The mesh is composed by $800 \times 400 = 320000$ points, taken for $x \in [x_0 - 0.1, x_0 + 0.3)$ and $y \in [y_0 - 0.1, y_0 + 0.1)$ equispaced a distance of 5×10^{-4}. For each of these points in the mesh we compute an approximation of the Lyapunov exponent at every application of the map P until the variation between two consecutive applications of the map P is below 10^{-5}.

In Figure 5.12, we show these points coloured according to their Lyapunov exponent, also two lines in green are included, at $x = x_0$ and $y = y_0$, in order to show where the selected point on the curve (p_c) is. Looking at this plot it is clear why we have defined the mesh with a larger range for x than for y. Some dark regions are recognised, that correspond to stable motion, but they are disposed in a nearly stripe pattern, surrounded by points whose Lyapunov exponent is high, specially in the area corresponding approximately to $x \in (-0.3, -0.25)$. This behaviour of the Lyapunov exponent for close initial conditions, suggests chaotic motion in the neighbourhood of the invariant tori we have found around the Moon in the BCP.

This is just a preliminary and basic analysis of the chaotic behaviour close to these tori disposed around the Moon in the Earth-Moon bicircular system. An improvement of this analysis could be to implement more sophisticated tools like, for example the Mean Exponential Growth factor of Nearby Orbits (MEGNO), see [CS00], a technique that allows to recognise stochastic components of the phase space.

Chapter 6

High dimensional reducible tori on Poincaré maps

This chapter is devoted to the effective computation of the stable/unstable invariant manifolds of reducible invariant tori of any dimension

$$\varphi(\theta) : \mathbb{T}^d \mapsto \mathbb{R}^n \quad \text{with } \theta \in \mathbb{T}^d \text{ and } d \geq 1.$$

In this case we analyse quasi-periodic solutions of the same angular dimension as the number of basic frequencies of the system. That are the simplest invariant object that one can find in the discrete dynamical system. Then we omit the case in which $d = 0$, since this corresponds to the case of autonomous Poincaré maps where the simplest invariant object is a fixed point.

As announced in the first chapter, when the dimension of the quasi-periodic orbits is high it is often not feasible to find these solutions through the computational methods we have employed until now in this dissertation. It was also mentioned there that, if the dynamical system is reducible (see Definition 1.2.2), there are other very efficient numerical methods that allow to compute the torus jointly with the Floquet change of variables and the reduced Floquet matrix, B. It turns out that the reduced dynamical system is very suitable for its computational resolution in parallel, as [Olm07, JO09] proposed and carried out. These works are based on the proofs about the existence of such reduced quasi-periodic solutions presented in [JS96].

Our aim in this chapter is to extend the work [Olm07, JO09]. There, the authors develop an algorithm to obtain, at the same time and through parallel computation, reducible invariant tori in stroboscopic maps along with their Floquet transformation, what gives the linear behaviour around the tori. It is remarkable that the number of operations and storage requirements are proportional to $N \log N$ and N respectively, where N denotes the number of Fourier modes used to represent the torus. A side benefit is that the method has a high degree of parallelism so it can take advantage of modern computers.

In the present work, we extend the methods in [JO09] so that now: *i)* the method provides a high-order parametrization of the stable and/or unstable manifolds of the tori if they exist; *ii)* we implement a C code that runs in a computer with several processors between which the computations are done concurrently using OpenMP [DM98] instead of the PVM library [GBD$^+$95] used in [JO09].

On the one hand, we implement a parametrization method for computing the Taylor-Fourier expansion of the stable/unstable invariant manifolds of invariant tori. As we have seen in Section 1.3, to implement this parametrization method on a Poincaré map we need to estimate the high-order deriva-

tives of this Poincaré map, which requires to compute high-order derivatives of the flow of the ODE. Therefore, we make use again of the jet transport tool developed in [GJJC$^+$21], see Section 1.3.1, to obtain the high order derivatives of the flow in the map, similarly as we did in Section 1.4.3.

On the other hand, the use of parallel computing allows to reduce the total computational time by using several processors. The parallelization presented in [JO09] was implemented on a cluster of PCs (with a distributed memory), making use of the PVM library for the communications through an Ethernet network using a master-slave scheme. Therefore, there was always a penalty time to pay for those communications. For this reason, the reduction in temporal costs of the parallelization was relevant for a small number of processors, but at some point, this reduction stagnates. Nowadays, the processors involved in our parallelizations belong to the same computer (hence, with a shared memory), so there is not communication penalty between the threads. Both, the computation of the tori and their invariant manifolds are implemented in parallel.

This chapter is distributed as follows. In Section 6.1 we talk about the reduced system and briefly summarise the algorithm to compute the quasi-periodic orbits jointly with the Floquet change introduced in [JO09]. Section 6.2 is devoted to the development of the code to compute the high order parametrization of the stable/unstable invariant manifolds in terms of the Floquet change. Sometimes the instability of the quasi-periodic solutions is so strong that we can not apply previous algorithms directly and we need to combine them with multiple shooting techniques. This situation is faced in Section 6.3. In Section 6.4 we give some details about the computer implementation. And finally, Section 6.5 is focused on two applications of the presented methods; a forced pendulum and one of the Simplified Solar System Models (SSSM) presented in [GM01].

This chapter is a joint work with Dr. Gimeno, Prof. Jorba and Dr. Olmedo, collected in [GJNO21].

6.1 The reduced torus

Assuming the existence of a torus for system (1.12),

$$\begin{cases} \bar{x} = P(x, \theta), \\ \bar{\theta} = \theta + \rho, \end{cases}$$

with $\theta \in \mathbb{T}^d$ $d \geq 1$, that satisfies invariance condition (1.13),

$$\varphi(\theta + \rho) = P(\varphi(\theta), \theta),$$

and that is reducible (see Definiton 1.2.2), À. Jorba and E. Olmedo [JO09] developed an iterative method based on Newton iteration (quadratically convergent) for finding the torus and the Floquet change at the same time. For this, it is necessary to know suitable initial conditions for $\varphi(\theta)$ and $C(\theta)$ (namely $x_0(\theta)$ and $C_0(\theta)$ respectively), such that $C_0^{-1}(\theta+\rho)D_xP(x_0(\theta),\theta)C_0(\theta)$ is close to a constant matrix B_0. Lets suppose by now that these approximations are available. Then, residual magnitudes $y_0(\theta)$ and $Q_0(\theta)$ indicate the magnitude of the error of these approximations to the real solution.

$$y_0(\theta) = x_0(\theta + \rho) - P(x_0(\theta), \theta), \tag{6.1}$$

$$Q_0(\theta) = C_0^{-1}(\theta + \rho)D_xP(x_0(\theta), \theta)C_0(\theta) - B_0. \tag{6.2}$$

Then, the norm of these magnitudes is a small quantity of order, say ε. Let us take, for example, infinite norm, $||y_0||_\infty \approx \varepsilon$ and $||Q_0||_\infty \approx \varepsilon$.

The idea is to use the reducibility assumption for finding a better approximation of the invariant torus, and with it, to improve the Floquet change, iteratively until the precision of both parametrizations is good enough. As all details and proofs are carefully described in [JO09], very brief description of the procedure is given here.

Note that in the present work we assume that the torus exists and that it is real analytic. In [JS96] the proof of its existence is given for flows and it can be easily translated for maps, as long as some hypothesis are satisfied. First hypothesis is referred to the smoothness of the map. Second hypothesis is that some Diophantine conditions, involving the frequency vector ρ and the eigenvalues $\lambda_1, \ldots, \lambda_n$ of the matrix B_0 are satisfied. Concretely, it is assumed that there exist real constants $c > 0$ and $\gamma > d - 1$ such that

$$|\exp(\langle \kappa, \rho \rangle \mathrm{i}) - \lambda_j| > \frac{c}{|\kappa|^\gamma}, \qquad \forall \kappa \in \mathbb{Z}^d \setminus \{0\}, \quad j = 1, \ldots, n, \tag{6.3}$$

$$\left|\exp(\langle \kappa, \rho \rangle \mathrm{i}) - \frac{\lambda_j}{\lambda_l}\right| > \frac{c}{|\kappa|^\gamma}, \qquad \forall\, \kappa \in \mathbb{Z}^d \setminus \{0\}, \quad j, l = 1, \ldots, n, \tag{6.4}$$

where i denotes the complex unit, $\langle \cdot, \cdot \rangle$ the standard scalar product, and $|\kappa| = |\kappa_1| + \cdots + |\kappa_d|$. Note that condition (6.3) is satisfied if all the eigenvalues λ_j have modulus different from 1, and condition (6.4) is satisfied if all eigenvalues have different modulus. As at every step of the iterative procedure, the Floquet matrix changes, a non-degeneracy condition on the eigenvalues is needed. For this, it is common to make eigenvalues depending on parameters such that Diophantine condition holds at every iterative step. In practice, we do not need to verify this condition but what we have to do is to check if the left-hand side of (6.3) and (6.4) is small. This can be done indirectly by checking the size of the Fourier modes of the correction given by the Newton method is not too big.

Assuming all these hypothesis to hold and that $x_0(\theta)$ and $C_0(\theta)$ are available (with $||y_0||_\infty \approx \varepsilon$ and $||Q_0||_\infty \approx \varepsilon$), let us summarise the iterative scheme in [JO09] to find good approximations of the torus and of the Floquet change. The iterative scheme is divided in two steps. The first one focuses on computing a better approximation of the torus, and the second one, on improving the Floquet change and Floquet matrix.

Algorithm 6.1.1 (Computation of invariant torus, Floquet change, and Floquet matrix)**.**

- ⋆ ***Input:*** *Discrete system as* (1.12)*, initial guesses* $x_0(\theta)$*,* $C_0(\theta)$*, and* B_0*.*
- ⋆ ***Output:*** *Torus* $\varphi(\theta)$*, Floquet change* $C(\theta)$*, and Floquet matrix* B*.*

First step:

1. *Compute the error* $y_0(\theta) = x_0(\theta + \rho) - P(x_0(\theta), \theta)$*.*
2. *Compute the function* $g(\theta) = -C_0^{-1}(\theta + \rho) y_0(\theta)$*.*
3. *Find* u *that verifies* $u(\theta + \rho) = B_0 u(\theta) + g(\theta)$*. For this, we expand functions* g *and* u *in real Fourier series (the expansion can be done in complex Fourier series, but we work with real expansions in the computer programs):*

$$g(\theta) = \frac{g^{(0)}}{2} + \sum_{\kappa \neq 0} g_\kappa^{(c)} \cos\langle \kappa, \theta \rangle + g_\kappa^{(s)} \sin\langle \kappa, \theta \rangle,$$

$$u(\theta) = \frac{u^{(0)}}{2} + \sum_{\kappa \neq 0} u_\kappa^{(c)} \cos\langle \kappa, \theta \rangle + u_\kappa^{(s)} \sin\langle \kappa, \theta \rangle,$$

where $\kappa \in \mathbb{N}^d$ *and* $\langle \kappa, \theta \rangle = \kappa_1 \theta_1 + \cdots + \kappa_d \theta_d$*, and solve the following system to find Fourier coefficients* $u^{(0)}$*,* $u_\kappa^{(c)}$*, and* $u_\kappa^{(s)}$

$$\begin{aligned} (Id - B_0)\frac{u^{(0)}}{2} &= \frac{g^{(0)}}{2}, \\ (B_0^2 - 2\cos\langle \kappa, \rho \rangle B_0 + Id) u_\kappa^{(c)} &= (\cos\langle \kappa, \rho \rangle Id + B_0) g_\kappa^{(c)} - \sin\langle \kappa, \rho \rangle g_\kappa^{(s)}, \\ (B_0^2 - 2\cos\langle \kappa, \rho \rangle B_0 + Id) u_\kappa^{(s)} &= (\cos\langle \kappa, \rho \rangle Id + B_0) g_\kappa^{(s)} + \sin\langle \kappa, \rho \rangle g_\kappa^{(c)}, \end{aligned} \tag{6.5}$$

where Id *denotes the identity matrix.*

4. *Compute* $h(\theta) = C_0(\theta)u(\theta)$.

5. *Compute* $x_1(\theta) = x_0(\theta)+h(\theta)$, *that is the new approximation of the torus, such that* $||y_1||_\infty \approx \varepsilon^2$, *with* y_1 *defined like in (6.1).*

Second step:

1. *Compute the matrices* $R(\theta) = C_0^{-1}(\theta+\rho)D_x f(x_1(\theta),\theta)C_0(\theta) - B_0$, $\tilde{R}(\theta) = R(\theta) - Avg(R)$, *and* $B_1 = B_0 + Avg(R)$, *where* $Avg(R)$ *is the average of the map* $\theta \mapsto R(\theta)$, *that is,*

$$Avg(R) = \frac{1}{(2\pi)^d}\int_{\mathbb{T}^d} R(\theta)\, d\theta$$

   and B_1 *is the new approximation to the Floquet matrix.*

2. *Find the matrix valued function* H *that verifies* $H(\theta+\rho)B_1 - B_1H(\theta) = \tilde{R}(\theta)$. *For this, we expand* R *and* H *in real Fourier series:*

$$H(\theta) = \sum_{\kappa\neq 0} H_\kappa^{(c)}\cos\langle\kappa,\theta\rangle + H_\kappa^{(s)}\sin\langle\kappa,\theta\rangle,$$
$$\tilde{R}(\theta) = \sum_{\kappa\neq 0} R_\kappa^{(c)}\cos\langle\kappa,\theta\rangle + R_\kappa^{(s)}\sin\langle\kappa,\theta\rangle,$$

   and we solve the following system to find Fourier coefficients $H_\kappa^{(c)}$ *and* $H_\kappa^{(s)}$ *(note that* $H^{(0)} = 0$*)*

$$\begin{aligned}(H_\kappa^{(c)}\cos\langle\kappa,\rho\rangle + H_\kappa^{(s)}\sin\langle\kappa,\rho\rangle)B_1 - B_1H_\kappa^{(c)} = R_\kappa^{(c)},\\ (H_\kappa^{(s)}\cos\langle\kappa,\rho\rangle - H_\kappa^{(c)}\sin\langle\kappa,\rho\rangle)B_1 - B_1H_\kappa^{(s)} = R_\kappa^{(s)}.\end{aligned} \tag{6.6}$$

3. *Compute* $C_1(\theta) = C_0(\theta)(Id+H(\theta))$, *that is the new approximation of the Floquet transformation, such that* $||Q_1||_\infty \approx \varepsilon^2$, *with* Q_1 *defined like in (6.2).*

Once we have $x_1(\theta)$, B_1, *and* $C_1(\theta)$, *we keep on iterating until either the norms of* y *and* Q *are small enough or the differences between one step and the previous one are small enough.*

Note that the computation of each pair of coefficients $(u_\kappa^{(c)}, u_\kappa^{(s)})$ in (6.5) is independent for each κ. The same happens with for each pair $(H_\kappa^{(c)}, H_\kappa^{(s)})$ in (6.6). That makes these linear systems very suitable for their computational resolution in parallel. With this, the dimension of each linear system depends on the dimension of the phase space and the number of linear systems to be solved on the number of Fourier modes used. On the other hand, the evaluation of the map P and D_xP can be perform independently of each θ, which leads to a straightforward parallelization.

6.2 High order parametrization of invariant manifolds

Here we continue the explanations given in Section 1.3 for invariant tori that have associated stable/unstable invariant manifolds. There we write the invariant manifold of an invariant torus as a formal Taylor-Fourier expansion in terms of two parameters, a parameter to move in the hyperbolic direction $\sigma \in \mathbb{R}$ and the angle vector $\theta \in \mathbb{T}^d$, Equation (1.29)

$$W(\theta,\sigma) = a_0(\theta) + a_1(\theta)\sigma + \sum_{k\geq 2} a_k(\theta)\sigma^k,$$

where a_k are the functions, from $\mathbb{T}^d$ to $\mathbb{R}^n$, parametrizating the manifold at order k that depend on the angles along the torus. Again, here we consider the case in which σ is one-dimensional.

In the particular case that the system is Hamiltonian, the stable eigenvalue corresponds to the inverse of the unstable one. And, since many of the classical mechanical systems show a symmetry when inverting the time, sometimes it is possible to have both parametrizations, the stable and the unstable, by just computing one of them and applying the corresponding symmetry. Here, we are going to explain the general case, valid for Hamiltonian and non-Hamiltonian systems and without considering, in advance, any symmetry.

6.2.1 Computation of the invariant manifold

Following Section 1.3, the functions a_k are found by solving invariance condition (1.30),

$$P(W(\theta,\sigma),\theta) = W(\theta+\rho,\lambda\sigma),$$

order by order. Recall that the order 0 and order 1 correspond to the invariant torus and the eigenfunction that are obtained through the Algorithm 6.1.1 summarised in previous section. More precisely, we have obtained the eigenvectors of the Floquet matrix B. Then, if v is the eigenvector of B associated with λ, the eigenfunction a_1 of the torus is $C(\theta)v$. Recall that the torus and its eigendirection give the linear approximation to the invariant manifolds.

For the functions at any other order m, assuming the functions up to order $m-1$ are known, in Section 1.3 we arrive to the following expression,

$$b_m(\theta)\sigma^m + D_xP(a_0(\theta),\theta)a_m(\theta)\sigma^m = a_m(\theta+\rho)\lambda^m\sigma^m,$$

where we recall that b_m is a θ-dependent function at order m that comes from the image under P of the invariant manifold at order $m-1$.

This expression, that involves a non-sparse matrix $D_xP(a_0(\theta),\theta)$, is the one that we solve directly in the case of invariant curves (Algorithm 1.4.3 applied in Chapters 4 and 5). Now, the dimension of this matrix is too large to work with it. Then, we introduce a Floquet change looking for a rewrite of this system that allows its decoupling and parallel resolution as it was done for finding the invariant torus and Floquet transformation.

Let us write the last expression in terms of the Floquet change $a_m(\theta) = C(\theta)u_m(\theta)$,

$$b_m(\theta) + D_xP(a_0(\theta),\theta)C(\theta)u_m(\theta) = C(\theta+\rho)u_m(\theta+\rho)\lambda^m,$$

and multiply by $C^{-1}(\theta+\rho)$ on both sides, leading to

$$C^{-1}(\theta+\rho)b_m(\theta) + Bu_m(\theta) = u_m(\theta+\rho)\lambda^m. \tag{6.7}$$

Under the generic condition of non-resonance, detailed in the Lemma 6.2.1, (6.7) determines uniquely the function u_m, that gives a_m through the Floquet transformation. So, let us assume that $g_m(\theta) = C^{-1}(\theta+\rho)b_m(\theta)$ admits a (real) Fourier series expansion, that is,

$$g_m(\theta) = \frac{g^{(0)}}{2} + \sum_{\kappa\neq 0} g_\kappa^{(c)}\cos\langle\kappa,\theta\rangle + g_\kappa^{(s)}\sin\langle\kappa,\theta\rangle.$$

Then, we have to find the coefficients of another Fourier expansion

$$u_m(\theta) = \frac{u^{(0)}}{2} + \sum_{\kappa\neq 0} u_\kappa^{(c)}\cos\langle\kappa,\theta\rangle + u_\kappa^{(s)}\sin\langle\kappa,\theta\rangle,$$

such that (6.7) is satisfied. Imposing the equation (6.7) on the Fourier coefficients and using a Cramer-block method, we end up with the following linear system of cohomological equations depending on κ,

$$\begin{aligned}(\lambda^m Id - B)\frac{u^{(0)}}{2} &= \frac{g^{(0)}}{2},\\ (B^2 - 2\lambda^m\cos\langle\kappa,\rho\rangle B + \lambda^{2m}Id)u_\kappa^{(c)} &= (\lambda^m\cos\langle\kappa,\rho\rangle Id + B)g_\kappa^{(c)} - \lambda^m\sin\langle\kappa,\rho\rangle g_\kappa^{(s)},\\ (B^2 - 2\lambda^m\cos\langle\kappa,\rho\rangle B + \lambda^{2m}Id)u_\kappa^{(s)} &= (\lambda^m\cos\langle\kappa,\rho\rangle Id + B)g_\kappa^{(s)} + \lambda^m\sin\langle\kappa,\rho\rangle g_\kappa^{(c)}.\end{aligned} \tag{6.8}$$

The linear systems in (6.8) are solvable as long as $B^{(\kappa)} = B^2 - 2\lambda^m\cos\langle\kappa,\rho\rangle B + \lambda^{2m}Id$ is invertible for all κ. If μ is an eigenvalue of B, then $B^{(\kappa)}$ has eigenvalues of the form

$$\mu^2 - 2\lambda^m\cos\langle\kappa,\rho\rangle\mu + \lambda^{2m}$$

which makes $B^{(\kappa)}$ invertible whenever μ is different to $\lambda^m\exp(\pm\langle\kappa,\rho\rangle\mathrm{i})$.

We have then proved the following lemma:

Lemma 6.2.1. *Let B be a Floquet matrix associated with the frequency vector ρ on $\mathbb{T}^d$ and let $|\lambda| \neq 1$ be a real number satisfying that for each eigenvalue μ of B and a fixed $m \in \mathbb{N}$, $m \geq 2$,*

$$\mu \neq \lambda^m\exp(\pm\langle\kappa,\rho\rangle i), \qquad \forall\,\kappa \in \mathbb{N}^d. \tag{6.9}$$

Then for all smooth function g_m on $\mathbb{T}^d$, there exists a unique smooth function u_m such that

$$\lambda^m u_m(\theta+\rho) = Bu_m(\theta) + g_m(\theta). \tag{6.10}$$

Remark 6.2.2. *Note that* (6.9) *is always satisfied when λ is the dominant eigenvalue of the Floquet matrix.*

Expressions in (6.8) recall those in (6.5) and (6.6). Therefore, it is clear that the computation of each pair of coefficients $(u_\kappa^{(c)}, u_\kappa^{(s)})$ of u_m is independent to each other. That makes the proposed invariant manifold computation highly parallelizable as it was the Algorithm 6.1.1. Hence, to find the unknowns $(u_\kappa^{(c)}, u_\kappa^{(s)})$, we solve a large number of small dimensional linear systems at the same time; the dimension of each linear system depends on the dimension of the phase space and the number of systems only depends on the number of Fourier modes used for the approximation of g_m and u_m.

Notice that, when we start the computation of the functions a_k for $k \geq 2$, we use the same number of Fourier modes N_i for each of the angular dimensions θ_i with $i = 1, \ldots, d$, as for the torus and the Floquet change Fourier series. However, it may happen that those numbers of modes, that were enough for distretising accurately the torus and the Floquet change, may not be enough for discretising some of the parametrization functions a_k for $k \geq 2$. If this happens for a given order, it is necessary to increase the number of Fourier modes from this order on, as we did following Algorithm 1.4.3 in Chapters 4 and 5 for the computation of invariant manifolds of invariant curves. This effect has not been appreciated in the examples of Section 6.5, where we have checked the size of the Fourier modes after the computation. Varying the number of Fourier modes during the computation has an extra penalty that depends on the number of Fourier modes added. Notice that in the present case, in which $N \in \mathbb{Z}^d$ for each dimension of the phase space, this penalty time may be too long.

Algorithm 6.2.3 summarises the process explained above.

Algorithm 6.2.3 (Invariant manifold of a torus through its Floquet transformation)**.**

- ⋆ ***Input:*** *Discrete system as in* (1.12)*, torus $\varphi(\theta)$, Floquet change $C(\theta)$, Floquet matrix B, real eigenvalue $|\lambda| \neq 1$ of B, and its eigenvector v.*

⋆ ***Output:*** *Coefficients* $a_k(\theta)$ *for* $k \geq 2$ *verifying* (1.30).

1. $a_0(\theta) \leftarrow \varphi(\theta)$.
2. $a_1(\theta) \leftarrow C(\theta)v$.
3. *For* $k = 2, 3, \ldots$
   a) $b_0(\theta) + \cdots + b_k(\theta)\sigma^k \leftarrow P(a_0(\theta) + \cdots + a_{k-1}(\theta)\sigma^{k-1} + \mathbf{0}\sigma^k, \theta)$ *using jet transport.*
   b) $g_k(\theta) \leftarrow C^{-1}(\theta + \rho)b_k(\theta)$.
   c) *Find* $u_k(\theta)$ *such that* $\lambda^k u_k(\theta + \rho) = Bu_k(\theta) + g_k(\theta)$ *using* (6.8).
   d) $a_k(\theta) \leftarrow C(\theta)u_k(\theta)$.

6.2.2 Stable invariant manifold

The procedure introduced above is valid for both, the stable and the unstable invariant manifold computation. However, as it has been mentioned previously along the text, when the Poincaré map is applied forward in time to compute the stable manifold, it approaches the torus and also the unstable invariant manifold. This computation affects the numerical accuracy of the stable manifold by increasing the numerical errors due to the effect of the unstable direction. This effect is more relevant when the unstable direction is strong. Because of that, it is more accurate to obtain the parametrization of the stable invariant manifold using the inverse of the Poincaré map in (1.12),

$$\begin{cases} x = P^{-1}(\bar{x}, \bar{\theta}), \\ \theta = \bar{\theta} - \rho. \end{cases} \tag{6.11}$$

In the case of the stable invariant manifold, i.e. the real $|\lambda| < 1$ eigenvalues of B in (1.18), the invariance condition (1.30) is written for (6.11) as,

$$P^{-1}(W(\theta + \rho, \sigma), \theta + \rho) = W\big(\theta, \frac{\sigma}{\lambda}\big). \tag{6.12}$$

We proceed as before, we consider a formal power expansion of W in (1.29) and solve (6.12) order by order to obtain the functions a_k that parametrize the stable invariant manifold.

Notice that in that case, we must introduce a Floquet change that removes the angle dependence when the dynamics is moving backward in time, i.e. when we apply P^{-1}. The Floquet transformation for the torus, and the torus itself, in the map P and in the map P^{-1} are related through a phase equal to the vector ρ.

Following the Algorithm 6.1.1, the invariant torus and its eigenfunction (order zero and one of the parametrization) are obtained by application of P. If we want to use them for the parametrization of the stable manifold, where we apply P^{-1}, we have to re-parametrize them as $a_0(\theta + \rho)$ and $a_1(\theta + \rho)$. Therefore, in this case we look for the functions a_k with $k \geq 2$ shifted a quantity ρ.

Then, assuming that we know the parametrization up to order $m - 1$, in order to find the function $a_m(\theta) = C(\theta)u_m(\theta)$, such that $u_m(\theta)$ satisfies

$$C^{-1}(\theta)b_m^-(\theta) + B^{-1}u_m(\theta + \rho) = \lambda^{-m}u_m(\theta), \tag{6.13}$$

where $b_m^-(\theta)$ denotes the term of order m resulting from the evaluation of the invariant manifold up to order $m - 1$ by the inverse Poincaré map. Now, multiplying by B and by λ^m the last expression, we have

$$\lambda^m u_m(\theta + \rho) = Bu_m(\theta) + g_m(\theta), \tag{6.14}$$

that has the same form as (6.10) with $g_m(\theta) = -\lambda^m BC^{-1}(\theta)b_m^-(\theta)$. Therefore, relaying on Lemma 6.2.1 and the solution of the linear systems in (6.8), there exists the function $u_m\colon \mathbb{T}^d \mapsto \mathbb{R}^n$, evaluated in $u_m(\theta+\rho)$, that satisfies (6.14). Note that, the condition in (6.9) remains the same.

Algorithm 6.2.4 (Stable invariant manifold of a torus through its Floquet transformation)**.**

- ⋆ ***Input:*** *Discrete system as in* (1.12)*, torus* $\varphi(\theta)$*, Floquet change* $C(\theta)$*, Floquet matrix* B*, real eigenvalue* $|\lambda| < 1$ *of* B*, and its eigenvector* v*.*
- ⋆ ***Output:*** *Coefficients* $a_k(\theta+\rho)$ *for* $k \geq 2$ *verifying* (6.12)*.*

1. $a_0(\theta+\rho) \leftarrow \varphi(\theta+\rho)$.
2. $a_1(\theta+\rho) \leftarrow C(\theta+\rho)v$.
3. *For* $k = 2, 3, \ldots$
   a) $b_0(\theta) + \cdots + b_k(\theta)\sigma^k \leftarrow P^{-1}(a_0(\theta+\rho) + \cdots + a_{k-1}(\theta+\rho)\sigma^{k-1} + \mathbf{0}\sigma^k, \theta+\rho)$ *using jet transport.*
   b) $g_k(\theta) \leftarrow -\lambda^k BC^{-1}(\theta)b_k(\theta)$.
   c) *Find* $u_k(\theta)$ *such that* $\lambda^k u_k(\theta+\rho) = Bu_k(\theta) + g_k(\theta)$ *using* (6.8)*.*
   d) $u_k(\theta+\rho) \leftarrow u_k(\theta)$.
   e) $a_k(\theta+\rho) \leftarrow C(\theta+\rho)u_k(\theta+\rho)$.

6.3 Multiple shooting

There are invariant objects so unstable that it is impossible to integrate accurately the flow around them during the time involved in the Poincaré map. In these cases, it is convenient to split the time into a certain number of temporal sections, such that the integration time between each two consecutive sections is considerably reduced and so the propagation of the numerical error. These methods are commonly known as multiple shooting or parallel shooting methods and they have been widely used to compute highly unstable periodic orbits [SB02]. A version of this methodology applied to the computation of invariant tori and their Floquet changes can be found in [Olm07].

A multiple shooting method splits the Poincaré map into a finite number of maps such that the composition of them gives the original one. Let $\phi(t; 0, x, \theta)$ be the time t flow of (1.5) from initial time 0 and initial conditions $x \in \mathbb{R}^n$ and $\theta \in \mathbb{T}^d$. The temporal Poincaré map is defined as

$$P(x, \theta) = \phi(\delta; 0, x, \theta),$$

with $\delta = 2\pi/\omega_0$. Let us assume that P admits a reducible torus $\varphi\colon \mathbb{T}^d \to \mathbb{R}^n$ with frequency vector $\rho \in \mathbb{T}^d$ given by $\rho = \omega\delta$ being ω in the given model (1.5). That is, φ must satisfy (1.13). A multiple shooting method with r sections splits the map P into $P_1, \ldots, P_r$ new maps such that their composition gives P. Therefore, the problem consists in finding a reducible torus given in r pieces $\varphi_1, \ldots, \varphi_r$ that are the intersections of the torus of the flow with respectively each temporal section.

A standard multiple shooting method is one that considers the r sections equidistantly in time. Let us then define

$$P_j(x, \theta) = \phi(j\delta/r; (j-1)\delta/r, x, \theta), \qquad j = 1, \ldots, r.$$

There are several options to define the new invariance equations associated with $\varphi_1, \ldots, \varphi_r$. For instance,

$$\begin{aligned} P_j(\varphi_j(\theta), \theta) &= \varphi_{j+1}(\theta), \qquad j = 1, \ldots, r-1, \\ P_r(\varphi_r(\theta), \theta) &= \varphi_1(\theta+\rho), \end{aligned}$$

or another example can be,

$$\begin{aligned} &P_j(\varphi_j(\theta), \theta + (j-1)\rho/r) = \varphi_{j+1}(\theta + j\rho/r), \qquad j = 1, \dots, r-1, \\ &P_r(\varphi_r(\theta), \theta + (r-1)\rho/r) = \varphi_1(\theta + \rho). \end{aligned}$$

However, these two examples do not scale with the Algorithms 6.1.1, 6.2.3, and 6.2.4 because, in both cases, the right hand side has no a uniform rotation angle for each $j = 1, \dots, r$. That forces us to change other steps in those algorithms besides the only evaluation of the Poincaré map.

Our goal is then to choose an expression that only change the evaluation of the P and $D_x P$ and the other steps in Algorithms 6.1.1, 6.2.3, and 6.2.4 remain the same. The previous proposed invariance equations require to consider a rotation vector of dimension d for each shooting. To keep the same shifting over the r new sections, we propose

$$\begin{aligned} &P_j(\varphi_j(\theta), \theta - (j-1)\rho/r) = \varphi_{j+1}(\theta + \rho/r), \qquad j = 1, \dots, r-1, \\ &P_r(\varphi_r(\theta), \theta - (r-1)\rho/r) = \varphi_1(\theta + \rho/r). \end{aligned} \tag{6.15}$$

Note that one can see a multiple shooting approach as a single shooting but with a larger phase space. The equations (6.15) do not recover P in (1.13) by a direct composition since they must be alternated with rotation operators. Similarly, the φ in (1.13) can be obtained from the $\varphi_1, \dots, \varphi_r$ in (6.15) by undoing rotations. The Lemma 6.3.1 makes explicit all these rotations and, in particular, says that $D_x P$ is a product of differentials of P_j with interlaced rotations.

Lemma 6.3.1. *Let α be an angle and let T_α be the operator defined as $T_\alpha x(\theta) = x(\theta + \alpha)$. Then the map P at the torus φ in* (1.13) *and P_j in* (6.15) *at the torus φ_j are related by*

$$P = T_{\rho - \rho/r} \circ P_r \circ T_{-\rho/r} \circ P_{r-1} \circ \cdots \circ T_{-\rho/r} \circ P_1.$$

6.3.1 Reducibility and multiple shooting

The linear skew-product associated to the linearization around a torus found with this multiple shooting has a uniform rotation over the sections. Thus, (6.15) has a linear behaviour expressed by

$$\begin{aligned} \bar{X}_{j+1} &= A_j(\theta) X_j, \qquad j = 1, \dots, r-1, \\ \bar{X}_1 &= A_r(\theta) X_r, \\ \bar{\theta} &= \theta + \rho/r, \end{aligned} \tag{6.16}$$

with $A_j(\theta) = D_x P_j(\varphi_j(\theta), \theta - (j-1)\rho/r)$ for $j = 1, \dots, r$.

Following the Definition 1.2.2, (6.16) is reducible if, and only if, there exist a change of variables of the form $X_j = C_j(\theta) Y_j$ for $j = 1, \dots, r$ such that (6.16) becomes

$$\begin{aligned} \bar{Y}_{j+1} &= B_j Y_j, \qquad j = 1, \dots, r-1 \\ \bar{Y}_1 &= B_r Y_r, \\ \bar{\theta} &= \theta + \rho/r, \end{aligned} \tag{6.17}$$

where the matrices $B_1, \dots, B_r \in \mathbb{R}^{n \times n}$ are defined by

$$\begin{aligned} B_j &= C_{j+1}(\theta + \rho/r)^{-1} A_j(\theta) C_j(\theta), \qquad j = 1, \dots, r-1 \\ B_r &= C_1(\theta + \rho/r)^{-1} A_r(\theta) C_r(\theta), \end{aligned} \tag{6.18}$$

and they do not depend on θ.

Remark 6.3.2 (Matrix-form)**.** *The linearization around a torus can also be formulated in a matrix-block form of a higher dimensional problem, that is, $n \cdot r$ dimension. Thus in practice, Algorithm 6.1.1*

can be used with multiple shooting just considering ρ/r instead of ρ and evaluating P_j and D_xP_j following (6.15)*. Indeed, if we consider the block matrices*

$$\tilde{A}(\theta) = \begin{pmatrix} A_1 & & & A_r \\ & \ddots & & \\ & & A_{r-1} & \end{pmatrix}(\theta), \qquad \tilde{B} = \begin{pmatrix} B_1 & & & B_r \\ & \ddots & & \\ & & B_{r-1} & \end{pmatrix}, \tag{6.19}$$

$$\tilde{C}(\theta) = \begin{pmatrix} & C_1 & & \\ & & \ddots & \\ & & & C_{r-1} \\ C_r & & & \end{pmatrix}(\theta), \qquad \tilde{C}^{-1}(\theta) = \begin{pmatrix} C_1^{-1} & & & C_r^{-1} \\ & \ddots & & \\ & & C_{r-1}^{-1} & \end{pmatrix}(\theta),$$

then using a little bit more memory to keep the zeros for each θ we can directly use Algorithm 6.1.1.

As a consequence of the Remark 6.3.2, we have the following straightforward lemma.

Lemma 6.3.3. *Let $B_1, \dots, B_r$ be the matrices in* (6.18) *and let $\tilde{B}$ be the matrix in* (6.19)*. Then μ is an eigenvalue of $\tilde{B}$ if, and only if, μ^r is an eigenvalue of $B_rB_{r-1}\cdots B_1$. In other words, the eigenvalues of $\tilde{B}$ are the complex roots of the eigenvalues of $B_rB_{r-1}\cdots B_1$.*

Lemma 6.3.4 (see §51 in [Wil65])**.** *Let $\mathcal{A}$ and $\mathcal{B}$ be square matrices. Then the spectrum of $\mathcal{AB}$ is the same as the spectrum of $\mathcal{BA}$.*

Combining Lemmas 6.3.1, 6.3.3, and 6.3.4, we prove Proposition 6.3.5. That result links the relation between the Floquet matrix with the one using the multiple shooting. To prove it, it is enough *i)* to observe that from Lemma 6.3.1 the spectrum of D_xP on the torus φ has the same spectrum as $(D_xP_r)\cdots(D_xP_1)$, respectively on $\varphi_r, \dots, \varphi_1$. *ii)* The different rotation operators $T_{-\rho/r}$ do not change the spectrum because of the Lemma 6.3.4. *iii)* The Floquet C_j do not change the spectrum of B_j. Therefore, Lemma 6.3.3 allows to finish the proof of the Proposition 6.3.5.

Proposition 6.3.5. *The eigenvalues of the Floquet matrix of a multiple shooting* (6.17) *with r sections are the complex r roots of the eigenvalues of the Floquet matrix with single shooting* (1.18)*.*

6.3.2 Multiple shooting applied to invariant manifolds

If the torus is very hyperbolic, the linear approximation to the manifold in one of the sections of the torus (single shooting) is enough to globalize the manifold with a good level of accuracy. This is because, as the manifold is very unstable, it is sufficient to use the unstable direction of the torus in one of the sections, say φ_1, to grow numerically the manifold [Ros20]. Other works, as [Dua19], use multiple shooting to compute the linear approximation to the invariant manifold. As here we are interested in a high-order approximation to these manifolds, we need to compute high-order derivatives of the map. Due to the strong instability of the torus, we have to continue with the multiple shooting scheme in order to compute the derivatives of the maps P_j accurately. Therefore, we will compute the Taylor-Fourier expansions for the torus φ_j, $j = 1, \dots, r$.

The parametrization of the manifold, as explained in Section 6.2, is done at each of the r sections. Let W_j be a formal power expansion for each $j = 1, \dots, r$ of the form

$$W_j(\theta, \sigma) = \sum_{k \geq 0} a_{j,k}(\theta)\sigma^k, \qquad \theta \in \mathbb{T}^d.$$

We denote the truncated power expansion of W_j of order m by $W_{j,m}$.

Let us assume, by simplicity, that $|\mu| \neq 1$ is real. Then, applying the invariance condition of the torus to the invariant manifold leads to the equations

$$\begin{aligned} &P_j(W_j(\theta,\sigma),\theta-(j-1)\rho/r) = W_{j+1}(\theta+\rho/r,\mu\sigma), \qquad j=1,\dots,r-1,\\ &P_r(W_r(\theta,\sigma),\theta-(r-1)\rho/r) = W_1(\theta+\rho/r,\mu\sigma). \end{aligned} \tag{6.20}$$

The zeroth order in σ of (6.20) is just the torus φ_j in (6.15), that is, $a_{j,0}=\varphi_j$. The first order in σ in (6.20) has the form

$$\begin{aligned} &D_xP_j(a_{j,0}(\theta),\theta-(j-1)\rho/r)a_{j,1}(\theta) = a_{j+1,1}(\theta+\rho/r)\mu, \qquad j=1,\dots,r-1,\\ &D_xP_r(a_{r,0}(\theta),\theta-(r-1)\rho/r)a_{r,1}(\theta) = a_{1,1}(\theta+\rho/r)\mu. \end{aligned}$$

Using the change $a_{j,1}(\theta)=C_j(\theta)v_j$ for $j=1,\dots,r$ and the definition of B_j in (6.18), we end up with

$$\begin{aligned} &B_jv_j = \mu v_{j+1}, \qquad j=1,\dots,r-1,\\ &B_rv_r = \mu v_1, \end{aligned}$$

and by the matrix-block form in Remark 6.3.2, we conclude that $v=(v_1,\dots,v_r)$ is an eigenvector of eigenvalue μ of $\tilde{B}$ that, by Proposition 6.3.5, means that μ is a r root of an eigenvalue of (1.18).

Let us now assume that we know the functions $a_{j,k}$ for $j=1,\dots,r$ and $k=0,\dots,m-1$. Then, using the induction hypothesis, for $j=1,\dots,r-1$, (and similarly for $j=r$)

$$\begin{aligned} &P_j(W_{j,m-1}(\theta,\sigma),\theta-\frac{j-1}{r}\rho)\\ &= P_j(W_{j,m-1}(\theta,\sigma),\theta-\frac{j-1}{r}\rho) + D_xP_j(W_{j,m-1}(\theta,\sigma),\theta-\frac{j-1}{r}\rho)a_{j,m}(\theta)\sigma^m + \mathcal{O}(\sigma^{m+1})\\ &= P_j(W_{j,m-1}(\theta,\sigma),\theta-\frac{j-1}{r}\rho) + A_j(\theta)a_{j,m}(\theta)\sigma^m + \mathcal{O}(\sigma^{m+1})\\ &= W_{j+1,m-1}(\theta+\frac{\rho}{r},\mu\sigma) + b_{j,m}(\theta)\sigma^m + A_j(\theta)a_{j,m}(\theta)\sigma^m + \mathcal{O}(\sigma^{m+1}), \end{aligned} \tag{6.21}$$

with $A_j(\theta)=D_xP_j(a_{j,0}(\theta),\theta-(j-1)\rho/r)$. Equating the order σ^m in (6.21) with the right hand side in (6.20), we end up with the expressions

$$\begin{aligned} &b_{j,m}(\theta)+A_j(\theta)a_{j,m}(\theta) = a_{j+1,m}(\theta+\rho/r)\mu^m, \qquad j=1,\dots,r-1,\\ &b_{r,m}(\theta)+A_r(\theta)a_{r,m}(\theta) = a_{1,m}(\theta+\rho/r)\mu^m. \end{aligned}$$

Introducing the Floquet change $a_{j,m}(\theta)=C_j(\theta)u_{j,m}(\theta)$ for all $j=1,\dots,r$, and using (6.18), we deduce

$$\begin{aligned} C_{j+1}(\theta+\rho/r)^{-1}b_{j,m}(\theta)+B_ju_{j,m}(\theta) &= \mu^m u_{j+1,m}(\theta+\rho/r), \qquad j=1,\dots,r-1,\\ C_1(\theta+\rho/r)^{-1}b_{r,m}(\theta)+B_ru_{r,m}(\theta) &= \mu^m u_{1,m}(\theta+\rho/r). \end{aligned} \tag{6.22}$$

The system of equations (6.22) can directly be solved as the one in (6.10) and independently on j.

This scheme works for real stable/unstable manifolds. For the reasons discussed in Section 6.2.2, to compute stable manifolds is numerically more precise to consider the inverse Poincaré map. We can then write similar conditions to (6.20) for P_j^{-1}.

Remark 6.3.6. *The parametrization* (6.20) *can also been seen as a single shooting in higher dimension. Thus we can skip the detailed expressions in* (6.22) *for each index j and apply directly the Section 6.2 but with the matrix-block in the Remark 6.3.2 and with ρ/r instead of ρ. In particular, the Algorithms 6.2.3 and 6.2.4 can be used with the penalty of more memory usage.*

6.4 Computer implementation

This section is devoted to provide some technical details and information concerning to the computer implementation of the introduced algorithms. Notice that, some detail has been already explained, as the idea of the jet transport technique used to obtain high-order derivatives of the Poincaré map through automatic differentiation, see Section 1.3.1.

Also, it is important to mention that an effective manipulation of Fourier series of several variables has a crucial impact on the performance of Algorithms 6.1.1, 6.2.3 and 6.2.4 to do the steps of shifting by ρ and to solve cohomological equations. We do not only need to be able to express the series in its Fourier coefficients and its tabulation on a grid of angles $\theta \in \mathbb{T}^d$; a process based on the Discrete Fourier Transform. We have to know how to perform operations affecting to its coefficients. In particular, we need to be able to know at each memory location which is its coefficient and vice versa. This is highly dependent on the package used. In this work, we have used the FFTW3 (Fastest Fourier Transform in the West) package [FJ05]. For the specific details of how this package was managed, we refer the interested reader to Section 5.1 of [GJNO21].

Since this work is focused on the parallelism of computations, Section 6.4.1 is devoted to the technical details in the implementation of our computations and an analysis of the degree of parallelism achieved. Finally, Section 6.4.2 collects some numerical tests to analyse the accuracy of the obtained results.

6.4.1 Parallelism

Algorithms 6.1.1, 6.2.3, and 6.2.4 contain steps that are highly parallelizable. Such a parallelism was already exploited in [JO09] in Algorithm 6.1.1 using the PVM library [GBD+95] running on a cluster of PCs connected through an Ethernet network. Here we use OpenMP 4.5 [Ope15] which runs concurrently in a PC with several CPUs and it provides an easier and efficient parallelism programming.

The use of profilers for the experiments in Section 6.5 shows that more than the 98% (in both algorithms) is spent in the evaluation of the discrete map P and its derivatives, which involves ODE integrations, and a lower percentage is required to solve the cohomological equations. Therefore, the parallelism strategy has consisted in running the evaluation of the ODE integrator, Taylor [JZ05] and Runge-Kutta-Verner 8(9) [Ver78] in the experiments, sequentially and independently in each of the different available CPUs of the PC. This provides an automatic parallelism since the algorithms require to evaluate the discrete map for each of the different angle values in the mesh in $\mathbb{T}^d$. Note that with this approach the use of jet transport does not provide any downside because we do not parallelize the integrator itself.

The second level of parallelism is in the cohomological equations, the shifting by ρ, and some of the matrix-solvers that are independent to each other either in a Fourier representation or in a table of values.

Finally, we parallelize the transformation between the table of values and the Fourier coefficients (and vice versa). That has been done by the feature already provided in the FFTW3 package and in combination with the OpenMP. We did not detect a major improvement because the package itself is already optimized enough and already the profiler indicated that these transformations do not contribute too much in the performance when one use the FFTW3.

We took care of the potential overhead in the initialization of the threads, that is, the different (sub)processes that are executed in the CPUs. Thus, we initialize the threads at the beginning of the algorithms to have ready the pool of threads and bifurcate the code execution when we reach those parallelizable steps.

6.4.2 Accuracy tests

In order to ensure that the computations are correct and to ensure that the level of accuracy is the required one, we implement some tests. First, regarding to the torus and the Floquet change, we implement three tests, two of them already introduced in [Olm07], let us call them Test 1, Test 2, and Test 3. Secondly, test presented in Section 1.4.5 is implemented to assess the parametrization of the hyperbolic invariant manifolds. The Tests 2 and 3 are run after the solutions have been obtained, which means that they can be used to check how good are these solutions in terms of the invariance equations they must satisfied.

In all the tests, we are going to use norms and tolerances that must be chosen depending on the model, precision arithmetic, and matching with other tolerances in the algorithms, such as, the one for the Newton's process or the ODE integrations. In Section 6.5, we will made explicit all these choices.

The invariance equation

Algorithm 6.1.1 stops when the invariance condition (1.13) for the torus φ and for the Floquet change (1.19) are satisfied within a certain threshold. On the other hand, Algorithm 6.2.3 and Algorithm 6.2.4 are not iterative processes and the steps in each algorithm are deduced by imposing (by power matching in σ) the invariance equations (1.30) and (6.12), respectively.

Test 1. *Let $\mathcal{A}$ be a mesh in $\mathbb{T}^d$. A function z is said to verify the equation $\mathcal{I}(z(\theta)) = 0$ with tolerance τ if, and only if,*

$$\max_{\theta \in \mathcal{A}} \; ||\mathcal{I}(z(\theta))|| \leq \tau.$$

Note that Test 1 can be defined in terms of the relative error instead of the absolute error.

The tail of the Fourier discretization

The test consists in checking that the truncated Fourier representation is accurate enough with the mesh size. We use the fact that, under a smoothness assumption, the Fourier coefficients decay. In the applications in Section 6.5, these functions are analytic and then their Fourier coefficients decay exponentially. The truncation error is approximated by the size of the last Fourier coefficients in its representation. To prevent potential symmetries that make zero some of the entries, we check the last two indexed coefficients.

Test 2. *A truncated real Fourier representation given by*

$$x(\theta) = \frac{x^{(0)}}{2} + \sum_{|\kappa|=1}^{N} x_\kappa^{(c)} \cos\langle \kappa, \theta \rangle + x_\kappa^{(s)} \sin\langle \kappa, \theta \rangle \,, \qquad \theta \in \mathbb{T}^d.$$

is said to verify the Test 2 with tolerance τ if, and only if, for all $\kappa \in \mathbb{N}^d$ such that $|\kappa| = N$ or $|\kappa| = N - 1$,

$$||(x_\kappa^{(c)}, x_\kappa^{(s)})||_2 \leq \tau.$$

We apply the Test 2 for each of the Fourier series involved in the torus, in its Floquet change, and its parametrized manifold. Moreover, Test 2 can be used to keep track which of the components of the angular variables vector $\theta \in \mathbb{T}^d$ have the biggest tail size in norm, and then increase the mesh size on that direction until either we reach a maximum mesh size or we reach the desired tolerance.

The mesh

The third test is computationally more expensive, it consists in checking the function that we want to make zero in a different mesh but with the same size. A way to do this check without the need of using more computational sources is just to perform a fixed shift by an angle, say γ, and then check if the equation is still verified with a prescribed tolerance.

Test 3. *Let $\mathcal{A}$ be a mesh in $\mathbb{T}^d$. A function z is said to verify the equation $\mathcal{I}(z(\theta)) = 0$ with tolerance τ and shifting $\gamma \in \mathbb{T}^d$ if, and only if,*

$$\max_{\theta \in \mathcal{A}} ||\mathcal{I}(z(\theta + \gamma))|| \leq \tau.$$

Note that as Test 1, Test 3 can be defined in terms of the relative error instead of the absolute error. In the case of the torus, the Test 3 consists first in performing the shift $\psi(\theta) = \varphi(\theta + \gamma)$ and then checking (1.13) but for ψ and with the same original mesh in θ, that is,

$$\max_{\theta \in \mathcal{A}} ||\psi(\theta + \rho) - P(\psi(\theta), \theta + \gamma)|| \leq \tau.$$

Similarly, we can apply Test 3 for the Floquet change C, and for the functions a_k.

6.5 Applications

In this section we implement two different applications. The first example is a classical quasi-periodically forced pendulum and the second one is an application to celestial mechanics; one of the Simplified Solar System Model (SSSM) introduced in [GMM02, Mon01].

In order to stress the independence of the integration method, we use a Taylor integration with jet transport and tolerance 10^{-16} for the first method and a Runge-Kutta-Verner 8(9) with jet transport and tolerance 10^{-14} for the celestial mechanic one. To verify the different tests described in Section 6.4.2, we consider the Euclidean norm for vectors, the Fröbenius norm for matrices, and a generic test tolerance of $\tau = 10^{-10}$.

In all the experiments we have used the `gcc` compiler, version 8.3.0, on a Linux computer with two Intel(R) Xeon(R) CPU E5-2680 @2.70GHz processors, which give a total of 16 cores. For the sake of simplicity, in what follows we use the terms core and processor equally, to refer to a single computational unit.

6.5.1 A quasi-periodically forced pendulum

This first application considers one of the examples included in [JO09]. The system describes the movement of a quasi-periodically forced pendulum

$$\begin{cases} \dot{x} = y \\ \dot{y} = -\alpha \sin x + \varepsilon \zeta(\theta_0, \ldots, \theta_d), \\ \dot{\theta}_i = \omega_i, \quad i = 0, \ldots, d \end{cases} \tag{6.23}$$

where $x, y \in \mathbb{R}$, and α is a parameter whose value is chosen as 0.8. For $i = 0, \ldots, d$, $\theta_i \in \mathbb{T}$ and ε accounts for the weight of the forcing function ζ:

$$\zeta(\theta_0, \ldots, \theta_d) = \left[d + 2 + \sum_{i=0}^{d} \cos \theta_i \right]^{-1}.$$

p	Total time	speed-up
1	8m3.286s	1.000
2	4m9.742s	1.934
4	2m18.073s	3.500
8	1m13.779s	6.550
16	39.234s	12.318

Table 6.1: Computational time needed for computing the torus of system (6.23) with frequency vector of dimension $d = 4$. First column corresponds to the number of processors used, second one to the total time employed according to the number of processors, and the last one designs the speed-up.

As frequencies we have chosen, with $d = 4$,

$$\omega_0 = 1, \quad \omega_1 = \sqrt{2}, \quad \omega_2 = \sqrt{3}, \quad \omega_3 = \sqrt{5}, \quad \omega_4 = \sqrt{7}. \tag{6.24}$$

We have applied the methodology summarized in Section 6.1, Algorithm 6.1.1, to obtain the torus, the Floquet transformation, and the Floquet matrix near $x = \pi$, $y = 0$ for $\varepsilon = 0.01$. Recall that according to the dimension of the frequency vector selected, d, the dimension of the resulting torus of the flow (6.23) near the point $(\pi, 0)$ is $d + 1$. By defining a returning map P to the section $\theta_0 = 0 \mod 2\pi$, the dimension of the torus is reduced by one. As initial seeds we used the point $(\pi, 0)$ for the torus, the identity for the Floquet transform, and the differential of P at $(\pi, 0)$ for the Floquet matrix.

Each of the angles has been discretized using $N = 31$ Fourier modes, that results to a total of $2N^4 = 1847042$ unknowns for the torus and $4N^4 = 3694084$ for the Floquet change. Note that a direct method to compute the torus and not using the advantage of the Floquet change needs to store $4N^8$ double precision variables which is totally unfeasible.

The Algorithm 6.1.1 was run with a Newton threshold of 10^{-10} and the Test 1 for the torus is satisfied with 10^{-13} after 3 Newton's iteration and with 10^{-12} for the Floquet transformation and Floquet matrix.

After the Newton convergence and the success in the Test 1, we apply the Test 2 reporting the different values for each of the angular directions, that is, respectively, 10^{-10}, 10^{-11}, 10^{-10}, and 10^{-11}. The Test 3 is also satisfied with 10^{-11} for the torus and 10^{-12} for the Floquet transformation.

The Floquet matrix, B, has hyperbolic real eigenvalues $\lambda_s = 3.625204837874207 \times 10^{-3}$ and $\lambda_u = 2.758464817115549 \times 10^{2}$. Note that $|\lambda_s \lambda_u - 1| = 1.13 \times 10^{-11}$. In the Table 6.1, we show the computational time required for computing the torus using different number of processors. In the same table, the speed-up factor is included. This factor measures the relation between the time needed for solving the system with `p` processors with respect to the time of the linear resolution, that is, using just one processor (`p` $= 1$). Ideally, when the parallelization is performed with `p` processors, the time should be divided by `p`. We can see in the table that this does not happen, specially when the number of processors increases and so the overhead in each of the processors. Some checks have been done regarding to this; for example, disabling the Hyper-threading of the processors the computational times remained the same. It is noteworthy that the analysis of the profiler to our program shows that 99.76% of the computations have been parallelized.

We compute the approximations to the stable/unstable invariant manifolds up to order 10 following the Algorithms 6.2.3 and 6.2.4. Table 6.2 shows the required times for these computations using different number of processors and the corresponding values for the speed-up. The Test 1 is satisfied in relative error for each of the order in σ starting with a 10^{-14} at zeroth order to 10^{-11} at order 10. Tests 2, 3, and the test described in Section 1.4.5 have also been successful at each of the orders.

	unstable		stable	
p	Total time	speed-up	Total time	speed-up
1	2h33m13s	1.000	2h33m31s	1.000
2	1h19m08s	1.936	1h28m59s	1.725
4	43m12s	3.546	48m23s	3.173
8	22m13s	6.894	25m03s	6.129
16	11m09s	13.746	12m32s	12.245

Table 6.2: Computational time needed for the stable/unstable manifolds up to order 10 of the torus in Table 6.1. First column corresponds to the number of processors used.

6.5.2 A quasi-periodically perturbed model for the Earth-Moon system

G. Gómez, J. J. Masdemont and J. M. Mondelo developed a methodology to generate simplified Solar Systems models (SSSM) using a set of basic frequencies, see [GMM02, Mon01]. The systems of equations introduced in those works describe the motion of a massless particle subjected to a series of time-periodic perturbations. These models are defined in such a way that if we remove all the time-periodic dependencies present in the SSSM, the resulting models correspond to the well-known Restricted Three-Body Problem (RTBP), [Sze67].

Among the simplified models introduced in [GMM02, Mon01], special attention is paid to the Earth-Moon case, including the gravitational effect of the Sun. For the description of this simplified model they use five basic frequencies for the accurate characterization of the lunar motion. The selection of these frequencies comes from the simplified Brown theory presented in [Esc68]. Their values in terms of cycles per lunar revolution (RTBP adimensional units) are the following:

- mean longitude of the Moon, $\omega_1 = 1$,
- mean elongation of the Moon from the Sun, $\omega_2 = 0.925195997455093$,
- mean longitude of the lunar perigee, $\omega_3 = 8.45477852931292 \times 10^{-3}$,
- longitude of the mean ascending node of the moon on the ecliptic, $\omega_4 = 4.01883841204748 \times 10^{-3}$,
- Sun's mean longitude of perigee, $\omega_5 = 3.57408131981537 \times 10^{-6}$.

So, this model includes the gravitational effect of the Sun (not only on the motion of the infinitesimal particle, but also on the motion of the Earth and the Moon), the lunar eccentricity, inclination between the orbital plane of the Moon and the ecliptic plane, and also between the orbital and equatorial planes.

In order to generate the model, the authors change these frequencies to a new basis $\nu = (\nu_1, \ldots, \nu_5)$ defined as $\nu_1 = \omega_2$, $\nu_2 = \omega_1 - \omega_3$, $\nu_3 = \omega_1 - \omega_2 + \omega_4$, $\nu_4 = \omega_1 - \omega_5$, and $\nu_5 = \omega_5 - \omega_2$, such that when the frequencies $\nu_1, \ldots, \nu_i$ are added to the unperturbed system (Earth-Moon RTBP), the simplified models SSSM_i are generated for $i = 1, \ldots, 5$, each of them subjected to $\nu_1, \ldots, \nu_i$ perturbations.

The equations of motion for an infinitesimal particle in these models SSSM_i, $i = 1, \ldots, 5$ are introduced in terms of time-dependent functions c_j^i, $j = 1, \ldots, 13$,

$$\begin{cases} \ddot{x} = c_1^i + c_4^i \dot{x} + c_5^i \dot{y} + c_7^i x + c_8^i y + c_9^i z + c_{13}^i \dfrac{\partial \Omega^i}{\partial x}, \\ \ddot{y} = c_2^i - c_5^i \dot{x} + c_4^i \dot{y} + c_6^i \dot{z} - c_8^i x + c_{10}^i y + c_{11}^i z + c_{13}^i \dfrac{\partial \Omega^i}{\partial y}, \\ \ddot{z} = c_3^i - c_6^i \dot{y} + c_4^i \dot{z} + c_9^i x - c_{11}^i y + c_{12}^i z + c_{13}^i \dfrac{\partial \Omega^i}{\partial z}, \end{cases} \tag{6.25}$$

being

$$\Omega^i = \frac{1-\mu}{\sqrt{(x-\mu)^2+y^2+z^2}} + \frac{\mu}{\sqrt{(x-\mu+1)^2+y^2+z^2}} + \frac{\mu_S}{\sqrt{(x-x_S^i)^2+(y-y_S^i)^2+(z-z_S^i)^2}}, \tag{6.26}$$

where μ is the Earth-Moon mass parameter, μ_S is the mass of the Sun with respect to the sum of masses of Earth and Moon, and x_S^i, y_S^i, z_S^i denote the positions of the Sun.

The quasi-periodic time-dependent functions c_j^i can be computed in terms of the positions, velocities, accelerations, and over-accelerations of the two selected primaries. The description of these time-dependent functions as well as the positions x_S^i, y_S^i and z_S^i, consists on a refined Fourier analysis, detailed in [GMS10a, GMS10b]. Note that, regardless of the model i, taking $c_j = 0$ except for $c_5 = 2$, $c_7 = c_{10} = c_{13} = 1$ and omitting the last term in (6.26), the system of equations in (6.25) becomes that of the RTBP.

Recall that the RTBP presents five equilibrium points ([Sze67]), $L_{1,\dots,5}$, where $L_{1,2,3}$, are the colinear points, of centre×centre×saddle type, and the other two, $L_{4,5}$, are the triangular points, that have a dynamics of centre×centre×centre for the mass parameter of the Earth-Moon system. The dynamics of the saddle parts of $L_{1,2}$ are numerically difficult to compute because its unstable parts are of order 10^8 and 10^6 respectively.

The angular dimension of these points increases as the frequencies of the SSSM are included. In the SSSM_1 the equilibrium points become periodic orbits, in the SSSM_2 become two-dimensional quasi-periodic solutions (or 2D tori), and so on. A way of computing these quasi-periodic solutions is to continue them from one SSSM_i to SSSM_{i+1} as the number of considered frequencies increases. This continuation is sometimes difficult due to appearance of resonances, [Olm07].

In order to reduce the continuation problems, we add a small dissipation parameter to the equations of the system when continuing from SSSM_i to SSSM_{i+1}. Thus, elliptic eigenvalues become hyperbolic and difficulties of convergence with the algorithm coming from possible resonances are likely removed. Once we have the invariant torus in the system SSSM_{i+1} plus the dissipation parameter, we remove that parameter and refine the invariant object in the original SSSM_{i+1}.

To prevent the numerical difficulties coming from the strong instability in $L_{1,2}$, we use multiple shooting with r sections, in particular, $r = 4$ and $r = 3$ respectively. Then we perform the computation of the torus, its Floquet change, and Floquet matrix until we reach the SSSM_3 model. With this, we have obtained the invariant tori that replace $L_{1,2}$ in the SSSM_3 model, which are tori of dimensions 3 for the flow, and their Floquet matrices. Note that, as we are using multiple shooting, we have computed r sections of the torus. Next, we have computed the unstable manifold of each torus. Table 6.3 shows the computational times and corresponding speed-up for the approximation of the unstable invariant manifolds up to order 10.

	L_1 unstable		L_2 unstable	
λ_u	1.469645480926268e+02		1.343539917760893e+02	
p	Total time	speed-up	Total time	speed-up
1	16m29s	1.000	6h41m46s	1.000
2	9m44s	1.886	3h58m09s	1.912
4	5m20s	3.450	2h39m36s	3.456
8	2m30s	6.610	1h52m39s	6.596
16	1m18s	12.740	26m02s	13.090

Table 6.3: Computational time with p CPUs of the unstable manifolds of L_1 and L_2 of SSSM_3 using meshes $N = (43, 43)$ and $N = (223, 223)$, and parallel sections 4 and 3 respectively.

6.6 Conclusions

This chapter has shown that the computation of high-order Taylor-Fourier expansions of stable and unstable invariant manifolds associated with high-dimensional tori are, nowadays, feasible. Even when the instability of the torus is very strong, where we have combined the algorithms with multiple shooting methods. We have provided explicit algorithms to compute all these invariant objects.

The developed methods look suitable to address computation of invariant manifolds generated by several eigendirections. We plan to modify the current code for such a context as well as to manage some of the eigenvalue cases not included here. Similar ideas can be applied to the case when the frequency vector ρ is not known or even when the internal dynamics is not a fixed rotation ρ, in particular, in a context when the dynamical system is autonomous. Some results in these directions have already been worked in [Olm07].

The method is highly parallelizable to compute torus, the Floquet transformation, and its invariant manifolds. In the experiments, we used OpenMP showing a really good speed-up. We are also aware of other approaches that can take advantage of the intrinsic parallelism of the algorithms such as a GPU approach. We plan exploring in future works a GPU parallelization scheme and providing experiments showing that there is no relevant penalty in the communication between the CPU and the GPUs.

Conclusions and future work

Throughout this dissertation we have faced dynamical systems under time-periodic perturbations, focusing specially on the Sun-perturbed Earth-Moon Bicircular Problem. We have given answers to many questions that we had before starting the research and to many others that arise as the investigation evolved.

In particular, we have extensively studied the horizontal family of two-dimensional quasi-periodic orbits around L_3, that was found to give rise to very rich transport phenomena. The stable/unstable invariant manifolds associated with these solutions are three-dimensional, but they can be seen as two-dimensional in a suitable defined stroboscopic map. This lead us to introduce the fundamental cylinders; a fundamental domain for the manifolds that allow to visualise in a generic and relatively simple way all the connections that may take place through each one of these quasi-periodic solutions. We highlight the connections from the Moon to the Earth that may give an insight about the travel the some lunar meteorites found in our planet. The results obtained in the BCP were translated through a non-autonomous change of coordinates to a more realistic model based on JPL ephemeris, arising a good agreement between the models. A natural extension to this part is to study these connections between the Eath and Moon in the spatial case, or to use a model that accounts for the eccentricity of the primaries.

Another application in the BCP framework that we have carefully accomplish is the use of the stable invariant manifolds associated with those quasi-periodic solutions to capture a NEA. For this we need to compute the high order approximation of the stable/unstable invariant manifolds; what has been done for stroboscopic maps and as a combination of the parametrization method with the jet transport technique to obtain automatically the derivatives of the map. There we conclude that not only it is possible the capture in the BCP through L_3, but also it may be really cheap. In this application, many further improvements can be performed, see also Section 4.3, as from the astronautical point of view (like looking for reducing the fuel costs or the time of flight) as from the point of view of the dynamical systems, like using the invariant manifolds of three-dimensional quasi-periodic orbits to perform the capture in the 3D BCP.

It must be noticed that, most of the ideas, strategies and tools employed in the analysis of this specific system has provided us a better understanding of its dynamics, but also, most of these procedures can be extended to many other dynamical systems under time-periodic perturbations, not only those related to the celestial mechanics.

As a final application we have developed an algorithm to compute in parallel the high order parametrization of stable/unstable invariant manifolds associated with reducible quasi-periodic solutions of any high dimension. This is a really powerful tool that not only makes feasible to solve the large dimensional systems related to those high dimensional tori, but also it reduces significantly the computational costs. In Section 6.6 we carefully detail the main conclusions and future work to perform in this direction. Also, when we work with invariant objects of large dimension it is extremely difficult to visualise the results in a generic way, therefore it may be interesting to develop an strategy that allow us to visualise and understand the dynamics in these high dimensional systems as we did for the BCP.

Bibliography

[ABB+15] D.G. Andrews, K.D. Bonner, A.W. Butterworth, H.R. Calvert, B.R.H. Dagang, K.J. Dimond, L.G. Eckenroth, J.M. Erickson, B.A. Gilbertson, N.R. Gompertz, O.J. Igbinosun, T.J. Ip, B.H. Khan, S.L. Marquez, N.M. Neilson, C.O. Parker, E.H. Ransom, B.W. Reeve, T.L. Robinson, M. Rogers, P.M. Schuh, C.J. Tom, S.E. Wall, N. Watanabe, and C.J. Yoo. Defining a successful commercial asteroid mining program. *Acta Astronautica*, 108:106–118, 2015.

[ADLBZB10] R. Armellin, P. Di Lizia, F. Bernelli-Zazzera, and M. Berz. Asteroid close encounters characterization using differential algebra: the case of Apophis. *Celestial Mech. Dynam. Astronom.*, 107(4):451–470, 2010.

[AFJ+08] E.M. Alessi, A. Farrés, À. Jorba, C. Simó, and A. Vieiro. Efficient usage of self validated integrators for space applications. Ariadna final report, contract no. 20783/07/NL/CB, ESTEC (European Space Agency), 2008.

[AFJ+09] E.M. Alessi, A. Farrés, À. Jorba, C. Simó, and A. Vieiro. Jet transport and applications to NEOs. In *Proceedings of the 1st IAA Planetary Defense Conference: Protecting Earth from Asteroids*, Granada (Spain), 2009.

[And98] M.A. Andreu. *The Quasi-Bicircular Problem.* PhD thesis, Departament de Matemàtica Aplicada i Anàlisi. Universitat de Barcelona, October 1998.

[And02] M.A. Andreu. Dynamics in the center manifold around L_2 in the quasi-bicircular problem. *Celestial Mech.*, 84(2):105–133, 2002.

[Arn63a] V.I. Arnold. Proof of A.N. Kolmogorov's theorem on the preservation of quasi- periodic motions under small perturbations of the Hamiltonian. *Russian Math. Surveys*, 18(5):9–36, 1963.

[Arn63b] V.I. Arnold. Small denominators and problems of stability of motion in classical and celestial mechanics. *Russian Math. Surveys*, 18(6):85–191, 1963.

[BM98] M. Berz and K. Makino. Verified integration of ODEs and flows using differential algebraic methods on high-order Taylor models. *Reliable Computing*, 4:361–369, 1998.

[BMO09] E. Barrabés, J.M. Mondelo, and M. Ollé. Numerical continuation of families of homoclinic connections of periodic orbits in the rtbp. *Nonlinearity*, 22, 2009.

[BO06] E. Barrabés and M. Ollé. Invariant manifolds of L_3 and horseshoe motion in the Restricted Three-Body Problem. *Nonlinearity*, 19, 2006.

[Bro68] R. Broucke. Periodic orbits in the restricted three-body problem with Earth-Moon masses. Technical Report 32-1168, Jet Propulsion Laboratory, NASA, 1968.

[Cas03] E. Castellà. *Sobre la dinàmica prop dels punts de Lagrange del sistema Terra-Lluna.* PhD thesis, Departament de Matemàtica Aplicada i Anàlisi. Universitat de Barcelona, October 2003.

[CFdlL03a] X. Cabré, E. Fontich, and R. de la Llave. The parameterization method for invariant manifolds. I. Manifolds associated to non-resonant subspaces. 52(2):283–328, 2003.

[CFdlL03b] X. Cabré, E. Fontich, and R. de la Llave. The parameterization method for invariant manifolds. II. Regularity with respect to parameters. 52(2):329–360, 2003.

[CFdlL05] X. Cabré, E. Fontich, and R. de la Llave. The parameterization method for invariant manifolds. III. Overview and applications. *J. Differential Equations*, 218(2):444–515, 2005.

[CG91] A. Celletti and A. Giorgilli. On the stability of the Lagrangian points in the spatial restricted problem of three bodies. *CLDA*, 50:31–58, 1991.

[CJ00] E. Castellà and À. Jorba. On the vertical families of two-dimensional tori near the triangular points of the Bicircular problem. *Celestial Mech.*, 76(1):35–54, 2000.

[CRR64] J. Cronin, P.B. Richards, and L.H. Russell. Some periodic solutions of a four-body problem. *Icarus*, 3:423–428, 1964.

[CS00] P. Cincotta and C. Simó. Simple tools to study global dynamics in non-axisymmetric galactic potentials – I. *Astron. Astrophys. Suppl. Ser. 147:205-228*, 2000.

[DBDO05] R. P. Di Sisto, Á. Brunini, L. D. Dirani, and R. B. Orellana. Hilda asteroids among jupiter family comets. *Icarus*, 174(1):81–89, 2005.

[DM98] L. Dagum and R. Menon. OpenMP: an industry standard API for shared-memory programming. *Computational Science & Engineering, IEEE*, 5(1):46–55, 1998.

[Dua19] G. Duarte. *On the dynamics around the collinear points in the Sun-Jupiter System.* PhD thesis, Departament de Matemàtiques i Informática. Universitat de Barcelona, Nov 2019.

[Esc68] P. Escobal. *Methods of Astrodynamics.* J. Wiley & Sons, 1968.

[FJ05] M. Frigo and S. G. Johnson. The design and implementation of FFTW3. *Proceedings of the IEEE*, 93(2):216–231, 2005. Special issue on "Program Generation, Optimization, and Platform Adaptation".

[FR81] V. Franceschini and L. Russo. Stable and unstable manifolds of the Hénon mapping. *J. Statist. Phys.*, 25(4):757–769, 1981.

[FV04] D. Folta and F. Vaughn. A comprehensive survey of Earth-Moon libration orbits: Stationkeeping strategies and intra-orbit transfers. *Collection of Technical Papers - AIAA/AAS Astrodynamics Specialist Conference*, 1, 2004.

[GBD+95] A. Geist, A. Beguelin, J. Dongarra, W. Jiang, R. Manchek, and V. Sunderam. PVM: Parallel Virtual Machine: a users' guide and tutorial for networked parallel computing. *Computers in Physics*, 9:607–607, 1995.

[GBD+96] B. J. Gladman, J. A. Burns, M. J. Duncan, P. Lee, and H. F. Levison. The exchange of impact ejecta between terrestrial planets. *Science*, 271(5254):1387–1392, 1996.

[GBDL95] B. J. Gladman, J. A. Burns, M. J. Duncan, and H. F. Levison. The dynamical evolution of lunar impact ejecta. *Icarus*, 118(2):302 – 321, 1995.

[GDF+89] A. Giorgilli, A. Delshams, E. Fontich, L. Galgani, and C. Simó. Effective stability for a hamiltonian system near an elliptic equilibrium point, with an application to the restricted three body problem. *Journal of Differential Equations*, 77(1):167–198, 1989.

[GJ04] F. Gabern and À. Jorba. Generalizing the Restricted Three-Body Problem. The Bianular and Tricircular Coherent Problems. *Astron. Astrophys.*, 420:751–762, 2004.

[GJJC+21] J. Gimeno, À. Jorba, M. Jorba-Cuscó, N. Miguel, and M. Zou. Numerical integration of high order variational equations of ODEs. Preprint, 2021.

[GJMS01] G. Gómez, À. Jorba, J. Masdemont, and C. Simó. *Dynamics and mission design near libration points. Vol. IV, Advanced Methods for Triangular Points*, volume 5 of *World Scientific Monograph Series in Mathematics*. World Scientific Publishing Co. Inc., 2001.

[GJNO21] J. Gimeno, À. Jorba, B. Nicolás, and E. Olmedo. Numerical computation of high order expansions of invariant manifolds of high dimensional tori. Preprint, 2021.

[GLMS85] G. Gómez, J. Llibre, R. Martínez, and C. Simó. Station keeping of libration point orbits. ESOC contract 5648/83/D/JS(SC), final report, European Space Agency, 1985. Reprinted as *Dynamics and mission design near libration points. Vol. I, Fundamentals: the case of collinear libration points*, volume 2 of World Scientific Monograph Series in Mathematics, 2001.

[GLMS01] G. Gómez, J. Llibre, R. Martínez, and C. Simó. *Dynamics and mission design near libration points. Vol. I, Fundamentals: the case of collinear libration points*, volume 2 of *World Scientific Monograph Series in Mathematics*. World Scientific Publishing Co. Inc., 2001.

[GM01] G. Gómez and J.M. Mondelo. The dynamics around the collinear equilibrium points of the RTBP. *Physica D: Nonlinear Phenomena*, 157(4):283–321, 2001.

[GMM02] G. Gómez, J. J. Masdemont, and J. M. Mondelo. Solar system models with a selected set of frequencies. *Astronomy & Astrophysics*, 390(2):733–749, 2002.

[GMS10a] G. Gómez, J. M. Mondelo, and C. Simó. A collocation method for the numerical fourier analysis of quasi-periodic functions. i: Numerical tests and examples. *Discrete & Continuous Dynamical Systems - B*, 14(1):41–74, 2010.

[GMS10b] G. Gómez, J. M. Mondelo, and C. Simó. A collocation method for the numerical fourier analysis of quasi-periodic functions. ii: Analytical error estimates. *Discrete & Continuous Dynamical Systems - B*, 14(1):75–109, 2010.

[Gri00] A. Griewank. *Evaluating Derivatives*. SIAM, Philadelphia, Penn., 2000.

[GVJ12] M. Granvik, J. Vaubaillon, and R. Jedicke. The population of natural Earth satellites. *Icarus*, 218(1):262 – 277, 2012.

[HCL+16] A. Haro, M. Canadell, A. Luque, J.-M. Mondelo, and J.-Ll. Figueras. *The Parameterization Method for Invariant Manifolds. From Rigorous Results to Effective Computations*, volume 195 of *Applied Mathematical Sciences*. Springer-Verlag, 2016.

[HdlL06a] À. Haro and R. de la Llave. A parameterization method for the computation of invariant tori and their whiskers in quasi-periodic maps: numerical algorithms. *Discrete Contin. Dyn. Syst. Ser. B*, 6(6):1261–1300, 2006.

[HdlL06b] À. Haro and R. de la Llave. A parameterization method for the computation of invariant tori and their whiskers in quasi-periodic maps: rigorous results. *J. Differential Equations*, 228(2):530–579, 2006.

[HdlL07] À. Haro and R. de la Llave. A parameterization method for the computation of invariant tori and their whiskers in quasi-periodic maps: explorations and mechanisms for the breakdown of hyperbolicity. *SIAM J. Appl. Dyn. Syst.*, 6(1):142–207, 2007.

[Hua60] S.S. Huang. Very restricted four-body problem. Technical note TN D-501, Goddard Space Flight Center, NASA, 1960.

[HXSW15] X. Y. Hou, X. Xin, D. J. Scheeres, and J. Wang. Stable motions around triangular libration points in the real Earth-Moon system. *Mon. Not. R. Astron. Soc.*, 454(4):4172–4181, 2015. https://doi.org/10.1093/mnras/stv2216.

[JCFJ18] M. Jorba-Cuscó, À. Farrés, and À. Jorba. Two periodic models for the Earth-Moon system. *Front. Appl. Math. Stat.*, 4:32, 2018.

[JJCR20] À. Jorba, M. Jorba-Cuscó, and J.J. Rosales. The vicinity of the earth–moon l1 point in the bicircular problem. *Celestial Mech. Dynam. Astronom.*, 132, 2020.

[JN20] À. Jorba and B. Nicolás. Transport and invariant manifolds near L_3 in the Earth-Moon Bicircular model. *Communications in Nonlinear Science and Numerical Simulation*, 89:105327, 2020.

[JN21] À. Jorba and B. Nicolás. Using invariant manifolds to capture an asteroid near the L_3 point of the Earth-Moon Bicircular model. *Communications in Nonlinear Science and Numerical Simulation*, 102:105948, 2021.

[JO09] À. Jorba and E. Olmedo. On the computation of reducible invariant tori on a parallel computer. *SIAM J. Applied Dynamical Systems*, 8:1382–1404, 2009.

[Jor00] À. Jorba. A numerical study on the existence of stable motions near the triangular points of the real Earth-Moon system. *Astron. Astrophys.*, 364(1):327–338, 2000.

[Jor01] À. Jorba. Numerical computation of the normal behaviour of invariant curves of n-dimensional maps. *Nonlinearity*, 14(5):943–976, 2001.

[JPL] `https://ssd.jpl.nasa.gov/?horizons`.

[JS96] À. Jorba and C. Simó. On quasi-periodic perturbations of elliptic equilibrium points. *SIAM Journal on Mathematical Analysis*, 27, 1996.

[JV97a] À. Jorba and J. Villanueva. On the normal behaviour of partially elliptic lower dimensional tori of Hamiltonian systems. *Nonlinearity*, 10:783–822, 1997.

[JV97b] À. Jorba and J. Villanueva. On the persistence of lower dimensional invariant tori under quasi-periodic perturbations. *J. Nonlinear Sci.*, 7:427–473, 1997.

[JZ05] À. Jorba and M. Zou. A software package for the numerical integration of ODEs by means of high-order Taylor methods. *Exp. Math.*, 14(1):99–117, 2005.

[KKP+09] T. Kwiatkowski, A. Kryszczyńska, M. Polińska, D.A.H. Buckley, D. O'Donoghue, P.A. Charles, L. Crause, S. Crawford, Y. Hashimoto, A. Kniazev, N. Loaring, E. Romero Colmenero, R. Sefako, M. Still, and P. Vaisanen. Photometry of 2006 RH120: An asteroid temporary captured into a geocentric orbit. *Astron. Astrophys.*, 495(3):967–974, 2009.

[Kol54] A.N. Kolmogorov. On the persistence of conditionally periodic motions under a small change of the Hamilton function. *Dokl. Acad. Nauk. SSSR*, 98(4):"527–530", 1954.

[LNJ21] Y. Liang, B. Nicolás, and À. Jorba. Leveraging L_3 to transfer to L_4 in Sun-perturbed Earth-Moon system. *Acta Astronautica*, 189:337–348, 2021.

[LRMG14] N. Lladó, Y. Ren, J.J. Masdemont, and G. Gómez. Capturing small asteroids into a Sun-Earth Lagrangian point. *Acta Astron.*, 95(Supplement C):176–188, 2014.

[MHO09] K. Meyer, G. Hall, and D.C. Offin. *Introduction to Hamiltonian Dynamical Systems and the N-Body Problem*, volume 90 of *Applied Mathematical Sciences*. Springer-Verlag, New York, second edition, 2009.

[MIW+06] S. Mikkola, K. Innanen, P. Wiegert, M. Connors, and R. Brasser. Stability limits for the quasi-satellite orbit. *Monthly Notices of the Royal Astronomical Society*, 369(1):15–24, 2006.

[MMBM15] D.D. Mazanek, R.G. Merrill, J.R. Brophy, and R.P. Mueller. Asteroid redirect mission concept: A bold approach for utilizing space resources. *Acta Astronautica*, 117:163–171, 2015.

[Mon01] J.M. Mondelo. *Contribution to the Study of Fourier Methods for Quasi–Periodic Functions and the Vicinity of the Collinear Libration Points*. PhD thesis, Departament de Matemàtica Aplicada i Anàlisi. Universitat de Barcelona, May 2001.

[Mos62] J. Moser. On invariant curves of area-preserving mappings of an annulus. *Nachr. Akad. Wiss. Göttingen, II*, 2:1–20, 1962.

[O'L77] B. O'Leary. Mining the Apollo and Amor asteroids. *Science*, 197(4301):363–366, 1977.

[Olm07] E. Olmedo. *On the parallel computation of invariant tori*. PhD thesis, Departament de Matemàtica Aplicada i Anàlisi. Universitat de Barcelona, May 2007.

[Ope15] OpenMP Architecture Review Board. OpenMP Application Programming Interface Version 4.5, November 2015.

[RJJC21] J.J. Rosales, À. Jorba, and M. Jorba-Cuscó. Families of halo-like invariant tori around L_2 in the Earth-Moon Bicircular problem. *Celestial Mech. Dynam. Astronom.*, 2021.

[Ros20] J.J. Rosales. *On the effect of the Sun's gravity around the Earth-Moon L_1 and L_2 libration points*. PhD thesis, Departament de Matemàtiques i Informática. Universitat de Barcelona, Jun 2020.

[SB02] J. Stoer and R. Bulirsch. *Introduction to numerical analysis*, volume 12 of *Texts in Applied Mathematics*. Springer-Verlag, New York, third edition, 2002.

[SGJM95] C. Simó, G. Gómez, À. Jorba, and J. Masdemont. The Bicircular model near the triangular libration points of the RTBP. In A.E. Roy and B.A. Steves, editors, *From Newton to Chaos*, pages 343–370, New York, 1995. Plenum Press.

[SGYAM12] J.P. Sánchez, D. García Yárnoz, E. M. Alessi, and C.R. McInnes. Gravitational capture opportunities for asteroid retrieval missions. volume 7, 2012.

[Sim89] C. Simó. Estabilitat de sistemes Hamiltonians. *Mem. Real Acad. Cienc. Artes Barcelona*, 48(7):303–348, 1989.

[Sim98] C. Simó. Invariant curves of analytic perturbed nontwist area preserving maps. *Regul. Chaotic Dyn.*, 3:180–195, 1998.

[SNU18] J.P. Sánchez, R. Neves, and H. Urrutxua. Trajectory design for asteroid retrieval missions: A short review. *Frontiers in Applied Mathematics and Statistics*, 4:44, 2018.

[SSST13] C. Simó, P. Sousa-Silva, and M. Terra. Practical stability domains near $L_{4,5}$ in the restricted three-body problem: some preliminary facts. In *Progress and challenges in dynamical systems*, volume 54 of *Springer Proc. Math. Stat.*, pages 367–382. Springer, Heidelberg, 2013.

[Sze67] V. Szebehely. *Theory of Orbits*. Academic Press, 1967.

[TMC17] M. Tan, C McInnes, and M Ceriotti. Direct and indirect capture of near-Earth asteroids in the Earth-Moon system. *Celestial Mechanics and Dynamical Astronomy*, 129:57–88, 2017.

[USB+14] H. Urrutxua, D. Scheeres, C. Bombardelli, J.L. Gonzalo, and J. Pelaez. What does it take to capture an asteroid? a case study on capturing asteroid 2006 rh120. *Advances in the Astronautical Sciences*, 152:1117–1136, 2014.

[Ver78] J.H. Verner. Explicit Runge-Kutta methods with estimates of the local truncation error. *SIAM J. Numer. Anal.*, 15(4):772–790, 1978.

[VMC20] M. Vergaaij, C.R. McInnes, and M. Ceriotti. Economic assessment of high-thrust and solar-sail propulsion for near-earth asteroid mining. *Advances in Space Research*, 2020.

[Wil65] J. H. Wilkinson. *The algebraic eigenvalue problem.* Clarendon Press, Oxford, 1965.

[WZ12] D. Wilczak and P. Zgliczyński. Cr-Lohner algorithm. *Schedae Informaticae*, 2011(20):9–42, 2012.